Doctoral Dissertation
博士論文

A search for $\mu^+ \to e^+\gamma$ with the highest sensitivity beyond the MEG experiment

（MEG実験を超える最高感度での$\mu^+ \to e^+\gamma$探索）

A Dissertation Submitted for the Degree of Doctor of Philosophy

May 2025

令和 7 年 5 月博士（理学）申請

Department of Physics, Graduate School of Science,
The University of Tokyo

東京大学大学院理学系研究科物理学専攻

Kensuke Yamamoto
山本 健介

Abstract

The lepton-flavour-violating muon decay $\mu^+ \to e^+\gamma$ has been searched for in several decades as a probe of new physics beyond the Standard Model of particle physics. The MEG II experiment in search of $\mu^+ \to e^+\gamma$ has collected data since 2021. This thesis presents a search for $\mu^+ \to e^+\gamma$ with a sensitivity of 2.2×10^{-13} using 1.34×10^{14} muons observed in 2021 and 2022 in the MEG II experiment, with excellent detector performance maintained during the long-term data-taking. The sensitivity is better by a factor of 2.4 than that of the predecessor experiment, MEG. No signal excess was found, yielding an upper limit on the branching ratio of

$$\mathcal{B}(\mu^+ \to e^+\gamma) < 1.5 \times 10^{-13}$$

at 90 % confidence level. This is the most stringent upper limit to date.

Contents

Preface

The Standard Model (SM) of elementary particle physics describes the fundamental structure of matter. It has achieved remarkable success in experimental validations and predictions. The SM, however, has crucial theoretical problems and cannot explain several experimental results. Therefore, it is expected that a more fundamental model than the SM is in existence, and the construction and experimental validation of the new physics model are desired.

The charged-lepton-flavour-violating muon decay $\mu^+ \to e^+\gamma$ is an interesting probe to search for new physics. Many promising new physics models predict experimentally reachable branching ratios of the decay, while the SM prohibits it by the lepton flavour conservation law. The decay has never been observed, even though many experimental searches have been conducted. The latest search was performed by the MEG experiment and its upgraded experiment, MEG II, which started data-taking in 2021. It had no excess and yielded the upper limit on the branching ratio of 3.1×10^{-13} (90 % confidence level) with the full MEG data and the first MEG II data [1, 2].

The main theme of this thesis is a search for $\mu^+ \to e^+\gamma$ with the MEG II data collected in 2021 and 2022, with a sensitivity of 2.2×10^{-13}, the highest to date. The MEG II experiment conducted long-term data-taking for four months in 2022, and the number of observed muon decays in this dataset was increased by a factor of five compared to the previous result with the 2021 data. Careful calibration of the detector is required to maintain the detector's performance during long-term data-taking. In addition to the increase in the statistics with the excellent detector performance, event reconstruction algorithms were upgraded to further suppress background events.

This thesis is organised as follows. Chapter 1 introduces to physics motivation of $\mu^+ \to e^+\gamma$ searches and experimental searches for the decay. Chapter 2 describes the MEG II apparatus and Chap. 3 summarises the physics and calibration runs in 2021 and 2022. Chapter 4 explains event reconstruction algorithms, and Chap. 5 describes the algorithm upgrade to further suppress photon background. Chapter 6 describes methods to calibrate the detectors, and Chap. 7 shows the detector performance with the described reconstruction and calibration methods. Chapter 8 describes the likelihood analysis to search for $\mu^+ \to e^+\gamma$. The results and possible improvements are described in Chap. 9. Finally, Chap. 10 concludes this thesis.

Chapter 1

Introduction to $\mu^+ \to e^+\gamma$

The charged-lepton-flavour-violating muon decay, $\mu^+ \to e^+\gamma$, is a probe to search for new physics. This is why the decay has been searched for in the past several decades. This chapter introduces the physics motivation behind $\mu^+ \to e^+\gamma$ searches and experimental searches for this decay.

1.1 Physics motivation of $\mu^+ \to e^+\gamma$ search

The Standard Model (SM) of particle physics describing the fundamental structure of matter has achieved remarkable success so far. It, however, has several fundamental theoretical and experimental problems. This is why the SM is regarded as a low-energy approximation of a more complete theory that describes higher-energy physics well.

One of the theoretical problems is the hierarchy problem: a huge discrepancy between the electroweak scale (10^2 GeV) and the reduced Planck scale (10^{18} GeV), where quantum gravitational effects become important [3, 4, 5, 6]. If the SM is required to remain valid up to very high energies (e.g., the Planck scale) while maintaining a Higgs mass of (125.20 ± 0.11) GeV [7], the radiative corrections become quadratically divergent as a function of the energy scale. As a result, one needs a very precise fine-tuning between the bare mass of the Higgs scalar and its radiative corrections. This is not really a difficulty with the SM itself, but unnatural. Phenomenological applications of Supersymmetry (SUSY) theories [8] have been considered since the late 1970s in connection with the hierarchy problem. Another theoretical problem with the SM is about descriptions of the four fundamental forces: electromagnetic, weak, strong, and gravity. The SM describes electroweak and strong interactions separately, while a more unified description of the forces is attractive. The physics models aiming at the grand unification have been constructed [9].

From the experimental point of view, phenomena that the SM cannot explain have been observed, for instance, the existence of dark matter [10]. New particles not in the SM but predicted in the new physics models, e.g. SUSY particles, are always considered candidates for dark matter. The SM, assuming massless neutrinos, also cannot explain neutrino oscillation, which needs non-zero neutrino mass [11].

The above problems have motivated us to construct new physics models beyond the SM, such as SUSY. I focus on lepton flavour (e, μ, τ) as a probe to experimentally validate the new models. The SM has the lepton flavour conservation law. However, some recognise the conservation as accidental, expecting a violation of the conservation law: lepton flavour violation (LFV). Several concrete new physics models beyond the SM predict the LFV in the charged lepton sector, charged lepton flavour violation (CLFV). Great theoretical and/or experimental reviews were published [12, 13, 14, 15, 16]. The experimental CLFV searches with muons have three golden channels:

Table 1.1: Muon decay modes in the SM.

Decay	Branching ratio	Remarks
Michel decay $\mu \to e\nu\bar{\nu}$	~ 1	–
Radiative decay $\mu \to e\nu\bar{\nu}\gamma$	$(6.0 \pm 0.5) \times 10^{-8}$ [17]	$E_e > 45\,\mathrm{MeV}$ and $E_\gamma > 40\,\mathrm{MeV}$
	$(1.4 \pm 0.4) \times 10^{-2}$ [18]	$E_\gamma > 10\,\mathrm{MeV}$
$\mu \to e\bar{\nu}_e\nu_\mu e\bar{e}$	$(3.4 \pm 0.4) \times 10^{-5}$ [19]	–

- $\mu \to e\gamma$,
- μ–e conversion ($\mu N \to eN$), and
- $\mu \to eee$.

Here, particle-antiparticle symmetry is assumed to be perfect. The following subsections introduce muon decays in the SM (Sect. 1.1.1) and in new physics frameworks (Sect. 1.1.2, 1.1.3) regardless of particles' charge, discussing the physics motivation behind the $\mu^+ \to e^+\gamma$ search.

1.1.1 Muon decay in the Standard Model

In the SM, the muon is the second-generation charged lepton, a 200 times heavier replica of an electron. It interacts through the electromagnetic and weak interactions and couples to the Higgs boson for mass generation. The Lagrangian for those interactions are given by

$$\begin{aligned}
\mathcal{L} &= e\bar{\mu}\gamma^\mu \mu A_\mu \\
&- \frac{g}{\sqrt{2}}\left(\bar{\nu}_{\mu L}\gamma^\mu \mu_L W^+_\mu + \bar{\mu}_L\gamma^\mu \nu_{\mu L} W^-_\mu\right) \\
&- \sqrt{g^2+g'^2}\left\{\bar{\mu}_L\gamma^\mu\left(-\frac{1}{2}+\sin^2\theta_W\right)\mu_L + \bar{\mu}_R\gamma^\mu \sin^2\theta_W \mu_R\right\} Z^0_\mu \\
&- \frac{m_\mu}{v}\bar{\mu}\mu H,
\end{aligned} \tag{1.1}$$

where g (g') is the gauge-coupling constant for SU(2) (U(1)); the Weinberg angle θ_W is defined by $\sin\theta_W = g'/\sqrt{g^2+g'^2}$; A denotes an electromagnetic field; $W^\pm$ and Z^0 are the gauge bosons in a weak interaction; m_μ is the muon mass ($(105.658\,375\,5 \pm 0.000\,002\,3)$ MeV [7]); v is a vacuum expectation value of the Higgs field (246.22 GeV [7]); and H denotes the Higgs boson field. Muon decay is described by a charged weak-current interaction mediated by the $W^\pm$ boson, expressed in the second line of Eq. (1.1). Table 1.1 summarises the decay modes and their branching ratios.

When considering neutrinos' non-zero mass and their mixing, the charged-lepton-flavour-violating $\mu \to e\gamma$ can occur via neutrino oscillation as shown in Fig. 1.1 [20, 21]. The branching ratio is, however, strongly suppressed due to tiny neutrino masses ($< 0.45\,\mathrm{eV}\,c^{-2}$ (90 % confidence level (C.L.)) [22]) as

$$\mathcal{B}(\mu \to e\gamma) = \frac{3\alpha}{32\pi}\left|\sum_{i=2,3} U^*_{\mu i}U_{ei}\frac{\Delta m^2_{i1}}{M^2_W}\right|^2 \sim 10^{-54}, \tag{1.2}$$

where α is the fine-structure constant; U is the Pontecorvo-Maki-Nakagawa-Sakata mixing matrix [23, 24]; Δm^2_{ij} is squared difference of neutrino masses; and M_W is a mass of W boson. Current detector technologies cannot reach the sensitivity of 10^{-54}.

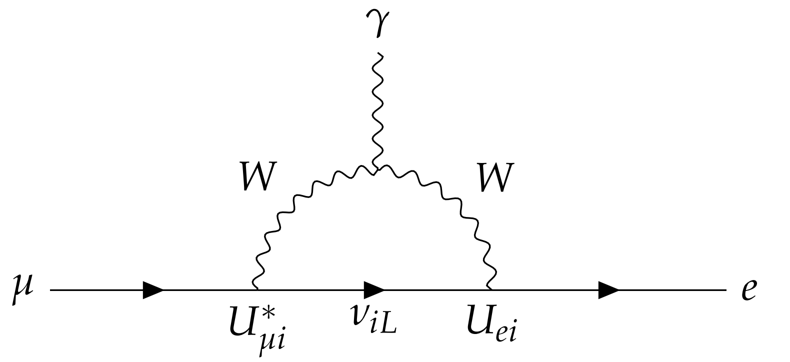

Figure 1.1: Feynman diagram for $\mu \to e\gamma$ via neutrino oscillation [16].

1.1.2 Model-independent approach to charged lepton flavour violation

In an extension of the SM, the effective Lagrangian for $\mu \to e\gamma$ (of a dipole-interaction type) can be given by [14, 25]

$$\mathcal{L}_D = y_D \frac{e m_\mu}{\Lambda_D^2} \left(\bar{\mu}_R \sigma^{\mu\nu} e_L + \bar{\mu}_L \sigma^{\mu\nu} e_R\right) F_{\mu\nu} + \text{h.c.}, \tag{1.3}$$

where Λ_D is an energy scale of new physics, y_D is an effective coupling constant, and $F_{\mu\nu}$ is the photon field strength. The subscripts L, R indicate the chirality of the different SM fermion fields. When the new interaction occurs at a tree level ($y_D \sim 1$), the branching ratio of $\mu \to e\gamma$ can be calculated as

$$\mathcal{B}(\mu \to e\gamma) = (1 \times 10^{-11}) \times \left(\frac{400\,\text{TeV}}{\Lambda_D}\right)^4 \left(\frac{y_D}{1}\right)^2, \tag{1.4}$$

and a search for $\mu \to e\gamma$ is sensitive to very high energy scale like $\mathcal{O}(100\,\text{TeV})$. On the other hand, when the new interaction occurs at a loop level and the effective coupling constant y_D is represented as $\theta_{\mu e} g^2/16\pi^2$ with an effective coupling parameter of new physics $\theta_{\mu e}$, the branching ratio is given by

$$\mathcal{B}(\mu \to e\gamma) = (1 \times 10^{-11}) \times \left(\frac{2\,\text{TeV}}{\Lambda_D}\right)^4 \left(\frac{\theta_{\mu e}}{10^{-2}}\right)^2. \tag{1.5}$$

It is sensitive to physics at $\mathcal{O}(1\,\text{TeV})$ with small effective coupling parameter $\theta_{\mu e}$ of 10^{-2} level. It would be the case for low-energy SUSY.

I can also consider an effective four-fermion interaction whose Lagrangian is given by[1]

$$\mathcal{L}_F = y_F \frac{1}{\Lambda_F^2} \left(\bar{\mu}_L \gamma^\mu e_L + \bar{\mu}_R \gamma^\mu e_R\right) \bar{f} \gamma_\mu f + \text{h.c.}, \tag{1.6}$$

where y_F and Λ_F are an effective coupling and an energy scale of new physics, respectively; and f is any SM fermions, which could be an electron for $\mu \to eee$ or light quarks for μ–e conversion. With an introduction of κ parameter representing the relative magnitudes for the dipole and the effective four-fermion interactions, one can combine the Lagrangians of Eq. (1.3) and Eq. (1.6), by [27],

$$\begin{aligned} \mathcal{L} &= \mathcal{L}_D + \mathcal{L}_F \\ &= \frac{m_\mu}{(\kappa+1)\Lambda^2} \left(\bar{\mu}_R \sigma^{\mu\nu} e_L + \bar{\mu}_L \sigma^{\mu\nu} e_R\right) F_{\mu\nu} \\ &\quad + \frac{\kappa}{(\kappa+1)\Lambda^2} \left(\bar{\mu}_L \gamma^\mu e_L + \bar{\mu}_R \gamma^\mu e_R\right) \bar{f} \gamma_\mu f + \text{h.c.}, \end{aligned} \tag{1.7}$$

[1] The most general effective Lagrangian including several other terms is given by Ref. [26].

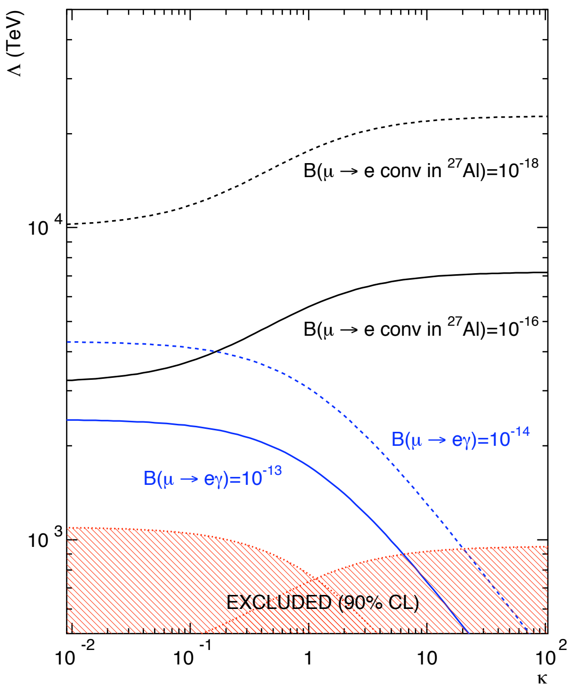

(a) μ–e conversion.

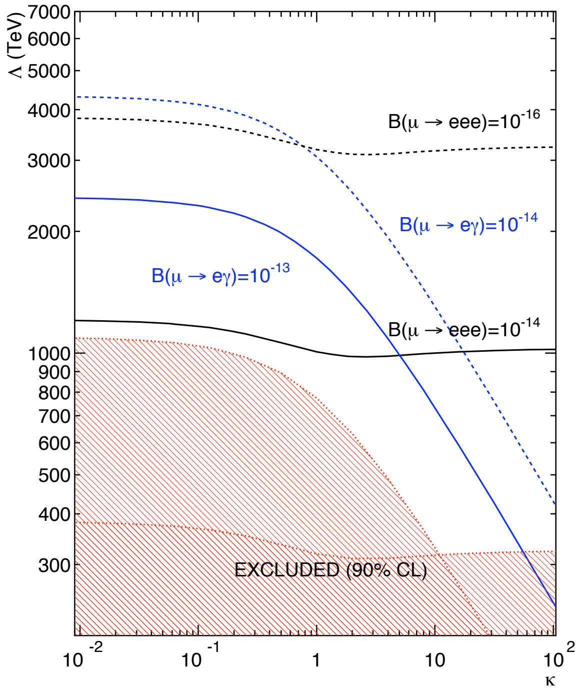

(b) $\mu \to eee$.

Figure 1.2: Sensitivity of muon CLFV golden channels to the new physics scale Λ as a function of κ, as defined in Eq. (1.7) [25]. The parameter κ interpolates between an effective dipole interaction ($\kappa \ll 1$) and an effective four-fermion interaction ($\kappa \gg 1$). Depicted is the excluded region of this parameter space as of when Ref. [25] was published.

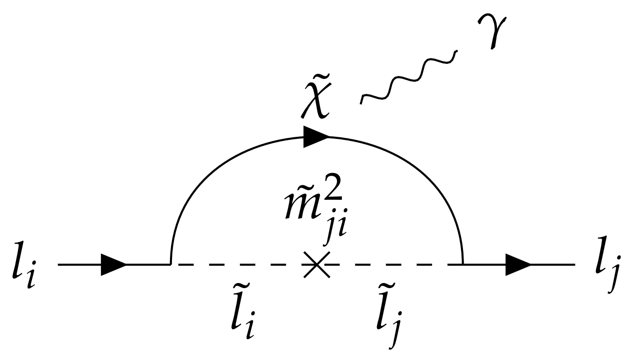

Figure 1.3: $l_i \to l_j\gamma$ in SUSY through sleptons mass mixing [16]. $\tilde{\chi}$ correspond to charginos and neutralinos (mass eigenstates of electroweak gauginos and higgsinos).

where κ and Λ are defined as

$$\kappa = \frac{y_F}{e y_D}\left(\frac{\Lambda_D^2}{\Lambda_F^2}\right), \tag{1.8}$$

$$\Lambda^2 = \frac{\Lambda_D^2 \Lambda_F^2}{y_F \Lambda_F^2 + y_D e \Lambda_D^2}. \tag{1.9}$$

Figure 1.2 shows the sensitivities of the muon CLFV golden channels to the new physics scale Λ as a function of κ. While $\mu \to e\gamma$ is sensitive to the region of $\kappa \ll 1$, μ–e conversion and $\mu \to eee$ are sensitive to the region of $\kappa \gg 1$. The three golden channels of CLFV with muons are, therefore, complementary to each other as a probe for new physics.

Let me concentrate on $\mu \to e\gamma$ among the muon CLFV golden channels. The effective Lagrangian for the dipole-type $\mu \to e\gamma$ process of Eq. (1.3) can be written using $A_{R(L)}$, the polarisation-dependent coupling constant that corresponds to $\mu \to e_{R(L)}\gamma$, by [28],

$$\mathcal{L}_{\mu\to e\gamma} = -\frac{4G_F}{\sqrt{2}}\left(m_\mu A_R \bar{\mu}_R \sigma^{\mu\nu} e_L F_{\mu\nu} + m_\mu A_L \bar{\mu}_L \sigma^{\mu\nu} e_R F_{\mu\nu} + \text{h.c.}\right), \tag{1.10}$$

where G_F is the Fermi coupling constant; and $e_{R(L)}$ is a right-handed (left-handed) electron. When the initial muon is polarised in $\mu^+ \to e^+\gamma$, the angular distribution of the branching ratio of $\mu^+ \to e^+\gamma$ is given by

$$\frac{d\mathcal{B}(\mu^+ \to e^+\gamma)}{d(\cos\theta_e)} = 192\pi^2\left[|A_R|^2(1 - P_\mu \cos\theta_e) + |A_L|^2(1 + P_\mu\cos\theta_e)\right], \tag{1.11}$$

where θ_e is the angle between the muon polarisation and the positron momentum, and P_μ is the magnitude of the muon spin polarisation.

The total branching ratio behaves proportionally to $|A_R|^2 + |A_L|^2$. On the other hand, a measurement of the positron emission angle distribution with polarised muons would give the relative amplitudes of A_R and A_L. As discussed in Sect. 1.1.3, the ratio A_R/A_L depends on new physics models predicting $\mu \to e\gamma$.

1.1.3 $\mu \to e\gamma$ predicted by models beyond the Standard Model

A sizable branching ratio of $\mu \to e\gamma$ is predicted in the supersymmetric grand unified theory (GUT) (SUSY-GUT) ([29, 30] for SU(5) and [31, 32] for SO(10)) and supersymmetric seesaw (SUSY-seesaw) models [33, 31, 34]. As shown in Fig. 1.3, CLFV would occur via the mixing of sleptons $\tilde{l}$ induced by non-zero off-diagonal elements in the slepton mass matrix, given by

$$m_{\tilde{l}}^2 = \begin{pmatrix} m^2_{\tilde{e}\tilde{e}} & \Delta m^2_{\tilde{e}\tilde{\mu}} & \Delta m^2_{\tilde{e}\tilde{\tau}} \\ \Delta m^2_{\tilde{\mu}\tilde{e}} & m^2_{\tilde{\mu}\tilde{\mu}} & \Delta m^2_{\tilde{\mu}\tilde{\tau}} \\ \Delta m^2_{\tilde{\tau}\tilde{e}} & \Delta m^2_{\tilde{\tau}\tilde{\mu}} & m^2_{\tilde{\tau}\tilde{\tau}} \end{pmatrix}, \tag{1.12}$$

where $\Delta m^2_{\tilde{l}_i\tilde{l}_j}$ (l is a lepton flavour and $i \neq j$) is an off-diagonal slepton mass matrix element.

The following discusses $\mu^+ \to e^+\gamma$ in specific models with SUSY, with reference to Ref. [26]. In the SU(5) SUSY-GUT model, quarks and leptons are classified in the three generations of $\bar{\mathbf{5}}$ and **10** representations, including superpartners. As the **10** representations containing up-type quarks and right-handed charged leptons contribute to the renormalisation from the Planck scale to the GUT scale, the off-diagonal elements of the right-handed slepton mass matrix are given by

$$\Delta m_{\tilde{l}_{R,i}\tilde{l}_{R,j}} \sim -\frac{3}{8\pi^2}(V_R)_{i3}(V_R^*)_{j3}|(y_u)_{33}|^2 m_0^2(3+|A_0|^2)\log\left(\frac{M_P}{M_{\mathrm{GUT}}}\right), \tag{1.13}$$

where V is the Cabibbo-Kobayashi-Maskawa (CKM) matrix at the GUT scale; y is the Yukawa coupling; m_0 and A_0 are the SUSY breaking mass parameter and their coupling; and $M_{P(\mathrm{GUT})}$ is the reduced Planck (GUT) energy scale. Since the slepton mixing appears only in the right-handed slepton sector, only $\mu^+ \to e^+_L\gamma$ occurs in this model. On the other hand, the SUSY-seesaw model introducing heavy right-handed neutrinos gives the off-diagonal elements of the left-handed slepton mass matrix as

$$\Delta m_{\tilde{l}_{L,i}\tilde{l}_{L,j}} = -\frac{1}{8\pi^2}(y_\nu^*)_{ki}(y_\nu)_{kj} m_0^2(3+|A_0|^2)\log\left(\frac{M_P}{M_R}\right), \tag{1.14}$$

where y_ν is a new Yukawa coupling matrix and M_R is the Majorana mass scale. Contrary to the SU(5) SUSY-GUT model, the slepton mixing appears only in the left-handed slepton sector because the left-handed sleptons are coupled with the heavy right-handed Majorana neutrinos by the new Yukawa coupling y_ν. Therefore, only $\mu^+ \to e^+_R\gamma$ occurs. In the SO(10) SUSY-GUT model, which naturally includes the seesaw mechanism, both left- and right-handed slepton have flavour mixing. Thus, a larger contribution to $\mu^+ \to e^+\gamma$ can be expected.

The above models with different slepton flavour mixing calculate different amplitudes in Eq. (1.11). The SU(5) SUSY-GUT predicts a vanishing A_R and non-zero A_L, yielding a $(1+P_\mu\cos\theta_e)$ distribution. On the other hand, for the SUSY-seesaw model, A_R is non-zero but A_L vanishes, giving a $(1-P_\mu\cos\theta_e)$ distribution. The SO(10) SUSY-GUT model predicts $A_R \sim A_L \neq 0$. If multiple signal events are expected to be detected, once $\mu \to e\gamma$ would be discovered, a measurement of the positron emission angle distribution enables the selection of physics models.

1.2 Principle of experimental searches for $\mu^+ \to e^+\gamma$

The principle of experimental $\mu^+ \to e^+\gamma$ searches is to precisely measure decay products from muons stopped in a material. For experimental reasons, discussed in Sect. 1.2.3, I search for positive anti-muons decaying to positrons and photons, $\mu^+ \to e^+\gamma$. Hereafter, signs are not explicitly written in this thesis, but μ (e) usually stands for positive anti-muon μ^+ (positron e^+). This section describes the event signature of $\mu \to e\gamma$ and backgrounds.

1.2.1 Signal kinematics

The decay $\mu \to e\gamma$ is a simple two-body decay. The kinematics are summarised as follows:

- Decay positron and photon have a monochromatic momentum of 52.83 MeV/c, which is a half of muon mass.
- Positron and photon decay back-to-back.
- Positron and photon are emitted at the same time.

The expected number of signal events N_{sig} can be expressed with the branching ratio of $\mu \to e\gamma$ $\mathcal{B}$ as

$$N_{\text{sig}} = k \cdot \mathcal{B} \tag{1.15}$$
$$k = R_{\mu} \cdot T \cdot \Omega \cdot \varepsilon_{\text{e}} \cdot \varepsilon_{\gamma} \tag{1.16}$$

where R_{μ} is the muon stopping rate at the target, T is measurement time, Ω is geometric acceptance, and $\varepsilon_{\text{e}(\gamma)}$ is the detection efficiency for positron (photon). The factor k corresponds to the number of effectively measured muon decays in an experiment. This is called the normalisation factor in this thesis.

1.2.2 Backgrounds

There are two major backgrounds mimicking the $\mu \to e\gamma$ signal. One is a physics background from radiative muon decay (RMD) $\mu \to e\nu\bar{\nu}\gamma$. The other is an accidental coincidence of a positron and a photon from different parent muons.

Physics background

A radiative decay $\mu \to e\nu\bar{\nu}\gamma$ becomes a physics background when the positron and photon are emitted back-to-back, with two neutrinos carrying off little energy. The differential branching ratio of RMD was calculated by several authors [35, 36] and measured as listed in Table 1.1.

Here, let me focus on interesting kinematic regions: both positron and photon energies are close to half of the muon mass. By defining positron (photon) energy normalised by a half of muon mass as $x = 2E_{\text{e}}/m_{\mu}$ ($y = 2E_{\gamma}/m_{\mu}$) for the below discussion, the regions are expressed by $x \sim 1$ and $y \sim 1$. In these energy regions, an opening angle between positron and photon $\Theta_{\text{e}\gamma}$ is almost 180°; $z = \pi - \Theta_{\text{e}\gamma} \sim 0$. Given the detector resolutions, the effective branching ratio of the RMD can be evaluated by integrating the differential branching ratio over the analysis region. Let me take δx, δy, and δz to be the kinematic range of the signal region for positron energy ($1 - \delta x \leq x \leq 1$), that for photon energy ($1 - \delta y \leq y \leq 1$), and that for the opening angle ($0 \leq z \leq \delta z$), respectively. The partial branching ratio after the integration over x, y and z is given by [28],

$$\mathrm{d}\mathcal{B}(\mu \to e\nu\bar{\nu}\gamma) = \frac{\alpha}{16\pi}\left[J_1(1 - P_{\mu}\cos\theta_{\text{e}}) + J_2(1 + P_{\mu}\cos\theta_{\text{e}})\right]\mathrm{d}(\cos\theta_{\text{e}}), \tag{1.17}$$

where J_1 and J_2 in Eq. (1.17) are given by

$$J_1 = \frac{8}{3}(\delta x)^3(\delta y)\left(\frac{\delta z}{2}\right)^2 - 2(\delta x)^2\left(\frac{\delta z}{2}\right)^4 + \frac{1}{3}\frac{1}{(\delta y)^2}\left(\frac{\delta z}{2}\right)^8, \tag{1.18}$$

$$J_2 = 8(\delta x)^2(\delta y)^2\left(\frac{\delta z}{2}\right)^2 - 8(\delta x)(\delta y)\left(\frac{\delta z}{2}\right)^4 + \frac{8}{3}\left(\frac{\delta z}{2}\right)^6, \tag{1.19}$$

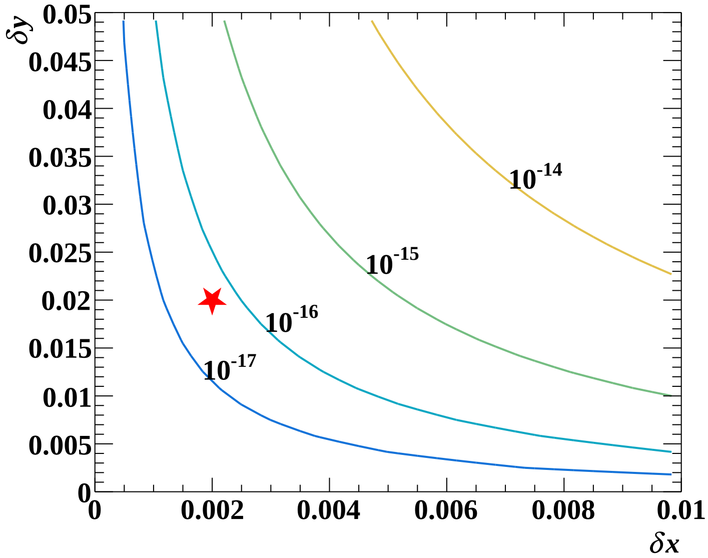

Figure 1.4: Effective branching ratio of radiative decay as a function of δx and δy calculated with Eq. (1.17). In our case ($\delta x \sim 0.2\,\%$ and $\delta y \sim 2\,\%$) shown as a solid star, the effective branching ratio of RMD is suppressed down to $\mathcal{O}(10^{-16})$.

when the angular resolution is better than the kinematically allowed angle of $2\sqrt{\delta x \delta y}$. This assumption fits into our case.

Figure 1.4 shows the effective branching ratio of RMD as a function of energy resolutions δx and δy. In our MEG II case ($\delta x \sim 0.2\,\%$ and $\delta y \sim 2\,\%$), the branching ratio is suppressed down to $\mathcal{O}(10^{-16})$. The physics background makes a limited contribution to the $\mu \to e\gamma$ search with a sensitivity of $\mathcal{O}(10^{-14})$.

Accidental background

An accidental coincidence of a positron and a photon from different parent muons can mimic the signal signature under a high-intensity environment. This background is dominant in the MEG II experiment. The positron source is the normal muon decay $\mu \to e\nu\bar{\nu}$, called the Michel decay. On the other hand, the photon source is the radiative decay $\mu \to e\nu\bar{\nu}\gamma$ and positron annihilation with electrons in a material $e^+e^- \to \gamma\gamma$.

The effective branching ratio of the accidental background can be estimated by [26],

$$\mathcal{B}_{\mathrm{ACC}} = R_\mu \cdot f_e^0 \cdot f_\gamma^0 \cdot (2\delta t_{e\gamma}) \cdot \frac{(\delta\Theta_{e\gamma})^2}{4}, \tag{1.20}$$

where R_μ is an instantaneous muon stopping rate; $f^0_{e(\gamma)}$ is the integrated fraction of positron (photon) spectrum within the signal region; $\delta t_{e\gamma}$ is the half-width of the time window; and $\delta\Theta_{e\gamma}$ is the angular resolution. Integrating the Michel spectrum having a flat distribution near $m_\mu/2$ and a sharp edge at higher energy side over $1 - \delta x \le x \le 1$ yields $f_e^0 \sim 2\delta x$. As for f_γ^0, if the radiative decay is considered as a source of the 52.8 MeV photon, it can be roughly given by [38],

$$f_\gamma^0 \approx \left(\frac{\alpha}{2\pi}\right)(\delta y)^2[\ln(\delta y) + 7.33]. \tag{1.21}$$

Equation (1.21) shows that f_γ^0 for the decay $\mu \to e\nu\bar{\nu}\gamma$ is roughly proportional to $(\delta y)^2$. From the above, the effective branching ratio of the accidental background Eq. (1.20) is summarised with the

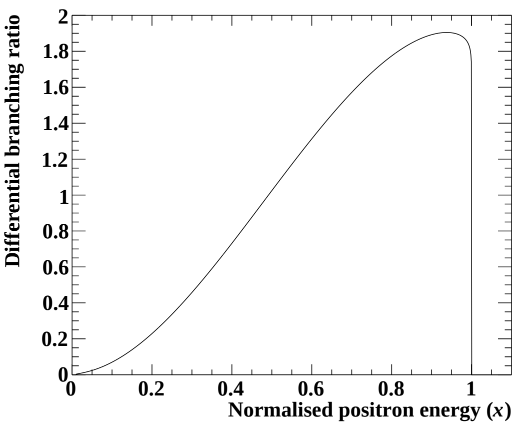

Figure 1.5: Michel spectrum calculated in [37].

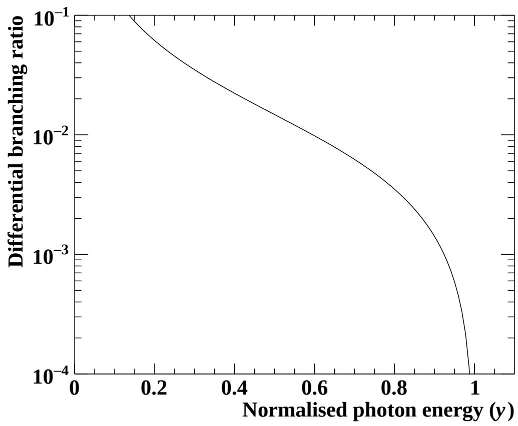

Figure 1.6: Differential branching ratio of the radiative decay $\mu \to e\nu\bar{\nu}\gamma$ as a function of photon energy y calculated with Eq. (1.17).

detector resolutions by

$$\mathcal{B}_{\mathrm{ACC}} \approx R_{\mu} \cdot (2\delta x) \cdot \left(\frac{\alpha}{2\pi}(\delta y)^2[\ln(\delta y) + 7.33]\right) \cdot (2\delta t_{e\gamma}) \cdot \frac{(\delta\Theta_{e\gamma})^2}{4}. \tag{1.22}$$

Equations (1.16), (1.22) indicate the number of accidental background events N_{ACC} is proportional to the squared muon stopping rate R_{μ}^2.

Let me further discuss the photon background. In radiative decays with a high photon energy, the positron energy is generally low due to kinematic constraints. Figure 1.7 shows the differential branching ratio as a function of the positron energy with photon energy of $0.9 < y < 1$. Coincident detection of low-energy positrons and high-energy photons allows us to identify the radiative decay event, suppressing the RMD photon background.

The other sources of high-energy photons are annihilation in flight (AIF) of positrons in Michel decay and external bremsstrahlung. The contribution from positron AIF depends on the materials along the positron's trajectory, depending on the experimental setup. This is discussed in Sect. 5.1.

1.2.3 Experimental requirements

Efficient experimental search for $\mu \to e\gamma$ requires suppressing the accidental background. A continuous muon beam is advantageous because of $N_{\mathrm{ACC}} \propto R_{\mu}^2$. Concerning a muon charge, negative muons (μ^-) form bound states in muonic atoms when captured by nuclei. This induces the nuclear recoil in muon decays, spoiling the kinematical simplicity of two-body decay. Therefore, positive anti-muons (μ^+) are preferred for use, and one searches for $\mu^+ \to e^+\gamma$ in experiments. Another key to suppressing the accidental background is the excellent detector resolution described in Eq. (1.22).

1.3 Past experiments in search of $\mu \to e\gamma$

A long quest for $\mu \to e\gamma$ started in the 1940s. Since then, no experiment has found the decay, and the experimental upper limits on the branching ratio of $\mu \to e\gamma$ have been established, as shown in Fig. 1.8. Especially, theoretical predictions, discussed in Sect. 1.1, have motivated experimental searches.

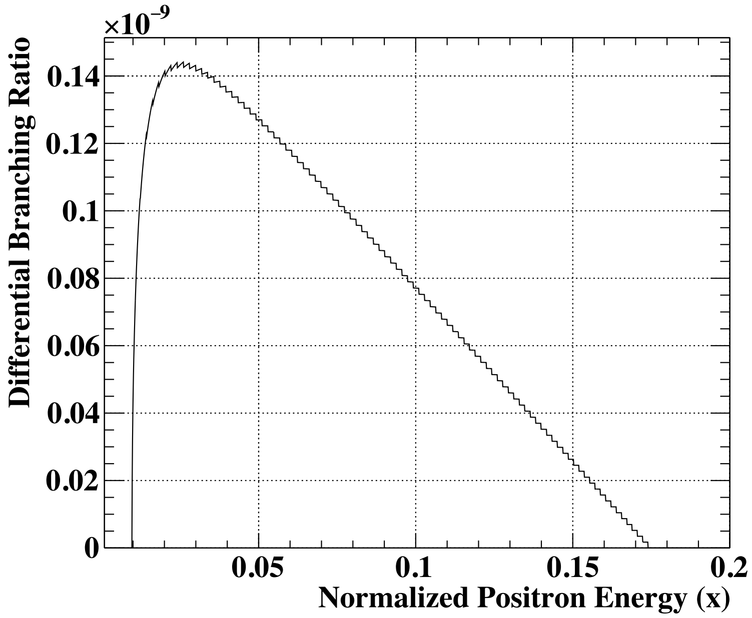

Figure 1.7: Differential branching ratio of the RMD as a function of the positron energy with photon energy $y \in [0.9, 1]$ [39]. The muon spin polarisation is set to -0.86, which is the measured value in the MEG experiment [40]. The lower edge of the distribution is given by the kinematics of $2m_e/m_\mu$.

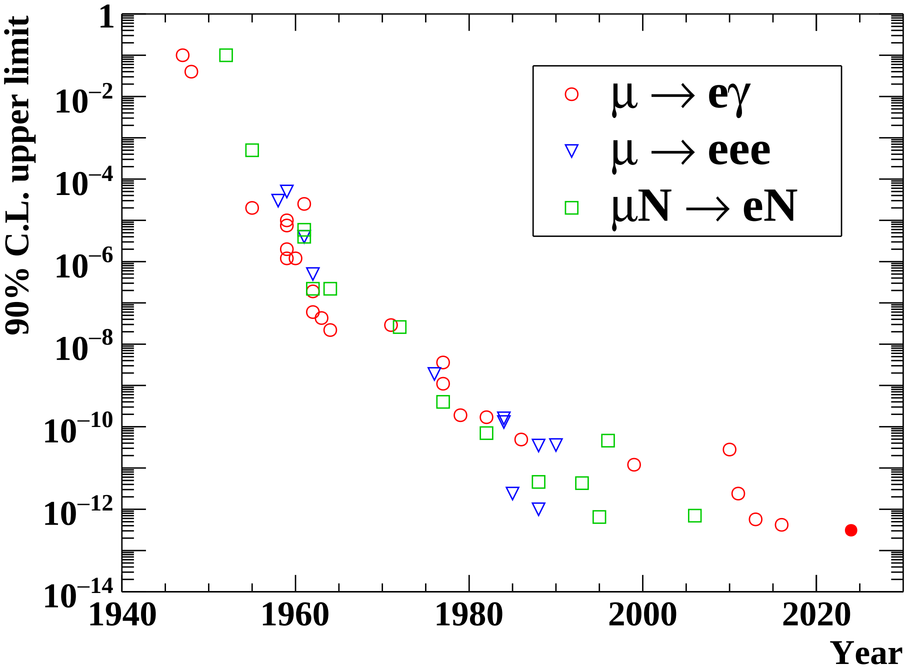

Figure 1.8: Chronology of upper limits on CLFV processes with muons. The results before 2013 were collected by Ref. [13], and the recent results correspond to Ref. [41, 42, 1].

The latest results are given by the MEG experiment [43] and its ongoing upgrade experiment, MEG II [44, 45]. The MEG experiment collected data from 2009 to 2013 and searched for $\mu \to e\gamma$ with a sensitivity of 5.3×10^{-13}. No signal excess was found, hence the upper limit on the branching ratio of $\mathcal{B}(\mu \to e\gamma) < 4.2 \times 10^{-13}$ at 90 % C.L. [42]. The MEG II experiment began collecting physics data in 2021 and plans to continue data-taking until 2026. The analysis of the first-year data, i.e. 2021 data, allowed the search with a sensitivity of 8.8×10^{-13}, and since no excess was found, an upper limit to $\mathcal{B}(\mu \to e\gamma) < 7.5 \times 10^{-13}$ was set at 90 % C.L. [1]. The combination of these results gave $\mathcal{B}(\mu \to e\gamma) < 3.1 \times 10^{-13}$ at 90 % C.L., which was the most stringent limit to date [1]. The first MEG II result showed that a sensitivity of 6×10^{-14}, which is the target sensitivity, can be achieved by continuing the experiment until 2026 [46].

1.4 Significance of this work

This work searches for $\mu \to e\gamma$ with the MEG II data collected in 2021 and 2022. The physics and calibration data-taking in 2022 was conducted for five and a half months, which was the first long-term data-taking of the MEG II experiment. This 2021–2022 dataset increased in the statistics by a factor of five compared to the first-year MEG II data in 2021. During the long-term data-taking, the detector performance must be maintained at a high level to realise the highly sensitive $\mu \to e\gamma$ search. I made a significant contribution to calibrating the photon detector and the active background tagging detector. In addition to the increase in statistics with excellent detector performance, I developed event reconstruction algorithms to further suppress the photon background. This development improved the analysis efficiency for the signal events and the reconstruction quality for multi-photon events. As a result, the highest sensitivity of 2.2×10^{-13} to date was achieved, which is an improvement by a factor of 2.4 compared to the MEG experiment (5.3×10^{-13}).

The author's major contributions are summarised as follows:

- The analysis of the collected dataset, discussed in Chapters 8, 9,
- The development of the reconstruction algorithm to further suppress the photon background, discussed in Chap. 5,
- The calibration of the photon detector and the active background tagging detector, discussed in Sections 6.2, 6.5, and
- The performance evaluation of the photon detector, discussed in Sect. 7.1.3.

Reference [47] is the publication based on these works.

Chapter 2

MEG II apparatus

The MEG II experiment in search of $\mu \to e\gamma$ has been conducted at the πE5 beamline in the high-intensity proton accelerator facility at Paul Scherrer Institut (PSI) in Switzerland. The facility allows the world's most intense continuous positive muon beam to be stopped in a thin target (Sect. 2.1). Figure 2.1 shows an overview of the MEG II detector to measure the decay products. A positron spectrometer measures positron kinematics (Sect. 2.3) and a photon detector with liquid xenon (LXe) measures photon kinematics (Sect. 2.4). A radiative decay counter (RDC) for the purpose of actively suppressing photon background detects low-energy positrons (Sect. 2.5).

The MEG coodinate system is defined as the right-handed Cartesian coordinate system: the z-coordinate is along the beam axis in the direction of the incident muon beam, the y-coordinate is in the vertical direction, and thus the x-coordinate is in the opposite direction to that towards the LXe detector. The origin of the MEG coordinates is the centre of the constant bending radius (COBRA) magnet composing the positron spectrometer. A cylindrical coordinate system (r, ϕ, z) is also used with the definition of

$$r := \sqrt{x^2 + y^2}, \tag{2.1}$$

$$\phi := \arctan \frac{y}{x}. \tag{2.2}$$

The polar angle θ with respect to the z-axis is also used. The region with $z < 0$ is called upstream, while the region with $z > 0$ is called downstream.

This chapter describes the MEG II apparatus and software framework. A more detailed description is available in Ref. [44, 45].

2.1 Beamline

The high-intensity proton accelerator facility at PSI produces a proton beam with up to 1.4 MW power at a kinetic energy of 590 MeV [48]. The final stage of the acceleration, the main ring cyclotron, has four 50.6 MHz cavities. The accelerated proton beam is directed at a 4 cm thick graphite target [49], generating pions. The pions subsequently decay via the process $\pi^+ \to \mu^+\nu_\mu$ on the surface of the graphite target, resulting in the production of surface muons at 28 MeV/c with 100 % polarisation. Since the muon lifetime of 2.2 µs is sufficiently longer than the proton cyclotron period (19.8 ns) and the pion lifetime (26 ns), the muon beam behaves as a direct current. This muon beam is then transported to the πE5 beamline.

Figure 2.2 shows the beamline layout from the graphite target up to the MEG II detector. Most beamline components are magnets that transport and focus the beam. The others are installed for different purposes: One of the slit systems (FS41) is used to adjust the beam intensity, and a Wien

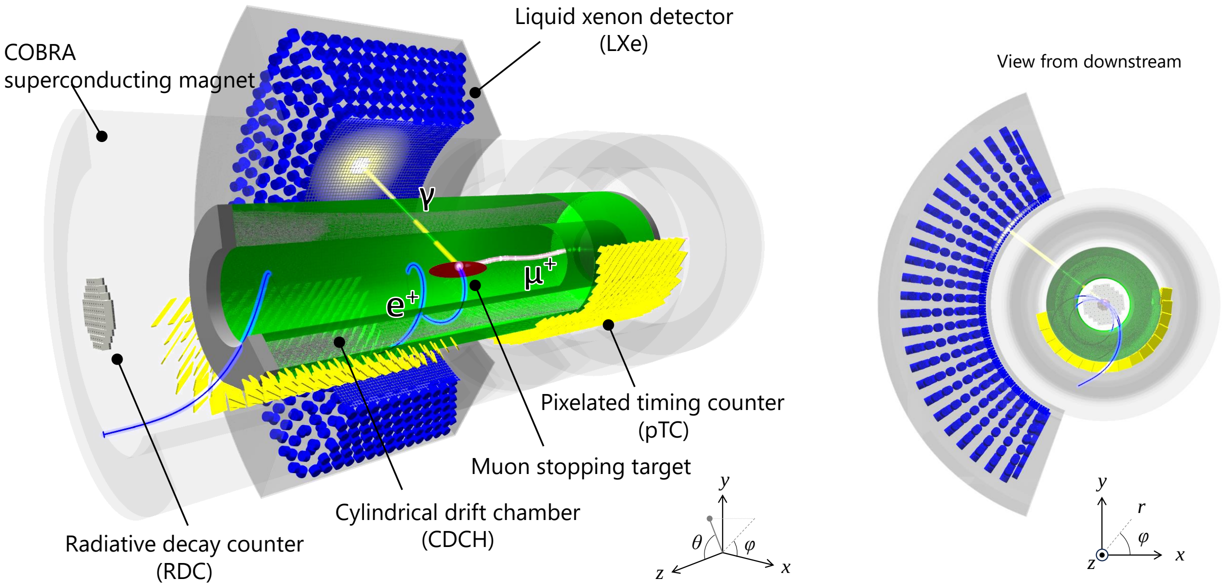

Figure 2.1: A sketch of the MEG II detector with a simulated $\mu \to e\gamma$ event [45].

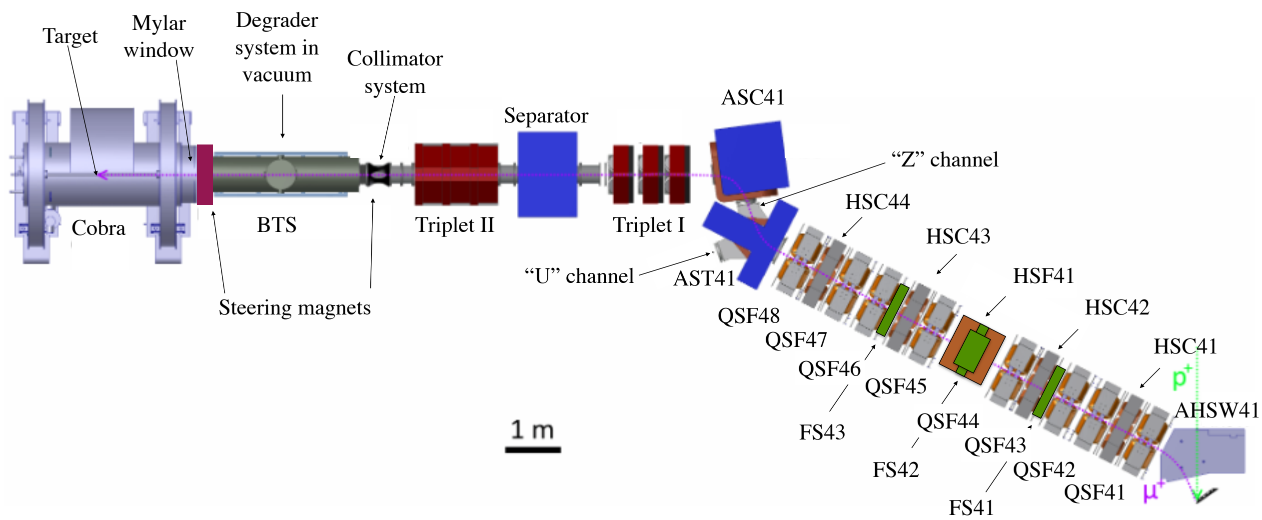

Figure 2.2: Beam transport system in πE5 beamline and the MEG II detector [45].

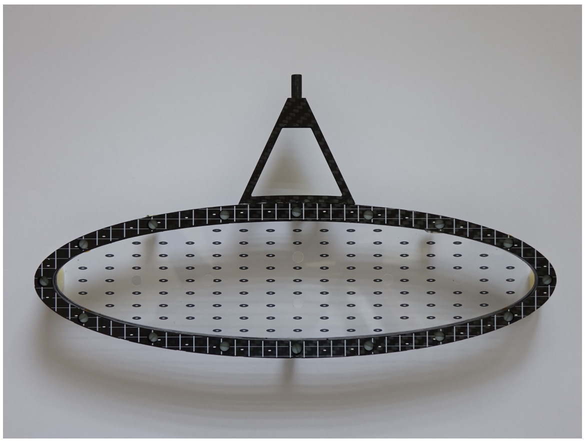

Figure 2.3: Muon stopping target with the dot pattern on the foil and the frame [45]. The six holes are located along the ellipse axes.

Figure 2.4: Picture of the installation of the photo-camera with the aluminium support in the inner cavity of the CDCH [50].

filter (Separator) separates surface muons from the comtamination (pions and positrons). A 300 µm thick Mylar degrader is installed in the beam transport solenoid (BTS) to maximise the stopping efficiency in the muon stopping target with the suppression of multiple scattering at the target. The muon beam is finally injected into the detector system through a Mylar window with a thickness of 190 µm, which separates the vacuum in the beamline from the helium atmospheric volume containing the muon stopping target.

Beam tuning at different intensities is performed in front of the BTS and at a position where the target is installed annually before data-taking begins. The beam size at a beam intensity was measured to a standard deviation of (11.4 ± 0.5) mm in both x and y coordinates.

2.2 Muon stopping target

The muon stopping target is required to maximise the muon stopping efficiency and minimise the material budget to suppress multiple Coulomb scattering of positrons, annihilation, and bremsstrahlung inside. It is an elliptical foil with the length of 270 mm, height of 66 mm, and average thickness of (174 ± 20) µm, whose material is the plastic scintillator (BC400), shown in Fig. 2.3. A carbon fibre frame supports the target foil.

The target is placed at the COBRA centre so that the long side aligns with the x-axis and the short side aligns with the y-axis, and forms a slant angle of $(75.0 \pm 0.1)^\circ$ from the x-axis along θ. The target foil alignment is crucial for precisely reconstructing the relative angles between photons and positrons, based on the experience of the MEG experiment. To trace the temporal variation of the target position transformation and foil deformation, a dot pattern is printed on both the frame and the foil and taken by a CMOS photo camera (Fig. 2.4) [50, 51]. Six holes are bored into the target and compared to dips in the reconstructed positron position distribution to align the target with the positron spectrometer.

2.3 Positron spectrometer

The positron spectrometer is designed to detect 52.83 MeV positrons under a high-rate environment and consists of

- Superconducting COBRA magnet (Sect. 2.3.1),

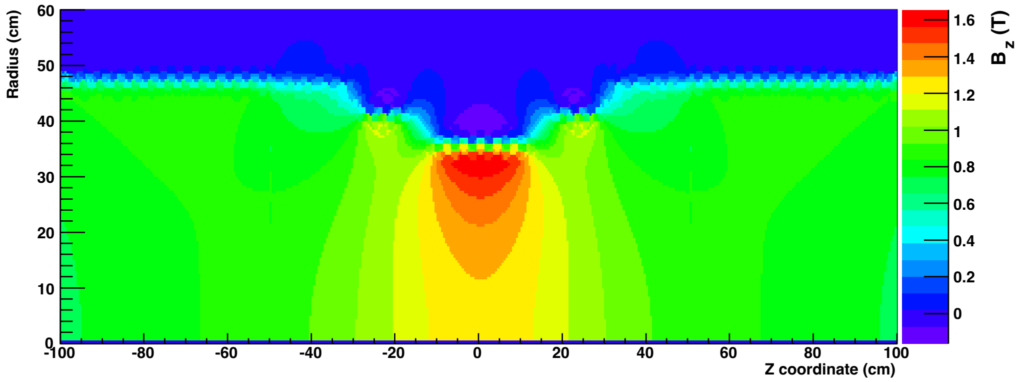

Figure 2.5: Gradient magnetic field inside the spectrometer generated by the COBRA magnet [52].

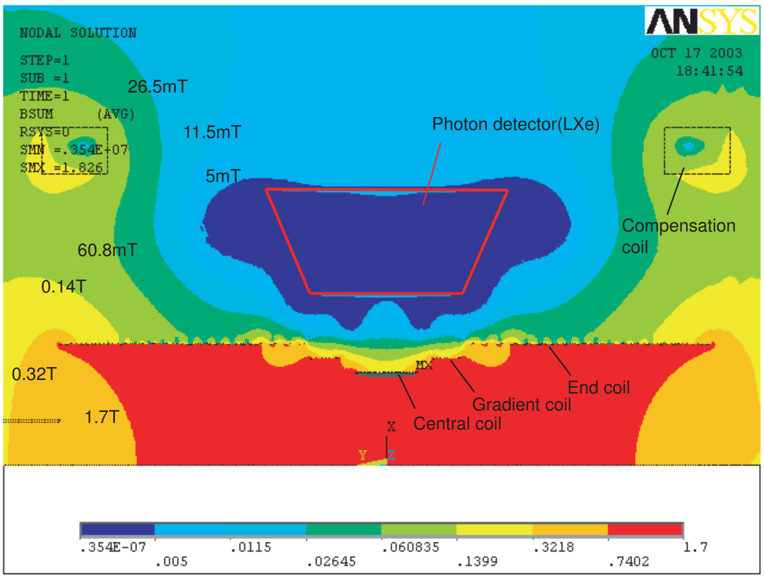

Figure 2.6: Distribution of the residual magnetic field around the LXe detector illustrated by the red trapezoidal box [52].

- Cylindrical drift chamber (CDCH) (Sect. 2.3.2), and
- Pixelated timing counter (pTC) (Sect. 2.3.3).

2.3.1 COBRA magnet

The COBRA magnet is a thin-wall superconducting magnet that generates a gradient field of 1.27 T (0.49 T) at the centre (edge) for efficient positron detection, illustrated in Fig. 2.5. The gradient magnetic field makes the positron emitted from the target follow a trajectory with an almost constant bending radius weakly dependent on the emission polar angle θ. Only high-momentum positrons can therefore reach the CDCH placed inside the inner bore of the COBRA magnet. In addition, this magnetic field configuration quickly sweeps away the positrons emitted at $\cos\theta \sim 0$. This was developed in the MEG experiment [43] and is inherited.

For the suppression of the effects on the photon detection, this is designed to have only $0.197X_0$ of material in the central part and to reduce the stray field around the LXe detector for the photomultiplier tube (PMT) operation. Figure 2.6 shows the residual magnetic field distribution, showing a sufficient magnetic field reduction below a requirement of 5×10^{-3} T around the LXe detector.

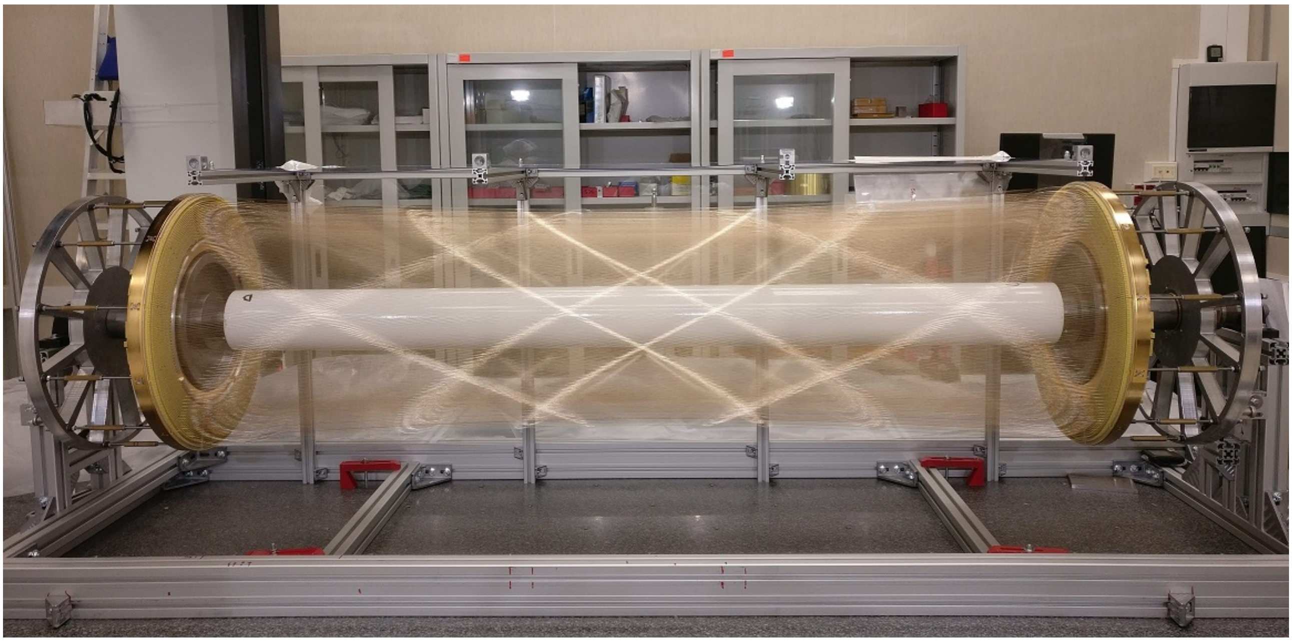

Figure 2.7: Picture of the open CDCH equipped with all the wires [44].

2.3.2 Cylindrical drift chamber

The positron tracking detector is a low-mass cylindrical drift chamber (CDCH) with the aim of minimising performance degradation due to multiple scattering and AIF-originating photon background generation. A 193 cm long single-volume detector, shown in Fig. 2.7, is designed with an inner (outer) radius of 17 cm (29 cm), a helium-based gas mixture, and very thin wires. This low-mass design suppresses the average total amount of material traversed by a positron emitted from the target to $1.6 \times 10^{-3} X_0$ for each chamber crossing, called "turn".

The chamber is filled with a gas mixture of He/isobutane/O_2/isopropyl with each fraction of 88.2/9.8/0.5/1.5. A dedicated gas system [53] supplies the mixed gas to maintain a stable isopropyl alcohol level, which is the most crucial item to ensure stable operation.

The CDCH is equipped with nine concentric layers of 192 gold-plated tungsten sense wires each and with approximately 10 000 silver-plated aluminium cathode and guard wires in total. These wires are arranged in a stereo configuration with two views, allowing for the reconstruction of longitudinal position. Each drift cell, with an approximate square shape of 6.7 mm (8.7 mm) width at the innermost (outermost) layer, is defined by sense and cathode wires, as shown in Fig. 2.8. About 100 cathode wires were broken during the construction and commissioning due to galvanic corrosion of the aluminium core, caused by air humidity penetrating through small cracks in the silver coating [54]. The impact of the missing cathodes on performance is negligible, which was assessed using Monte Carlo (MC) simulations. Ionisation signals are read out at both ends of the sense wires. The fraction of the readout sense wires is only 2/3, considering the acceptance of the C-shaped LXe photon detector.

2.3.3 Pixelated timing counter

The detector for measuring positron time consists of two semi-cylindrical sectors, one situated upstream and the other downstream, which is located between the CDCH and the inner wall of the COBRA magnet. Each sector has 256 scintillation counters, as illustrated in Fig. 2.9, aiming to improve the time resolution by multiple positron hits. Each scintillation tile, shown in Fig. 2.10, comprises a fast-response plastic scintillator (BC-422, Saint-Gobain) with the size of L = 120 mm in width,

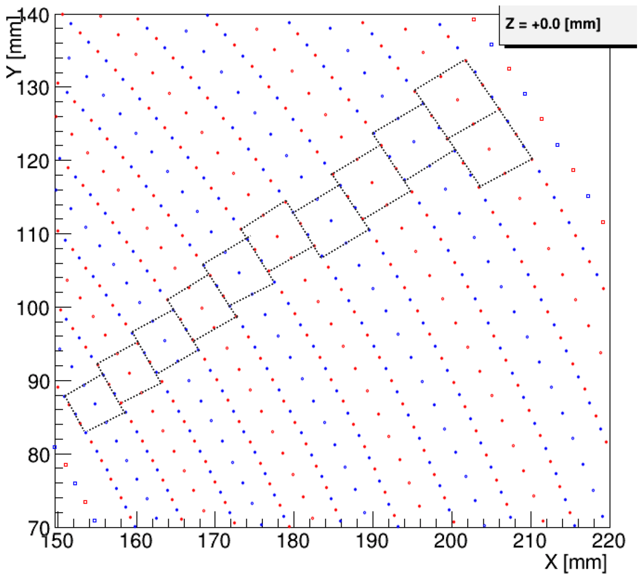

Figure 2.8: Drift cells configuration at the centre of CDCH [44]. Red and blue markers correspond to two stereo angles. Drift cells are square. The outermost (tenth) layer was not installed.

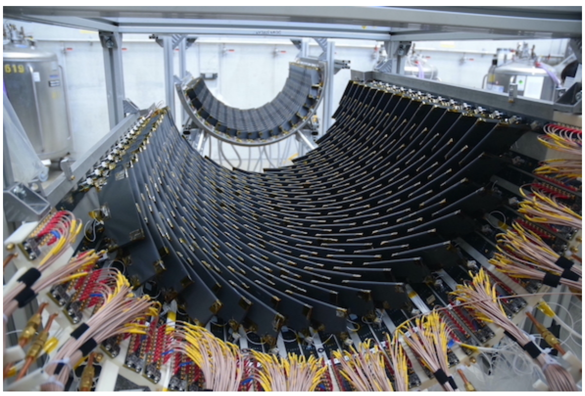

Figure 2.9: Picture of pTC [55].

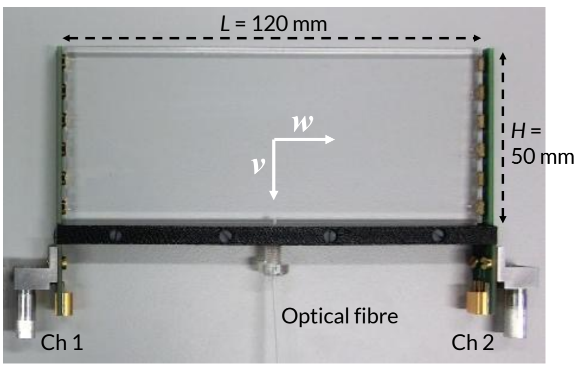

Figure 2.10: A naked pTC counter with H = 50 mm (Modified from [44]). The coordinates (v, w) is the counter local coordinates.

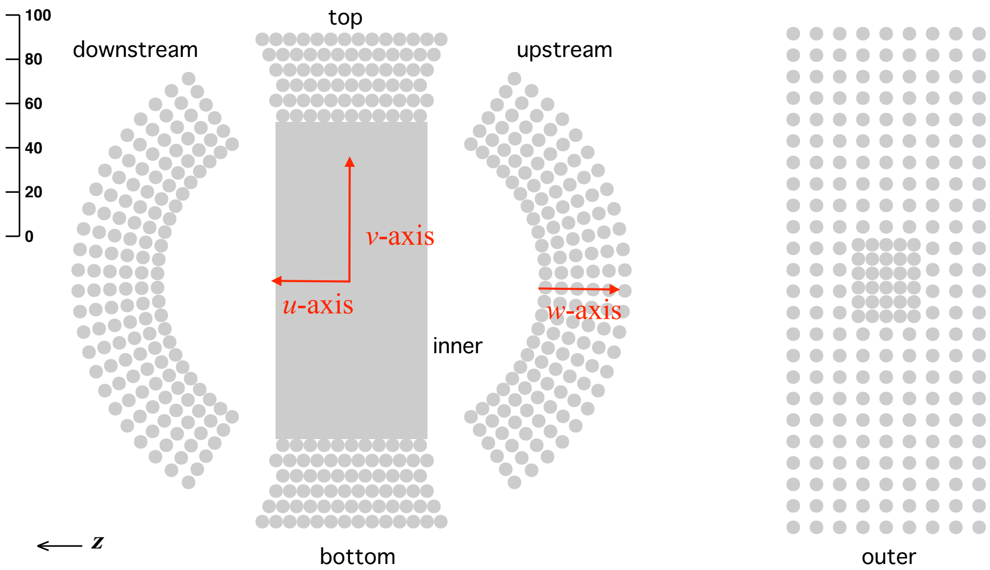

Figure 2.11: An unfolded view of the LXe detector and the local coordinate system [45].

H = 40 mm or 50 mm in height and 5 mm in thickness. Each is wrapped with a reflector for increased light reflectance and a black film for light-tightness. Six silicon photomultipliers (SiPMs) (ASD-NUV3S-P-High-Gain, AdvanSiD) are connected in series at both ends. The optical fibre is attached to calibrate time offset based on the laser system [56], which is discussed in Sect. 6.3.2. The counter local coordinate (v, w) is defined as illustrated in Fig. 2.10.

Reference [57] reported that radiation damage to the SiPMs increases the dark current and deteriorates the time resolution. To mitigate this effect, a cooling system maintains an operational temperature of 10 °C.

2.4 Liquid xenon photon detector

The photon detector is a C-shaped homogeneous calorimeter with 900 L liquid xenon (LXe) designed to measure the position, time, and energy of the 52.83 MeV photons, placed outside the COBRA magnet. The geometrical acceptance of the experiment is defined by the size of the LXe detector, which is approximately equal to $|\cos\theta_\gamma| < 0.35$ and $\phi_\gamma \in (\frac{2}{3}\pi, \frac{4}{3}\pi)$, giving an overall acceptance of 11 %. References [58, 59] describe the details of the R&D, construction, and commissioning of the LXe detector.

As shown in Fig. 2.11, the LXe detector is surrounded by six faces: inner, outer, upstream, downstream, top, and bottom faces. The local coordinate of the LXe detector is defined as

$$\begin{aligned} u &= z, \\ v &= \arctan\left(-\frac{y}{x}\right) \cdot R_{\mathrm{in}}, \\ w &= \sqrt{x^2 + y^2} - R_{\mathrm{in}}, \end{aligned} \tag{2.3}$$

where R_{in} = 64.76 cm is the inner radius of the active volume, of which details are given in Appendix A.

2.4.1 Liquid xenon as a scintillation medium

LXe possesses a lot of excellent properties such as high stopping power, high light yield, fast response, and good uniformity. Thus, it is used in various detectors, as reviewed in Ref. [60].

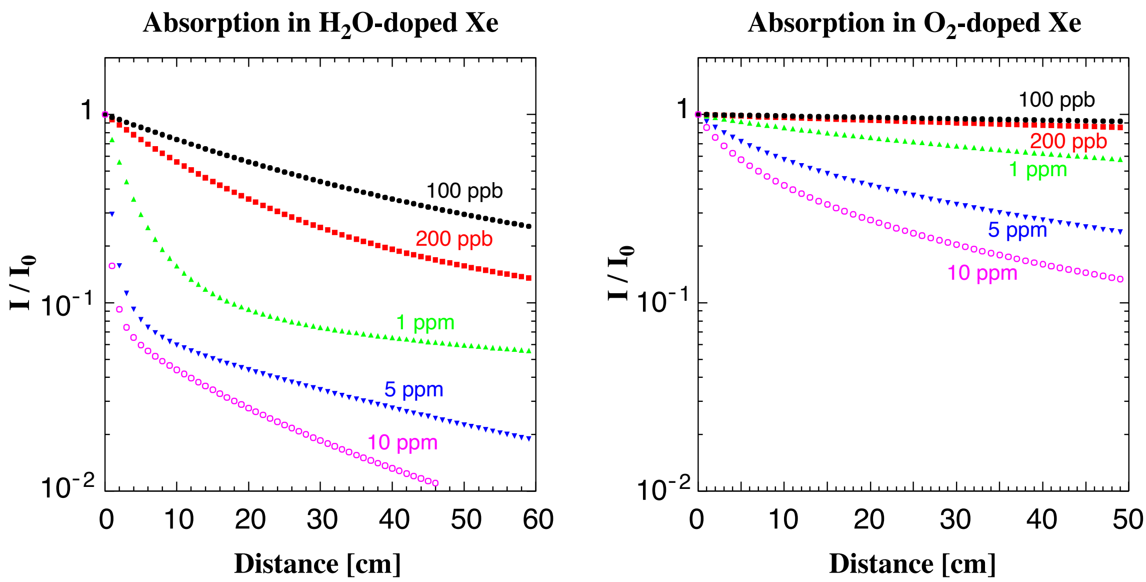

Figure 2.12: Scintillation light intensity as a function of the distance from the light source for various concentrations of water and oxygen in LXe [64].

Scintillation process A scintillation process is attributed to the decay of excited dimers (excimers, in short) Xe_2^* to the ground state Xe. The scintillation light is emitted in two different processes. The first process involves excited atoms (Xe^*) via

$$\begin{aligned} Xe^* + Xe + Xe &\rightarrow Xe_2^* + Xe, \\ Xe_2^* &\rightarrow 2Xe + h\nu, \end{aligned} \tag{2.4}$$

where $h\nu$ has a vacuum ultraviolet (VUV) wavelength of the mean of $(174.8 \pm 0.1 \pm 0.1)$ nm and the full width at half maximum (FWHM) of $(10.3 \pm 0.2 \pm 0.2)$ nm (two uncertainties are statistic and systematic, respectively) [61]. This process has two decay components, whose time constants are 4.2 ns and 22 ns for α particles, due to deexcitation of singlet and triplet states of Xe_2^*, respectively. The other process involves an electron-ion recombination [62] via

$$\begin{aligned} Xe^+ + Xe &\rightarrow Xe_2^+, \\ Xe_2^* + e^- &\rightarrow Xe^{**} + Xe, \\ Xe^{**} &\rightarrow Xe^* + \text{heat}, \\ Xe^* + Xe + Xe &\rightarrow Xe_2^* + Xe, \\ Xe_2^* &\rightarrow 2Xe + h\nu, \end{aligned} \tag{2.5}$$

with a decay time of 45 ns, which is dominant for electrons. This recombination process is disturbed by electronegative impurities, such as oxygen and nitrogen [63]. Thus, realising high light yield requires excellent purity of the xenon.

Absorption Impurities dissolved in LXe may absorb the VUV photons, reducing the observed scintillation light yield. Light attenuation can be described by

$$I(x) = I_0 \exp\left(-\frac{x}{\lambda_{att}}\right), \tag{2.6}$$

where λ_{att} is the photon attenuation length, which consists of the absorption length and the scattering length. Figure 2.12 shows the calculated light intensity as a function of the distance from the light

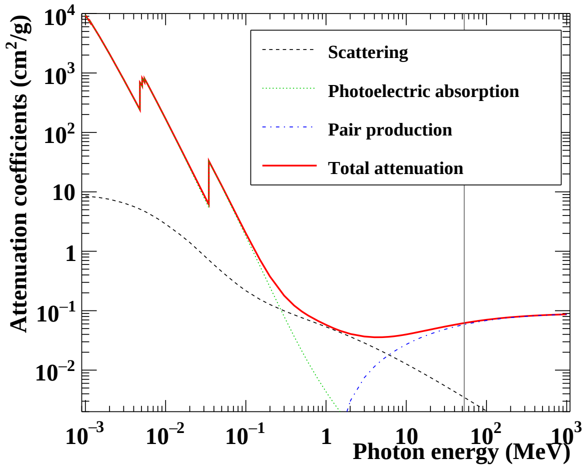

Figure 2.13: Photon cross section of xenon as a function of photon energy [65]. The grey line shows a signal photon energy of 52.83 MeV in the MEG II experiment.

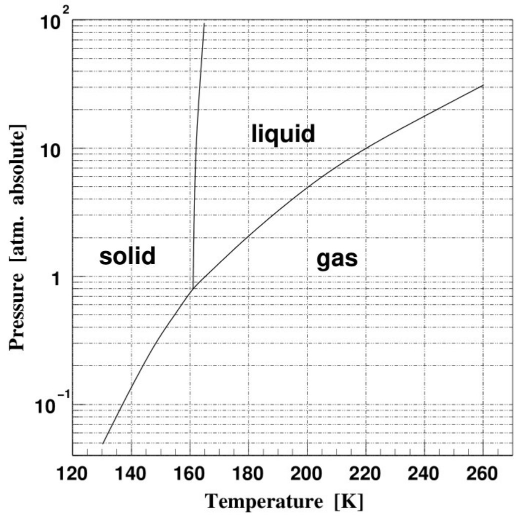

Figure 2.14: Phase diagram of xenon [60].

source for various contaminant concentrations, given the wavelength-dependent absorption coefficient for VUV light. The most serious impurity for the VUV light of LXe is water vapour. The water contamination must be suppressed down to a level of $\mathcal{O}(100\,\text{ppb})$ to achieve excellent detector performance [64].

Use in MEG II experiment When a signal photon with 52.83 MeV energy impinges onto the LXe, it creates an electron-positron pair, as shown in Fig. 2.13, and then forms electromagnetic (EM) shower, emitting scintillation light in the VUV region (175 nm) until electrons (and positrons) created in the shower deposit all energy. In order to suppress an event-by-event fluctuation of the detected amount of scintillation light, two types of purification systems in the gaseous and liquid phases have been established since the MEG experiment [64, 66], and have also been used for the MEG II experiment. Moreover, careful control of temperature and pressure is required to maintain a liquid xenon state. As shown in Fig. 2.14, the liquid phase region is 161–169 K at a nominal detectror pressure of 1.2 atm. The temperature control system has been established since the MEG experiment [67], as well as the purification system.

2.4.2 VUV-sensitive photosensors

The scintillation photons in LXe are read out by two types of VUV-sensitive photosensors: two-inch PMTs (R9869, Hamamatsu Photonics K.K.) inherited from the MEG experiment and newly developed MPPCs (S10943-4372, Hamamatsu Photonics K.K.) (Fig. 2.15a). The inner face (photon entrance face) is covered by 4092 MPPCs and the other faces are covered by 668 PMTs, as shown in Fig. 2.15b.

Photomultiplier tubes

The PMTs use a VUV-sensitive photo-cathode made of bialkali (K–Cs–Sb) and a synthetic quartz window. Figure 2.16 shows the divider circuit of the PMT. The last two stages of the 12-stage dynode are equipped with Zener diodes to ensure stable operation even under a high-intensity environment.

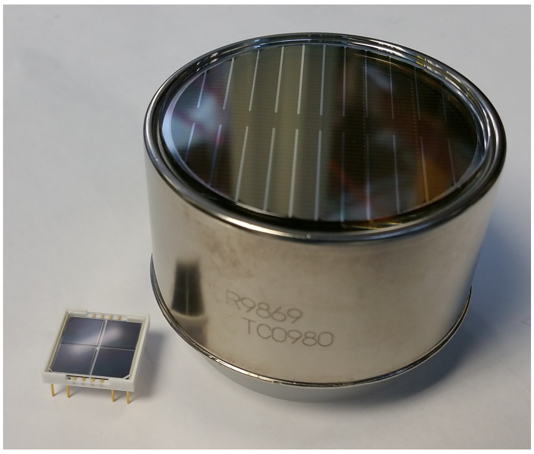

(a) An MPPC and a PMT.

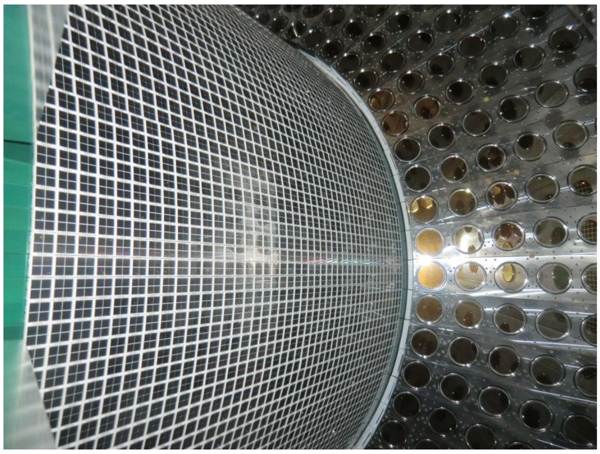

(b) The inside of the LXe photon detector after the multi-pixel photon counters (MPPCs) and PMTs are assembled [44].

Figure 2.15: Pictures of VUV-sensitive MPPCs and PMTs.

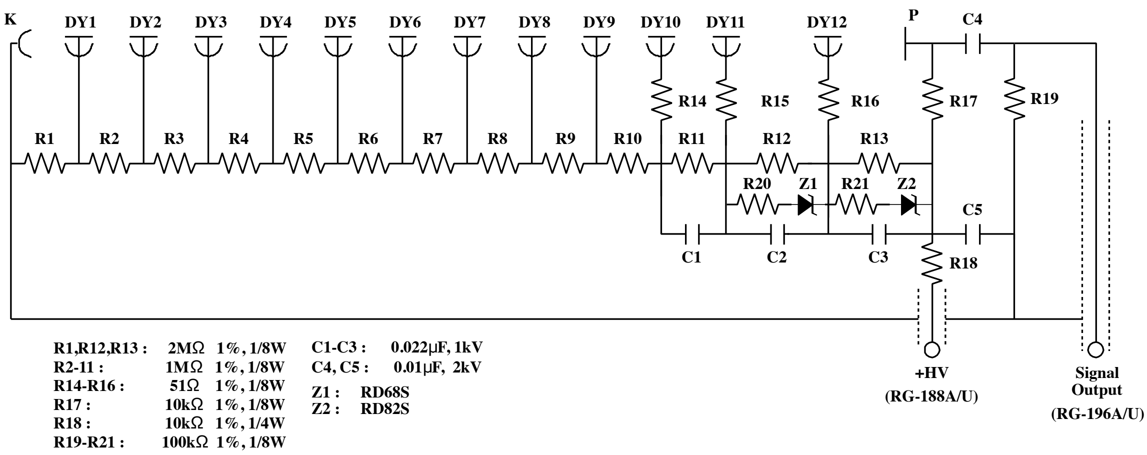

Figure 2.16: Divider circuit of the PMT [68].

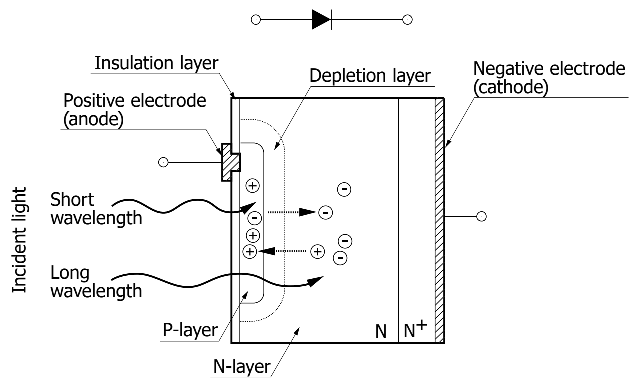

Figure 2.17: Detection mechanism of MPPC with p-on-n structure [70].

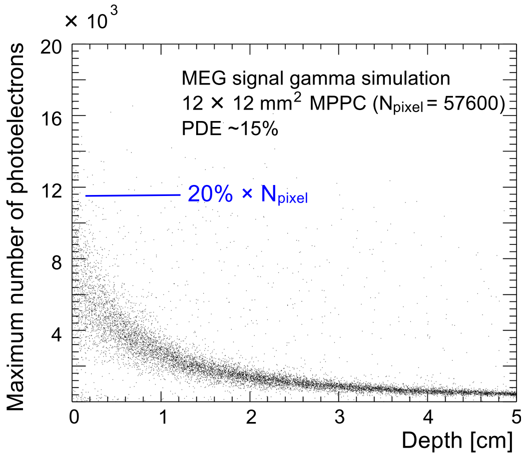

Figure 2.18: The number of photoelectrons expected from a $12 \times 12\,\mathrm{mm}^2$ MPPC vs conversion depth in the MC simulation [44].

The quantum efficiency (QE) is about 16 % for the LXe scintillation light at a LXe temperature of 165 K, of which value was provided by Hamamatsu Photonics K.K.

Based on the experience in the MEG experiment, it is known that the gain of the PMT changes under a high-rate environment. The gain is degraded due to the large photoelectric current induced by scintillation photons. In addition, in $\mathcal{O}(10\,\mathrm{sec})$–$\mathcal{O}(10\,\mathrm{min})$ after a change in beam operation, the gain shifts by 10 % at maximum, which is called "gain shift". This gain shift is due to lattice defects in dynodes, which already exist as of production, creating a new trap level to capture electrons [69]. When a high-intensity beam starts coming to the MEG II detector, the trap level in the dynodes is occupied with electrons. Once the trap level is occupied, more electrons can be released, resulting in an increase in the gain. Because more electrons hit the second or later dynodes, it is faster to occupy the trap level. The fact results in several time constants of the gain shift; i.e. the slowest component is for the first-stage dynode. The trapped electrons will be released by thermal energy, and the gain will be stabilised after equilibrium is reached. When the beam stops, the trapped electrons are released from the trap level, decreasing the gain. The gain shift depends on the number of lattice defects in PMTs, meaning sensor-by-sensor calibration is needed, which is discussed in Sect. 6.2.1.

Multi-pixel photon counters

The VUV-sensitive MPPCs that have the p-silicon on an n-substrate (p-on-n) structure (Fig. 2.17) were newly developed for the MEG II experiment [71]. This design addresses the short absorption length of the VUV light in silicon. To further enhance VUV light transmission, a protection coating layer uses a thin high-quality quartz window with an approximate transparency of 75 % at 175 nm. Consequently, these MPPCs achieve a photon detection efficiency (PDE) exceeding 15 %. Another innovation is the enlarged active area of $12 \times 12\,\mathrm{mm}^2$, achieved by connecting four $6 \times 6\,\mathrm{mm}^2$ MPPCs in series. This reduces the number of readout channels. For very shallow signal events, these MPPCs are expected to detect up to 12 000 p.e. (approximately 20 % of the 57 600 pixels), as shown in Fig. 2.18. While initially not considered a major concern, non-linear response is now suspected to have a non-negligible effect on the energy resolution, as discussed in Sect. 7.1.3 and Sect. 9.4.

The MPPCs were produced in four production lots. They show different characteristics, such as waveform and excess charge factor (ECF). To obtain a uniform response, the printed circuit board (PCB) strips that mount MPPCs in a single production lot are arranged so that they are not next

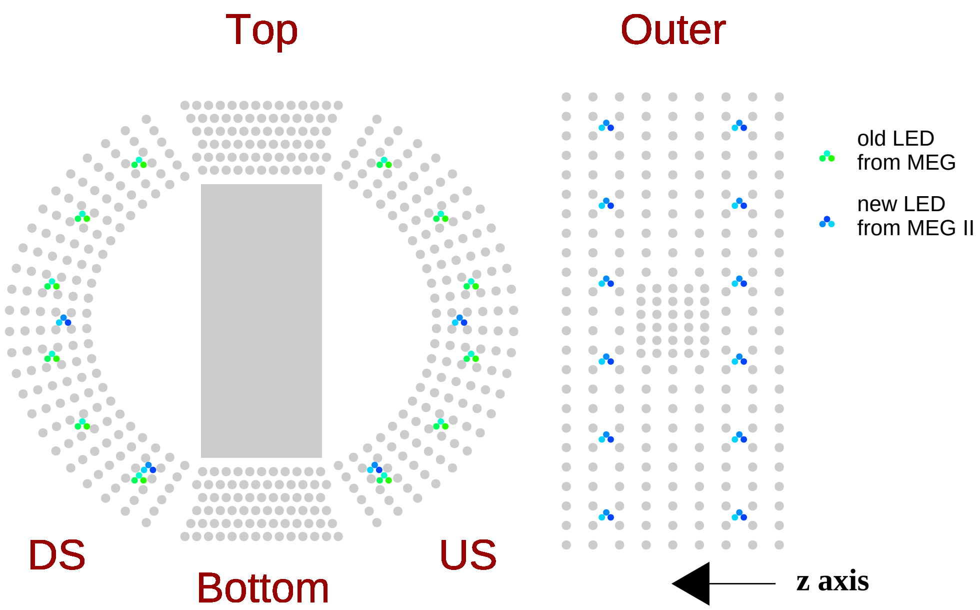

Figure 2.19: Location of the LEDs in the LXe detector [59]. Green and blue dots show the LEDs reused from the MEG and those installed for the MPPC calibration in the MEG II, respectively.

to the strip with the MPPCs in the same production lot.

The MPPCs are damaged during the operation in a high-intensity beam, resulting in a decrease of PDE [72]. This can be recovered by the thermal annealing, as discussed in Sect. 3.1

2.4.3 Internal calibration sources

To calibrate the gain and PDE (QE) for MPPCs (PMTs), blue light emitting diode (LED) sources and α-particle sources are installed inside the LXe detector.

LED Blue-light LEDs (E1L49-3B1A-02, Toyoda Gosei [73]; and KA-3021QBS-D, Kingbright [74]) are installed on the outer face and lateral faces, as illustrated in Fig. 2.19, which are used for the gain calibration. These LEDs are covered by a Teflon sheet to diffuse the light and to operate LEDs at a higher voltage for stable operation. A function generator (81150A, Agilent [75]) controls the LED illumination, and outputs a synchronised signal to trigger the data acquisition (DAQ).

α-particle sources The PDE (QE) calibration utilises 25 α-particle sources of ^{241}Am installed inside the LXe detector, as illustrated in Fig. 2.20. Five 100 µm tungsten wires are stretched between the upstream and the downstream faces, and five α-particle sources are crimped at 12.4 cm intervals [76]. Since the activity of each α-particle source is 200 Bq at most, they are negligible in the physics data-taking.

2.4.4 External calibration apparatuses

The LXe detector requires monochromatic photons to calibrate and monitor the energy scale. Three calibration apparatuses are dedicated to the LXe detector calibration.

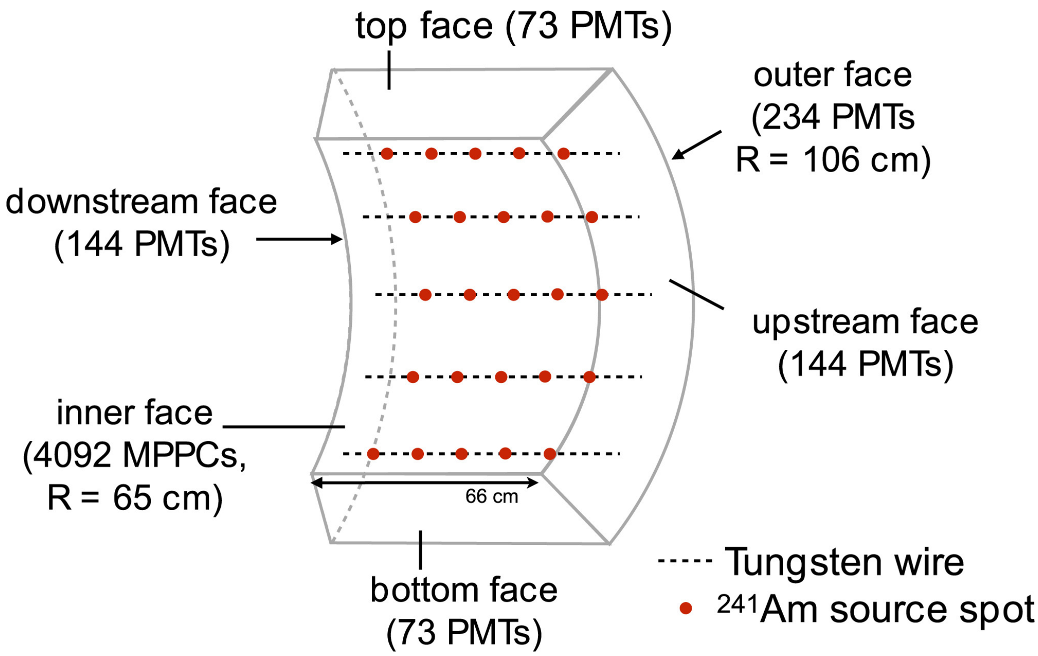

Figure 2.20: Location of 25 ^{241}Am spots in the detector [72]. Red circles show the positions of the sources.

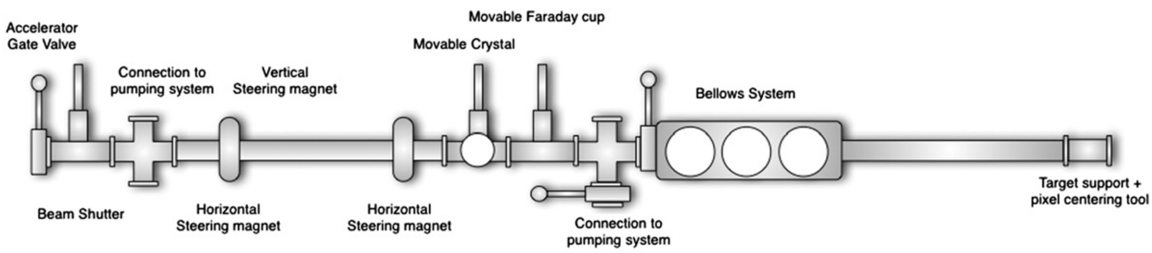

Figure 2.21: A scheme of the proton beam optics, control elements, and bellows system [77]. The figure is not to scale. The proton beam comes from the left-hand side and interacts with the $Li_2B_4O_7$ target supported by the mechanical structure.

A Cockcroft-Walton accelerator

The main calibration and monitoring method for the energy scale of the LXe detector during the physics run utilise 17.6 MeV photons produced by the reaction ^{7}Li(p, γ)^{8}Be. The integration of a Cockcroft-Walton (C-W) accelerator enabled the generation of the reaction [77]. Figure 2.21 shows a scheme of the proton beam optics and control system. Protons accelerated by the C-W accelerator up to 500 keV interact with a lithium tetraborate ($Li_2B_4O_7$) target. The reaction ^{7}Li(p, γ)^{8}Be is resonant at proton kinetic energy of 440 keV with a resonance-width of about 15 keV. It produces a 17.6 MeV line and a less intense and wider 14.6 MeV line.

During the normal data-taking, the calibration system, such as the proton beamline and the Li target, is positioned downstream outside the COBRA spectrometer, as shown in Fig. 2.22. When starting a calibration, the muon stopping target and the RDC are removed from the muon beam line, and then the C-W system is inserted into the COBRA centre. After the calibration data-taking, the C-W system is extracted, and then the muon stopping target and the RDC return to the normal position in the opposite procedure to the insertion. The insertion (or extraction) takes ten minutes, but the time is not wasted by taking other calibration data during that. To prevent them from colliding, an interlock system is implemented.

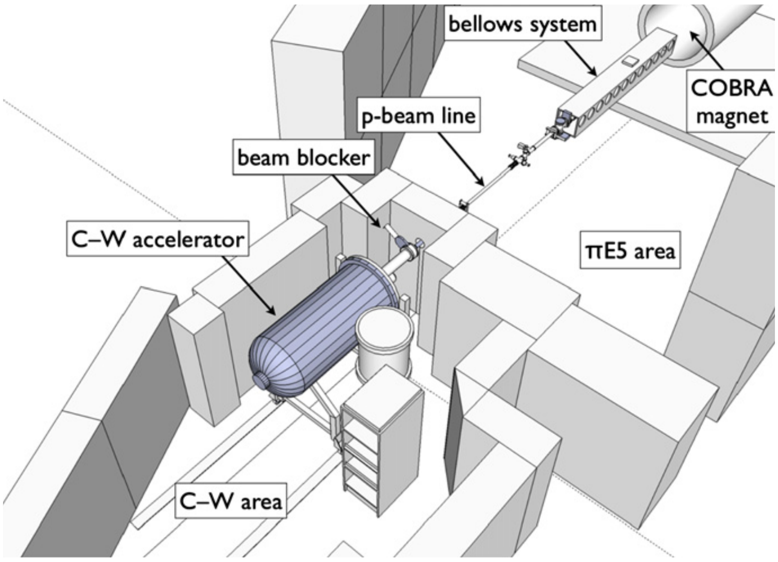

Figure 2.22: Layout of the MEG and C-W experimental areas [77].

Neutron generator

A pulsed D–D generator (Thermo Fisher Scientific) produces neutrons with 2.5 MeV kinetic energy, based on the $d(d, {}^3He)n$ nuclear reaction. The produced neutrons are thermalised in polyethylene and then captured by nickel nuclei via the reaction ${}^{58}Ni(n, \gamma){}^{59}Ni$, resulting in 9 MeV photon emission [43, 78]. Since thermal neutron capture events follow the pulsed neutron generation by a typical average delay of 50–100 µs, 9 MeV photon events are efficiently triggered using the neutron emission signal pulse.

π^0 calibration

The above two monochromatic photons have factor three and five lower energies of 17.6 MeV and 9 MeV than the signal ones (52.83 MeV), respectively. Another beam mode of the πE5 beamline, a pion beam with 70.6 MeV/c, allows to produce photons whose energy range is 54.9 MeV and 82.9 MeV. Since this calibration requires a dedicated beam mode and target, note that this cannot be performed in parallel with the physics data-taking.

A negative-charged pion π^- exchanges its charge with proton via

$$\pi^- p \to \pi^0 n, \tag{2.7}$$

which is called “charge exchange (CEX) reaction”. Then, the generated neutral pion π^0 immediately decays to two photons:

$$\pi^0 \to \gamma\gamma \tag{2.8}$$

Due to the π^0 boost, the emitted two-photon pair has energies

$$E_\gamma = \frac{E_{\pi^0}}{2} \pm \sqrt{\frac{E_{\pi^0}^2}{4} - \frac{m_{\pi^0}^2}{2(1 - \cos\Theta_{\gamma\gamma})}}, \tag{2.9}$$

where $E_{\pi^0} = 137.85$ MeV is an energy of π^0, $m_{\pi^0} = (134.9768 \pm 0.0005)$ MeV [7] is a mass of π^0, and $\Theta_{\gamma\gamma}$ is an opening angle of two photons. The energies are 54.9 MeV and 82.9 MeV when the opening angle $\Theta_{\gamma\gamma}$ is 180°.

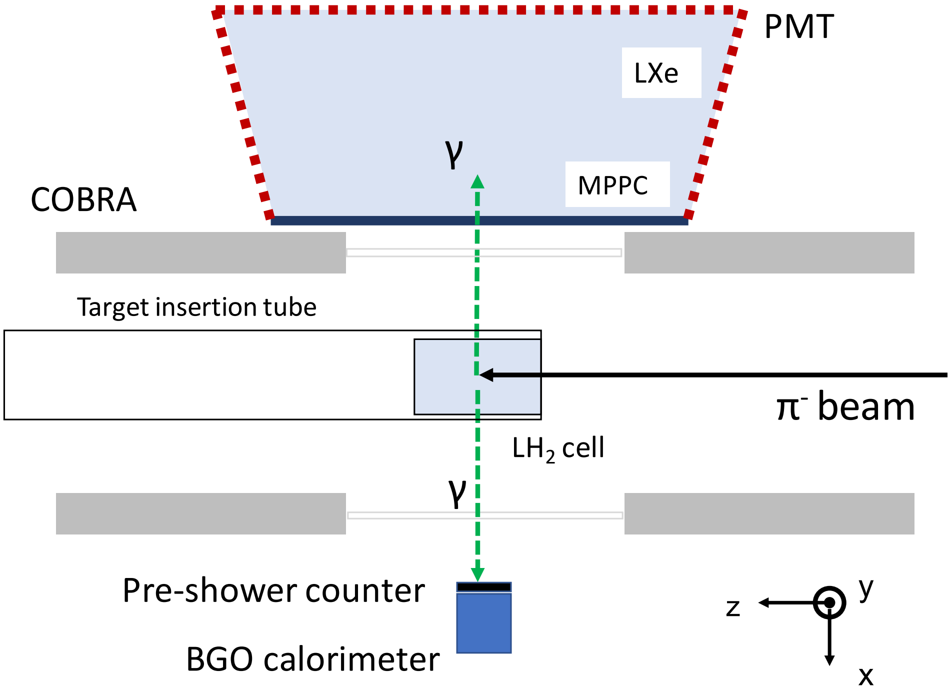

Figure 2.23: Schematic view of the experimental setup of the π^0 calibration (top view) [59].

The other channel of the CEX reaction is a radiative capture:

$$\pi^- p \to \gamma n,$$

in which the photon has 129 MeV. The ratio of the cross-sections of two channels is known as the Panofsky ratio,

$$P = \frac{\sigma(\pi^- p \to \pi^0 n)}{\sigma(\pi^- p \to \gamma n)}, \tag{2.10}$$

which was measured to be 1.546 ± 0.009 [79].

Figure 2.23 shows the schematic view of the setup of the π^0 calibration. A negative pion beam is incident on the liquid hydrogen (LH_2) target and stops here, producing two photons via the CEX reaction. One of the back-to-back photons can be detected in the LXe detector to study its detector response by tagging the other photon using the dedicated detector located on the opposite side of the LXe detector.

Pion beam A negative pion beam can be transported from the proton target to the MEG II detector system with appropriate settings of the Wien filter and BTS. It has a bunch structure with the same frequency as the proton acceleration (50.6 MHz). The beam intensity is adjusted by the slit system, which is the same as the muon beam intensity adjustment.

Liquid hydrogen target The hydrogen has to be kept liquid (below 20.39 K at 1 atm) and to be in the centre of the COBRA magnet, requiring a cell below 20 K and a two-metre-long cryogenic infrastructure. The target consists of a closed-volume hydrogen circuit, a cooling system based on copper and liquid helium, and vacuum insulation, as shown in Fig. 2.24. The cell containing LH_2 is a stainless steel cylinder of 0.5 mm thick, 60 mm diameter, and 75 mm length. A more detailed discussion is given by Refs. [80, 81].

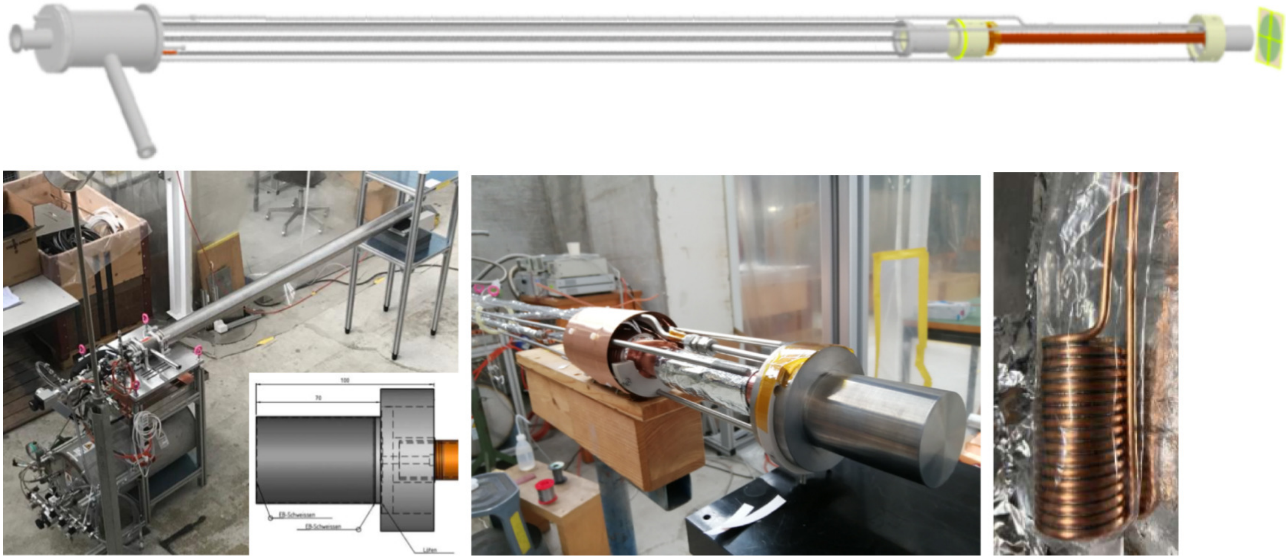

Figure 2.24: Drawings and pictures of the LH_2 target [80]. (Top) Drawing of the LH_2 target and cooling system. (Left) Target picture and cell drawing. (Centre) A copper cold finger holding the cell. (Right) Cooling copper coil.

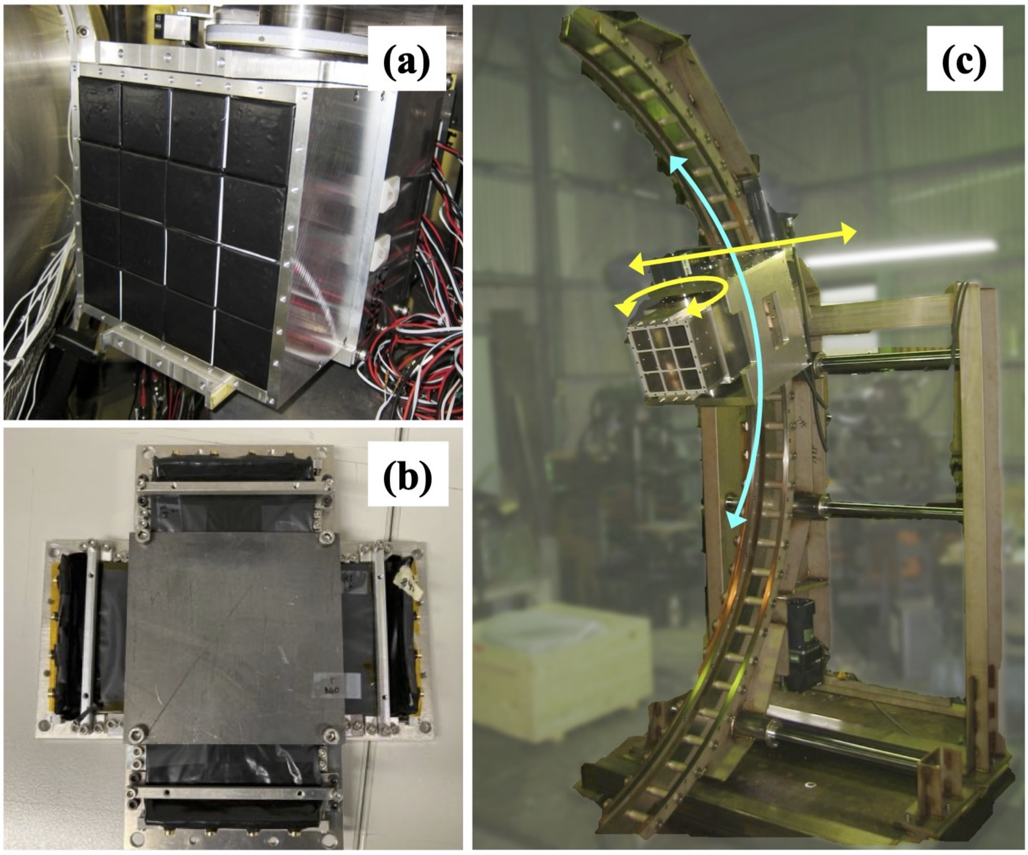

Figure 2.25: Pictures of the bismuth germanium oxide (BGO) calorimeter (a), the pre-shower counter (b), and a tagging detector mover (c) [82, 83]. The old 3×3 crystals in (c) were replaced with the BGO calorimeter and the pre-shower counter.

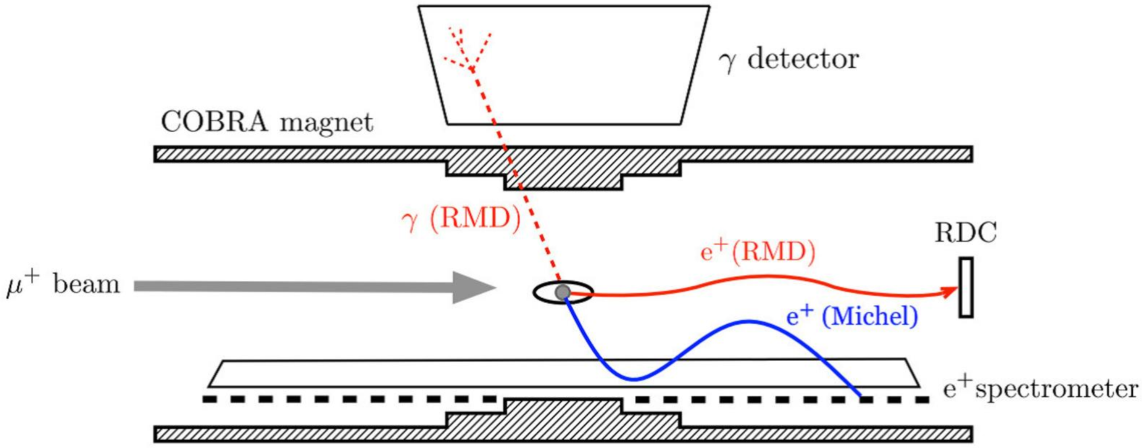

Figure 2.26: Schematic view of the detection of RMD with the RDC [44].

Photon-tagging detector The photon-tagging detector consists of the BGO calorimeter to measure energy and the pre-shower counter for the time calibration of the LXe detector. The calorimeter is comprised of 16 BGO crystals, each of which is attached to the PMT (H8409-70, Hamamatsu Photonics K.K.) for scintillation light detection, as shown in Fig. 2.25(a). The pre-shower counter, shown in Fig. 2.25(b), consists of a lead converter and two plastic scintillators (EJ-230, Eljen Technology) in which scintillation light is read out by four five-series-connected MPPCs (S14160-3050HS, Hamamatsu Photonics K.K.) attached on both sides. The pre-shower counter is placed in front of the BGO calorimeter. The combined detector is installed in a detector mover (Fig. 2.25(c)) to cover the whole acceptance of the LXe detector.

2.5 Radiative decay counter

When a photon with high energy above 48 MeV is emitted from RMD ($\mu \to e\nu\bar{\nu}\gamma$), most of the accompanying positrons have a low energy of 1–5 MeV, as discussed in Sect. 1.2. In the COBRA spectrometer, such low-energy positrons follow an almost helical trajectory with a small radius around the magnetic field lines. An RDC aims to detect such low-energy positrons to identify RMD photons detected by the LXe detector (Fig. 2.26), and, as a consequence, background photons causing the accidental background can be suppressed. Among background photons with 48–58 MeV, 65 % come from RMD events [44].

Two RDCs were initially planned to be installed in the beamline upstream and downstream of the muon stopping target. However, the upstream RDC is still under development due to its difficulties in satisfying all the requirements and fabrication techniques, while the downstream one was installed in 2017. Due to muon polarisation, the fraction of RMD positrons flying downstream is 48 %. The rest of the positrons flying upstream could not be detected unless the upstream RDC was installed. Hereafter, “RDC” indicates only the downstream one.

Detector design The RMD events are identified by the time coincidence between RDC hits and a photon measured by the LXe detector, as shown in Fig. 2.27. The Michel positrons also hit the RDC, but at a random time. Since the Michel positrons have relatively larger energy than the RMD positrons (Fig. 2.28), the energy measurement enables better distinguishing the two sources of positrons. Therefore, the RDC comprises two parts: the one measuring the timing and the other measuring the energy, as shown in Fig. 2.29. When considering the positron trajectories in the

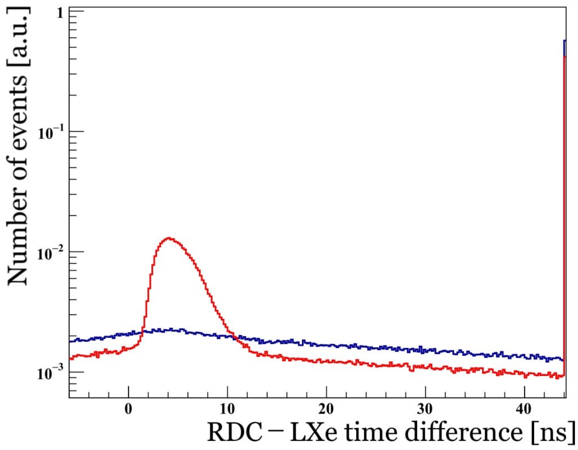

Figure 2.27: Simulated time differences between the RDC hits and photons for accidental background events (red) and signal events (blue) [44].

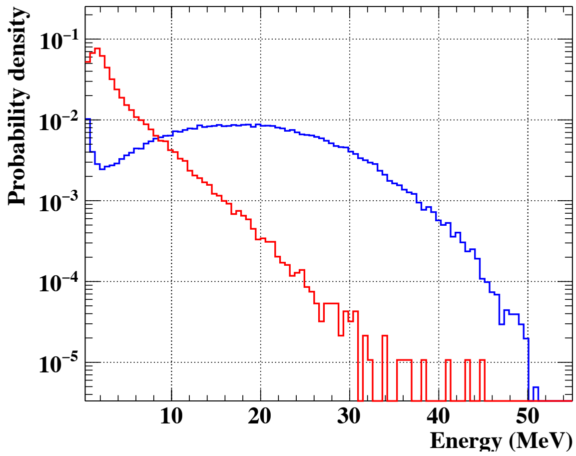

Figure 2.28: Expected energy distribution at the RDC for RMD events with $E_\gamma > 48\,\mathrm{MeV}$ (red) and for the Michel events (blue) [84].

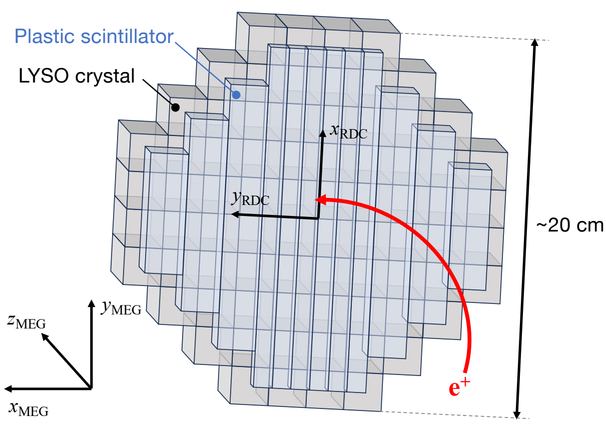

(a) Sketch.

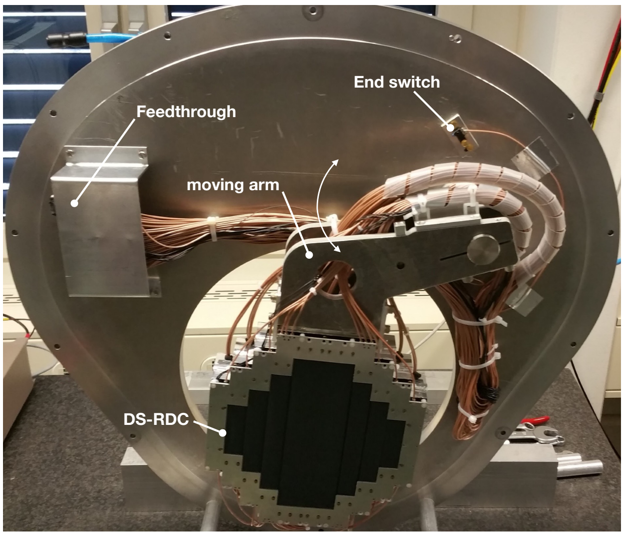

(b) Picture [45].

Figure 2.29: Overview of RDC.

magnetic field, the acceptance for the RMD positrons is 88 % with the designs explained below.

The first part is 12 plastic scintillators (BC-418, Saint-Gobain) whose thickness is 5 mm to measure the positron timing. Because the hit rate is larger close to the beam axis, the width of the plates in the central region is 1 cm while it is 2 cm at the outer part. The farther from the beam axis plates, the shorter their length is. The scintillation light is read out by MPPCs (S13360-3050PE, Hamamatsu Photonics K.K.) attached to both ends of each plate. Two (three) MPPCs are connected in series for 1 cm (2 cm) wide plates.

The second part is 76 lutetium-yttrium oxyorthosilicate (LYSO) crystals (Shanghai Institute of Ceramics) to measure the positron energy. LYSO contains the radio isotope ^{176}Lu, which decays to ^{176}Hf with emission of a β ray, followed by a cascade of 307 keV, 202 keV and 88 keV γ rays. The decay rate per crystal was measured to be small enough ($\sim$ 2 kHz) not to affect the RMD positron detection. The energy spectrum has a peak at 597 keV, which is used for the energy scale calibration (Sect. 6.5.1). The size of each crystal is $(2 \times 2 \times 2)\,\mathrm{cm}^3$. Each MPPC (S12572-025P, Hamamatsu Photonics K.K.) reads the signal and is attached to the back of each crystal.

Control system The temperature around the RDC strongly depends on the operation status of the CDCH frontend electronics. When the frontend electronics are switched on, the temperature increases by 3–5 °C. The temperature increase changes the breakdown voltage of the MPPCs, resulting in a change in the reconstructed energy if no correction is made. Two thermometers (PT100) are, therefore, installed in the RDC to monitor the temperature.

A moving arm supports the RDC and can be moved between the parking and measurement positions to allow us to insert the beamline of protons accelerated by the C-W accelerator introduced in Sect. 2.4.4. It is rotated by 83° in a beam axis when it is in the measurement position. The RDC local coordinates are defined as

$$\begin{aligned} x_{\mathrm{RDC}} &= -x\cos\theta + y\sin\theta, \\ y_{\mathrm{RDC}} &= x\sin\theta + y\cos\theta, \\ z_{\mathrm{RDC}} &= z, \end{aligned} \tag{2.11}$$

where θ is a rotation angle of 83°[1].

2.6 Trigger and data acquisition

Digitised waveform data is acquired in approximately 9000 channels to separate and eliminate pileups under the high-rate environment in the offline analysis. The WaveDAQ system [85, 86], a highly integrated custom trigger and DAQ system, is installed in the MEG II experiment, as shown in Fig. 2.30. It consists of 35 crates, each containing up to 16 waveform DRS4 readout modules (WaveDREAMs) introduced in Sect. 2.6.1, a trigger concentrator boards (TCB) that decides to trigger the event, and a data concentrator board (DCB) that sends the digitised waveforms to the readout computer. The full system is controlled by the maximum integrated data acquisition system (MIDAS) [87].

2.6.1 Waveform acquision

The domino ring sampler (DRS) [88] plays a role in the waveform digitisation of which principle is shown in Fig. 2.31. The generation of a sampling signal by a ring of series-connected inverter

[1] The local coordinates are left-handed.

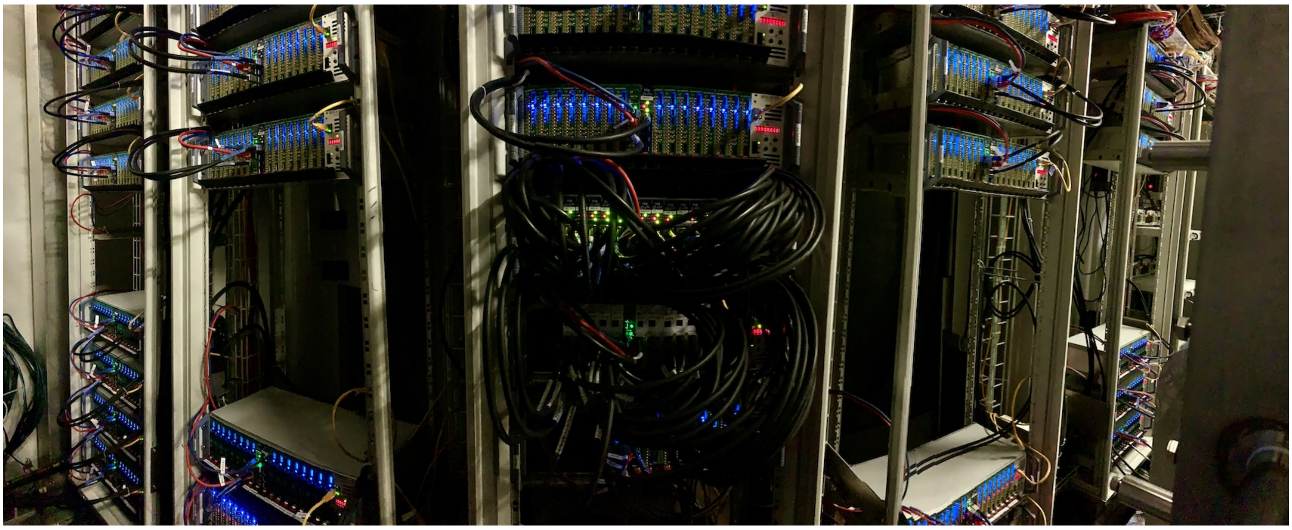

Figure 2.30: Panoramic view of the MEG II WaveDAQ system installed in the πE5 area [85]. The DAQ crates filled with WaveDREAMs have the blue LED shining, the trigger and clock distribution crates, fully cabled, are at the centre of the picture.

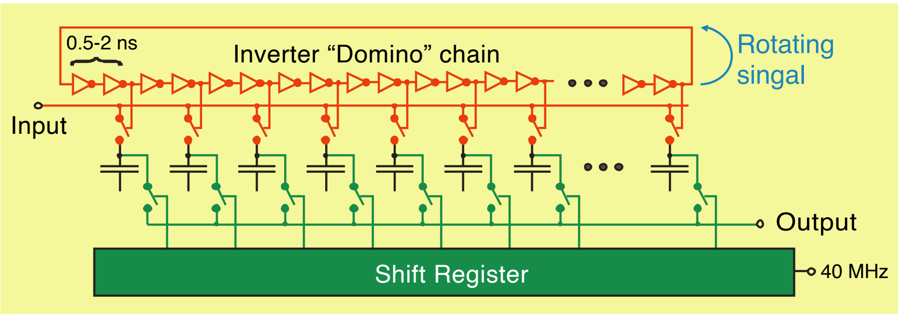

Figure 2.31: Simplified schematic of the DRS chip [88].

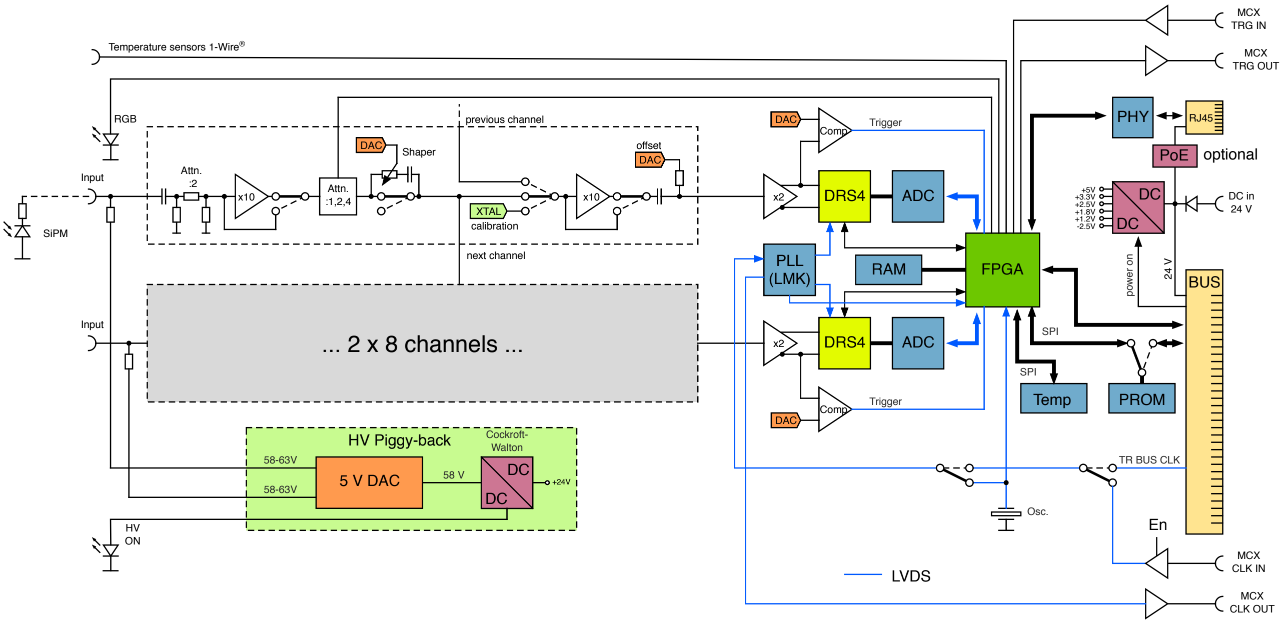

Figure 2.32: Simplified schematics of the WaveDREAM board [44]. It contains 16 variable-gain input amplifiers, two DRS4 chips, 16 ADC channels and a FPGA. An optional HV generator for SiPM biasing can be mounted as a piggy-back board.

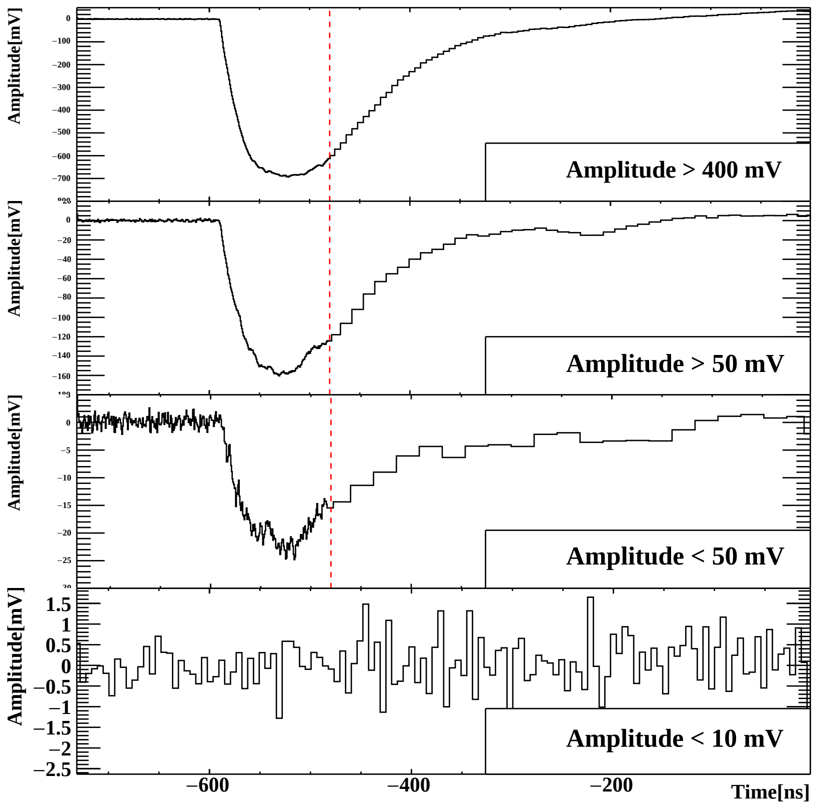

Figure 2.33: MPPC waveforms of a gamma-ray event with different rebinning configurations [59].

delay chains leads to the storage of information about the voltage by each capacitor. Once an event is triggered, the sampling signal is stopped, resulting in the subsequent extraction of the voltage value by the shift register. The WaveDREAM, shown in Fig. 2.32, is a fully contained 16-channel DAQ platform that employs two DRS4 chips [89] at sampling speed up to 5 GSPS. The sampling frequency is set to 1.4 GSPS for the pTC, the LXe detector, and the RDC; and 1.2 GSPS for the CDCH. The DRS output is connected to the analog-to-digital converters (ADCs), which continuously digitises the waveform at 80 MSPS, for the field programmable gate array (FPGA) to build the trigger logic finally. The ADC output is also read out and used in the offline analysis, as discussed in Sect. 5.2.

In addition to the DRS chips, the WaveDREAM contains amplifiers to preserve the time characteristics of the detector signals and high voltage (HV) supply for SiPMs in a limited space. Switchable gain-10 amplifiers and programmable attenuators allow an overall input gain from 0.5 to 100 in steps of two. A pole-zero cancellation circuit shapes the waveform flexibly. The HV up to 240 V for the SiPMs is provided by the C-W multipliers, which can be further tuned on each channel by the 5 V digital-to-analog converter (DAC).

Data reduction A full MEG II event is as large as 16 MB, which is enormous in terms of the data transmission and the disk capacity. The following methods to reduce the event size are implemented:

- Waveform re-binning: merge the waveform bins in groups of 2^n ($n = 1,\ 2,\ 3,\ 4$ and 5).
- Region of interest (ROI): cut the waveform outside the ROI which is around the trigger time.
- Zero suppression: discard waveform without pulses.

The waveform re-binning applies to the CDCH waveform data by a factor of two and the LXe detector's one, with the grouping determined dynamically according to the observed amplitude (Fig. 2.33). The

Table 2.1: List of trigger settings.

Label	Logic
E_γ trigger	Weighted sum of all photosensors in the LXe detector
Time coincidence trigger	Time coincidence of pTC hit and LXe hit
DM trigger	Back-to-back hit positions in pTC and LXe detector
MEG trigger	(E_γ trigger) $\wedge$ (Time coincidence trigger) $\wedge$ (DM trigger)
Random trigger	Random timing
LED trigger	Signal from LED driver
α trigger	Pulse shape discrimination using outer PMTs
Neutron generator trigger	Neutron generator signal
pTC laser trigger	Laser pulser signal
pTC self trigger	$n_{\mathrm{pTC}} \geq 1$
RDC LYSO self trigger	One or more hits in RDC LYSO
BGO self trigger	Weighted sum of all PMTs in the BGO calorimeter
π^0 trigger	(E_γ trigger) $\wedge$ (BGO self trigger) $\wedge$ (Back-to-back photon positions) $\wedge$ (Time coincidence)

ROI method applies to the pTC and RDC, in which ROI is defined as the first 512 bins. In addition to the ROI method, the zero suppression applies to the pTC and RDC plastic scintillators. The total reduction power is about 10.

2.6.2 Trigger

The WaveDAQ system allows for flexible data collection by supporting up to 64 independent trigger settings, each with its own prescaling factor. This ensures the correct mixing of various conditions within the same dataset. The trigger for the physics data is called the “MEG trigger”, and has three conditions based on the photon energy, the time difference, and the opening angle. Other trigger settings are also prepared for the detector calibrations. Table 2.1 summarises the trigger settings used for the data-taking.

Because of constraints on the DRS4 buffer length when operating at 1.2 GSPS and 1.4 GSPS, a group of dedicated FPGA TCBs arranged in a tree-layer structure must generate the trigger decision in approximately 600 ns. The trigger logic is, thus, implemented based on information provided from the LXe and the pTC, in which the CDCH information is not used due to the long drift time of 300 ns.

The trigger efficiency is defined as the fraction of the events that pass the trigger condition to the defined event topology. For instance, the efficiency of the MEG trigger is the fraction of the events that pass the MEG trigger condition among all the signal events where the photon is incident on the fiducial volume of the LXe detector and deposits energy above 48 MeV and that the positron track is reconstructed. Section 8.6 discusses the trigger efficiency evaluation in the runs 2021 and 2022.

MEG trigger The MEG trigger is based on the simultaneous fulfilment of three online-reconstructed conditions:

(1) E_γ trigger: The weighted sum of all photosensors in the LXe detector exceeds a predefined threshold.

(2) Time coincidence trigger: The time difference between a detected photon and a positron hit on the pTC falls within a programmable time window.
(3) Direction match (DM) trigger: The photon conversion point in the LXe detector and the positron's impact position on the pTC are consistent with a two-body muon decay originating from the target.

The above triggers can be issued independently; in particular, the E_γ trigger is often used to study a photon spectrum without additional biases at the triggering stage. In order to investigate the efficiencies, all the above triggers have two wider and tighter thresholds, which is discussed in Sect. 8.6. The detailed yearly trigger settings are described in Sect. 3.2.

Triggers for calibration Other trigger settings are prepared for the detector calibration. Electric noise studies require data without a pulse, acquired by randomly triggering events.

The pTC is calibrated daily with the laser-based system. The laser pulse generator provides a signal synchronous with the laser pulse, triggering events. The minimum biased dataset is also useful for the positron analysis. Hence, the pTC self-trigger requiring one or more hits in the pTC is implemented.

Calibrating the LXe detector requires several dedicated trigger settings. LED events (9 MeV photon events from the neutron generator) are triggered by the LED (neutron generator) driver signals. The α events are triggered by a real-time pulse discrimination logic developed by the MEG experiment [90]. Adjusting the E_γ trigger threshold can take other monochromatic photon events and cosmic-ray events.

The energy scale of RDC LYSO crystals is calibrated by the intrinsic radioactivity. The LYSO self-trigger is used to acquire the self-radiation events.

Triggers for π^0 calibration The π^0 calibration requires the dedicated trigger settings since the photon-tagging detector (BGO calorimeter and pre-shower counter) is used. To efficiently acquire back-to-back two-photon events, the π^0 trigger imposes the following conditions:

(1) E_γ trigger.
(2) The weighted sum of all 16 PMTs in the BGO calorimeter is above the threshold, which is called "BGO self trigger".
(3) A photon detection time difference between the LXe and tagging detectors is within the time window.
(4) The online reconstructed conversion position in the LXe detector is opposite to the tagging detector position.

The BGO-self-triggered data sample is used for the detection efficiency measurement, as discussed in Sect. 7.1.4.

2.7 Detector simulation

The MEG II detector simulation has two parts: The first part is a simulation for the event generation and particle propagation; the latter takes care of event mixing and waveform simulation. The first part is constructed based on the Geant4 package [91]. In the generation of muon beam events and the SM muon decay events, the muon polarisation is considered according to the measured one in the MEG experiment [40]. As for the photon propagation simulation inside the LXe detector, the reflectivity of aluminium used in the PMT holder is set differently in different MC configurations, resulting in different scintillation light distributions for an identical event in different samples. Here, let me define two detector configurations in the MC simulation: "*configuration A*" setting zero reflectivity, and "*configuration B*" setting a 0.5 reflectivity after the investigation [59]. The gas ionisation process in the CDCH drift cells is simulated by the Garfield++ [92].

In the latter part of the simulation, the generated events are mixed with various relative timings with respect to each other and the trigger so as to reproduce the high-rate environment. Then, the waveform digitisation is performed based on the impulse responses of the detectors as well as the white noise. The responses are derived from data for pTC, LXe detector, and RDC; while those for the CDCH are based on the SPICE software [93].

$\mu \to e\gamma$ **sample** The signal $\mu \to e\gamma$ event is simulated by generating the decay products of a positron and a photon with signal kinematics. The angular distribution of positrons is assumed to be isotropic, i.e. $A_R = A_L$ in Eq. (1.11). Both detector configurations A and B are simulated. To reproduce pileups, background events where a muon with momentum is generated in front of the BTS (Sect. 2.1) are mixed into the signal event at $R_\mu = 2\text{–}5 \times 10^7\,\mathrm{s}^{-1}$.

Background photon sample The photon energy probability density function (PDF) for the accidental background event and LXe detector calibration require the simulated spectrum of background photons. Thus, I generated a dedicated background photon sample. This sample consists of photons originating from AIF, RMD, and decay in flight (DIF), with the energy above $m_\mathrm{e} = 0.511\,\mathrm{MeV}$ at a muon stopping rate of $3 \times 10^7\,\mathrm{s}^{-1}$ for mixing. It is generated with configuration A.

Chapter 3

Run

The MEG II experiment started taking physics data on 25th September 2021 and successfully accumulated the statistics as shown in Fig. 3.1. The π^0 calibration runs for the LXe detector's calibration were conducted after the physics run each year. A major detector maintenance work was annealing MPPCs of the LXe detector to recover their PDE. This chapter summarises the situation of data-taking and the detector condition during the runs 2021 and 2022. A more detailed description of the run 2021 is available in Ref. [46].

3.1 Detector condition

Target camera

Two target cameras were installed but not fully operational during the run 2021. The proper additional uncertainty was assigned to the period when either the cameras did not work [46]. During the run 2022, a camera out of two worked well, taking photographs every three minutes in July and August and every hour since September. The taken photographs became dark because the LED intensity to illuminate the target decreased gradually since August. This problem was solved by pre-processing the photographs.

Positron spectrometer

The CDCH was stably operated during the whole physics run with few occasions of discharges. Only approximately 3 % of all the CDCH readouts were not active, which did not have a critical impact on the performance [46]. It increased 64 readout wires on which signal positrons leave hits in the run 2022. They were found to improve the signal positron detection based on studies in 2021. In September 2022, damage to the CDCH electronics suddenly appeared and continued for approximately two weeks, making a large high-frequency noise in the acquired waveform. The offline waveform processing described in Sect. 4.2.2 can deal with this noise.

The pTC was also operated in a stable condition. Only one channel was inactive during the run 2021, and four channels were inactive during the run 2022. The readout had a large electronic noise at the beginning of each year's run, which was reduced during the run by removing problematic elements in the circuit. In addition, the bias voltages were optimised in the first month of the run 2022. They caused an unstable detector condition. The time measurement under the unstable condition required the careful time offset calibration, which was discussed in Sect. 6.3 and Ref. [45].

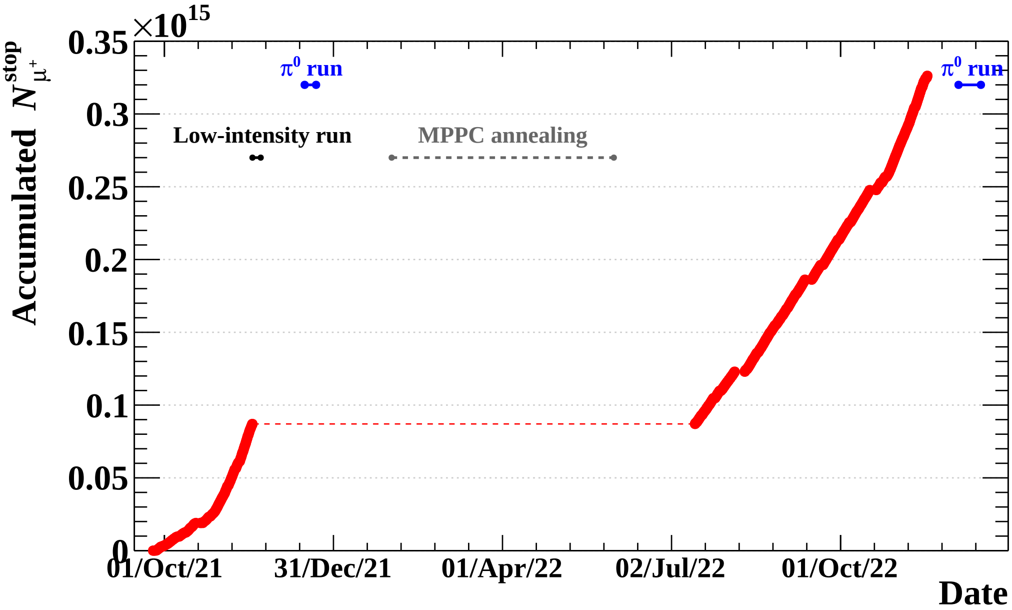

Figure 3.1: The accumulated number of stopped muons over time and periods for calibration runs and MPPC annealing campaign.

LXe detector

The LXe detector was stably operated to take data during the runs 2021 and 2022, although some condition changes occurred. The most impactful activity on the detector condition was the annealing of MPPCs to recover their PDE, which was conducted between the runs 2021 and 2022. This subsection first summarises the annealing method and results, and then discusses other conditions of the LXe detector.

MPPC annealing campaign A thermal annealing was carried out to recover the PDE of all the MPPCs for the first time during the accelerator shutdown period between the runs 2021 and 2022. The Joule heating of the MPPCs served as the heat source [45, 94]. This annealing process recovered the PDE from 6 % to 15.4 % which was high enough to tolerate radiation damage during the physics run for a whole year. Then, the averaged PDE decreased to 14.0 % during the commissioning.

Cabling I realised miscabling when analysing data taken in the run 2021, in the summer of 2023. If mis-cabling was made, the expected location of photosensors differed from the actual one. Since the DM logic was constructed in a unit of WaveDREAM boards, it could cause trigger inefficiency if the miscabling crossed WaveDREAM boards. Figure 3.2 shows the miscabled MPPCs, and miscabling across different WaveDREAM boards crossed was only spot 7 in Fig. 3.2a.

In the annealing procedure, cables were unplugged and plugged, causing additional miscabling by mistake. In addition, the cabling was modified to improve the efficiency of the DM trigger, as discussed in Sect. 3.2. Methods to check cable assignment, discussed in Sect. 6.2.5, have not yet been established as of the shutdown period between 2021 and 2022. These two cabling works ended up increasing the MPPC miscabling, as shown in Fig. 3.2b[1].

[1]The checking methods were established in 2023 and 2024. The cabling was carefully cross-checked and fixed in the most recent two annealing campaigns in 2024 and 2025.

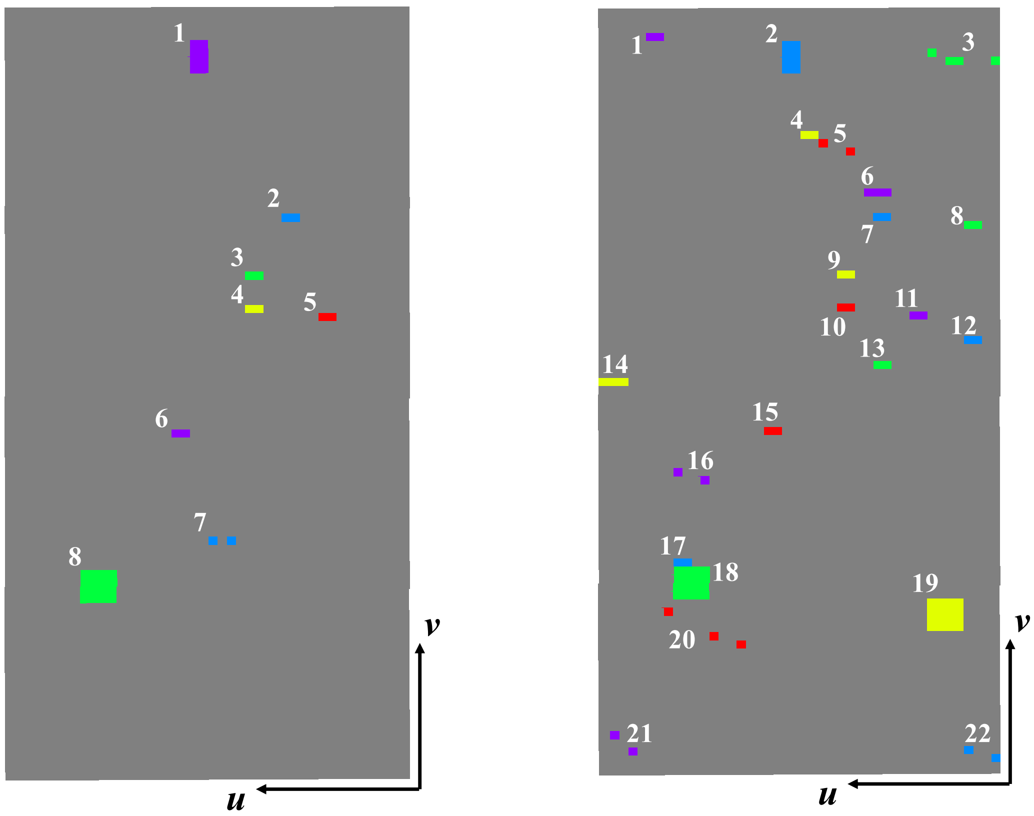

(a) 2021.

(b) 2022.

Figure 3.2: A map of the miscabled MPPC channels when we took data. There were eight spots in 2021 and 22 spots in 2022. Only a spot in 2021 crossed WaveDREAM boards, of which the impact on the trigger efficiency is negligible.

Inactive channels The readout had a few problematic channels; 34 MPPC channels and 37 PMT channels, as shown in Fig. 3.3a. This was due to a short circuit, the HV supply, and a photosensor malfunction. Twenty MPPCs became inactive during the annealing, which seemed due to the cabling work. Some core pins would become detached from the core wires, and other core pins would touch the ground regions by tilting[2]. The number of inactive MPPCs was increased to 54 in 2022 (Fig. 3.3b).

The event-by-event fluctuation of scintillation light impinging on the inactive photosensors worsens the energy resolution. Thus, the compensation algorithm was applied, as discussed in Sect. 4.1.5.

LXe level The level of LXe inside the detector was $y = 83\,\mathrm{cm}$ based on the measurement with α particles in the run 2021 [59]. This is below the position of some PMTs in the top region, meaning that such PMTs could not efficiently collect scintillation light emitted in liquid. New xenon was added to the detector at the beginning of the run 2022 to meet the required xenon volume covering all photosensors with LXe. The level of LXe inside the detector became $y \sim 90\,\mathrm{cm}$. However, it was later discovered that the xenon was contaminated with water, resulting in a shorter absorption length. The gaseous purification in parallel with data-taking got rid of impurities, recovering the amount of scintillation light detected by PMTs to 96 % of that in 2021 at the end of the run 2022. The temporal evolution has to be calibrated, which is discussed in Sect. 6.2.9.

PMT HV adjustment HVs of the PMTs were adjusted to have a gain of 0.8×10^6 at the beginning of each year's run. In the run 2022, the HVs were adjusted twice on 3rd August and 15th September to maintain a suitable signal size, ensuring good time resolution for the entire run 2022.

RDC

The RDC kept a good condition during the run with all the channels actively read out in the run 2021 and only an inactive channel in the LYSO crystals in the run 2022. Until the end of October 2021, however, its installation was delayed because of a safety problem that an interlock system missed to avoid crashes between the RDC and the proton beamline of C-W accelerator. The fraction of the physics runs in which the RDC was in the measurement position was 51 %. In the run 2022, thanks to the interlock system having worked since the beginning of the run, the RDC was in the measurement position for 88 % of the physics runs[3]. There was a problem with the thermometer readout. Section 6.5.1 discusses how to deal with the temperature stability.

3.2 Physics run

The physics run was conducted between 25th September (14th July) after the commissioning of the detector and trigger and 18th November (17th November) in 2021 (2022). The total DAQ time fraction was 63 % of the whole period in the run 2021, whose period dependence is shown in Fig. 3.4. The inefficiency came from the daily calibration routine, the transitions related to the changes in recorded data files, and the lack of proton beam delivery due to issues in the accelerator. The DAQ fraction increased to 72 % in the run 2022 including three four-day interruptions due to accelerator development, thanks to optimisation of the daily calibration routine.

---

[2] Since some of the newly dead MPPCs detected signal during the run 2023, I do not consider that it is damage to the MPPC itself.

[3] Electric spikes in the readout system sometimes called the interlock system, making the RDC move to the parking position.

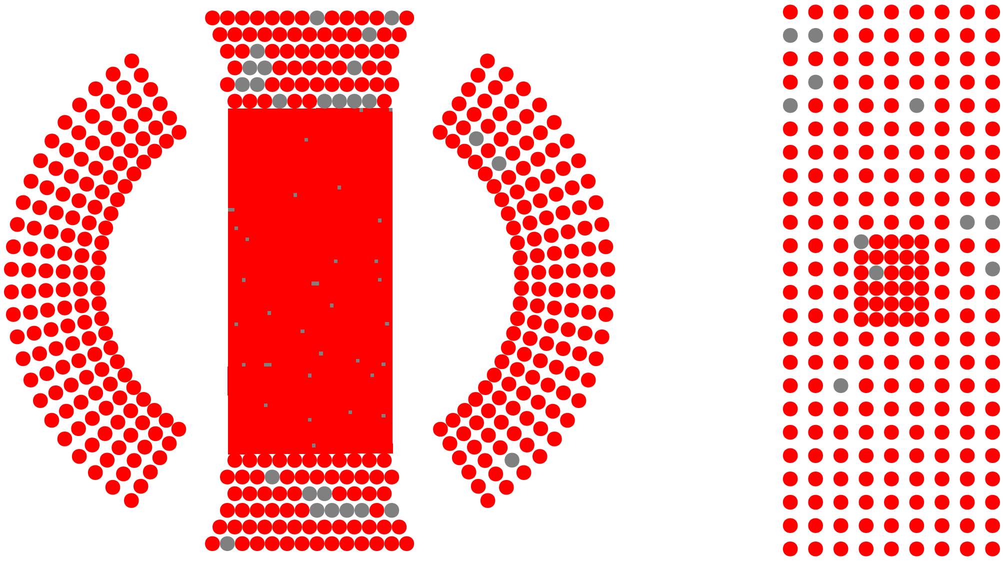

(a) 2021.

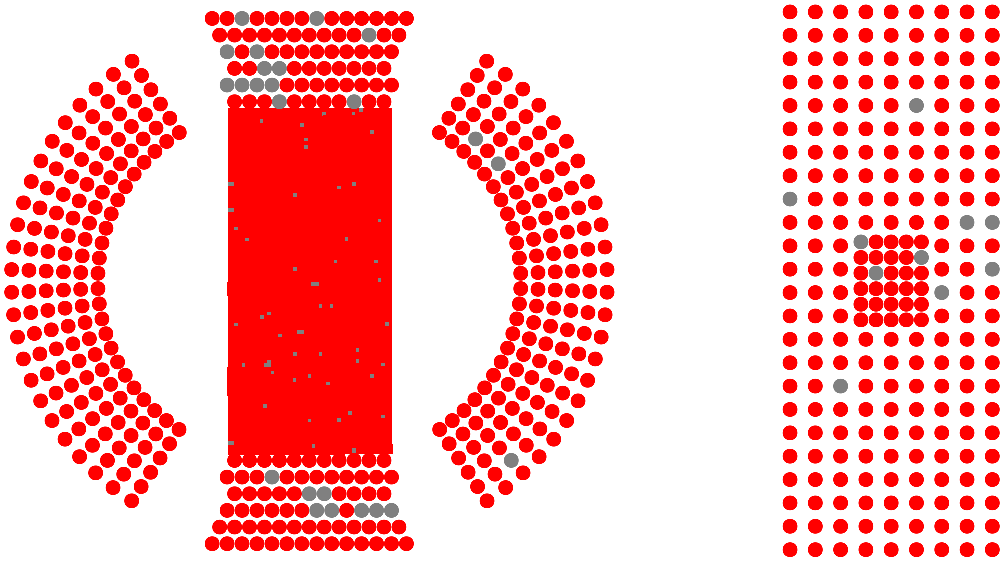

(b) 2022.

Figure 3.3: A map of active photosensors in the LXe detector. Red (grey) indicates active (inactive) channels.

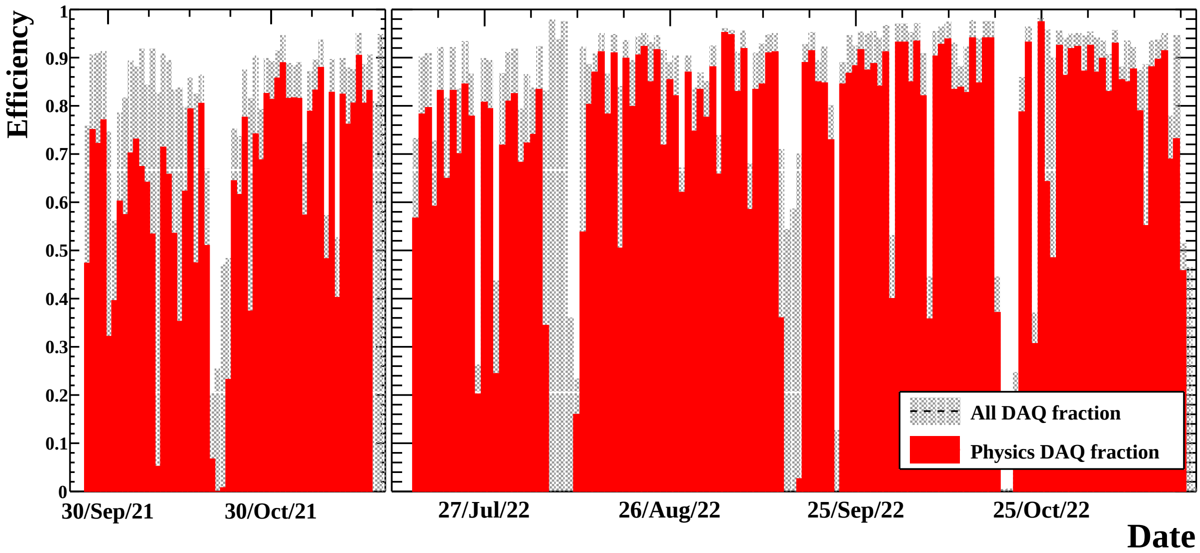

Figure 3.4: DAQ time fraction every 24 hours during physics runs 2021 and 2022.

Table 3.1: Nominal and measured muon stopping rate R_μ. The muon stopping rate decreased by tens % in the last few days at a nominal rate of $5 \times 10^7\ \mathrm{s}^{-1}$ in 2021 due to a lower proton current in the main ring.

Year	Period	Nominal R_μ (s^{-1})	Measured R_μ (s^{-1})
2021	25 Sept. – 15 Oct.	3×10^7	3.4×10^7
	15 Oct. – 28 Oct.	2×10^7	2.3×10^7
	28 Oct. – 2 Nov.	3×10^7	3.4×10^7
	2 Nov. – 10 Nov.	4×10^7	4.6×10^7
	10 Nov. – 18 Nov.	5×10^7	5.8×10^7
2022	14 Jul. – 27 Oct.	3×10^7	2.80×10^7
	27 Oct. – 7 Nov.	4×10^7	4.07×10^7
	7 Nov. – 17 Nov.	5×10^7	5.02×10^7

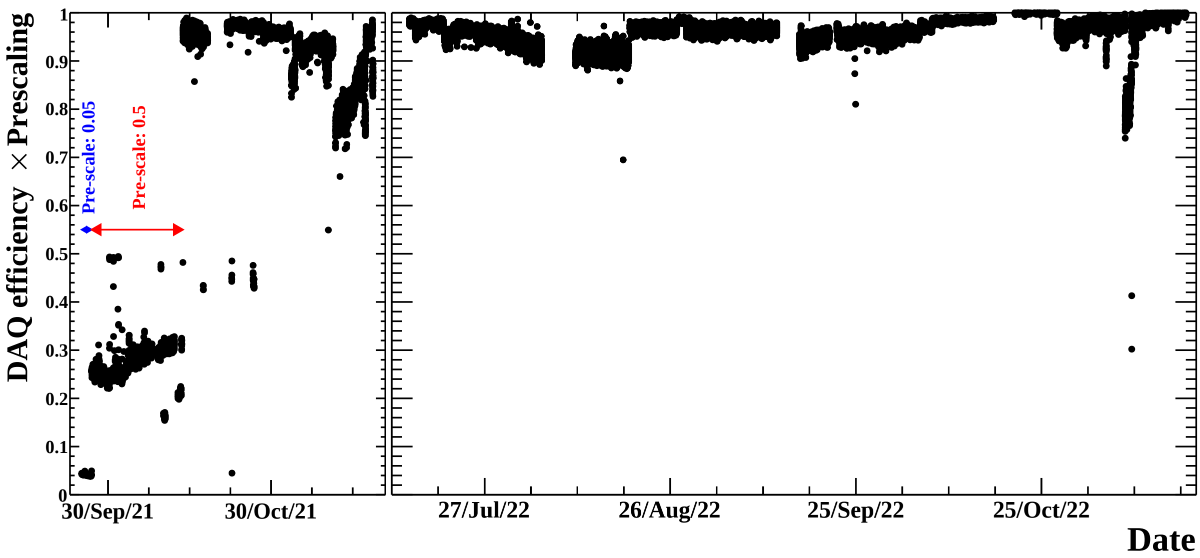

Figure 3.5: DAQ efficiency during the physics runs 2021 and 2022. The large inefficiency at the beginning of the run 2021 came from the pre-scaling of the MEG trigger, which was applied to keep the data rate below the capacity.

During the physics run 2021, the beam intensity increased step-by-step to confirm a stable detector operation and data recording, as summarised in Table 3.1. Regarding the data recording, the data rate must not exceed an upper limit of 130 MB/s [85]. Initially, since the data rate exceeded the limit, the trigger pre-scaling was applied to drop some of the triggered events. Figure 3.5 shows the DAQ efficiency, defined as the fraction of recorded events out of pre-scaled events meeting the trigger logic, during the physics runs 2021 and 2022. The time evolution of the number of muons stopped in the target is shown in Fig. 3.1, where the final value during the physics run 2021 was 0.87×10^{14}.

At the beginning of the run 2022, the beam intensity was set to $3 \times 10^7\ \mathrm{s}^{-1}$ to secure the PDE of the MPPCs in the LXe detector from the resolution degradation. It was found that the PDE could be kept high enough until the end of the run 2022 in October. Then, the beam intensity increased up to $5 \times 10^7\ \mathrm{s}^{-1}$, as summarised in Table 3.1, in order to investigate the detector and trigger performance for future runs[4]. As seen in Fig. 3.5, the DAQ efficiency was higher than 90 % expect for the beginning of the period at $5 \times 10^7\ \mathrm{s}^{-1}$, thanks to improvement of data recording bandwidth. The time evolution of the number of muons stopped in the target is also shown in Fig. 3.1, where the final value during the physics run 2022 was 2.39×10^{14}.

Daily calibration

The LXe detector and the pTC require daily calibration. Table 3.2 shows the calibration routine in the final period of the physics runs. The LXe detector calibration, which required frequent and precise calibration to correct for the time variations, dominated the calibration time consumption. Conservatively high calibration statistics were collected at the beginning, and then the necessary calibration routine was established. The calibration statistics in 2022 were reduced by half with respect to the run 2021, except for monochromatic photons. This is because the temporal evolution

[4] The beam rate has been set to $4 \times 10^7\ \mathrm{s}^{-1}$ since 2023 based on the detector performance measured with the 2021 and 2022 data.

Table 3.2: Calibration routine.

Dataset	DAQ frequency in 2021	DAQ frequency in 2022	Time comsumption
Random trigger data	2 day^{-1}	1 day^{-1}	10 min
LXe LED data (long)	1 day^{-1}	3 $week^{-1}$	40 min
LXe LED data (short)	1 day^{-1}	4 $week^{-1}$	10 min
LXe weak LED data		3 $week^{-1}$	30 min
LXe α-particle data	2 day^{-1}	1 day^{-1}	10 min
Cosmic-ray data	1 day^{-1}	3 $week^{-1}$	10 min
9 MeV photon data	3 $week^{-1}$	3 $week^{-1}$	15 min
17.6 MeV photon data	3 $week^{-1}$	3 $week^{-1}$	1 hour
pTC laser data	1 day^{-1}	3 $week^{-1}$	10 min

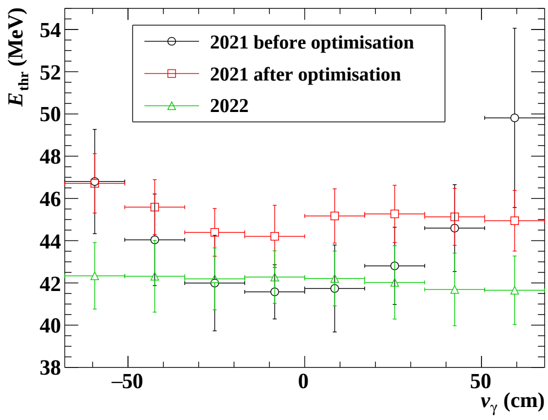

Figure 3.6: E_γ trigger threshold as a function of the v position of a photon v_γ. Error bars represent a standard deviation of the threshold. The threshold values before (black) and after the optimisation (red) in 2021 are shown. Those in 2022 (green) are also shown.

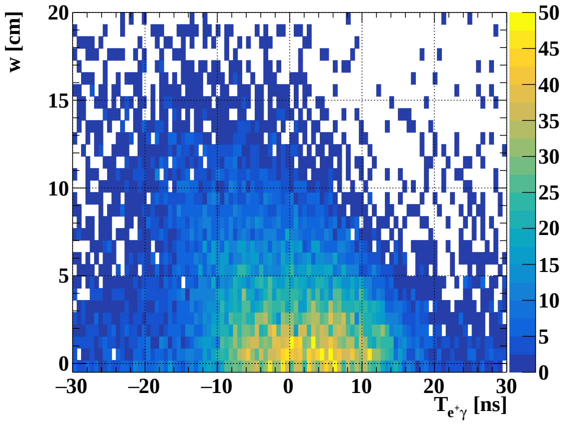

Figure 3.7: Time difference between a position and a photon $t_{e\gamma}$ as a function of the photon conversion depth w_γ in the 2021 MEG-triggered data [45].

was expected to be smooth unless any accidents happened, based on the experience in run 2021.

Trigger setting

In the initial phase of the physics run 2021, there was 10 % non-uniformity on the online E_γ reconstruction, in particular in the v direction [59]. The online E_γ uniformity was improved, resulting in better uniformity in the E_γ trigger threshold, as shown in Fig. 3.6. The online timing of the LXe detector was computed based on MPPC signals in the run 2021, resulting in a significant time walk effect (Fig. 3.7). As a photon interacted in a deeper region, more events were distributed outside the coincidence window. In addition to being out of the coincidence window, an effective threshold for the signal amplitude of MPPCs was imposed to make the online timing calculation robust. Both trigger configurations reduced deeper events.

Each trigger logic composing the MEG trigger in the run 2022 had one or two updates from the run 2021. The E_γ trigger threshold was much more uniform, as shown in Fig. 3.6, than in 2021, thanks to

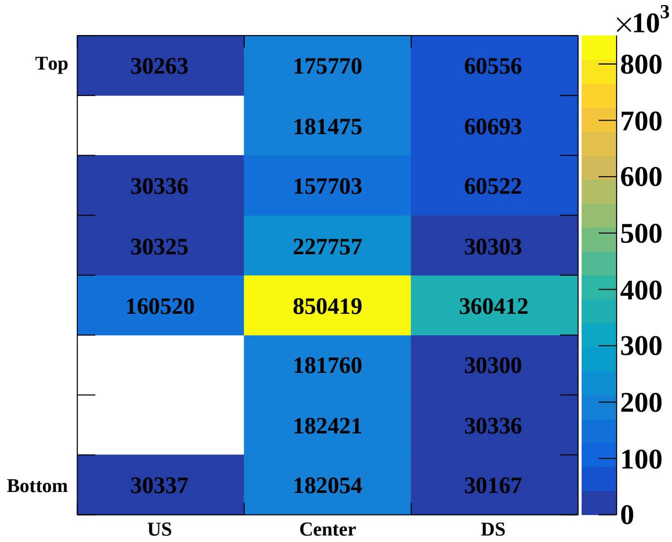

Figure 3.8: The number of events acquired for each region in the 2021 π^0 run [59].

the online E_γ computation optimisation. The time coincidence trigger logic utilised the PMT signals for the online photon time computation instead of the MPPC ones, mitigating the time-walk effect. The DM trigger logic was updated to reduce fake positron candidates generated by multi-turn positrons. In addition to the pTC side, cabling for the MPPCs in the LXe detector was updated so that MPPCs which were physically close to each other were connected to the same WaveDREAM board.

The trigger performance is assessed by the trigger efficiency, introduced in Sect. 2.6.2. The efficiency was evaluated to be (91 ± 2) % ((88 ± 2) %) in 2022 (2021), as discussed in Sect. 8.6.

3.3 Calibration runs

Low-intensity muon run 2021 The calibration run with a very low beam intensity of $R_\mu \sim 1{\times}10^6\ \mathrm{s}^{-1}$ was conducted in the 18th–21st November 2021. This low-intensity run aimed to efficiently collect the RMD events for the $t_{e\gamma}$ offset calibration at the first phase of the offline analysis. These events can also be used to tune the parameters of the multi-photon event analysis because pileups are suppressed, which is described in Sect. 4.1.2.

π^0 calibration run 2021 The π^0 calibration run was conducted during 16th–22nd December 2021, after the preparation of the liquid hydrogen target. Although the goal was the full scan of the whole LXe detector for calibration and performance assessment, it was not completed because of an issue with the liquid hydrogen target. It had insufficient cooling power to stably keep the hydrogen in a liquid state. This resulted in a lack of experimental time and no DAQ in several regions as shown in Fig. 3.8.

π^0 calibration run 2022 The π^0 calibration data were taken during 4th–16th December 2022. The goal of the π^0 calibration run 2022 was to complete the full scan of the whole detector, which was not achieved in the run 2021. The cooling system of the liquid hydrogen target was significantly improved by optimising thermal contact and insulation [80]. Thanks to this improvement, the full scan was completed for the first time in the MEG II experiment.

Chapter 4

Event reconstruction

Figure 4.1 shows the reconstruction overview. The photon position, time at the conversion point, and energy are measured by the LXe detector, as explained in Sect. 4.1. The positron kinematics at the decay vertex on the muon stopping target are reconstructed by the positron spectrometer, as described in Sect. 4.2. Based on the reconstructed positron decay vertex, one reconstructs relative angles and time between the photon and positron, as discussed in Sect. 4.3.

4.1 Photon reconstruction

Figure 4.2 shows a photon reconstruction scheme. The photon reconstruction begins with waveform analysis to obtain an integrated charge Q_i and a pulse timing t_i for the i-th photosensor. The integrated charge Q_i is converted into the number of impinging scintillation photons on a photosensor $N_{\mathrm{pho},i}$ by

$$N_{\mathrm{phe},i} = \frac{Q_i}{G_i \times F_{\mathrm{EC},i}}, \tag{4.1}$$

$$N_{\mathrm{pho},i} = \frac{N_{\mathrm{phe},i}}{\epsilon_i}, \tag{4.2}$$

where G_i is gain; $F_{\mathrm{EC},i}$ is ECF for MPPCs; and ϵ_i is PDE (QE) for MPPCs (PMTs). The $N_{\mathrm{pho},i}$ distribution on the inner face gives the photon conversion position, and the t_i distribution provides the photon with conversion time. The total $N_{\mathrm{pho},i}$ is converted into the photon energy.

4.1.1 Waveform analysis

The photon reconstruction begins with waveform analysis. The event reference time is defined as the crossing time of the signal at a 10 % fraction of the amplitude in the PMT summed waveform.

A single-channel waveform analysis searches for the maximum amplitude in the range from −50 ns to 300 ns with respect to the reference time (Fig. 4.3). The constant-fraction time at 10 % for the found pulse represents the pulse time t_i, shown by a blue star in Fig. 4.3. The pulse time t_i is corrected by the time-walk t_{walk} and time offset t_{offset}, which is notated as

$$t_{\mathrm{pm},i} = t_i - t_{\mathrm{walk},i}(N_{\mathrm{phe},i}) - t_{\mathrm{offset},i}. \tag{4.3}$$

Section 6.2.6 describes the time-walk and time offset calibration.

The waveform is integrated in [−20 ns, 130 ns] with respect to the reference time (drawn as a green arrow), computing the integrated charge Q_i. The narrower integration width than the peak search allows us to suppress the pileup photons' contamination. Because a large signal pulse saturates the

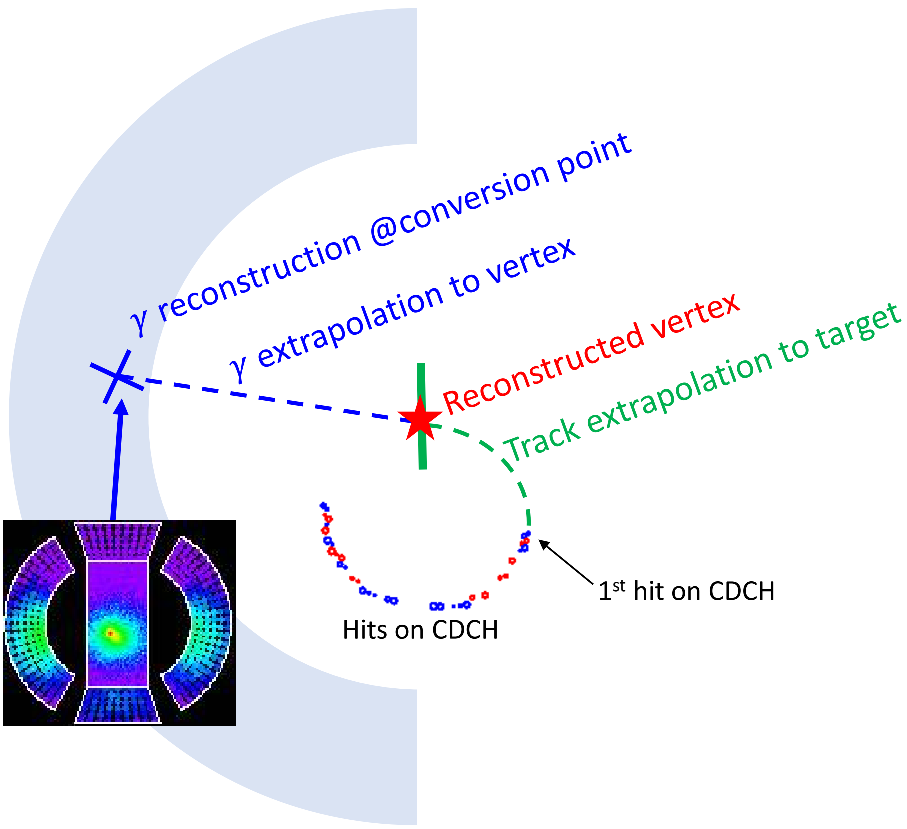

Figure 4.1: An overview of event reconstruction procedure [46].

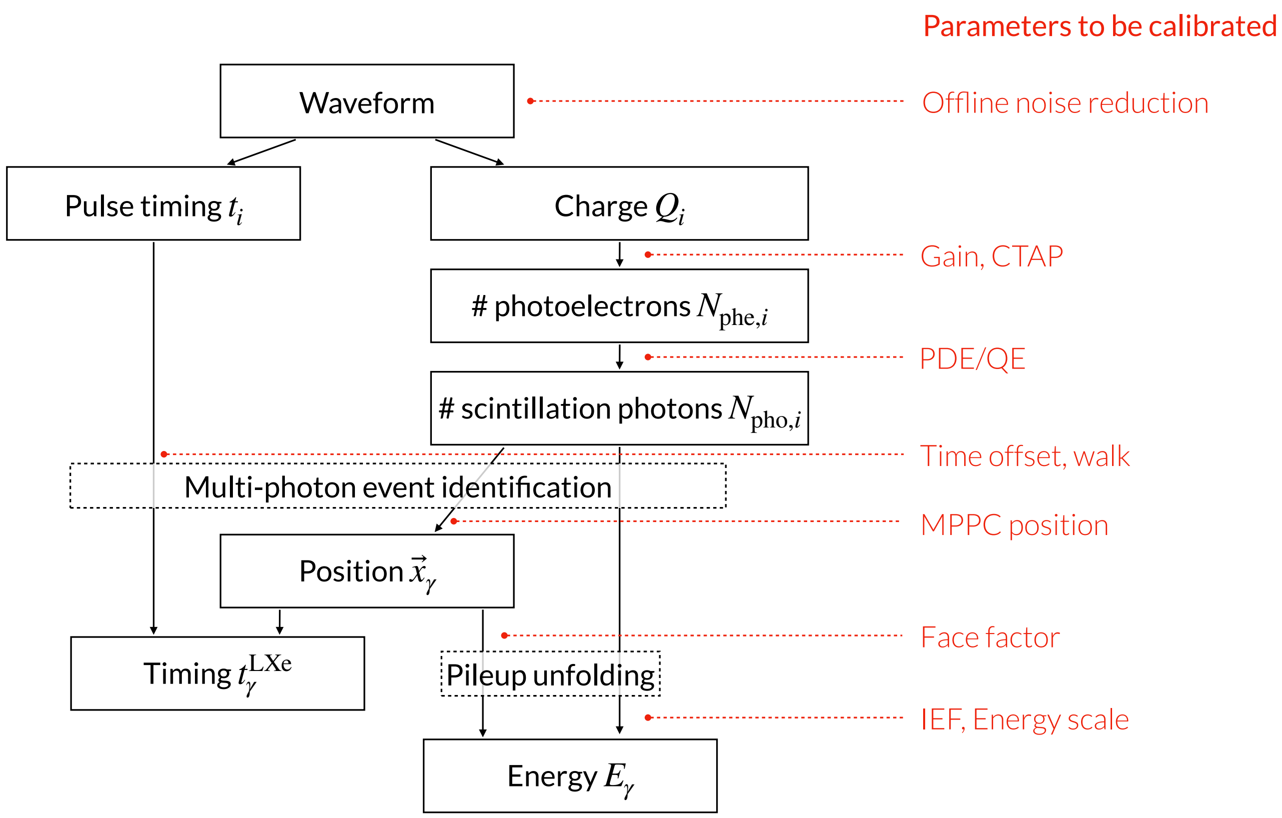

Figure 4.2: A photon reconstruction flowchart. The photon reconstruction begins with waveform analysis and measures the photon's conversion position, timing, and energy.

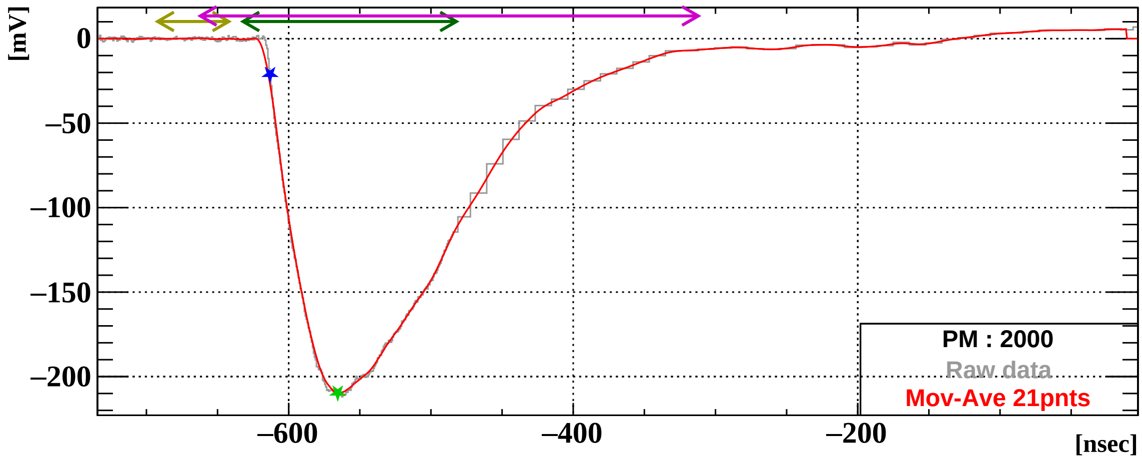

Figure 4.3: An MPPC single-channel waveform in an event. A raw waveform drawn in black is moving-averaged by 21 bins, drawn in red. A yellow arrow shows a range to calculate the baseline, a magenta arrow shows the one to search for the maximum amplitude, and a green arrow shows the one to integrate. A blue star shows the constant-fraction threshold of 10 % and its timing, and a green star shows the maximum amplitude and its timing.

DRS voltage range and photosensor's response, a method based on the time over threshold (TOT) gives Q_i instead of integrating the waveform, in case the pulse height is above a threshold of 600 mV. The integrated charge Q_i is converted into $N_{\mathrm{pho},i}$ with Eqs. (4.1) and (4.2).

4.1.2 Multi-photon event identification

Multiple off-timing (on-timing) photons can be detected within the DRS time window due to pileup (positron's AIF: $e^+e^- \to \gamma\gamma$), as discussed in Sect. 5.1. In order to give their position and time for the subsequent analyses and identify the multi-photon event candidates, spatially separated peaks in the $N_{\mathrm{pho},i}$ distribution are searched for. This peak search finds local maxima of the $N_{\mathrm{pho},i}$ larger than a threshold [39]. The threshold is adjusted to obtain a consistent event fraction of multi-photon events between the simulated background photon sample without event mixing (Sect. 2.7) and data at a low muon beam rate. Photosensors are clustered into groups based on the found peaks, and the photosensor having the maximum N_{pho} in a group is selected as a representative photosensor.

If multiple peaks are found, one must determine which peak is reconstructed in the subsequent reconstruction schemes, called the "main photon", because only a single photon is reconstructed. The main photon is required to satisfy the following conditions:

- t_{pm} of the representative photosensor is within 30 ns with respect to the reference time, and
- N_{pho} of the representative photosensor is the largest among all the representative photosensors.

4.1.3 Position reconstruction

The photon position $\vec{x}_\gamma$ is defined as the first conversion point. The reconstruction utilises the $N_{\mathrm{pho},i}$ distribution viewed only by the MPPCs on the inner face to suppress event-by-event fluctuation of shower development. It has two steps: a one-dimensional projection fit and a local solid angle fit. The initial uv position of the first fitting step is given by the roughly estimated position for the main photon in the preceding analysis.

In the projection fit, the $N_{\mathrm{pho},i}$ distribution in the uv plane is projected in the u or v axis, and then fitted by a symmetric response function. An estimated peak position gives the u and v position, and

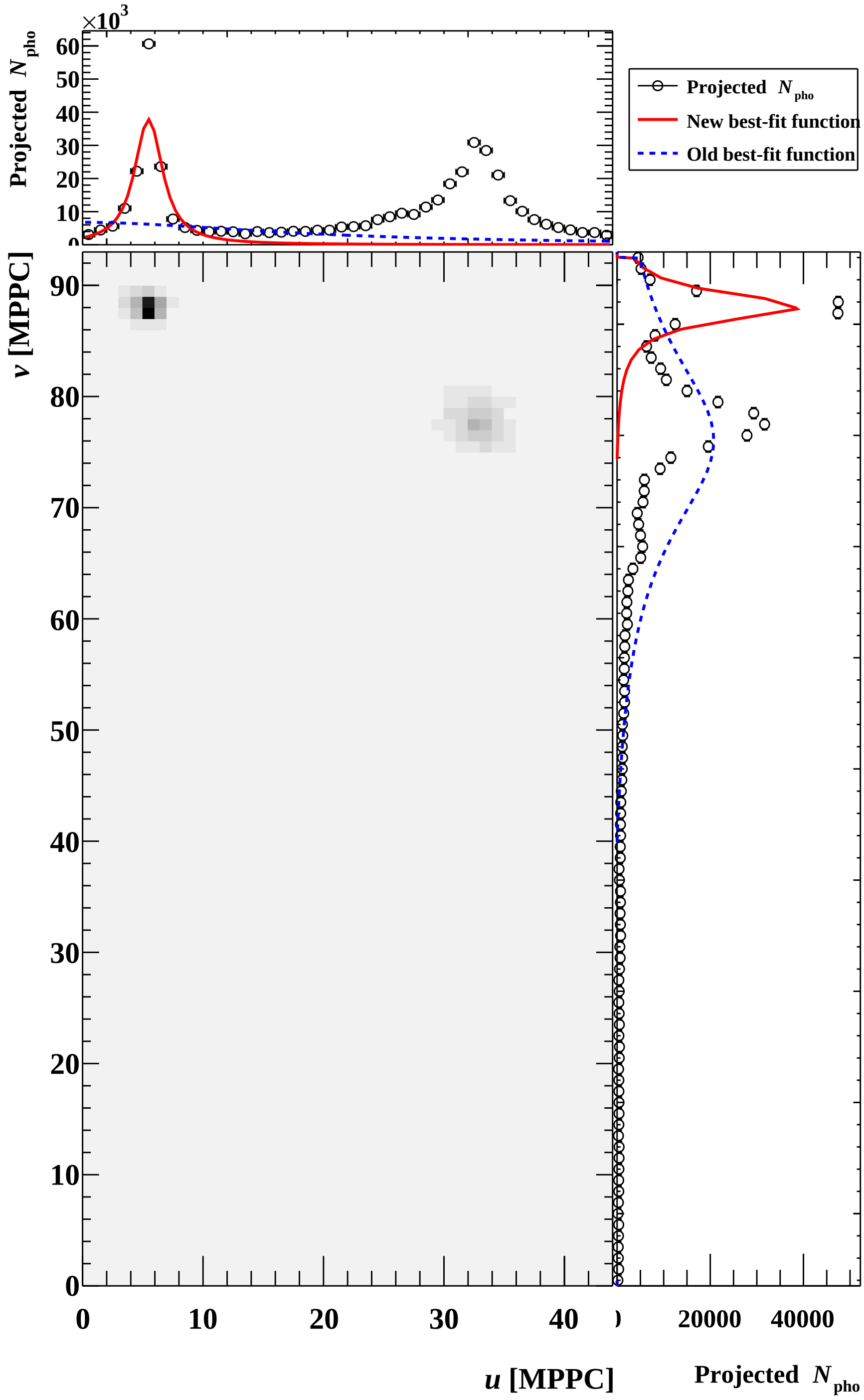

Figure 4.4: An example of an event where the projection fit failed to estimate the position before, but represents data well after using the information on the fitting quality. The black open circles show the projected $N_{\mathrm{pho},i}$ distribution. The solid red function is fitted with the satisfied quality, and the dashed blue one is a failed fit.

a peak width gives the w position. The best-fit position provides an initial position and a localised circular region used in the subsequent solid angle fit. When multiple peaks were found, particularly those close to each other, the projection fit sometimes failed to estimate the position in the previous analysis, as shown in the dashed blue function of Fig. 4.4. I newly utilised the information on fitting quality so as to prevent the fitting from failing the position estimation. Figure 4.4 shows an example of an event where the projection fit failed to estimate the position before using the fitting quality, but succeeds with it. The usage of this information mitigates the w_γ dependence of the event category (defined in Sect. 5.2), which was not realised in the previous analysis.

The local solid angle fit determines the position by fitting the expected light distribution calculated from the solid angles to the observed $N_{\mathrm{pho},i}$ distribution. It minimises a χ^2_{pos} defined as

$$\chi^2_{\mathrm{pos}}(\vec{x}_{\gamma,\mathrm{fit}}) = \sum_{i \in \mathrm{region}} \left[\frac{N_{\mathrm{pho},i} - S_{\mathrm{light}} \times \Omega_i(\vec{x}_{\gamma,\mathrm{fit}})}{\sigma_{\mathrm{pho},i}} \right]^2, \tag{4.4}$$

$$\sigma_{\mathrm{pho},i} = N_{\mathrm{pho},i} / \sqrt{N_{\mathrm{phe},i}}, \tag{4.5}$$

where S_{light} is the scale of light distribution and $\Omega_i(\vec{x}_{\gamma,\mathrm{fit}})$ is the solid angle at position $\vec{x}_{\gamma,\mathrm{fit}}$ subtended by the photosensor.

This minimisation in Eq. (4.4) assumes a point-like source of scintillation light. However, due to the finite spatial extent of EM showers, particularly their directional development correlated with the photon incident angle, the fitted position $\vec{x}_{\gamma,\mathrm{fit}}$ may exhibit systematic bias. To correct for this effect, two empirical corrections derived from MC simulations are applied [59], yielding the final reconstructed photon conversion position $\vec{x}_\gamma$.

4.1.4 Time reconstruction

The photon conversion time is reconstructed with both MPPCs and PMTs by minimising

$$\chi^2_{\mathrm{time}}(t^{\mathrm{LXe}}_{\gamma,\mathrm{fit}}) = \sum_{N_{\mathrm{phe},i} > 50} \frac{\left(t_{\mathrm{pm},i} - t_{\mathrm{prop},i} - t^{\mathrm{LXe}}_{\gamma,\mathrm{fit}}\right)^2}{\sigma^2_{\mathrm{pm},i}}, \tag{4.6}$$

where $t_{\mathrm{pm},i}$ is the detected pulse time written in Eq. (4.3); $t_{\mathrm{prop},i}$ is the travel time of the scintillation light from the reconstructed first interaction point to the i-th photosensor using the effective velocity of scintillation light in LXe (8.4 cm/ns [46]); $t^{\mathrm{LXe}}_{\gamma,\mathrm{fit}}$ is the estimated conversion time; and $\sigma_{\mathrm{pm},i}$ is single-photosensor resolution as a function of $N_{\mathrm{phe},i}$.

The initial $t^{\mathrm{LXe}}_{\gamma,\mathrm{fit}}$ is given by the averaged pulse time of the photosensors in the circular region used in the preceding position fit. In order to make the time fit robust against pileup photons, the fitting is iterated until it converges up to eight times with outlier rejection. The number of photosensors used in the time fit is typically a few hundred for signal photons. In the previous analysis, the initial $t^{\mathrm{LXe}}_{\gamma,\mathrm{fit}}$ was given by the pulse time of the photosensor with the maximum $N_{\mathrm{pho},i}$ and the filtration procedure was not fully optimised. The new algorithm provides a good resolution regardless of the presence of pileup photons.

Finally, the best-fit time $t^{\mathrm{LXe}}_{\gamma,\mathrm{fit}}$ is corrected by the position-dependent time offset, giving the photon conversion time $t^{\mathrm{LXe}}_{\gamma}$ as,

$$t^{\mathrm{LXe}}_{\gamma} = t^{\mathrm{LXe}}_{\gamma,\mathrm{fit}} - F_t(u, v, w), \tag{4.7}$$

where $F_t(u, v, w)$ is the position dependence correction function, which is discussed in Sect. 6.2.6.

4.1.5 Energy reconstruction

The photon energy is reconstructed by collecting all scintillation light from the EM shower emitted by a photon and scaling it by a factor S_{E_γ} as

$$E_\gamma = S_{E_\gamma} \times T(t) \times U(u_\gamma, v_\gamma, w_\gamma; t) \times N_{\mathrm{sum}}, \tag{4.8}$$

$$N_{\mathrm{sum}} = N_{\mathrm{MPPC}} \times (1 + F_{\mathrm{IE}}(t)) + N_{\mathrm{PMT}}, \tag{4.9}$$

$$N_{\mathrm{MPPC(PMT)}} = \sum_{\mathrm{MPPC(PMT)}} W_i(u_\gamma, v_\gamma, w_\gamma) \times N_{\mathrm{pho},i}, \tag{4.10}$$

where $T(t)$ and $F_{\mathrm{IE}}(t)$ are correction functions for the temporal evolution, $U(u_\gamma, v_\gamma, w_\gamma; t)$ is a function to correct the non-uniformity, and $W_i(u_\gamma, v_\gamma, w_\gamma)$ is a position-dependent weight for each photosensor.

Weight calculation

The weight $W_i(u_\gamma, v_\gamma, w_\gamma)$ is a product of the reciprocal of the photosensor coverage C_i, the compensation factor of dead channels $F_{\mathrm{dead},f}$, and the factor of light collection efficiency depending on the reconstructed photon position and the face of the detector $F_{\mathrm{face},f}$ (*face factor*), that is,

$$W_i(u_\gamma, v_\gamma, w_\gamma) = C_i \times F_{\mathrm{dead},f}(u_\gamma, v_\gamma, w_\gamma) \times F_{\mathrm{face},f}(u_\gamma, v_\gamma, w_\gamma), \tag{4.11}$$

where f is an index of face to which the i-th photosensor belongs[1].

Dead channel compensation The existence of dead channels causes position dependence on the light collection efficiency. To mitigate the position dependence, I estimate the number of scintillation photons impinging on the dead channel using photosensors within 20 cm distance around it. If the number of scintillation photons detected by the surrounding photosensors $\sum_i N_{\mathrm{pho},i}$ is above 50, that of the dead channel $N_{\mathrm{pho,dead}}$ is estimated with solid angles as

$$N_{\mathrm{pho,dead}} = \Omega_{\mathrm{dead}}(u_\gamma, v_\gamma, w_\gamma) \times \frac{\sum_i N_{\mathrm{pho},i}}{\sum_i \Omega_i(u_\gamma, v_\gamma, w_\gamma)}, \tag{4.12}$$

where $\Omega_{\mathrm{dead}(i)}$ is a solid angle of the dead (i-th) channel from the reconstructed position $(u_\gamma, v_\gamma, w_\gamma)$. On the other hand, if not, it is estimated with the average, that is,

$$N_{\mathrm{pho,dead}} = \frac{\sum_i N_{\mathrm{pho},i}}{n_{\mathrm{surround}}}, \tag{4.13}$$

where n_{surround} is the number of surrounding channels. A factor to recover the dead channels is calculated for a face with index f as

$$F_{\mathrm{dead},f} = \frac{\sum_{\mathrm{meas}} N_{\mathrm{pho},i} + \sum_{\mathrm{dead}} N_{\mathrm{pho},j}}{\sum_{\mathrm{meas}} N_{\mathrm{pho},i}}. \tag{4.14}$$

The solid angle method with Eq. (4.12) overestimates the dead channel compensation factor $F_{\mathrm{dead},f}$ when the reconstructed position is very close to dead channels, making a very-high-energy tail as shown in Fig. 4.5. An event selection criterion based on the solid angle to dead channels is, thus, introduced, as discussed in Sect. 4.1.6. I, however, observed the 0.4 % better energy resolution in the MC simulation. At the same time, I did not see the improvement in the data of 54.9 MeV photons from $\pi^0 \to \gamma\gamma$ due to its too small contribution. The solid angle method is adopted, given its potential for improving energy resolution.

[1]Face indices: 0, Inner; 1, Outer; 2, Upstream; 3, Downstream; 4, Top; 5, Bottom.

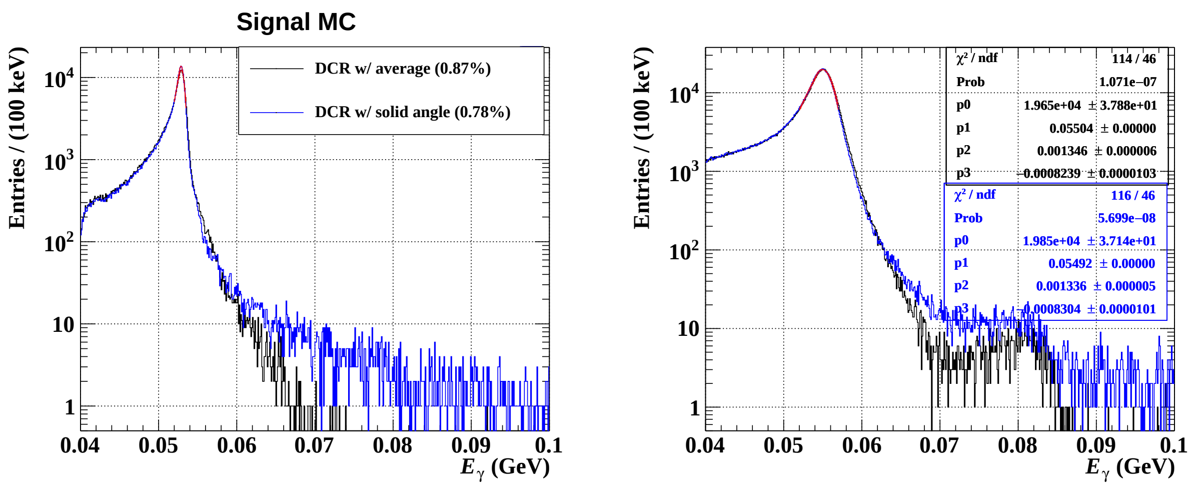

(a) 52.8 MeV photon in MC simulation.

(b) 54.9 MeV photon in data.

Figure 4.5: Energy spectra with dead channel compensation with two methods of Eq. (4.12) (blue) and Eq. (4.13) (black). A very-high-energy tail is seen in both samples.

Face factor The other factor to mitigate the position dependence of light collection efficiency is the so-called "*face factor*" [59]. The idea is to give the sharpest N_{sum} peak by weighting the number of scintillation photons detected by photosensors on each face N_{face} depending on the reconstructed $(u_\gamma, v_\gamma, w_\gamma)$ position. The face factors mitigate the position dependence of N_{sum} and give a relatively sharp spectrum peak. Section 6.2.7 describes its optimisation.

Pileup unfolding

When multiple photons impinge on the LXe detector in a high-intensity muon beam, the energy resolution is degraded without any dedicated analyses. I unfold temporally separated photons using waveform analysis techniques to obtain the energy of a single photon. The details are discussed in Sect. 5.2. I reconstruct the weighted sum of scintillation photons N_{MPPC} and N_{PMT} in Eq. (4.10) through the pileup unfolding analysis.

Conversion from the number of scintillation photons to energy

Different trends of the temporal evolution of N_{MPPC} and N_{PMT} were observed in the runs 2021 and 2022. The face factors $F_{\mathrm{face},f}$, however, do not consider the temporal variation of the difference. An introduction of inner excess factor (IEF) $F_{\mathrm{IE}}(t)$ corrects the temporal evolution of the difference in MPPC and PMT overall responses. It can be understood as correcting the temporal evolution of the inner face factor. The correction function is designed to keep $(1 + F_{\mathrm{IE}})N_{\mathrm{MPPC}}/N_{\mathrm{PMT}}$ at a constant value throughout each year's run. The constant value is yearly set to $N_{\mathrm{MPPC}}/N_{\mathrm{PMT}}$ at the beginning of the π^0 calibration run T_{π^0}; i.e. $F_{\mathrm{IE}}(T_{\pi^0}) = 0$. Section 6.2.8 describes the construction of the correction function $F_{\mathrm{IE}}(t)$. The weighted sum of scintillation photons N_{sum} is reconstructed with Eq. (4.9).

Finally, N_{sum} is converted to the photon energy E_γ with Eq. (4.8). The conversion factor S_{E_γ} is determined by extracting the N_{sum} peak for quasi-monochromatic 54.9 MeV photons whose conversion position is in the fiducial volume at the time T_{π^0}. This implies that the energy scale's temporal variation and non-uniformity cause energy resolution degradation. The correction functions $T(t)$ and $U(u_\gamma, v_\gamma, w_\gamma; t)$, therefore, must be made to achieve the best energy resolution, which is discussed in Sect. 6.2.9.

Table 4.1: Background rejection power and signal analysis efficiency of photon selection.

	Background rejection power	Signal analysis efficiency
Reconstruction quality cut		(99.6 ± 0.1) %
Pileup analysis	22 % at $R_{\mu} = 5 \times 10^{7}\,\mathrm{s}^{-1}$	(94.2 ± 0.5) %
Cosmic-ray event cut	19 %	(99.9 ± 0.1) %
Cut based on solid angle to inactive photosensors	94 %	(99.7 ± 0.3) %
Total		(93.4 ± 0.6) %

4.1.6 Event selection

Definition of fiducial volume

The fiducial volume of the LXe detector is defined with the local coordinate system as

$$\begin{aligned} |u| &< 23.9\,\mathrm{cm}, \\ |v| &< 67.9\,\mathrm{cm}. \end{aligned} \tag{4.15}$$

The w fiducial range is not defined because a lower bound of the depth is restricted, and no very deep event at $w_{\gamma} \gtrsim 30\,\mathrm{cm}$ is reconstructed due to the algorithm of the solid angle fit.

Quality cut and background rejection

Table 4.1 summarises the selection criteria, their background rejection power, and signal analysis efficiency of each selection. The signal analysis efficiency is evaluated as (93.4 ± 0.6) % in total. The following discusses each selection.

Cut based on reconstruction quality The reconstruction quality is evaluated by χ^2 values of the position and time fits in Eq. (4.4) and Eq. (4.6), respectively. A failure in representing the $N_{\mathrm{pho},i}$ distribution enlarges large position fit χ^2 value, χ^2_{pos}, which happens when the best-fit w_{fit} is behind MPPCs and EM shower develops asymmetically in the v axis. The latter asymmetric shower development is likely due to cosmic-ray muons instead of photons. On the other hand, the χ^2_{pos} is often large as $O(10)$ when the the conversion depth is very shallow. Therefore, the position fit quality cut threshold was set to 100. The time fit quality is ensured by imposing a χ^2_{time} cut with a threshold of 1.8 to achieve a good time resolution. In addition to the χ^2_{time} cut, the number of photosensors used in the time fit is required to be above 100.

Pileup event categories Pileup unfolding analysis categorises events based on fit convergence and the presence of on-time multiple photons, which is explained in Sect. 5.2. Two categories, *Coincidence* and *NotConverged*, out of four listed in Table 5.1 are rejected from the analysis sample.

Cosmic-ray event rejection A cosmic-ray spectrum has a flat distribution while the background photon spectrum sharply drops around 52.83 MeV, which requires a dedicated cut to suppress the high-energy tail in 48 MeV to 58 MeV. Most cosmic-ray events are rejected by the fiducial volume cut in Eq. (4.15) since cosmic rays depositing energy of 48 MeV to 58 MeV typically pass through the corner of the detector. The rest of the cosmic-ray events are characterised by a deep reconstructed w position. In very deep cosmic-ray events, the time fit is often not converged. Figure 4.6 shows the

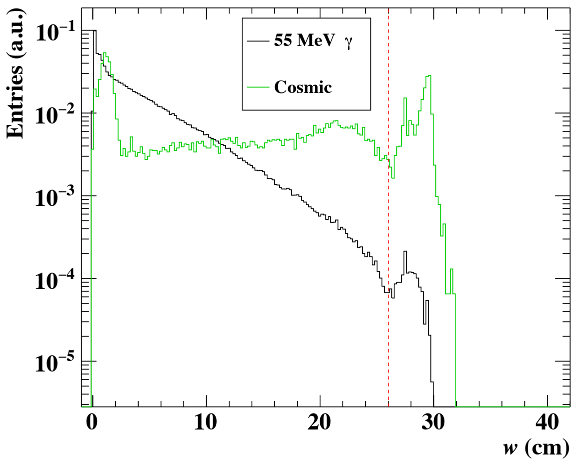

Figure 4.6: Reconstructed w distributions for cosmic-ray events (green) and 54.9 MeV photons. The cut threshold is set to 26 cm drawn in a red line.

w distribution of the remaining cosmic-ray events and 54.9 MeV photons with imposing the selection discussed above, showing the clear difference. The cut threshold is optimised to 26 cm to further reject cosmic-ray events.

Cut based on solid angle to dead channels As discussed in Sect. 4.1.5, the compensation factor of dead channels overestimates the photon energy when the photon position is very close to dead channels. To reject events with overestimated energy, only events that satisfy the following condition are selected:

$$\sum_{\text{dead}} \Omega_i(\vec{x}_\gamma) < 0.8, \tag{4.16}$$

where $\Omega_i(\vec{x}_\gamma)$ is the solid angle to the i-th dead channel from the $\vec{x}_\gamma$.

4.2 Positron reconstruction

Figure 4.7 shows the positron reconstruction flowchart. The positron reconstruction begins with the hit reconstruction via waveform analysis in the pTC and CDCH channels. Then, the positron trajectory is reconstructed through track finding and fitting. The fitted track is propagated both forward to the pTC and backwards to the muon stopping target, providing the positron kinematics at the target. This section describes the positron reconstruction algorithms. A more extensive discussion on the pTC is given by Refs. [95, 96, 45] and on the CDCH is by Ref. [97].

4.2.1 Hit reconstruction and clustering in pTC

Waveform analysis Waveform analysis is performed using a digital constant-fraction method to extract the pulse time t_i for each channel. The optimal fraction for time resolution is determined individually for each channel (usually 25 %).

Hit reconstruction The positron impact time t_{hit} and the position along the long side of the scintillator w_{hit} for each counter are reconstructed from the time of the SiPM signals at the both ends ($t_{\text{Ch1(2)}}$

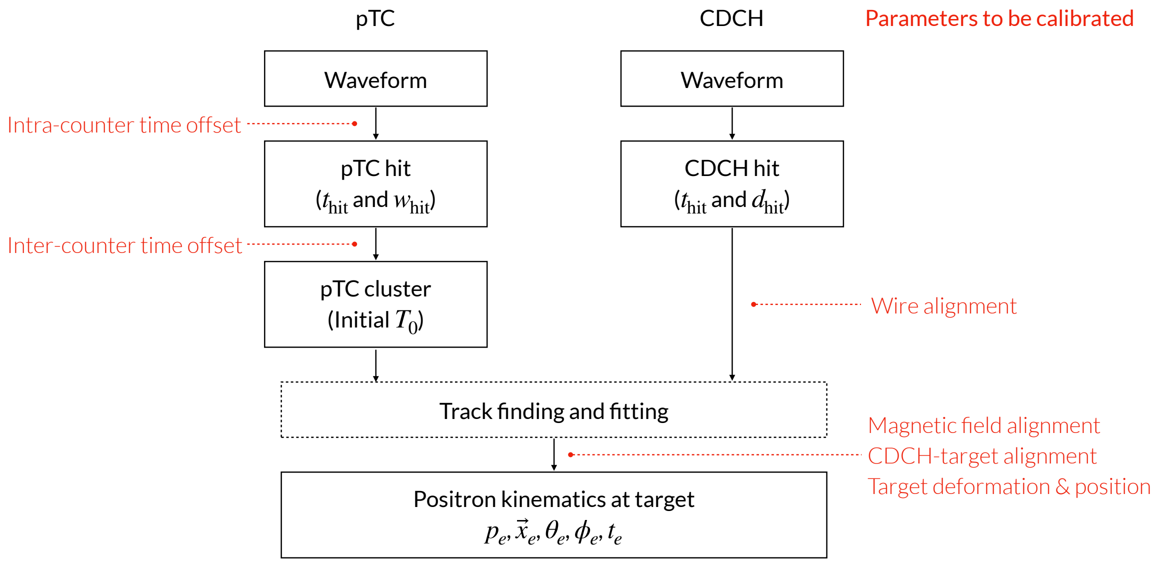

Figure 4.7: Positron reconstruction flowchart.

for channel 1 (2) of the counter):

$$t_{\mathrm{hit}} = \frac{t_{\mathrm{Ch1}} + t_{\mathrm{Ch2}}}{2} - \frac{t_{\mathrm{offset,Ch1}} + t_{\mathrm{offset,Ch2}}}{2} - \frac{L_{\mathrm{counter}}}{2v_{\mathrm{eff}}}, \tag{4.17}$$

$$w_{\mathrm{hit}} = v_{\mathrm{eff}} \left(\frac{t_{\mathrm{Ch1}} - t_{\mathrm{Ch2}}}{2} - \frac{t_{\mathrm{offset,Ch1}} - t_{\mathrm{offset,Ch2}}}{2} \right), \tag{4.18}$$

where $L_{\mathrm{counter}} = 120\,\mathrm{mm}$ is the length of the scintillator, $t_{\mathrm{offset,Ch1(2)}}$ is the time offset for the channel, and v_{eff} is the effective speed of light in the scintillator. $t_{\mathrm{Ch1(2)}}$ and v_{eff} are counter-dependent parameters discussed in Sect. 6.3.

Hit clustering A positron usually leaves hits in multiple counters. Clusters of hits are formed by grouping temporally and spatially correlated hits. The same positron can hit counters after exiting the pTC region and entering the region again through another half-turn. These hits are grouped into different clusters.

The highly granular counter configuration can estimate the positron trajectory from the hit pattern of each cluster. A look-up table derived from MC simulations is employed to estimate the radial coordinate (v_{hit}) of each hit within a cluster. The cluster time and position serve as inputs for the subsequent track-finding algorithm, and seed the tracks in CDCH at time T_0.

4.2.2 Hit reconstruction in CDCH

Waveform analysis The CDCH analysis begins with waveform analysis to identify the signals induced by drift electrons in cells traversed by positrons, called "hits". Two waveform processing algorithms have been developed to detect hits with high efficiency.

The first algorithm is a conventional threshold-based method with suppression of coherent low-frequency and incoherent high-frequency noises. The coherent low-frequency noise is suppressed using the averaged waveform over each DRS chip corresponding to eight channels, excluding the region with signal pulses. The incoherent high-frequency noise above 200 MHz, which is negligible for the signal power, is suppressed by applying a low-pass filter with a cut-off frequency of 225 MHz to the waveform using a discrete Fourier transform technique.

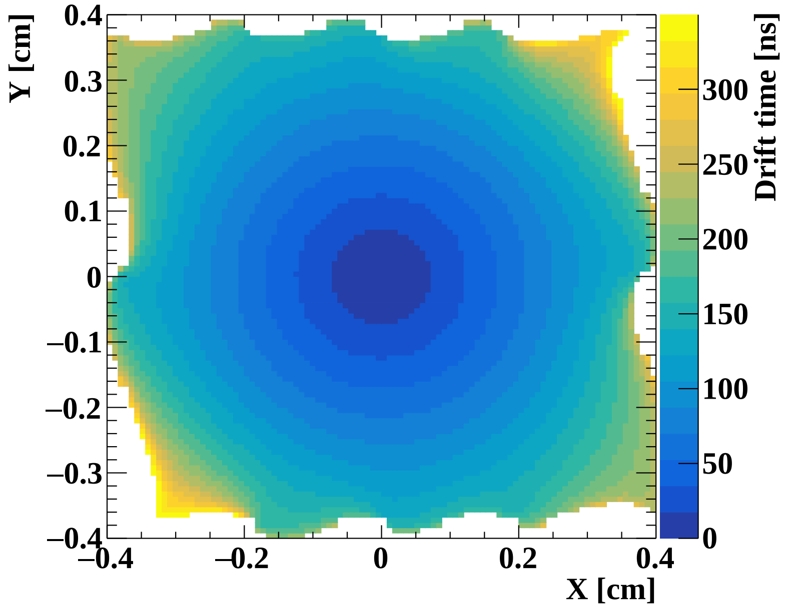

Figure 4.8: An example of time-distance relationship in a drift cell [46].

The other method utilises a deep learning (DL) algorithm based on a convolutional neural network (CNN) trained on simulated waveforms overlaid with real noise data taken without a beam. The network model accepts waveforms from eight channels in a DRS chip as input to learn the pattern of the coherent noise as well as that of the signal, and outputs the probability of the first cluster arrival time of a hit.

Combining the results of the two methods obtains a higher hit efficiency but also a higher fake hit rate than the first method. To maximise the effectiveness of the results from the two methods, the subsequent tracking procedure is repeated twice: the first with only the hits found with the first method, and the second with the hits found with a combination of the two methods. The results from each tracking procedure are finally combined. This approach improves the final tracking efficiency (Sect. 7.2.4) by 26 % compared to applying only the first method.

A signal is always induced on both ends of the wire with similar shapes. A cross-fitting algorithm, in which one end of a waveform is used as the fitting function of the other waveform, computes the time difference and the relative signal size on the two ends of the wire for the subsequent hit position reconstruction.

Hit reconstruction The difference in arrival times and the ratio between the total charges collected on the two ends of the sense wire facilitate a preliminary reconstruction of the longitudinal (z) coordinate of the hit. Although the approximate resolution of the z-coordinate is 15 cm with this reconstruction, it helps to ensure that the track finding process is efficient and robust against pileup[2]. The hit time t_{hit} is measured from the summed waveform of the two ends after adjusting the relative timing of the two.

Another important parameter is the drift distance of ionisation clusters, i.e., the particle's distance of closest approach (DOCA) to the anode wire. The drift distance is calculated from the wire hit time t_{hit} and the T_0 input from the pTC, that is,

$$d_{\text{hit}} = \zeta_{\text{TXY}}(t)(t_{\text{hit}} - T_0), \tag{4.19}$$

[2]The z-coordinate resolution is finally assessed by exploiting the stereo configuration of the wires in the tracking stage.

where $\zeta_{\mathrm{TXY}}(t)$ is the time-distance relationship (TXY tables) shown in Fig. 4.8, which is based on Garfield++ simulation results [92].

4.2.3 Track finding and fitting

The positron track reconstruction using the reconstructed hits is performed in two steps: the track finding, which combines hits produced by the same positron into a track candidate, and the track fitting, which extracts the best estimate of the positron's kinematics at the target. Both steps are based on the Kalman filter [98].

Track finding The track-finding algorithm utilises a pattern recognition method that initiates from hit pairs in the outer CDCH layers, where occupancy is relatively low. To construct track seeds, all feasible combinations of two hit pairs associated with T_0 across different layers are considered. Each track seed is subsequently propagated inwards through adjacent layers, with the Kalman filter algorithm employed to iteratively assess the compatibility between the seed trajectory and candidate hits, while simultaneously updating the track parameters. Upon reaching the innermost layer, the track is then propagated outwards to identify additional compatible hits, thereby enabling the reconstruction of complete single-turn track candidates.

Track fitting The track fitter uses an extension of the Kalman filter, deterministic annealing filter (DAF) [99], implemented in the GENFIT package [100]. This method accounts for material effects and iteratively refines the track parameters. The fitter first fits the individual track candidates from the track finder and then merges the fitted segments to form full multi-turn tracks inside the CDCH.

Then, the tracks are propagated forward to the pTC. Once the track matches a pTC cluster, the measurement on each hit in the track is refined. The T_0 is corrected by the time of flight (TOF) from each hit to the pTC. The DOCA is also iteratively updated to consider the cell crossing angle of the track. The track is re-fitted after refining the DOCA of each hit. This re-fitting also searches for missing hits that the track finder could not associate with the track. Frequently, hits in the final half turn are missed by the track finder but can be added in this process, resulting in improved momentum resolution.

4.2.4 Positron kinematics at target

The fitted track is propagated from its first hit to the muon stopping target. The target foil deformation and temporal-varying position are taken into account in this propagation. The target crossing point $(x_{\mathrm{e}}, y_{\mathrm{e}}, z_{\mathrm{e}})$ is used as the muon decay vertex. Here, the positron is assumed to be produced at half-thickness depth inside the target foil for the energy loss and multiple scattering calculations. The propagation to the target provides the best estimate of the positron kinematics (p_{e}, $\vec{x}_{\mathrm{e}}$, θ_{e}, and ϕ_{e}) at the target, including an estimate of the uncertainty and of the correlations among these quantities in the form of a covariance matrix $\vec{\sigma}_{\mathrm{e}}$.

Positron emission time The length of the trajectory from the target to the matched pTC counter is converted to the TOF and subtracted from the pTC hit time to determine the positron emission time at the target t_{e}:

$$t_{\mathrm{e}} = \frac{1}{n_{\mathrm{pTC}}} \sum_{i=1}^{n_{\mathrm{pTC}}} \left(t_{\mathrm{hit},i} - t_{\mathrm{e},i}^{\mathrm{TOF}} \right), \tag{4.20}$$

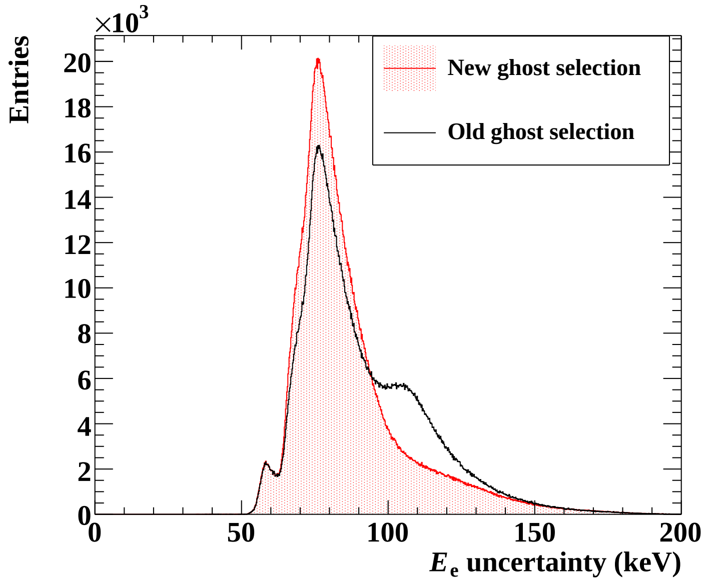

Figure 4.9: Distribution of E_e uncertainty estimated by the track fitting for the best track in the ghost tracks. A red (black) histogram shows the distribution with the new (old) ghost track selection.

where n_{pTC} is the number of hits in the cluster, and $t^{\mathrm{TOF}}_{\mathrm{e},i}$ is the TOF from the target to the i-th hit calculated from the track length.

4.2.5 Quality cuts and track selection

In the above reconstruction, it is common for multiple tracks to be reconstructed from a single physical positron, which is referred to as "ghost tracks". The following selection processes are applied to select the best measured track per physical positron and to ensure the reconstruction quality is suitable for physics analyses:

(1) Cut on the quality of the track fit,

(2) Cut on the track's propagation consistency to both the target and the pTC,

(3) Identification and grouping of ghost tracks,

(4) Ranking of ghost tracks and selection of the optimal candidate.

The quality cuts in the first two steps are based on the number of hits used in the fitting, the track-fit outputs, and geometrical consistency.

The fourth step of rating the ghost tracks is improved from the previous analysis on the 2021 dataset by adding information on the last half turn. This changed the rating of the ghost tracks, suppressing the E_e uncertainty estimated by the track fitting, as shown in Fig. 4.9.

4.3 Reconstruction of combined kinematics

4.3.1 Relative angle reconstruction

While positron kinematics are reconstructed at the target, the photon ones are at the conversion point in the LXe detector. It is assumed that photons are emitted at the paired positron decay vertex on the target, giving photon emission angles θ_γ and ϕ_γ based on the direction from the vertex to the conversion point. The relative angles are defined as

$$\theta_{e\gamma} \coloneqq (\pi - \theta_e) - \theta_\gamma, \tag{4.21}$$

$$\phi_{e\gamma} \coloneqq (\pi + \phi_e) - \phi_\gamma. \tag{4.22}$$

The opening angle between positron and photon is notated as $\Theta_{e\gamma}$.

4.3.2 Relative time reconstruction

The photon emission time at the target, t_γ, is calculated from the conversion time and the TOF from the target to the conversion point, that is, $t_\gamma^{\mathrm{LXe}} - t_\gamma^{\mathrm{TOF}}$. The TOF from the target to the conversion point is estimated from the distance between them. Then, the relative time is defined as

$$t_{e\gamma} \coloneqq t_\gamma - t_e. \tag{4.23}$$

4.3.3 Pair selection

Multiple positrons are reconstructed in general, and the combined kinematics is reconstructed for all the possible positron and photon pairs. However, only a single pair must be finally selected so as not to bias the $\mu \to e\gamma$ search, which demands that the data samples should be independent of each other. Therefore, a single-pair selection is introduced and applied in the following steps:

(1) Pre-select pairs with a wide window for E_e, $t_{e\gamma}$ and $\Theta_{e\gamma}$, just to reduce the number of candidates,
(2) Select the pair having the largest opening angle $\Theta_{e\gamma}$ from the pre-selected pairs.

The signal inefficiency due to this single-pair selection is as low as $\mathcal{O}(0.01\,\%)$.

4.4 RDC reconstruction

The RDC measures positrons' energy E_{RDC} and time t_{RDC}. Figure 4.10 shows the reconstruction algorithm flowchart. The RDC analysis begins with the waveform analysis, and then hits in plastic scintillators (*plates*) and LYSO crystals (*crystals*) are reconstructed separately. Positrons detected by the RDC are finally reconstructed by matching plate and crystal hits. The details are discussed in Sect. 5.3.

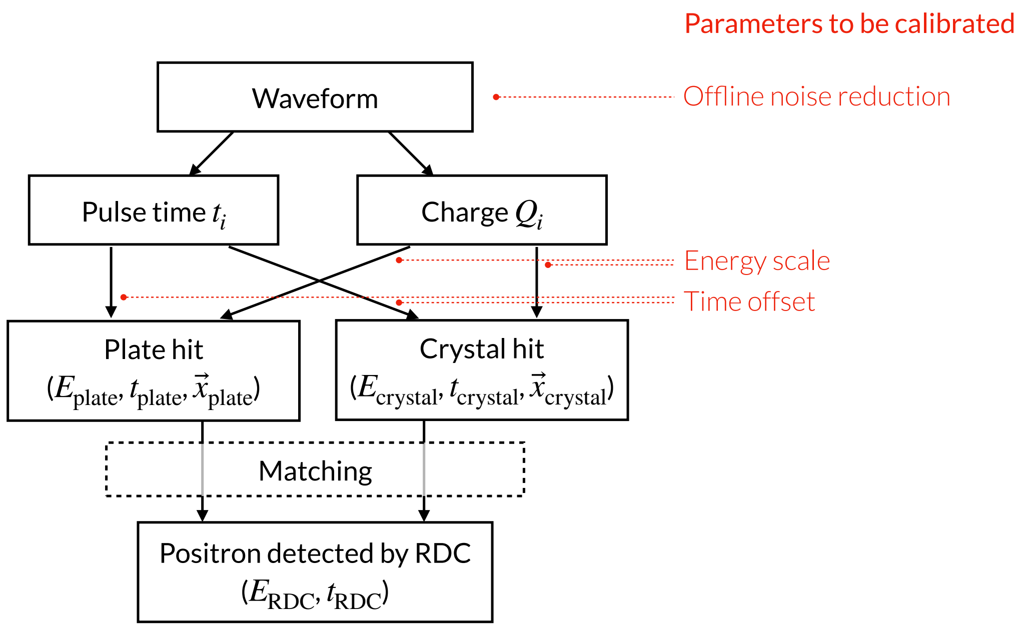

Figure 4.10: RDC reconstruction flowchart.

Chapter 5

Further photon background suppression

There are major updates from the last results [1] on the algorithm improvement aiming to further suppress photon backgrounds. This chapter concentrates on the improvement. Section 5.1 first explains the characteristics of the photon backgrounds. Then, Sect. 5.2 and Sect. 5.3 discuss updates on the pileup unfolding and RDC reconstruction algorithm, respectively.

5.1 Characteristics of photon backgrounds

The dominant background events in the MEG II experiment are an accidental coincidence of positrons and photons with signal-like kinematics. As discussed in Sect. 1.2, the photons causing the accidental background come from two sources:

- Radiative muon decay (RMD): $\mu \to e\nu\bar{\nu}\gamma$, and
- Annihilation in flight (AIF) with materials: $e^+e^- \to \gamma\gamma$.

The AIF events can be classified into two cases. In the first case, one of the emitted photons comes to the LXe detector with a large energy up to 52.83 MeV. Since one carries most of the positron energy, the other photon is emitted nearly backwards and cannot reach the detector. This type of the AIF event is called "AIF1γ". In the second case, the opening angle of two photons is relatively small, and both come to the LXe detector. This type of event is called "AIF2γ". Then, let me discuss the characteristics of three photon background cases (RMD, AIF1γ, and AIF2γ) and how to suppress each of them.

The full simulation of the background photons (Sect. 2.7) gives the energy spectra and the fraction of each background class, as shown in Fig. 5.1. The RMD dominates around 48 MeV, which is the lower bound of the analysis region. On the other hand, the AIF2γ has a dominant contribution around the signal energy of 52.83 MeV. The fraction of each class averaged in the E_γ analysis region ($48\,\mathrm{MeV} < E_\gamma < 58\,\mathrm{MeV}$) is given by

$$f_{\mathrm{RMD}} : f_{\mathrm{AIF1}\gamma} : f_{\mathrm{AIF2}\gamma} = 65 : 21 : 14. \tag{5.1}$$

Two coincident photons Only the AIF2γ event provides the LXe detector with two coincident photons. This, hence, must be identified and discarded from the analysis sample.

RMD event tagging with RDC The fraction of the RMD events in the photon background after eliminating two-photon events is 76 %. As explained in Sect. 2.5, the RMD photon background can

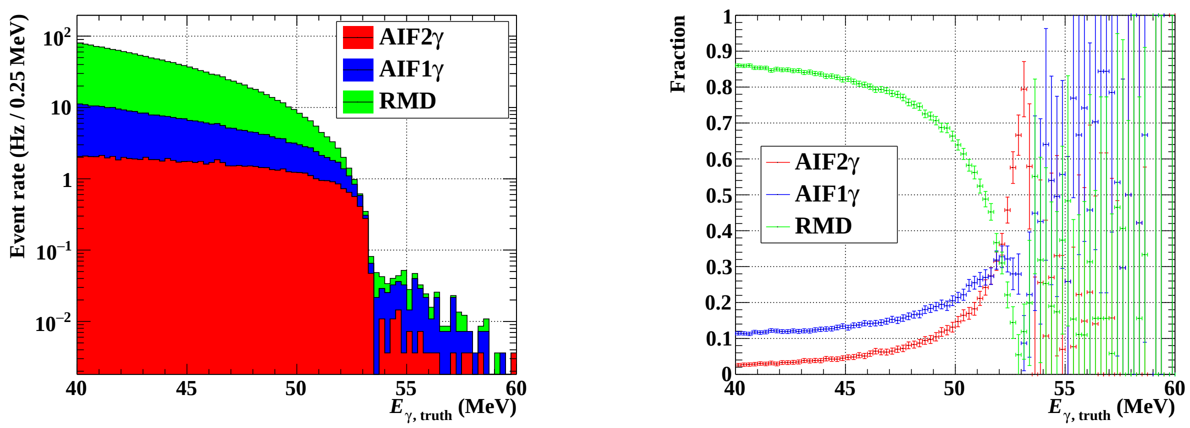

(a) Simulated energy deposit in the LXe detector.

(b) Fraction.

Figure 5.1: Simulated energy spectra in each photon background case. The fraction of each case is also shown (b).

be tagged by detecting the accompanying positron in the RDC. The fraction of RMD-photon events tagged by the RDC, f_{tagged} can be naively calculated as

$$f_{\mathrm{tagged}} = f_{\mathrm{RMD}} \cdot f_{\mathrm{DS}} \cdot \Omega_{\mathrm{RDC}} \cdot f_{\mathrm{meas}}, \tag{5.2}$$

where f_{RMD} is an RMD event fraction to the number of background events (76 % (65 %) without (with) AIF2γ events); f_{DS} is the fraction of RMD positrons flying downstream (48 %); Ω_{RDC} is geometrical acceptance (88 %); and f_{meas} is the fraction of events where RDC was in the measurement position out of those with a photon energy of 48–58 MeV. In 2021 (2022), f_{meas} was 74 % (90 %). The fraction f_{tagged} named "tagged-RMD fraction" is simulated to be 32 % after two-photon event elimination.

Pileup photons The above discussions assume that a single photon background is detected in an event. However, due to the high intensity of the muon beam (2–5 $\times$ 10^7 s^{-1}), multiple photons are accidentally piled up within a time window of hundreds of nanoseconds, which is called "*pileup*". Figure 5.2 shows the simulated photon energy deposit from muon decays at the muon stopping target. The summed energy becomes higher, resulting in more events distributed in the high-energy region, as shown in Fig. 5.3. Not only background high-energy photons, but signal photons can be piled up in an accidental coincidence with low-energy photons. Therefore, each individual photon must be unfolded to reconstruct the energy of a single photon.

The following sections discuss methods to deal with the above three cases. Section 5.2 describes the unfolding of each individual photons and elimination of AIF2γ events. Then, Sect. 5.3 describes RMD-event tagging with the RDC.

5.2 Pileup unfolding

The conventional pileup unfolding algorithm [59, 39] for the 2021 data analysis had a critical issue: a logical loophole to miss on-time multi-photon events. Since it was found on the last stage of the analysis and further investigation was expected to take much time, an ad-hoc quality cut was imposed to reject such events at that time. This work investigated and reviewed this algorithm. I also

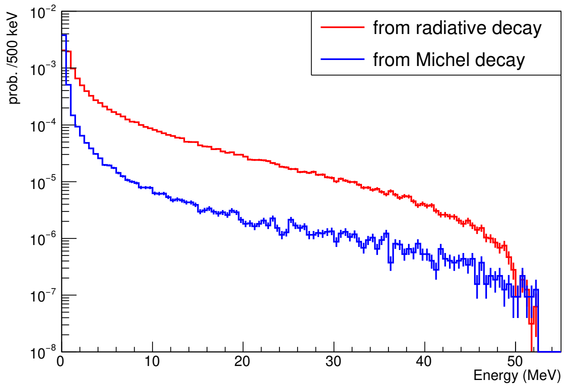

Figure 5.2: Simulated photon energy deposit in the LXe detector [58]. The blue histogram stands for photons emitted from Michel positrons' AIF. The red one stands for photons emitted from the RMD.

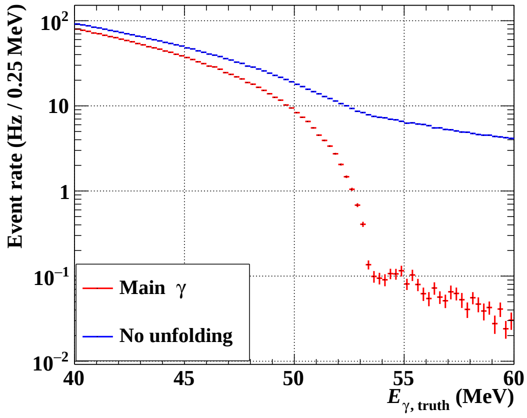

Figure 5.3: Simulated energy spectra with pileup photons mixed at $3 \times 10^7\ \text{s}^{-1}$.

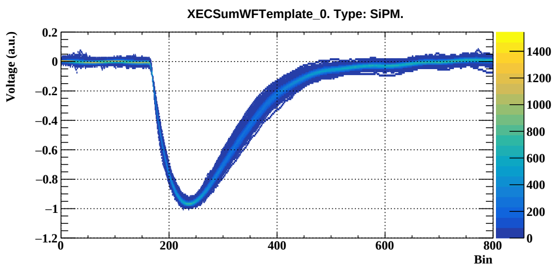

(a) MPPC.

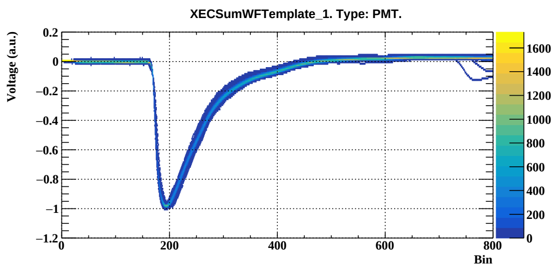

(b) PMT.

Figure 5.4: Template summed waveforms [59].

introduced new methods to further improve the background reduction and analysis efficiency for the signal photons.

5.2.1 Unfolding algorithm

A template waveform fit for the summed waveforms V of MPPCs and PMTs unfolds multiple pulses in and before the DRS time window. Recorded waveforms are summed up with the position-dependent weight $W_i(u_\gamma, v_\gamma, w_\gamma)$ in Eq. (4.11) to convert the integrated area into N_{MPPC} or N_{PMT}. When summing up waveforms, $t_{\text{offset},i}$ and $t_{\text{prop},i}$ are subtracted. The template summed waveforms f shown in Fig. 5.4 were created beforehand using an analysis sample in a run. Observed waveforms have event-by-event fluctuation, especially in MPPCs. This fluctuation is represented by a deviation σ_f as a function of time (bin). The template fit minimises χ^2_{wf} defined as

$$\chi^2_{\text{wf}} = \sum_{\text{MPPC,PMT}} \int \frac{\left(V(\tau) - \sum_i^{n_{\text{pulse}}} f(\tau; A_i, T_i)\right)^2}{\sigma_f^2(\tau)} \mathrm{d}\tau, \tag{5.3}$$

where n_{pulse} is the number of fitted pulses, and A_i, T_i are fit parameters of amplitude and timing of the i-th pulse.

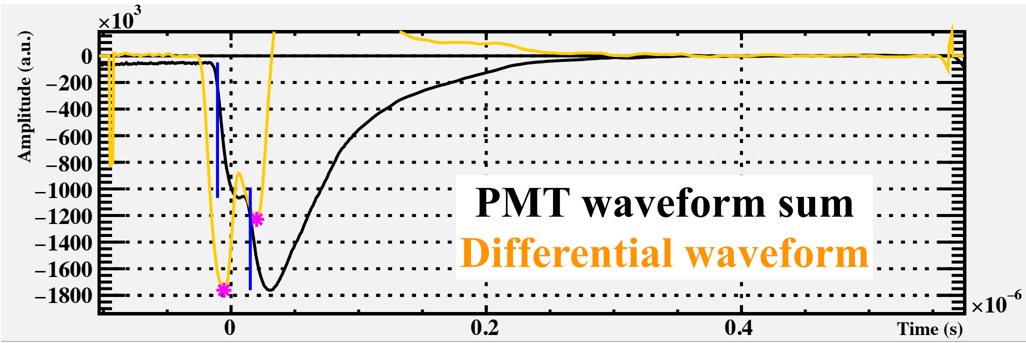

Figure 5.5: Multi-peak search in the PMT differential waveform [101]. Magenta markers show the detected peaks in the differential waveform. Blue lines show the calculated pulse time to be input as T_i.

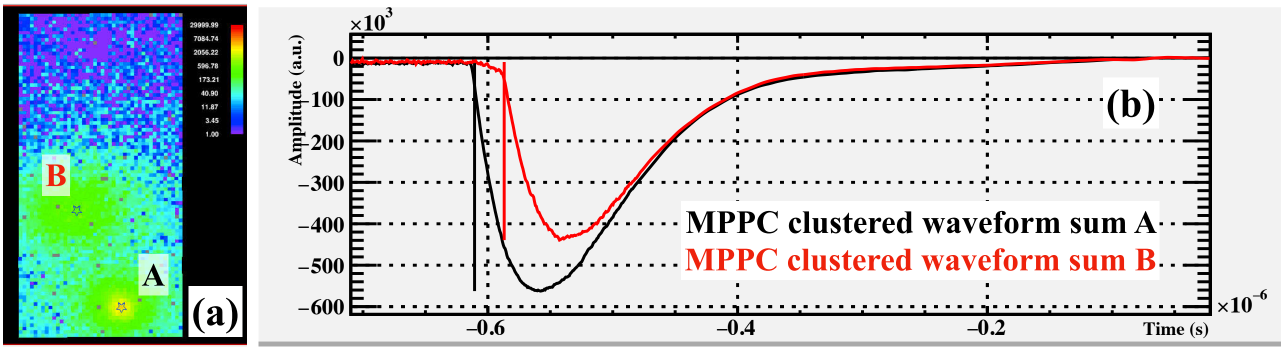

Figure 5.6: Multi-peak search based on the $N_{\text{pho},i}$ distribution. (a) $N_{\text{pho},i}$ distribution. (b) Summed waveforms of each cluster. The lines show the estimated pulse time.

Initial fit parameters' determination The number of pulses n_{pulse} is first calculated by three methods: a peak search in the PMT differential waveform, $N_{\text{pho},i}$ peaks on the inner and outer faces, and the ADC signal.

The first method involves identifying pileup photons in the time domain from the summed waveform of the photosensors. Here, one searches for pileups from the PMT waveform, which is sharper than that of MPPC. An additional algorithmic waveform processing is applied to create a differential waveform dedicated to the pileup search, making the waveform even sharper. As shown in Fig. 5.5, this processing makes waveform peaks more distinguishable than those before the waveform processing. The detected peaks, shown as magenta markers in Fig. 5.5, provide initial T_i shown as blue lines in Fig. 5.5. This technique can distinguish pulses with a time difference of 15–20 ns and larger, depending on the amplitude of the pulses.

The second method involves clustering the photosensors based on the $N_{\text{pho},i}$ distribution and analysing the summed waveforms of each cluster shown in Fig. 5.6. The waveform analysis provides initial T_i shown as vertical lines in Fig. 5.6. This technique can distinguish distant photons with slight time differences of a few to 20 ns, which are not distinguishable by the differential waveform.

The last method uses the ADC signal used for the trigger, introduced in Sect. 2.6.1, whose time window is 1600 ns (Fig. 5.7). The time window is more than twice as wide as the DRS time window (approximately 700 ns), though its sampling frequency is 80 MSPS. This signal enables the acquisition of information on pulses arriving before the DRS time window. The information is beneficial for better estimating the amplitude and time of pulses of interest around the triggered time in events where the pulses of interest overlie the waveform tail of the pileup photons.

One needs to make a decision on how many pulses are fitted, i.e. what n_{pulse} is, based on the

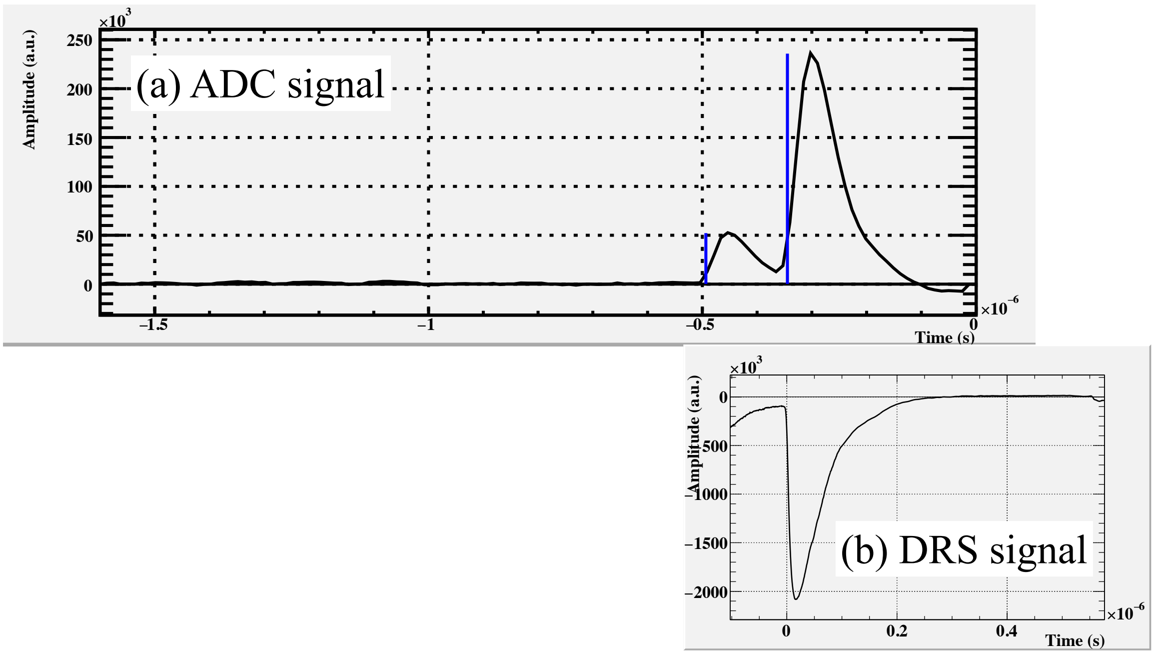

Figure 5.7: The ADC signal used for the trigger (a) and DRS signal (b) for PMTs in an event where a pileup photon comes before the DRS time window. Pulse search before the DRS time window takes advantage of the wide time window of 1600 ns. Blue lines show the calculated pulse timings in the ADC signal.

detected photons, since these three methods usually detect the same photons. Also, note that the template waveform fit is not sensitive to separating two coincident photons. In order to prevent too many pulses from being input, n_{pulse} is counted if

(1) Photons detected by different methods have a time difference larger than 30 ns or

(2) Photons detected by the spatial peak search have a time difference larger than 10 ns.

During a sequence of the fitting, n_{pulse} is fixed.

Re-fitting The fitting attempts are repeated with incrementing n_{pulse} based on residual waveforms if the first fitting fails, until the fitting is converged with a maximum of three attempts. The first fitting attempt is performed if the peak-to-peak value of the residual waveform in the range of the baseline calculation, defined as

$$V(\tau) - \sum_{i}^{n_{\text{pulse}}} f(\tau; A_i, T_i), \tag{5.4}$$

is larger than the thresholds corresponding to 1 MeV. This attempt aims to detect a remaining pulse in a baseline region. The second attempt is performed if the peak-to-peak value in the range from 20 ns after the reference time to the end of the fit range in the residual waveform is larger than the threshold. This attempt aims to detect a remaining pulse in the tail of the waveforms. The final attempt is performed if the squared residual divided by the deviation of the template waveforms over time, that is,

$$\frac{\left(V(\tau) - \sum_{i}^{n_{\text{pulse}}} f(\tau; A_i, T_i)\right)^2}{\sigma_f^2(\tau)}, \tag{5.5}$$

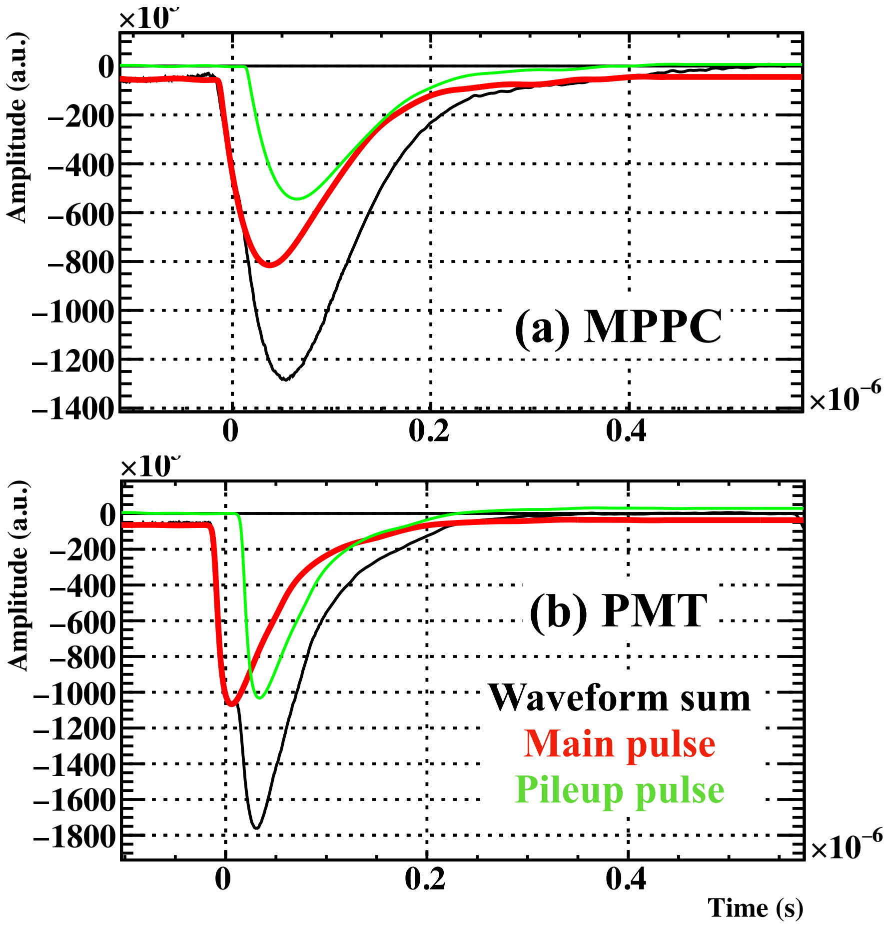

Figure 5.8: Unfolded multiple pulses for the event shown in Figs. 5.5, 5.6 [101]. The weighted sums N_{MPPC} and N_{PMT} are calculated by integrating the waveform for the main pulse (red).

has the peak above 50. This attempt aims to detect a remaining pulse whose timing is very close to the main pulse.

These attempts sometimes increment too many pulses. Finally, some invalid pulses are removed based on the following criteria:

- The best-fit amplitude A_i is less than the thresholds, or
- The best-fit timing T_i differs within 10 ns from the timing of the other pulses.

The re-fitting is performed after removing the invalid pulses, with the final number of pulses.

Main pulse selection Figure 5.8 shows the unfolded pulses. Once the multiple pulses have successfully unfolded, I decide which pulses will be eliminated based on the results of the preceding position and timing reconstructions. For the event in Figs. 5.5, 5.6, and 5.8, the position and timing of the photon A in Fig. 5.6 were reconstructed. Therefore, the latter pulse labelled the “pileup pulse” in Fig. 5.8 is eliminated, and the first pulse (the “main pulse”) remains for the subsequent energy reconstruction. The weighted N_{MPPC} and N_{PMT} sums for the main pulse are calculated by integrating the waveform of the main pulse.

Event categorisation The number of pulses n_{pulse} and the number of incident photons can differ if coincident photons impinge on the detector. The events are finally categorised based on these

Table 5.1: Event categories.

Category	Definition
NoPileup	Single photon event.
Unfolded	Multiple photons detected and unfolded.
Coincidence	Multiple photons detected, but not unfolded due to coincident photons.
NotConverged	Fit failure ($\chi^2_{\mathrm{wf}} > 5$).

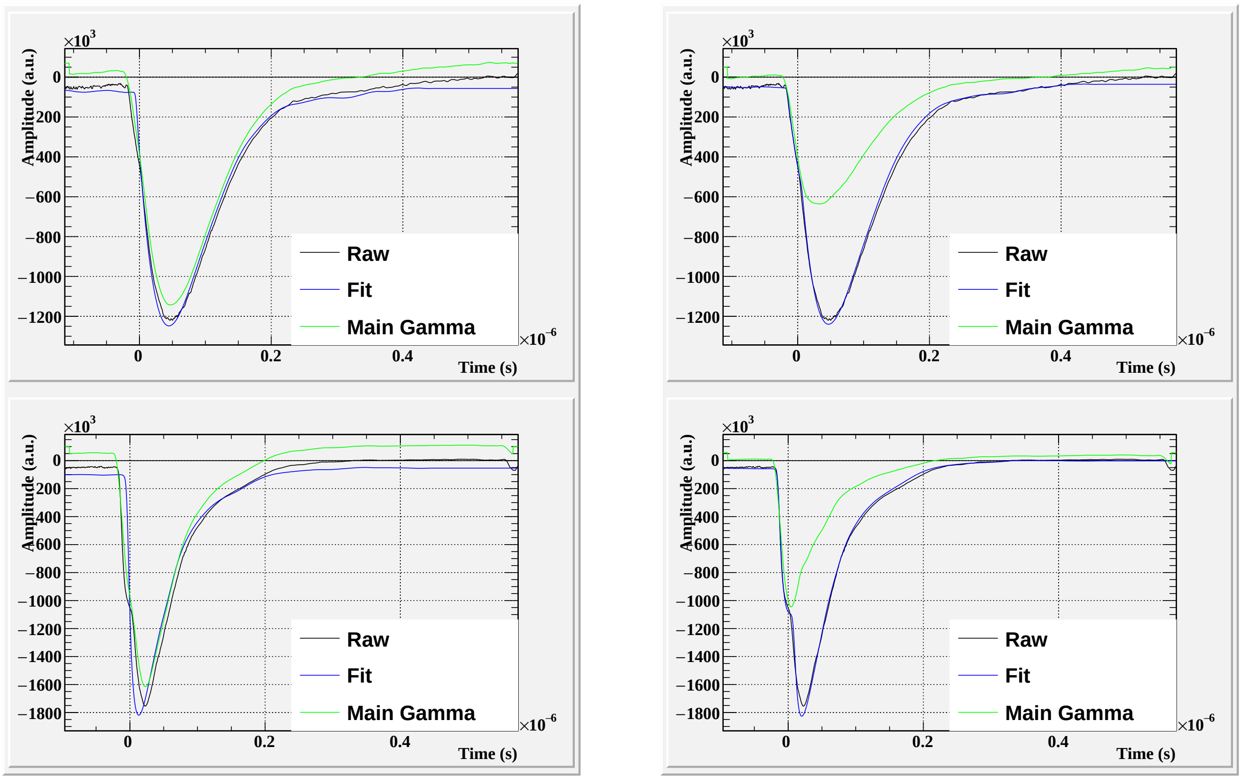

(a) With the conventional algorithm.

(b) With the updated algorithm.

Figure 5.9: An example of events where the fitting failed in the conventional analysis (a) and converged after updating the algorithm (b).

numbers and the fitting convergence as defined in Table 5.1. Events categorised as *Coincidence* and *NotConverged* are discarded from the analysis sample because they are not fully unfolded.

5.2.2 Performance evaluation

I evaluated the performance of pileup unfolding analysis based on the reduction of background events in $E_\gamma \in [48\,\mathrm{MeV}, 58\,\mathrm{MeV}]$ with and without pileup analysis and the efficiency for the signal events. These two are usually trade-offs; i.e., too strict thresholds result in reducing many background events and a huge loss of signal efficiency, and vice versa.

Event category distribution for background events

This algorithm update significantly improved the fitting convergence, particularly for events where pileup photons came in a small time difference of 10–30 ns from the main pulse. Figure 5.9 shows

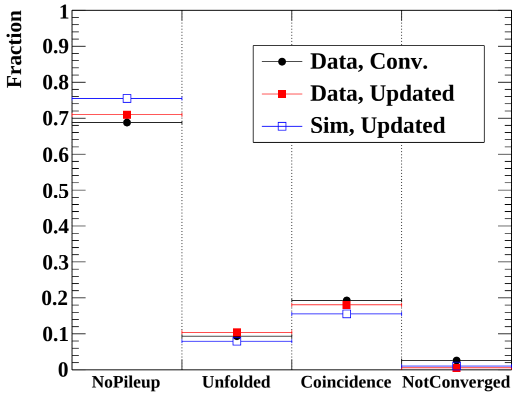

Figure 5.10: Event category distribution at a muon stopping rate of $3 \times 10^7\ \mathrm{s}^{-1}$. The photon energy range is $48\,\mathrm{MeV} < E_\gamma < 58\,\mathrm{MeV}$.

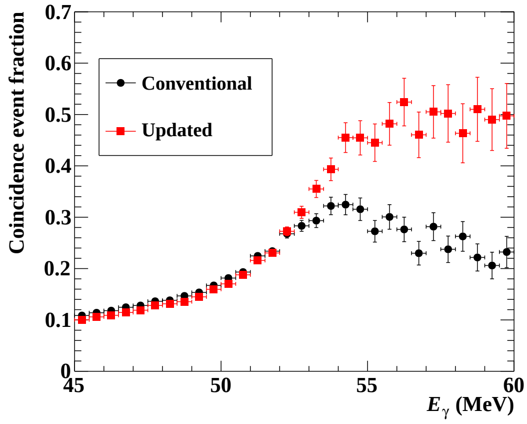

Figure 5.11: *Coincidence* event fraction over E_γ. It increases shaper in 52 MeV to 54 MeV with the update analysis than in the conventional one.

an example of events where the fitting failed in the conventional analysis and converged in the new analysis. The fraction of *NotConverged* events decreased by relatively 78 %, as shown in Fig. 5.10.

The fraction of *Coincidence* events at 48–58 MeV is expected to be 14 %, as discussed in Sect. 5.1. Figure 5.10 shows the event category distribution at $R_\mu = 3 \times 10^7\ \mathrm{s}^{-1}$. The *Coincidence* event fraction in Fig. 5.10 is 1–4 % higher for both the simulation and the data than the expectation. This is because accidental coincident events within 12.5 ns are enhanced due to the trigger, which requires the amplitude computed every 12.5 ns to be higher than the threshold. Since the simulation does not fully reproduce triggering, the fraction in the data is 3 % higher than the simulation.

The photon energy dependence of the *Coincidence* event fraction gives a better understanding of the performance. When accounting for the energy resolution in data (Sect. 7.1.3), the sharp peak in the distribution of the AIF2γ event fraction seen in Fig. 5.1b broadens [58]. Figure 5.11 shows the *Coincidence* event fraction as a function of E_γ in data[1]. The *Coincidence* event fraction increases more sharply in 52 MeV to 54 MeV with the update analysis than in the conventional one. Moreover, the fraction in the low-energy region below 48 MeV is a little lower in the updated analysis than the conventional one, even though both analyses result in a fraction twice higher than the expectation shown in Fig. 5.1b. Based on these observations, it is concluded that the updated analysis identifies the AIF2γ events better.

Background photon reduction

Figure 5.12a shows the spectra without pileup elimination analysis and with the conventional and updated analyses at $R_\mu = 3 \times 10^7\ \mathrm{s}^{-1}$, in which background events are reduced by 18.5 % (22.3 %) in $48\,\mathrm{MeV} < E_\gamma < 58\,\mathrm{MeV}$ with the updated (conventional) analysis. The muon stopping rate dependence is shown in Fig. 5.12b. The updated algorithm shows 2–5 % fewer reduction than the conventional one, which is interpreted as categorising too many events as *Coincidence* in the conventional algorithm.

In Fig. 5.12a, there are more events in the high-energy region above 55 MeV by the updated

[1] E_γ in the *Coincidence* events is calculated as the energy sum of multiple coincident photons.

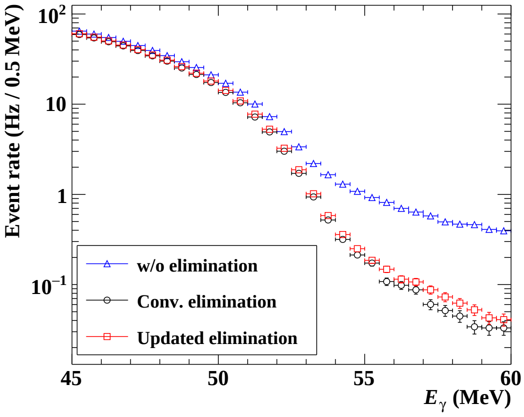

(a) Energy spectra for background photons at $R_\mu = 3 \times 10^7\,\mathrm{s}^{-1}$.

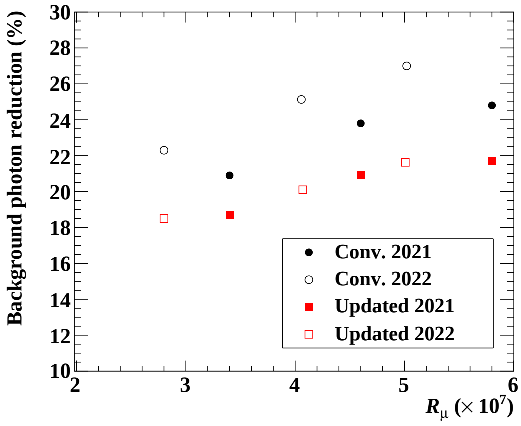

(b) Muon stopping rate dependence.

Figure 5.12: Background photon reduction.

algorithm. This is because of the lower detection of the pileup photon in the tail of the preceding pulse. The conventional analysis often detected such pulses at different timings between MPPC and PMT summed waveforms, e.g. the pulse timings measured by the MPPC and PMT summed waveforms differ at tens of nanoseconds. This implied that the conventional analysis would have detected too many pulses without considering a proper uncertainty. This observation also supports the reliability of this improvement.

Signal efficiency

The signal efficiency was evaluated with the MC simulation for signal photons and the RMD-enhanced sample. The simulation-based evaluation counts the number of *NoPileup* and *Unfolded* events with $E_\gamma \in [48\,\mathrm{MeV}, 58\,\mathrm{MeV}]$, resulting in 94.6 % at $3 \times 10^7\,\mathrm{s}^{-1}$. There are two major causes of the inefficiency. The first is a photon escaping from the main EM shower and generating another shower far from the main, as shown in Fig. 5.14. Figure 5.13 shows the light distribution in this type of simulated event, which cannot be distinguished from two-photon events. This type of event dominates the inefficiency: 4 % of all signal events. The other is an accidental coincidence of the signal photon and pileup photons. This inefficiency depends on the beam intensity, which is estimated to be 0.4 % per $10^7\,\mathrm{s}^{-1}$, as shown in Fig. 5.15.

The evaluation with RMD-enhanced samples allows for studying the consistency between data and simulation, which corrects the simulation-based efficiency. The RMD-enhanced sample is given by collecting coincident positrons detected by the RDC. Events composing the peak in Fig. 5.16, called an "RMD peak", are expected to originate from RMD $\mu \to e\nu\bar{\nu}\gamma$ and to have a single photon. Meanwhile, *Coincidence* events are likely two-photon events originating from AIF and expected to have a flat distribution of $t_{\mathrm{RDC}} - t_\gamma^{\mathrm{LXe}}$. More *Coincidence* events distributed in the RMD peak than those out of time suggest an inefficiency. I calculated the fraction of *Coincidence* events to all events in the RMD peak using background photon MC simulation and the E_γ-triggered data, obtaining (8.2 ± 0.2) % and (9.3 ± 0.2) %, respectively. The fraction is generally higher than the MC-based inefficiency (5.4 %) because E_γ trigger enhanced multi-photon events with slight time differences of less than 12.5 ns. The discrepancy of the calculated fractions between the MC simulation ((8.2 ± 0.2) %) and data ((9.3 ± 0.2) %) would come from not only the detector response difference but also trigger bias, which only exists in the data, and it is not fully understood. Therefore, I adopted (8.8 ± 0.5) % for the fraction

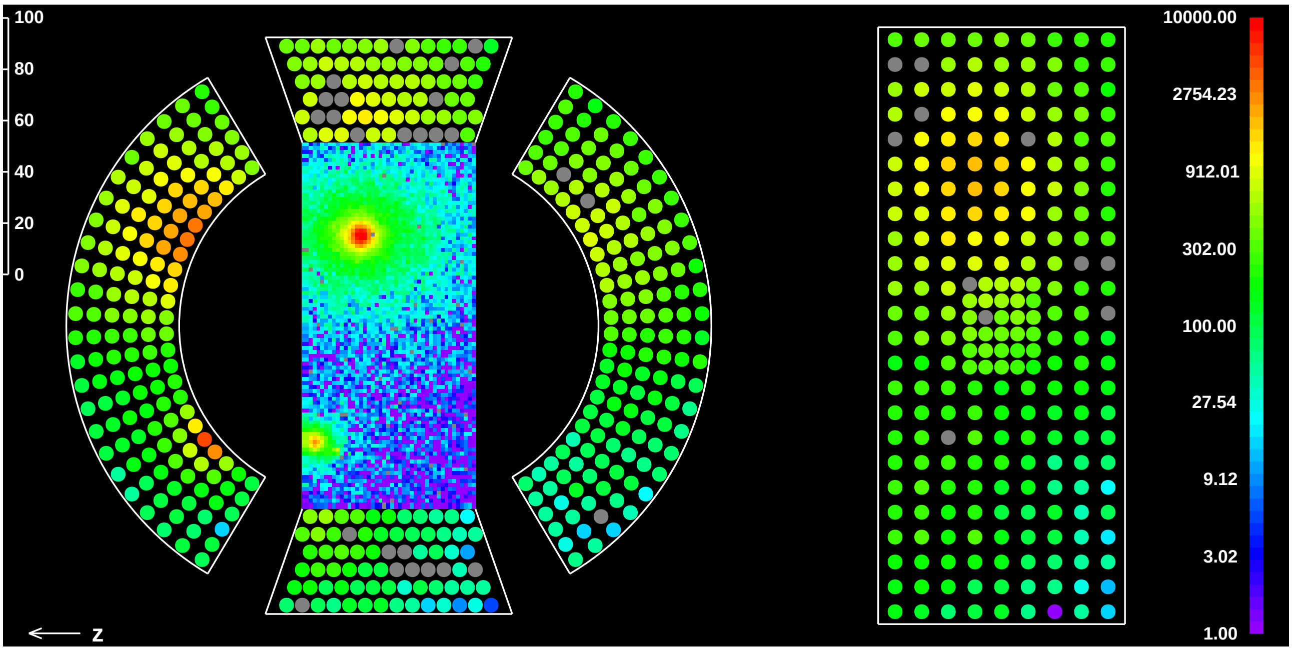

Figure 5.13: $N_{\text{pho},i}$ distribution of a simulated two-peak event where a single photon impinges on the LXe detector.

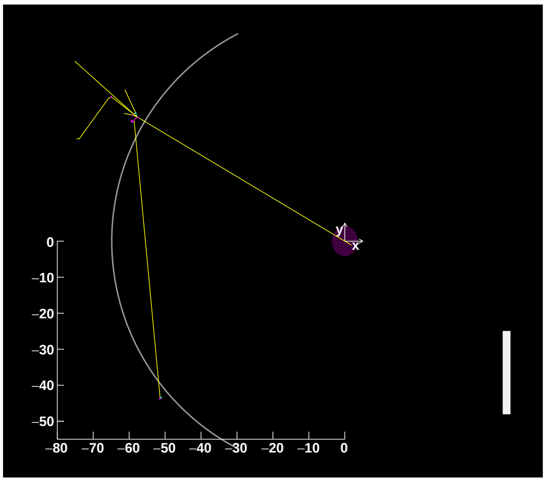

Figure 5.14: Particle track of a simulated signal event shown in Fig. 5.13. Yellow, magenta, and cyan tracks represent photons, electrons, and positrons, respectively.

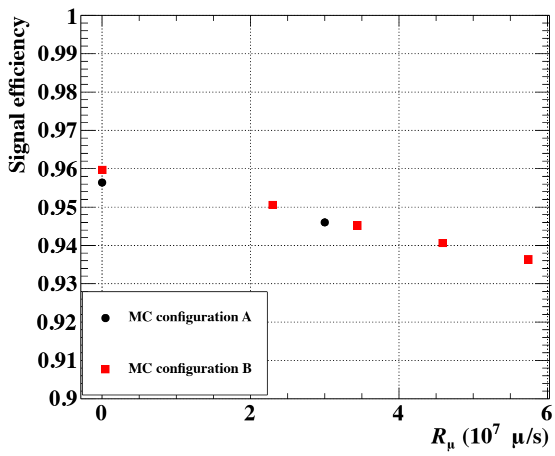

Figure 5.15: A pileup analysis efficiency depending on the beam intensity.

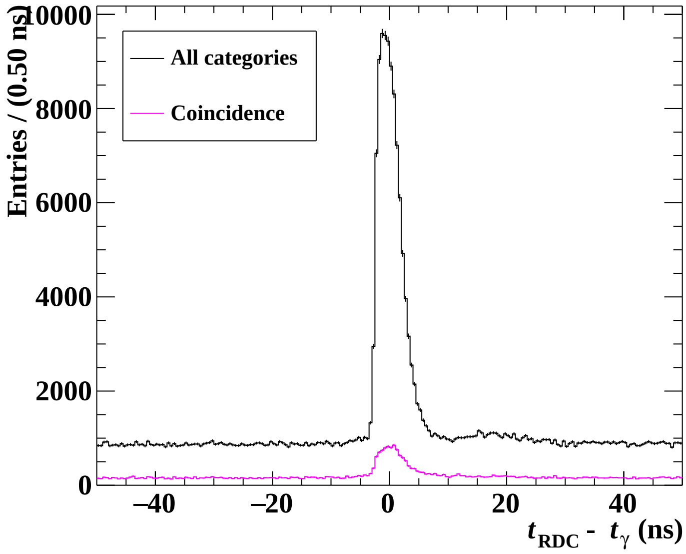

Figure 5.16: $t_{\mathrm{RDC}} - t_{\gamma}^{\mathrm{LXe}}$ distributions with *Coincidence* events selected (magenta) and without event status selection for the E_{γ}-triggered data in 2022.

by taking a mean and corrected the analysis inefficiency by multiplying 8.8/8.2, obtaining the analysis efficiency of (94.2 ± 0.5) % at $3 \times 10^{7}\ \mathrm{s}^{-1}$.

Energy resolution improvement in events with pre-window pileup

The introduction of ADC signal to input fit parameter sets $(n_{\mathrm{pulse}}; A_i, T_i)$ gives a more precise estimation of the amplitude and timing of pulses coming before the DRS time window. Figure 5.17 shows the time distribution of found pileup photons in the π^0 calibration run, indicating that more pileup photons incident before the DRS time window are identified. Figure 5.18 shows the energy spectra for such events in the conventional and updated analyses. The energy resolution is 5 % better in the update analysis than the conventional one. The introduction of the ADC signal results in the energy resolution improvement for the events where pileup photons come before the DRS time window.

5.3 RMD photon tagging by RDC

The RDC aims to tag 32 % of the photon background with an energy of 48–58 MeV after the multi-photon event elimination, as discussed in Sect. 5.1. However, the fraction was evaluated to be (16.53 ± 0.15) % with the RDC installed in 74 % of the events with 48–58 MeV photons for the 2021 dataset. The discrepancy could not be explained only by the number of events where the RDC was installed, being suspected due to reconstruction inefficiency. This section explains the updates on the reconstruction algorithm to improve the efficiency and discusses the performance.

5.3.1 Reconstruction inefficiencies in conventional analysis

The conventional RDC reconstruction began with the waveform analysis for the plates, which detected pulses by the threshold of 100 mV crossing. The pulse time of the plates was then input to the subsequent crystal waveform analysis. This procedure was beneficial when searching for associated crystal pulses, integrating their charge for energy measurement, and then clustering the hits from the

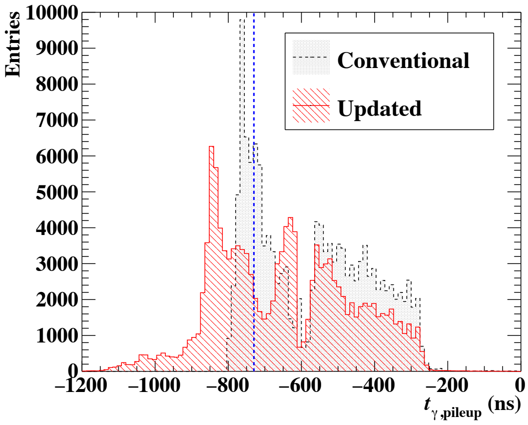

Figure 5.17: Pileup photon timing. A blue dotted line shows the lower bound of the DRS time window.

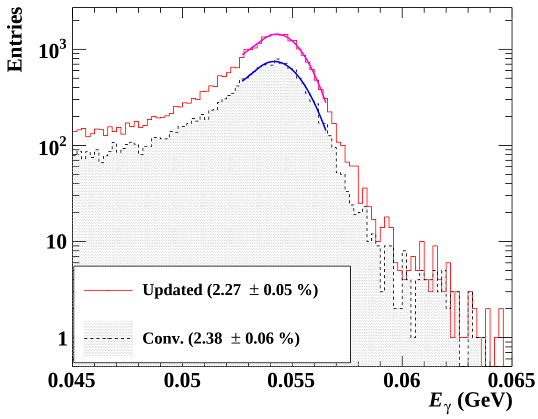

Figure 5.18: E_γ spectra when pileup photons come before the DRS time window.

identical positron. In the conventional reconstruction, two inefficiencies existed: pulse detection in plates and dead time in crystal pulse search.

The first inefficiency was in the pulse search in plates. A Landau peak is expected to be seen in the pulse height distribution as shown in a plate channel 12 in Fig. 5.19. It was not seen in three channels in plates, channels 2, 14 and 15, for which reason it was suspected that MPPCs were detached from the plastic scintillator. The pulse detection was inefficient in these channels since the threshold for pulse search was too high (100 mV) for these.

The second inefficiency came from the reconstruction dead time with pileups, which was the inefficiency for crystal pulses immediately followed by a pileup. The dead time depended on the amplitude of the pileup, which can be up to 50 ns in the worst case. Figure 5.20 shows the time difference between RDC hits and photons categorised by the plate-crystal matching status. The number of the RDC hits with the associated crystal hits decreased in $t_{\mathrm{RDC}} - t_\gamma^{\mathrm{LXe}} \in [10\,\mathrm{ns}, 40\,\mathrm{ns}]$ due to this inefficiency. The RDC hits originating from the RMD, which were distributed around zero, made asymmetric distributions of the time difference.

5.3.2 Reconstruction algorithm

Figure 4.10 shows the reconstruction scheme. The following subsections describe the reconstruction algorithm, focusing on the efficiency of recovery.

Plate hit reconstruction

The plate hit reconstruction begins with the waveform analysis. The key to increasing pulse detection efficiency is to lower the pulse search threshold. It requires further noise reduction because the past threshold of 100 mV was set to avoid noise detection as a positron hit. Therefore, I introduced two new methods to suppress noise pulses. The first is to apply a Notch filter, a bandstop filter to reject the specific frequency range. A prominent peak in the frequency domain is detected, and then the peak component is rejected in this method, as shown in Fig. 5.21. The second is to cut burst noise based on a positive and negative amplitude ratio. A characteristic of burst noise is to have a relatively large positive amplitude (Fig. 5.22a). The ratio to a negative amplitude is used as a selection criterion to assess a good pulse with the threshold of 0.5 (Fig. 5.22b). With these two noise subtraction methods,

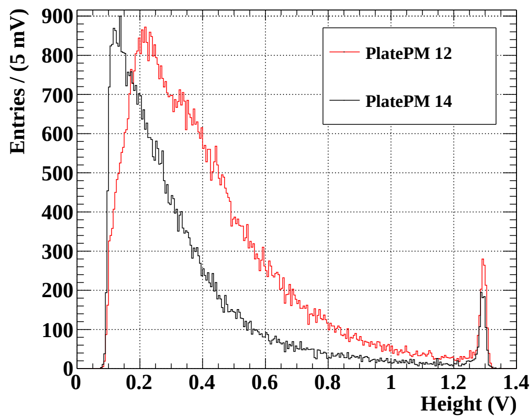

Figure 5.19: Pulse height distributions of plate channels 12 and 14. A Landau peak is seen in channel 12, as expected, while it is not in channel 14.

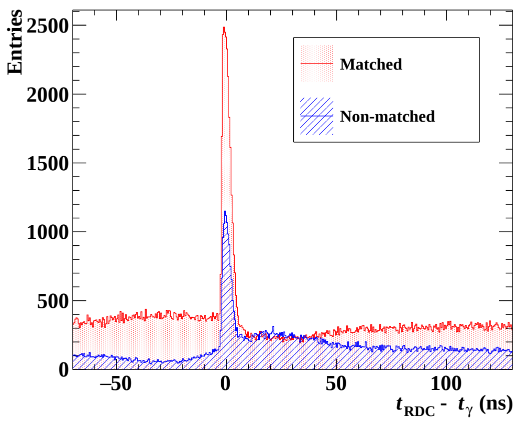

Figure 5.20: Timing distribution for RDC hits with (red) and without (blue) associated crystal hits. The dip in [10 ns, 40 ns] suggests that the LYSO hits become inefficient when followed by another hit.

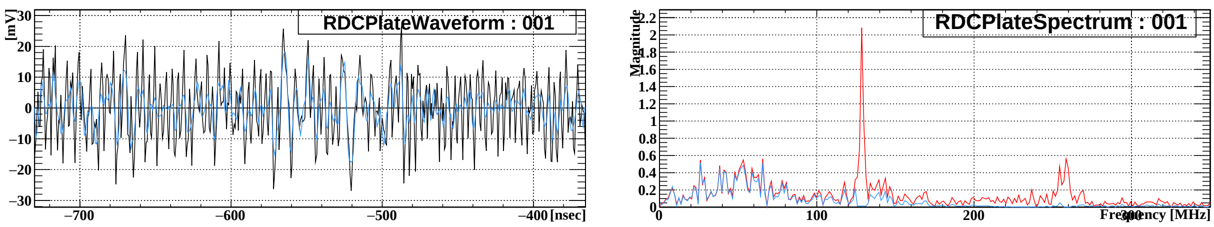

(a) Time domain.

(b) Frequency domain.

Figure 5.21: Waveform before and after a Notch filter. A black (red) line is the time (frequency) domain before applying. Blue lines are after applying.

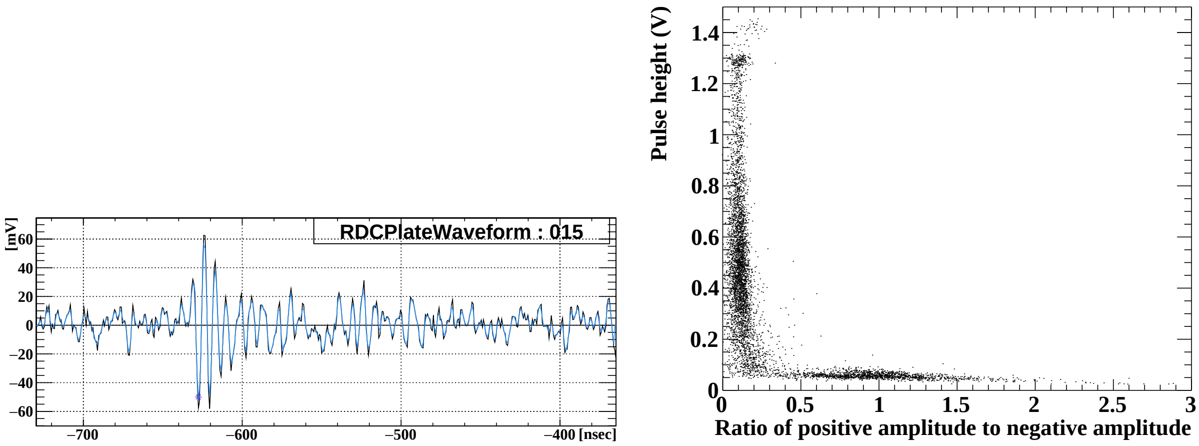

(a) Typical waveform of burst noise.

(b) Positive amplitude ratio to negative.

Figure 5.22: Burst noise cut. Burst-noise-like pulses are concentrated in a small-height region.

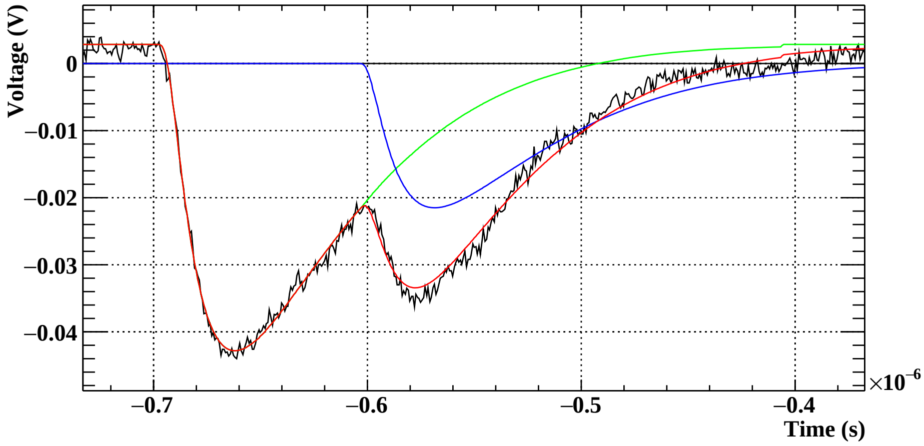

Figure 5.23: Template waveform fit. A black line is a raw waveform. A red is a fitted waveform. Blue and green ones are fitted waveforms for each pulse.

the pulse search threshold is set to 50 mV, twice lower than the conventional one.

Hits at a plate are reconstructed based on the detected pulses in the MPPCs attached to the plate. Most hits are expected to have coincident pulses on both ends of the plate. The pulse coincidence is judged by the time difference within the coincidence window of 3 ns. Even if the pulse over the threshold is detected only on one side, it is reconstructed since noise is subtracted well, and such a situation can happen physically when a positron hits very close to the end. Deposit energy E_{plate}, hit time t_{plate}, and hit x position x_{plate} are reconstructed as

$$E_{\mathrm{plate}} = \sqrt{q_{\mathrm{left}} \cdot S_{\mathrm{left}} \times q_{\mathrm{right}} \cdot S_{\mathrm{right}}}, \tag{5.6}$$

$$t_{\mathrm{plate}} = \frac{t_{\mathrm{left}} + t_{\mathrm{right}}}{2}, \tag{5.7}$$

$$x_{\mathrm{plate}} = v \cdot (t_{\mathrm{left}} - t_{\mathrm{right}}), \tag{5.8}$$

where q is a charge, S is a energy scale factor, t is constant fraction time, and v is scintillation light velocity in a scintillator. Finally, coincident hits within 3 ns reconstructed in neighbouring plates are unified.

Crystal hit reconstruction

Crystal hit reconstruction begins with waveform analysis as well as plates. A template waveform fit with a similar technique to the pileup unfolding of the LXe detector, discussed in Sect. 5.2, is newly introduced to solve the inefficiency due to pileups (Fig. 5.23). It is performed only in case multiple pulses are detected within the charge integration range of 220 ns so as to reduce computing cost. It minimises the sum of squared residual amplitudes defined as

$$\int \left(V(\tau) - \sum_{i}^{n_{\mathrm{pulse}}} f(\tau; A_i, T_i) \right)^2 \mathrm{d}\tau, \tag{5.9}$$

where n_{pulse} is the number of fitted pulse; $V(\tau)$ is observed waveform; and $f(\tau; A_i, T_i)$ is a fitted template waveform with an amplitude A_i and a time T_i for the i-th pulse. The pulses detected by the first waveform analysis give n_{pulse} and an initial parameter set of A_i, T_i, and baseline. The best-fit amplitudes are, finally, converted to the charge of the pulses.

A crystal hit is reconstructed by clustering the detected pulses based on the time coincidence and fired crystal position. At first, the charge of detected pulses is converted to energy $E_{\text{crystal},i}$ by

$$E_{\text{crystal},i} = q_i \cdot S_i. \tag{5.10}$$

Then, clustering is started in order of $E_{\text{crystal},i}$. A coincident pulse within 10 ns in the neighbouring channels is judged as the same hit as in the central channel. Deposit energy E_{crystal}, hit time t_{crystal}, and hit position $\vec{x}_{\text{crystal}}$ are reconstructed as

$$E_{\text{crystal}} = \sum E_{\text{crystal},i}, \tag{5.11}$$

$$t_{\text{crystal}} = \frac{1}{E_{\text{crystal}}} \sum t_{\text{crystal},i} \cdot E_{\text{crystal},i}, \tag{5.12}$$

$$\vec{x}_{\text{crystal}} = \frac{1}{E_{\text{crystal}}} \sum \vec{x}_{\text{crystal},i} \cdot E_{\text{crystal},i}. \tag{5.13}$$

Matching plate and crystal hits

Plate and crystal hits are matched if the time difference $|t_{\text{plate}} - t_{\text{crystal}}|$ is within 5 ns and if the y position difference $|y_{\text{plate}} - y_{\text{crystal}}|$ is within 2 cm. Non-matched plate hits are recognised as positron hits while non-matched crystal hits are not because RMD positrons must hit plates given the origin of them[2]. The plate hit time t_{plate} is used as the reconstructed time t_{RDC} regardless of matching with crystal hits. Reconstructed energy E_{RDC} and position $\vec{x}_{\text{RDC}}$, however, depends on the matching status. If a matched crystal hit is found in the plate hit, the reconstructed energy E_{RDC} is reconstructed as the sum of E_{plate} and E_{crystal} and the position $\vec{x}_{\text{RDC}}$ is the crystal hit position $\vec{x}_{\text{crystal}}$. On the other hand, if not, the energy E_{RDC} and the position $\vec{x}_{\text{RDC}}$ are E_{plate} and $\vec{x}_{\text{plate}}$, respectively.

The physics analysis, discussed in Chap. 8, practically requires only one RDC hit. Using the time difference between the RDC hit and a photon,

$$t_{\text{RDC}-\gamma} \coloneqq t_{\text{RDC}} - t_{\gamma}^{\text{LXe}}, \tag{5.14}$$

the RDC hit with the smallest $t_{\text{RDC}-\gamma}$ is selected.

5.3.3 Performance

The performance of the RDC is characterised by the timing, energy distributions, and parameters extracted from those distributions. One must adequately select events used in the performance evaluation since the performance depends on the photon energy as discussed in Sect. 5.1. I used single-photon (*NoPileup*) or fully unfolded (*Unfolded*) events whose photon energy was in 48 MeV to 58 MeV. The other selection criteria discussed in Sect. 4.1.6 were also applied to ensure the reconstruction quality.

Timing and energy distributions

Figure 5.24 shows the $t_{\text{RDC}-\gamma}$ distributions. Peak width is a few nanoseconds dominated by the TOF of positrons, with negligible resolution (90 ps) of plastic scintillators [102]. The peak is aligned, thanks to the calibration (Sect. 6.5.2). Thanks to the introduction of the template waveform fit, the asymmetric structure, depending on the plate-crystal matching status, was solved.

[2]Non-matched pulses of crystals could be due to the self-luminescence signal.

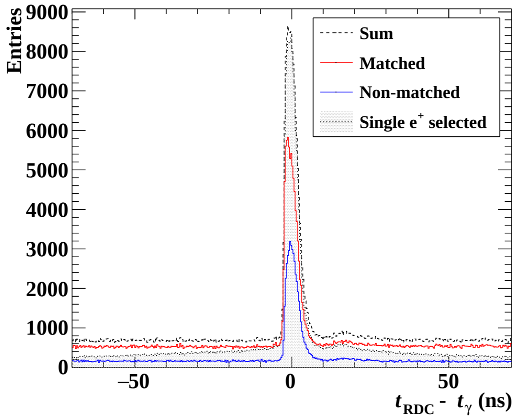

Figure 5.24: Time difference $t_{\mathrm{RDC}-\gamma}$ distribution at $R_\mu = 3 \times 10^7\,\mathrm{s}^{-1}$. The asymmetric distribution observed in Fig. 5.20 disappeared thanks to the template waveform fit in the crystal waveform analysis.

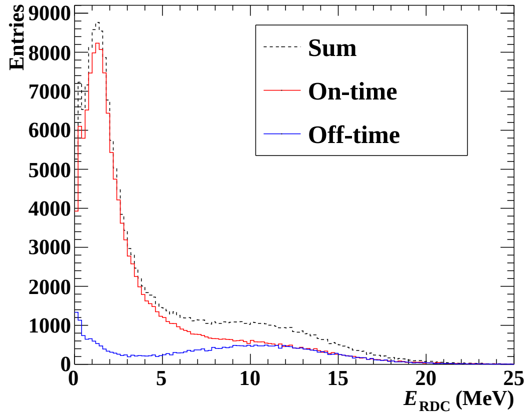

Figure 5.25: E_{RDC} distribution at $R_\mu = 3 \times 10^7\,\mathrm{s}^{-1}$. A blue (red) histogram is based on on- (off-) peak hits. A black is the sum of on-peak and off-peak events.

Table 5.2: Tagged-RMD fraction evaluated with the accidental background events. The fraction increased relatively by 17 %, thanks to the analysis update, which was consistent with the overall hit rate increase.

Year	Analysis version	f_{meas} (%)	f_{tagged} (%)
2021	Conventional	74	16.53 ± 0.15
2021	Updated	74	19.36 ± 0.16
2022	Updated	90	22.89 ± 0.07

The reconstructed energy in RDC E_{RDC} distributes widely. When on-peak ($-8\,\mathrm{ns} < t_{\mathrm{RDC}-\gamma} < 8\,\mathrm{ns}$) and off-peak ($-36\,\mathrm{ns} < t_{\mathrm{RDC}-\gamma} < -20\,\mathrm{ns}$) hits are seperately treated (Fig. 5.24), the E_{RDC} distributions shown in Fig. 5.25 differ because the dominant positron source differs. The off-peak hits are due to Michel positrons having relatively high energy. A peak appears around 12 MeV due to the detector acceptance and turning radius of positrons' trajectories. On the other hand, the on-peak hits are due to RMD positrons having low energy at typically 1–5 MeV.

Hit rate

A hit rate at each scintillator allows me to confirm the reconstruction status. The hit rate is calculated by counting hits in $50\,\mathrm{ns} < t_{\mathrm{RDC}-\gamma} < 180\,\mathrm{ns}$. Figure 5.26 shows the hit rate in plates at $3.4 \times 10^7\,\mathrm{s}^{-1}$ in 2021. The hit rate is the highest at the centre and decreases as the scintillator position is closer to the edge. The hit rate at the plate located in $1\,\mathrm{cm} < y_{\mathrm{RDC}} < 2\,\mathrm{cm}$, which was inefficient with the conventional algorithm, increased by 60 %. The algorithm improvement increased the overall hit rate by 17 %.

Tagged-RMD fraction

The fraction of positron and photon coincident events, whose naive calculation is given by Eq. (5.2), is a barometer to evaluate the RDC performance. The tagged-RMD fraction is evaluated by counting

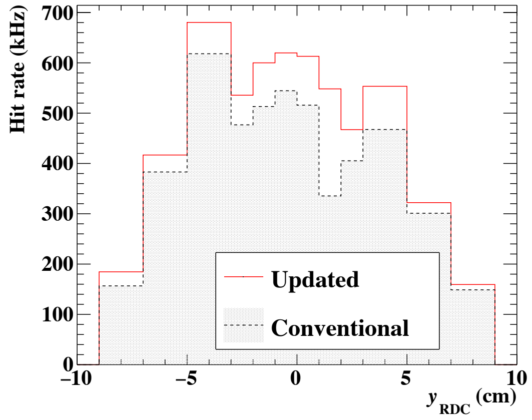

Figure 5.26: Hit rate in plates at $3.4 \times 10^7\ \mathrm{s}^{-1}$ with the updated algorithm (red solid) and the conventional algorithm (black dashed).

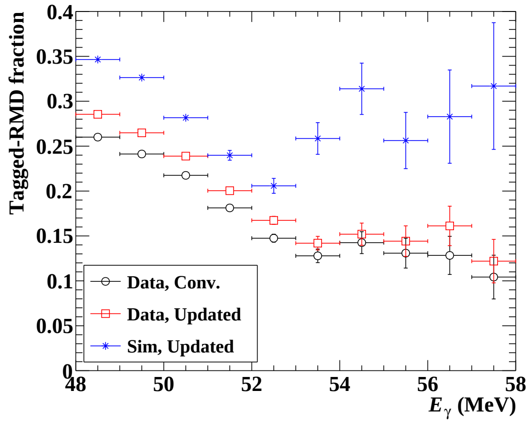

Figure 5.27: Tagged-RMD fraction corrected by f_{meas} as a function of E_γ at $2.80 \times 10^7\ \mathrm{s}^{-1}$. The y axis is $f_{\mathrm{tagged}}/f_{\mathrm{meas}}$.

RDC hits and background photons, that is,

$$f_{\mathrm{tagged}} = \frac{n_{\mathrm{RDC,on}} - n_{\mathrm{RDC,off}}}{n_\gamma}, \tag{5.15}$$

where $n_{\mathrm{RDC,on(off)}}$ is the number of RDC hits in an on- (off-) timing region of [−8 ns, 8 ns] ([20 ns, 36 ns]), and n_γ is the number of events with photons in $48\ \mathrm{MeV} < E_\gamma < 58\ \mathrm{MeV}$. Table 5.2 summarises the yearly tagged-RMD fraction using the accidental background events. The tagged-RMD fraction was 17 % higher with the updated analysis than the conventional one, which was consistent with the overall hit rate increase.

Figure 5.27 shows the E_γ dependence of the tagged-RMD fraction corrected by f_{meas} for the E_γ-trigger data in 2022 and the simulation. The fraction decreases for higher E_γ, as expected from Fig. 5.1b. The measured fraction, however, did not fully reach the simulated and naively calculated values of (31.3 ± 0.2) % and 32 %, respectively, which disagrees relatively by about 18 %. Among this 18 % discrepancy, 6 % is derived from the event mis-categorisation of the multi-photon event analysis. The *Coincidence* events in Fig. 5.10 include a part of RMD events, which are discarded from the analysis sample. Therefore, f_{RMD} is lower than 76 %, resulting in a lower tagged-RMD fraction in data. The rest of the discrepancy is not fully understood, but it is suspected to be due to the RDC detection inefficiency and/or additional materials in the real experimental environment.

Chapter 6

Calibrations

The high-sensitivity search for $\mu \rightarrow e\gamma$ requires good detector calibrations for the whole data-taking period. This chapter describes the detector calibrations.

6.1 DRS calibrations

All detectors' analyses begin with analysing waveforms obtained by DRS modules. It requires good calibration to achieve high-resolution measurements. This section presents the synchronisation of DRS chips and the voltage calibration.

6.1.1 Time calibration

The sampling interval between the DRS capacitor cells is calibrated by inputting sine wave signals before taking data. When taking data, the 80 MHz master clock signal from the DCB is input to a dedicated DRS channel in order to synchronise among different DRS chips. The clock waveform is fitted with a sine function to evaluate the leading-edge point closest to a trigger latency of −590 ns, as shown in Fig. 6.1. The difference in the fitted zero-crossing time among different DRS chips is used for the time alignment.

6.1.2 Voltage calibration

A calibration of the voltage offset in each capacitor cell of the DRS is performed before the run. This procedure involves measuring multiple reference voltages spanning the full dynamic range. Despite

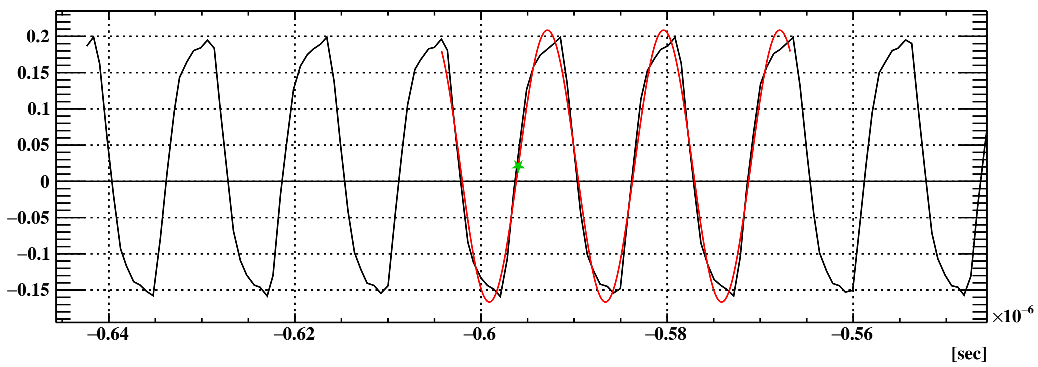

Figure 6.1: Display of clock analysis, which is used to align the DRS time offset [46].

Table 6.1: Offline noise subtraction method applied in each detector. Each noise component is written in text.

	LXe	CDCH	pTC	RDC
Temperature-dependent noise	∘			
Clock-signal cross-talk	∘		∘	∘
Cell pedestal	∘			∘
Start-cell-dependent noise	∘			

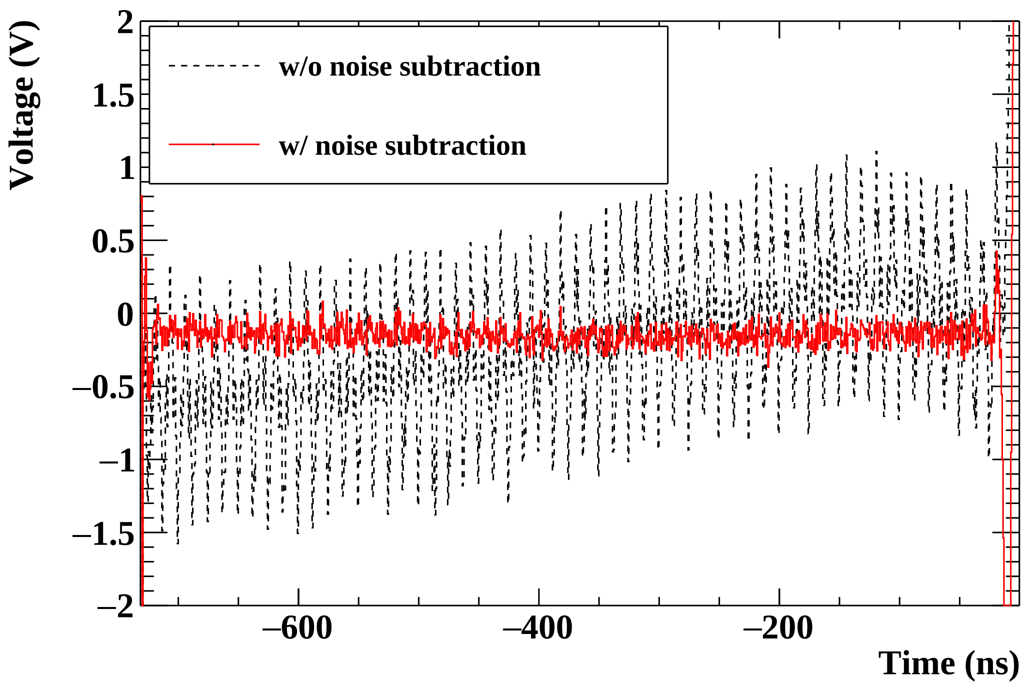

Figure 6.2: A comparison of the summed MPPC waveform of the LXe detector with (red solid) and without (black dashed) noise subtraction.

the application of this calibration during DAQ, non-negligible voltage offsets remain. To mitigate their impact on measurement precision, several offline noise subtraction techniques are employed depending on the detectors, summarised in Table 6.1. Figure 6.2 shows a comparison of the summed MPPC waveform of the LXe detector before and after the offline noise subtraction, in which the noise situation significantly improves. The following paragraphs explain four types of noise subtraction methods.

Temperature-dependent noise The DRS cells exhibit a small but non-negligible leakage current, which varies with the temperature of the DRS chip. Since the voltage drop induced by this leakage current depends on the duration for which the charge is held prior to readout, temperature fluctuations appear in the waveform as a gradual slope in the baseline. The baseline slope causes a non-zero charge offset in the integrated charge. To correct this effect, template waveforms were extracted from a random-triggered dataset at various temperatures. These templates were then used to calibrate and correct the baseline slope on an event-by-event basis, accounting for the temperature at the time of both template acquisition and data collection.

Clock-signal cross-talk The clock signal used to synchronise the DRS chips (Sect. 6.1.1) generates phase-correlated noise due to electrical cross-talk, which deteriorates the time resolution. This noise component can be reduced by subtracting a typical noise template. I extracted the template from a random-trigger dataset by accumulating the waveform after event-by-event alignment with the clock timing.

Cell pedestal The residual voltage offset in each DRS cell, called a “cell pedestal”, generates low-frequency noise in the waveform. I extracted the template of the cell pedestal from the random-triggered dataset by accumulating the waveform as a function of the DRS cell, and it is subtracted from the data.

Start-cell-dependent noise The coherent noise correlated with the “start-cell”, the first DRS cell of the waveform, causes $\mathcal{O}(1\,\mathrm{MeV})$ variation of the energy reconstructed by the LXe detector. The reason for the dependence remains unknown, but it is clearly dependent on the start-cell. I, therefore, reduced the noise by making and subtracting a start-cell-dependent waveform template.

Noise contribution to photon energy resolution

The DRS electric noise greatly impacts the LXe detector’s energy resolution because of its reconstruction method. Thus, I must carefully monitor and calibrate it. Figure 6.3 shows the stability of the offset and fluctuation of the reconstructed energy for the random trigger events during the runs 2021 and 2022 after noise subtraction. The energy spread was 0.09 MeV at maximum through the runs, and the energy offset had only 0.04 MeV (0.01 MeV) as a standard deviation for 2021 (2022), which is negligible for the photon measurement.

6.2 LXe detector calibrations

The LXe detector requires the following calibrations:

- Photosensor calibration to reconstruct $N_{\mathrm{pho},i}$ (Sects. 6.2.1–6.2.3),
- Photosensors’ position to reconstruct the photon position (Sects. 6.2.4–6.2.5),

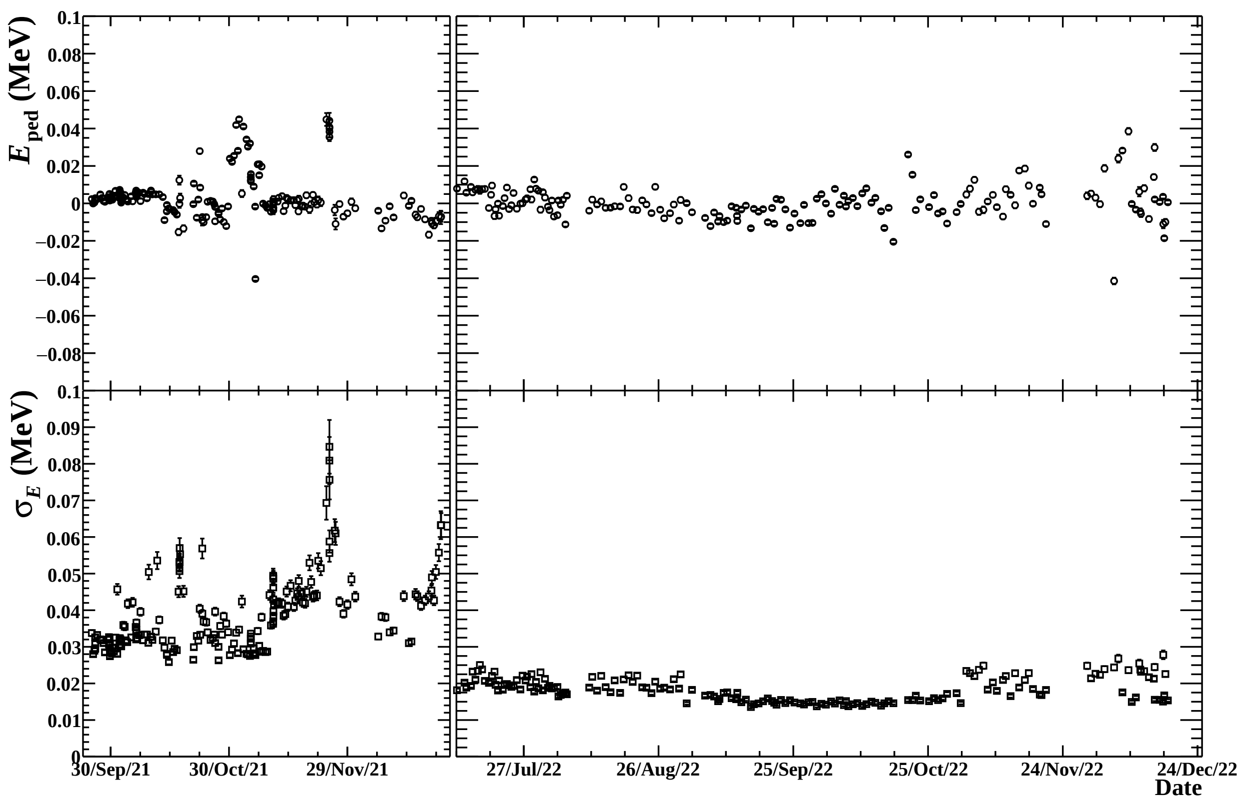

Figure 6.3: Energy offset (top) and energy spread (bottom) measured with random trigger datasets collected in the runs 2021 and 2022 after noise subtraction.

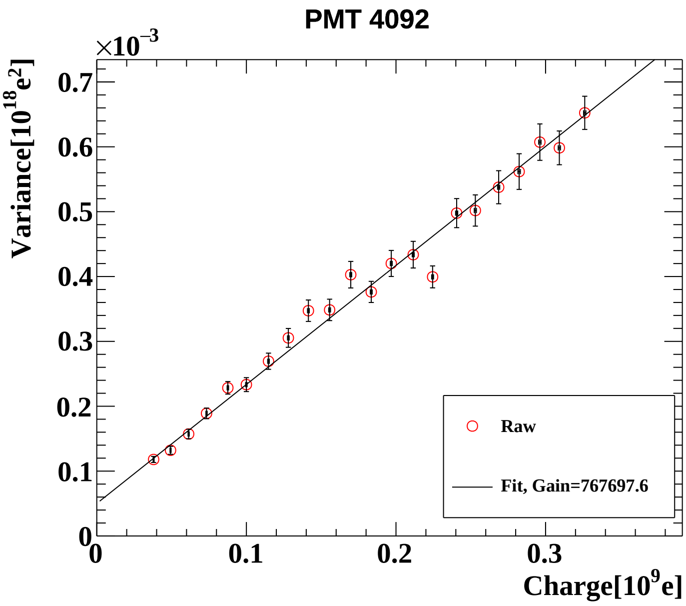

Figure 6.4: Measured relation between the variance and mean of the charge distribution under LED light with different intensities [59].

- Time offset, walk, and position dependence correction to reconstruct the photon time (Sect. 6.2.6), and
- Energy scale to reconstruct the photon energy (Sects. 6.2.7–6.2.9).

6.2.1 PMT gain

The gain of PMTs is calculated based on the photoelectron statistics of LED light. One can calculate the average of integrated charge $\langle Q_i \rangle$ with the average number of photoelectrons $\langle N_{\mathrm{phe},i} \rangle$ and gain G_i:

$$\langle Q_i \rangle = \langle N_{\mathrm{phe},i} \rangle \cdot G_i. \tag{6.1}$$

Since $N_{\mathrm{phe},i}$ follows a Poisson distribution, $\langle N_{\mathrm{phe},i} \rangle$ is equal to the variance of the $N_{\mathrm{phe},i}$ distribution $\sigma^2_{\mathrm{phe},i}$. The variance of the charge distribution can be expressed as

$$\begin{aligned} \sigma_Q^2 &= G_i^2 \cdot \sigma^2_{\mathrm{phe},i} + \sigma^2_{\mathrm{noise}}, \\ &= G_i \cdot \langle Q_i \rangle + \sigma^2_{\mathrm{noise}}, \end{aligned} \tag{6.2}$$

where σ_{noise} is an electric noise term.

LEDs located on the upstream and downstream faces as shown in Fig. 2.19 illuminate PMTs with different 22 intensities to obtain the relation between $\sigma^2_{\mathrm{phe},i}$ and $\langle Q_i \rangle$ in Eq. (6.2), which is called an “intensity scan”. Figure 6.4 shows the relation between them measured from the charge distribution. The slope of a fitted linear function is the gain G_i.

Temporal evolution

A relative gain variation in time can be traced by the temporal evolution of the integrated charge mean $\langle Q_i \rangle$ under stable LED light as

$$\frac{G_i(t_1)}{G_i(t_2)} = \frac{\langle Q_i(t_1) \rangle}{\langle Q_i(t_2) \rangle}, \tag{6.3}$$

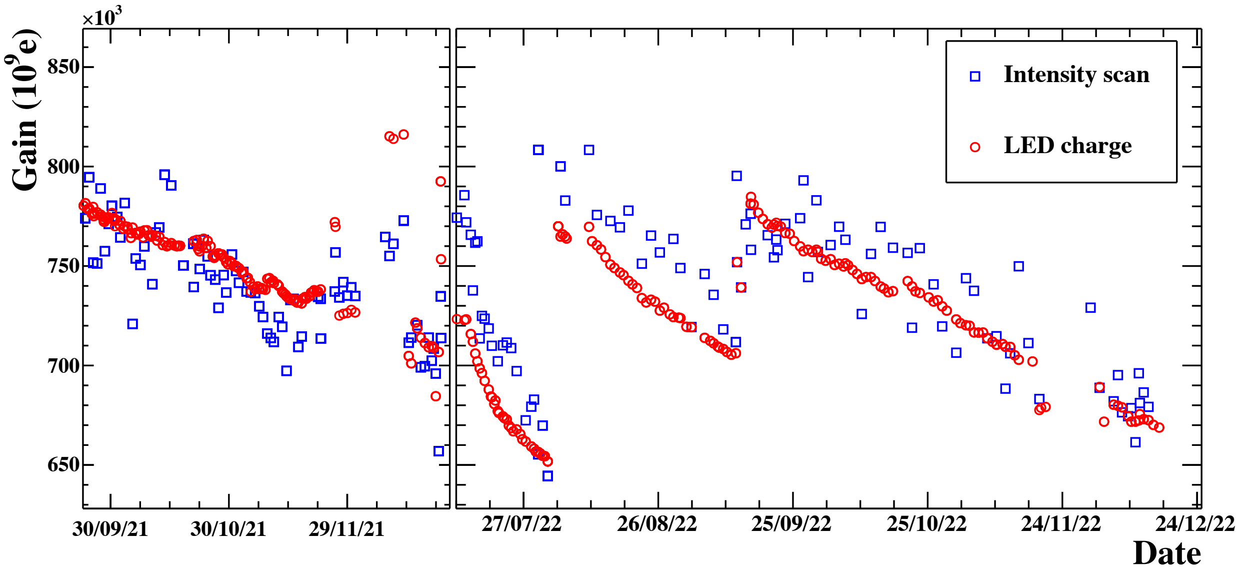

Figure 6.5: Temporal evolution of the gain of a representative PMT during the runs 2021 and 2022. Blue dots show averaged gain values calculated with the intensity scan method. The red ones show those based on the relative charge, which is scaled to agree with the blue dot on 15th September 2021 (left) and 7th November 2022 (right).

where $t_{1(2)}$ is an arbitrary time to measure integrated charge for LED light. This method enabled stable gain monitoring and showed a consistent tendency by correcting collection efficiency (CE) and QE for visible light. It was established in the MEG experiment and was taken over.

Figure 6.5 shows the temporal evolution of the gain of a PMT measured by the intensity scan and relative charge for LED light. The temporal evolutions of the two methods differ because of the lack of correction of CE and QE for visible light. However, this difference can be corrected by QE for VUV light, as discussed in Sect. 6.2.3.

Beam-rate-dependent gain shift

As discussed in Sect. 2.4.2, the gain of PMTs was shifted when the high-intensity beam came to the MEG detector, which required PMT-by-PMT calibration. This so-called gain shift is calibrated by a charge ratio for LED light in the beam to that without the beam $R_{\mathrm{on/off}} = \langle Q_{i,\mathrm{on}} \rangle / \langle Q_{i,\mathrm{off}} \rangle$. Figure 6.6 shows the ratio during the physics run at $3 \times 10^7\,\mathrm{s}^{-1}$ and during the π^0 calibration run in 2022. Since the photon irradiation rate is approximately twice as high during the π^0 calibration run as during the physics run, the shift during the π^0 calibration run is larger than that during the physics run. A product of off-beam gain and these ratios was utilised as the gain in the in-beam data analysis.

6.2.2 MPPC gain and excess charge factor

The single-photoelectron gain and the excess charge factor (ECF) of MPPCs are calculated based on an integrated charge spectrum of low-intensity LED light. Twelve LEDs located on the outer face in Fig. 2.19 are flashed with the intensity that MPPCs detect approximately 1 p.e. on average.

Charge integration was performed with multiple integration widths of 50, 60, 70, 80, 90, 100, 110, 120, 130, 140, 150, 200 and 250 ns, with 150 ns being the default. The shorter integration widths allow studies with suppressed electric noise. Figure 6.7 shows the integrated charge distributions with

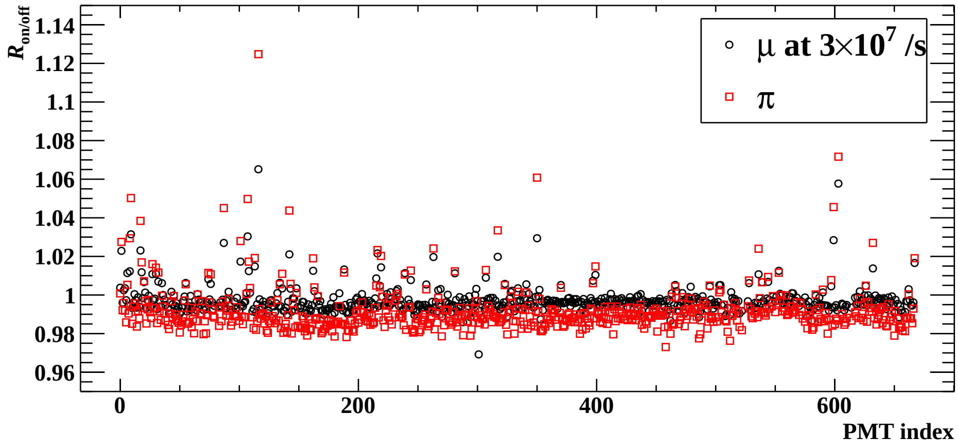

Figure 6.6: A charge ratio in the beam to that without the beam as a function of PMT indices. Black dots stand for the ratio during the physics run at $R_\mu = 3 \times 10^7\ \mathrm{s}^{-1}$ and red ones for that during the π^0 calibration run 2022.

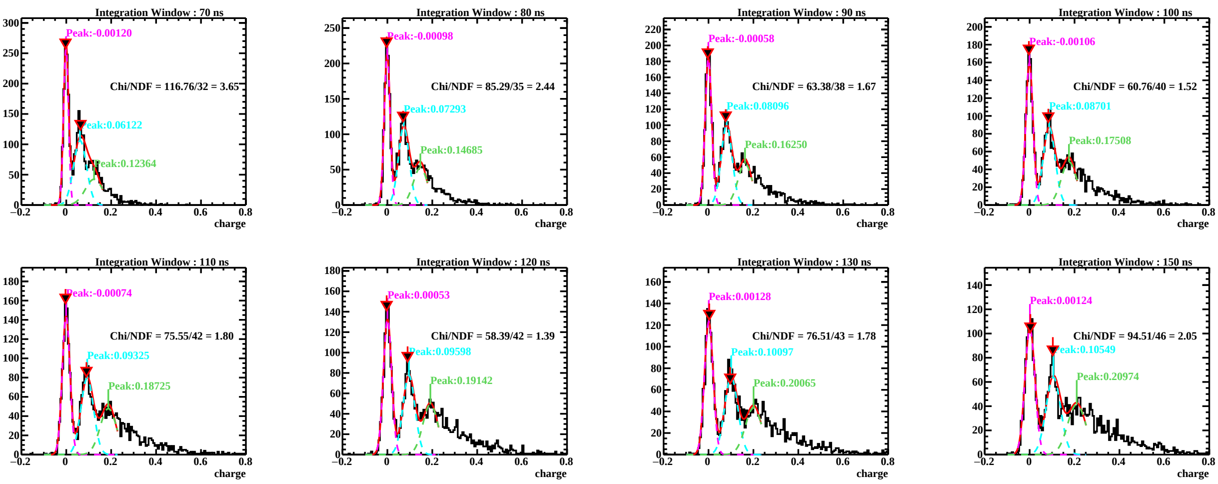

Figure 6.7: An example of charge distributions with integration widths between 70 ns to 150 ns. The red lines indicate the best fit of Eq. (6.6) to each histogram. Magenta, cyan, and green functions represent the 0, 1 and 2 p.e. components, respectively.

different integration widths. I first searched for pedestal and 1 p.e. peaks in the distribution, μ_{ped} and $\mu_{1\,\mathrm{p.e.}}$, respectively. The distance between these peaks is regarded as the single-photoelectron gain G_i.

If there is no correlated noise, i.e. cross-talk and after-pulse, the $N_{\mathrm{phe},i}$ distribution from an LED follows a Poisson distribution with the mean λ:

$$P(k) = \frac{e^{-\lambda}\lambda^k}{k!}. \tag{6.4}$$

In the past analysis [59], applied to the 2021 data, the mean λ is given by

$$\lambda = -\log\left(\frac{n_{\mathrm{ped}}}{n_{\mathrm{total}}}\right), \tag{6.5}$$

where n_{ped} is the number of pedestal events and n_{total} is the total number of events. The distribution is modelled with a probability that excess charge is detected, $p \in [0, 1]$, in order to better estimate ECF for the 2022 data analysis. The charge distribution is fitted with the function defined as

$$\begin{aligned}
&n_{\mathrm{total}} \cdot P(k=0) \cdot \frac{d}{\sigma_{\mathrm{ped}}\sqrt{2\pi}} \exp\left[-\frac{(x-\mu_{\mathrm{ped}})^2}{2\sigma_{\mathrm{ped}}^2}\right] \\
&+n_{\mathrm{total}} \cdot P(k=1) \cdot p \cdot \frac{d}{\sigma_{1\,\mathrm{p.e.}}\sqrt{2\pi}} \exp\left[-\frac{(x-\mu_{1\,\mathrm{p.e.}})^2}{2\sigma_{1\,\mathrm{p.e.}}^2}\right] \\
&+n_{\mathrm{total}} \cdot P(k=2) \cdot \left[\left\{p^2 + 2p(1-p)\right\} + \lambda(1-p)\right] \cdot \frac{d}{\sigma_{2\,\mathrm{p.e.}}\sqrt{2\pi}} \exp\left[-\frac{(x-\mu_{2\,\mathrm{p.e.}})^2}{2\sigma_{2\,\mathrm{p.e.}}^2}\right],
\end{aligned} \tag{6.6}$$

where the first term corresponds to the pedestal peak, and the second and third correspond to 1 p.e. and 2 p.e. peaks; d is the bin width of the histogram; and $\mu_{2\,\mathrm{p.e.}}$ is the 2 p.e. peak position which equals $2\mu_{1\,\mathrm{p.e.}} - \mu_{\mathrm{ped}}$.

Let me discuss a Gaussian width σ expressing a finite resolution and electric noise. The Gaussian width of the pedestal peak σ_{ped} represents the electric noise. I consider that the resolution for single photoelectron detection contributes to the Gaussian width of the 1 p.e. peak in addition to the noise contribution, that is,

$$\sigma_{1\,\mathrm{p.e.}} = \sqrt{\sigma_{\mathrm{ped}}^2 + \sigma_{\mathrm{res}}^2}. \tag{6.7}$$

The analogy gives the Gaussian width of the 2 p.e. peak

$$\sigma_{2\,\mathrm{p.e.}} = \sqrt{\sigma_{\mathrm{ped}}^2 + 2\sigma_{\mathrm{res}}^2}. \tag{6.8}$$

Fit parameters in Eq. (6.6) are, therefore, summarised to be λ, p, σ_{ped}, and σ_{res}. Finally, the ECF is calculated as

$$F_{\mathrm{EC},i} = \frac{\langle Q_i \rangle}{\lambda \cdot G_i}, \tag{6.9}$$

where $\langle Q_i \rangle$ is the mean value of the charge distribution with the pedestal peak exclusion.

The next step after the gain and ECF calculations with multiple integration widths is the parametrisation of their integration width dependence. The integration width dependence on gain, called a "gain curve", was fitted with an empirical function defined as

$$G_0\left\{1 - \exp\left(-\frac{x - x_{G,0}}{\tau_G}\right)\right\}, \tag{6.10}$$

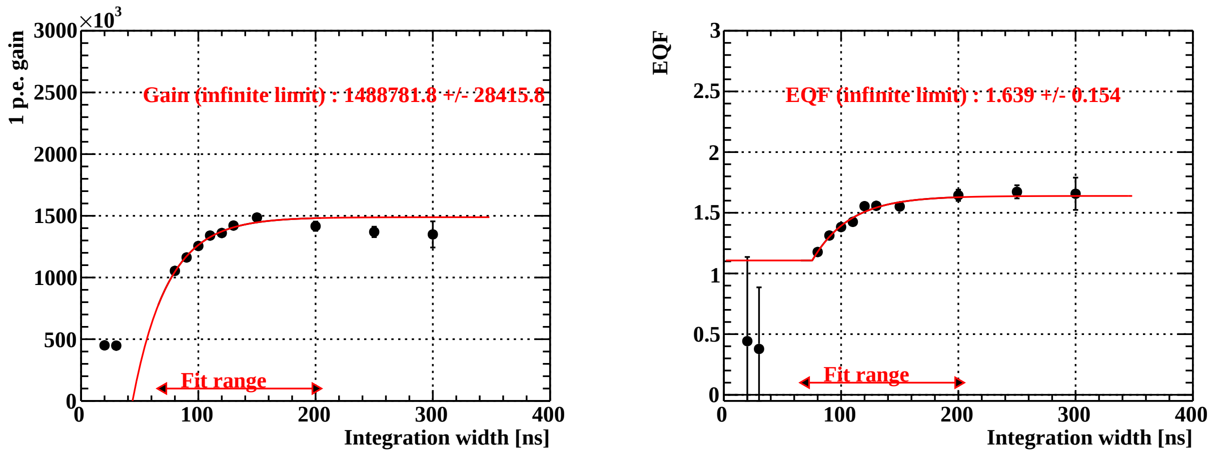

Figure 6.8: An example of integration width dependence of gain, ECF and the fitting results. A dataset and a channel shown here correspond to those used in Fig. 6.7. A discrepancy in gain between measured dependence and the best-fit curve in wider integration ranges can be understood due to the electric noise.

where G_0 is the gain at an infinite integration width; $x_{G,0}$ is a crossing point to $G = 0$; and τ_G is the time constant of the gain curve. On the analogy of the gain, the ECF curve is fitted with the following function:

$$\begin{cases} F_{\mathrm{CT}} & \text{if } x < x_{F,0}, \\ F_{\mathrm{CT}} + F_{\mathrm{AP}}\left[1 - \exp\left(-\dfrac{x - x_{F,0}}{\tau_{\mathrm{AP}}}\right)\right] & \text{if } x > x_{F,0}, \end{cases} \tag{6.11}$$

where $F_{\mathrm{CT(AP)}}$ is a cross-talk (after-pulse) factor[1]; $x_{F,0}$ is a crossing point; and τ_{AP} is the time constant of after-pulse. Figure 6.8 shows the gain and ECF curves, and the best-fit functions. A discrepancy between the measured dependence and the best-fit curve in wide integration ranges can be understood due to electric noise widening the pedestal, 1 p.e., and 2 p.e. peaks. The fit range is, thus, limited from 70 ns to 200 ns. Finally, I obtained gain and ECF values at the integration widths of 150 ns.

Temporal evolution during the run 2021

The temporal variation was monitored and calibrated using the charge for strong LED light in the run 2021 [59]. This was because the LED data with a low intensity was taken once in the run 2021 due to a malfunction of the LED driver. The gain was measured in the middle of November and used to scale the temporal evolution of the charge. Figure 6.9 shows the temporal evolution of the gain of an MPPC during the runs 2021 and 2022. In this method, the PDE for visible light, decreasing during the run due to radiation damage, influenced the charge measurement, which would finally be corrected by the PDE for VUV light.

Temporal evolution during the run 2022

The low-intensity LED data were taken three times per week thanks to the establishment of its flashing system. The gain was, thus, calibrated without the charge for strong LED light, i.e. only based on the

[1] This is not a cross-talk or after-pulse probability. The after-pulse factor F_{AP} can be above 1 due to secondary after-pulse.

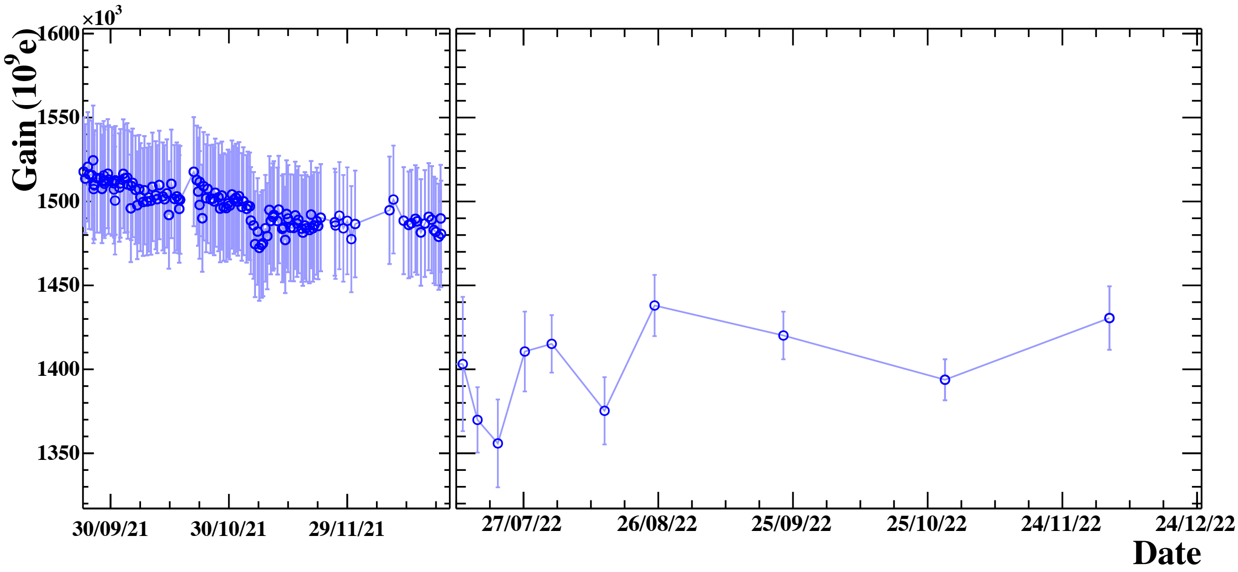

Figure 6.9: Temporal evolution of the gain of an MPPC during the runs 2021 and 2022. The gain decreased at the beginning of November 2021 because of a temperature variation.

integrated charge distribution for weakly flashing LED light, in order to eliminate the effect of the PDE for visible light. I combined the gains measured with several calibration sets in a subdivided period to suppress statistical uncertainty.

The temporal evolution of the gain of an MPPC is shown in Fig. 6.9. Although it was expected to be stable during the run, the measured gains fluctuated within 2 %. This fluctuation is interpreted as the measurement precision.

All of the measured ECFs were combined for the whole run 2022 because they were stable, as done in the run 2021 [59]. Figure 6.10 shows the ECFs as a function of serial number of MPPCs. The general tendency, such as the dependence on production lots, is consistent with the run 2021.

Beam-rate-dependent gain shift

The MPPC gain decreased due to the voltage drop in resistors in the bias circuit by the induced current under a high-rate environment. Figure 6.11 shows the current through MPPCs and their bias circuits during the π^0 calibration run 2022. Since the irradiation rate basically correlates with the u position, sensor-by-sensor gain calibration under an in-beam environment is required.

A charge ratio with an integration width of 150 ns from LEDs, measured with and without beam with a proper trigger prescaling, corrects the gain difference under in-beam and off-beam environments. The ratio during the π^0 calibration run was measured to be 1 % lower than that during the physics run because the currents differed by a factor of two between the two runs, as it was in the run 2021 [59]. The in-beam gain was given by multiplying the off-beam gain by the ratio.

6.2.3 MPPC PDE and PMT QE

The PDE of MPPCs and the QE of PMTs ϵ_i are calibrated based on a comparison of the detected number of scintillation photons $N_{\mathrm{pho},i} = N_{\mathrm{phe},i}/\epsilon_i$ between data and a simulation. They are defined as

$$\epsilon_i = \frac{\langle N^{\mathrm{data}}_{\mathrm{phe},i} \rangle}{\langle N^{\mathrm{MC}}_{\mathrm{pho},i} \rangle} \times F_{\mathrm{LY}}, \tag{6.12}$$

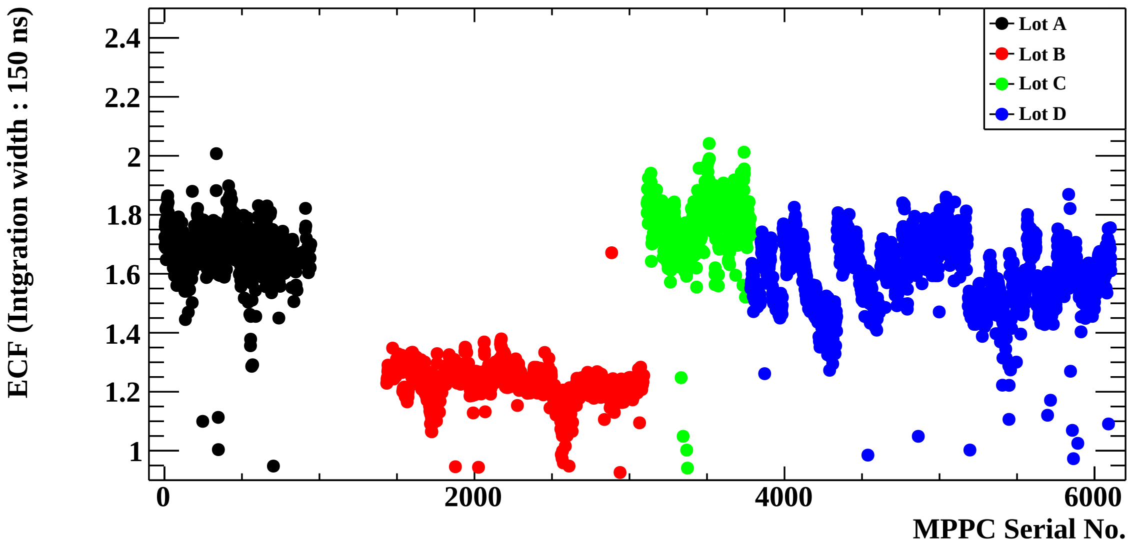

Figure 6.10: ECFs with an integration width of 150 ns as a function of MPPC serial number. Colours correspond to production lots.

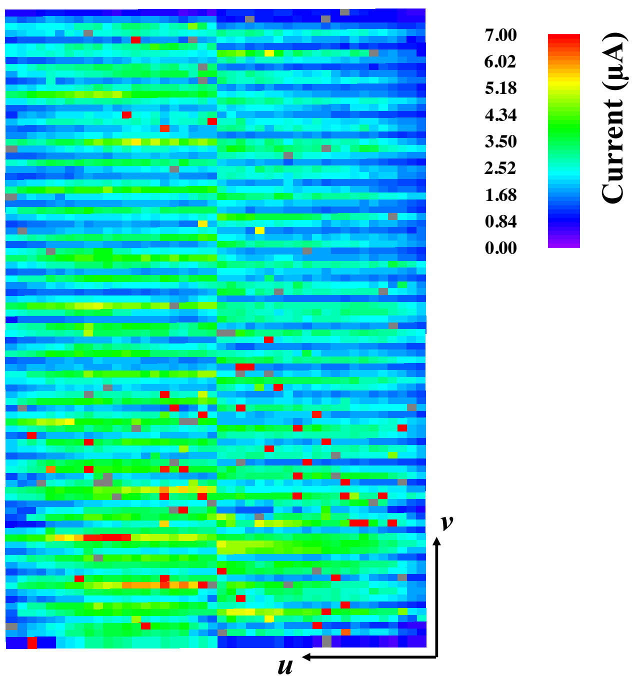

Figure 6.11: Current flowing through MPPCs during the π^0 calibration run in 2022. The current is higher in the centre of the figure. These MPPCs are closer to the target. In addition, the current strongly depends on the production lot.

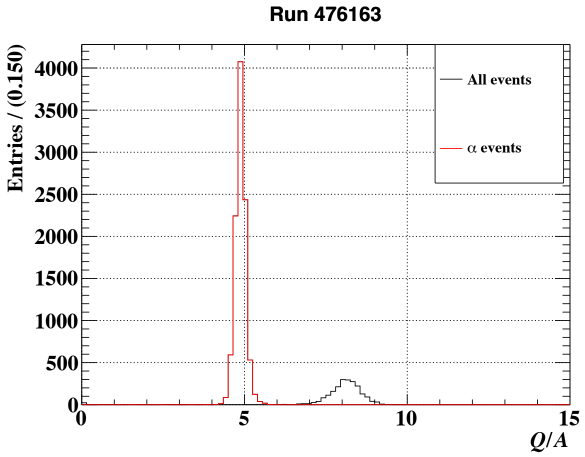

Figure 6.12: Distributions of Q/A, used as one of the selection criteria. Black histograms show distributions before event selection. Red ones show after the selection.

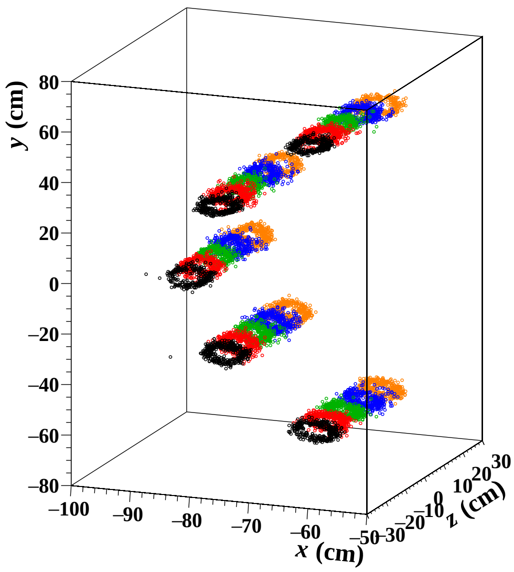

Figure 6.13: Reconstructed positions of each α particle.

where F_{LY} is a light yield correction factor. For the calibration, α-particles with 5.5 MeV energy from ^{241}Am, introduced in Sect. 2.4.3, are used.

The analysis begins with discriminating the α-particle events from cosmic-ray events, which are the dominant background. The selection criteria are

- The ratio of charge to amplitude $Q/A < 6$ as shown in Fig. 6.12, and
- $\sum_i (N_{\mathrm{pho},i} \cdot C_i) < 4 \times 10^6$ where C_i is photosensors' coverage.

Then, the source from which an α particle is emitted has to be identified based on the scintillation light distribution measured by PMTs for the selected events. A wire is identified based on the light distribution in the upstream and downstream faces, and then the position among the wire is reconstructed based on the weighted mean of PMT z position with a weight of $N_{\mathrm{phe},i}$. Figure 6.13 shows the reconstructed position, showing that the α-particle sources are successfully identified.

The mean of $N_{\mathrm{phe},i}$ for each α-particle source is compared with the simulated mean of $N_{\mathrm{pho},i}$ with the MC configuration B, defined in Sect. 2.7. The 25 points of the $\langle N_{\mathrm{pho},i} \rangle$ ratio between the data and the simulation have a linear relationship, as shown in Fig. 6.14. The PMT QE is considered not to change over time based on the experience in the MEG experiment, and thus is fixed to be 16 % on average, which Hamamatsu K.K provided. The light yield correction factor F_{LY} can be calculated by the reciprocal of PMT-averaged $N_{\mathrm{pho},i}$ ratio. By calculating Eq. (6.12), one can obtain MPPC PDE and PMT QE values.

Temporal evolution

The PDE and QE values from each measurement were moving-averaged with five points to suppress statistical fluctuations. Not all the points are necessary to trace the temporal evolution, especially in a period with a stable decrease. Thus, factor two or three samplings were done based on stability. Figure 6.15 shows the temporal evolution of the PDE of an MPPC located in the central region during the runs 2021 and 2022. The PDE decreased over time due to radiation damage [72] and was recovered

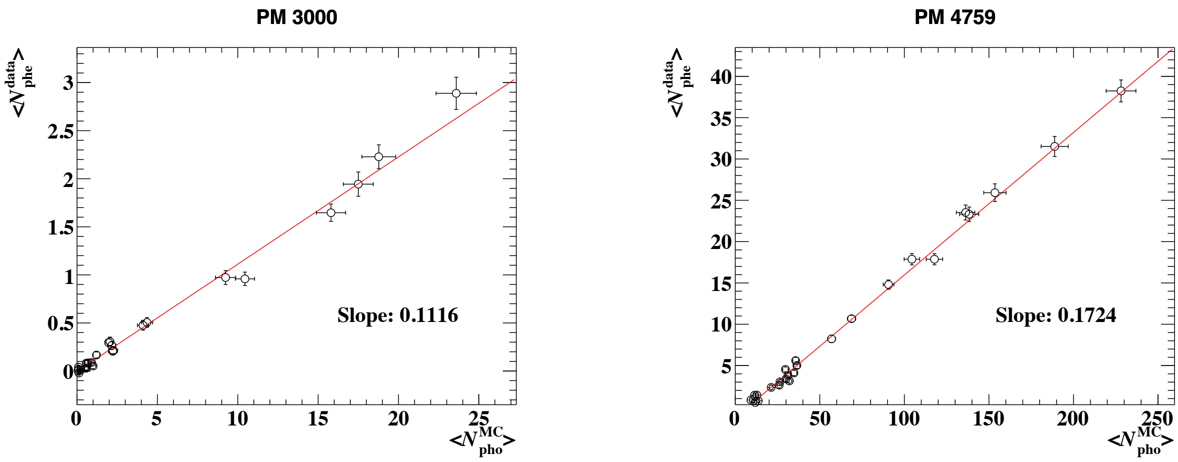

(a) An example of an MPPC channel. (b) An example of a PMT channel.

Figure 6.14: $N_{\text{phe},i}$ comparison between data and the MC simulation. Each dot corresponds to each α-particle source, showing the mean of $N^{\text{data}}_{\text{phe}}$ vs that of $N^{\text{MC}}_{\text{pho}}$.

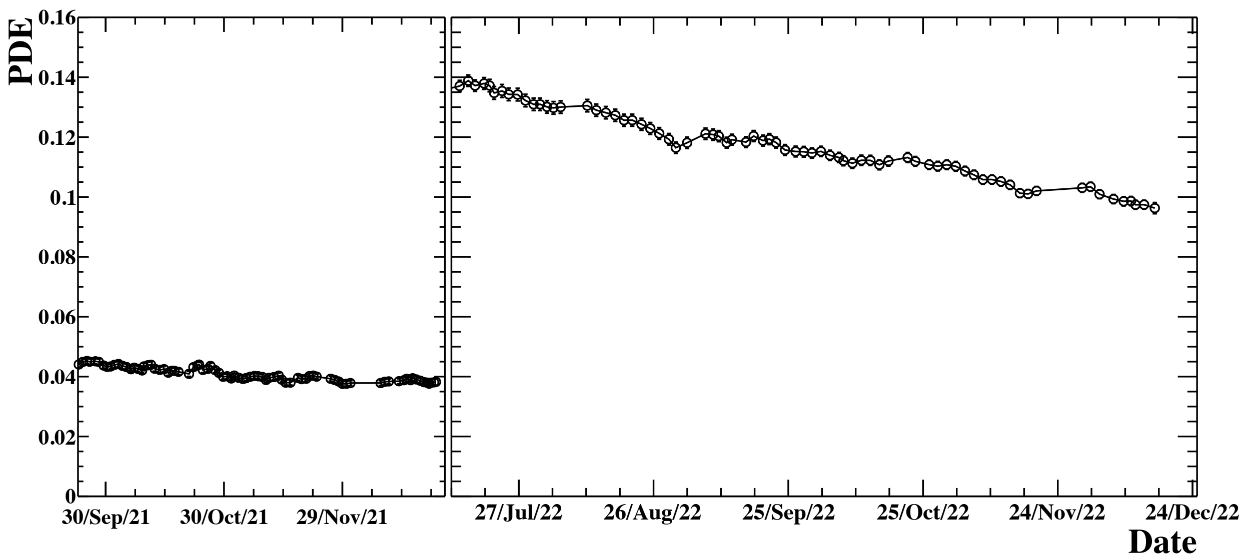

Figure 6.15: The temporal evolution of the PDE of an MPPC located in the central region.

by an annealing campaign discussed in Sect. 3.1. On average, the PDE value decreased from 8.6 % (14.0 %) to 6.1 % (10.8 %) in 2021 (2022).

6.2.4 MPPC alignment

The MPPCs were aligned by combining an optical survey at room temperature and an X-ray measurement at a low temperature in 2018. A yearly optical survey of various reference points was conducted to calibrate the yearly movement of the detector.

MPPC position measurement in 2018 The real MPPCs support is segmented along ϕ and consists of four pieces of carbon fibre reinforced plastics (CFRP). The constructed detector was surveyed at room temperature using a Faro laser scanner [103, 59]. For each of the four CFRP, a cylindrical surface was fitted to the corresponding MPPC positions. The resulting four cylinders describe the MPPC positions with an accuracy of 180 µm.

Afterwards, the detector was cooled down and filled with liquid xenon. The inner surface was scanned with a source of X-rays along z and ϕ [104]. Lead strips in defined positions allowed precise reconstruction of the MPPC positions inside the filled detector. The results of the two alignment techniques are combined and result in a model consisting of four perfectly cylindrical shells on which the MPPCs are placed.

Yearly alignment Various reference points located on the outer surface of the LXe detector were regularly surveyed to trace a yearly detector transformation. The transformations refer to the measured position in 2018. Thus, no cumulative uncertainty increases throughout the years since the results only depend on measurements in 2018 and each year. The alignment uncertainty is estimated to be 500 µm. The technical details of the yearly alignment are given by Appendix A.

6.2.5 Photosensor location

As mentioned in Sect. 3.1, some signal cables were wrongly assigned to WaveDREAM boards during runs 2021 and 2022. Though it could cause inefficiency in triggering, the offline analysis had no problem once the recorded waveform was assigned to a proper photosensor. This subsection describes methods of finding misassignment and correspondence between a photosensor and a DRS channel storing waveform.

MPPC channel assignment

Misassignment in MPPCs can be found by having a look at the scintillation light distribution as shown in Fig. 6.16. However, it is not easy to look at all events and find the misassignment. The misassignment enhances χ^2_{pos} defined in Eq. (4.4) because the observed $N_{\mathrm{pho},i}$ distribution around the peak is distorted. Figure 6.17 shows the uv event map with large χ^2_{pos} before and after fixing the assignment, and highlighted spots (dotted in black) correspond to misassigned photosensors. A look at events where the photon position is around the spots gives clues to identify the correct assignment.

This method requires precise calibrations for gain, ECF, and PDE. Especially regarding the PDE, because a comparison of $N_{\mathrm{pho},i}$ between data and a simulation, discussed in Sect. 6.2.3, several iterations of calibrating PDE and fixing the assignment are usually required. However, six misassigned spots out of 22 shown in Fig. 3.2b were identified at the final stage of the analysis, as a certain level of precision in gain and PDE calibrations is required. The PDE of those MPPCs was not recalibrated

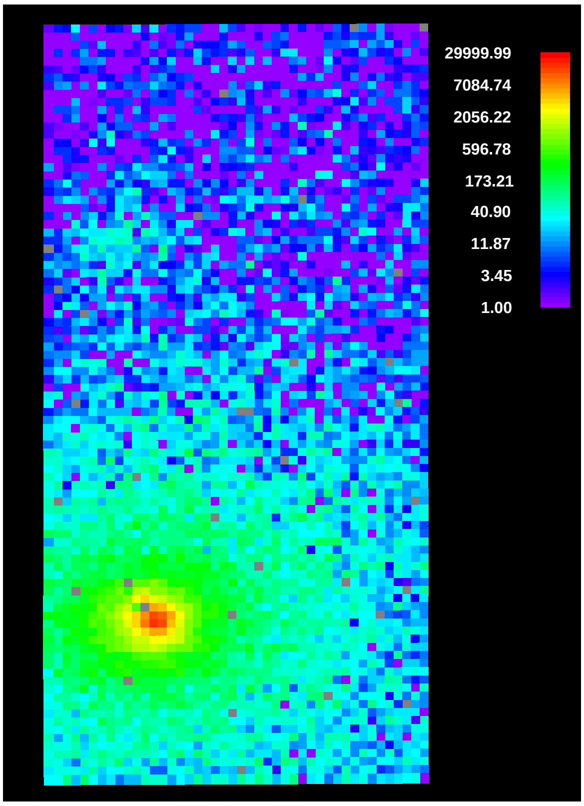

Figure 6.16: $N_{\mathrm{pho},i}$ distribution in an event where the photon position is close to a channel misassignment spot.

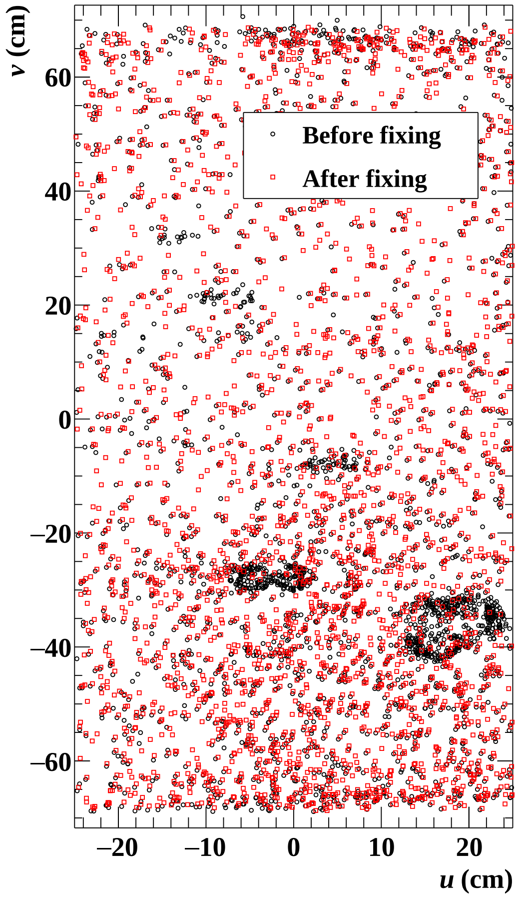

Figure 6.17: The map of events with $\chi^2_{\mathrm{pos}} > 30$ in the part of the physics data taken in 2021. Event concentration shows that the MPPCs around the structure are likely to be misassigned.

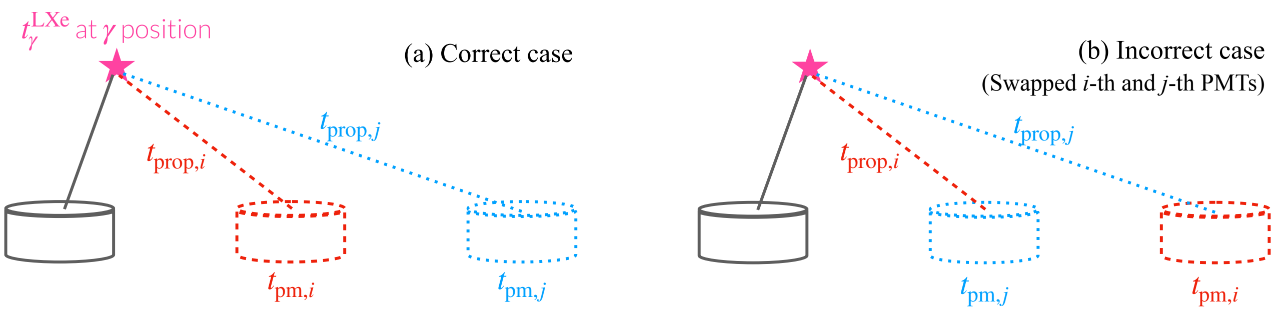

Figure 6.18: Schematic drawing of time-based miscabling correction. (b) shows the case that PMTs next to each other are swapped.

but swapped with the agreement of the MPPC assignment, given the target schedule and negligible size of the effect.

PMT channel assignment

Several methods to identify misassigned PMT channels and to fix them have been established. The full details are provided by Appendix B.

The LED data taken during LXe filling into the detector uncovered the channel misassignment of PMTs on the top face. As more LXe was transferred to the detector, more PMTs were immersed in LXe, starting with the PMTs located in the lower y position. PMTs above the liquid level detect less light because most of the light from LEDs in LXe reflects at the surface of LXe [105]. The unexpected integrated charge Q_i for the LED light identifies misassigned channels in the vertical direction. This analysis is sensitive to the misassignment only in the vertical direction, requiring another method to fully identify the correct assignment.

The consistency of channel assignment was quantified by comparing the timing of different PMTs to each other in photon events. Figure 6.18 shows the schematic drawing of the analysis concept. The detected pulse time difference between the i-th PMT and the j-th PMT ($t_{\mathrm{pm},i} - t_{\mathrm{pm},j}$) must correlate with the propagation time difference between them ($t_{\mathrm{prop},i} - t_{\mathrm{prop},j}$), with the correct channel assignment. However, in case the i-th and j-th PMTs are misassigned, as shown in Fig. 6.18(b), these pulse and propagation time differences are anti-correlated. I looked for the correct channel assignment with the best correlation. When more than two channels are involved in a set of permuted channels, i.e. not just a swapping, some trial and error are usually necessary to fully identify the correct assignment.

I modified the channel assignment for ten PMTs on the top face and five PMTs on the outer face in total. Since I detected these channel misassignments in PMTs at the last stage of the analysis as well as MPPCs, the gain and QE of those PMTs were not recalibrated but just swapped.

6.2.6 Time walk, offset, and position dependence

Calibrating the time walk, offset, and position dependence utilises two photons emitted from a π^0 decay. The pre-shower counter, introduced in Sect. 2.4.4, detects one of the two photons and the detection time t_{PS} is used as a reference with the TOF correction $t_{\mathrm{TOF}}^{\gamma\gamma}$ for the hit time of the other photon in the LXe detector, that is,

$$t_{\mathrm{ref}} = t_{\mathrm{PS}} - t_{\mathrm{TOF}}^{\gamma\gamma}. \tag{6.13}$$

Time walk and offset The time-walk parameter $t_{\mathrm{walk},i}$ is obtained as a function of $N_{\mathrm{phe},i}$ for the remaining time from the reference time in six groups: the PMTs on the outer face, the PMTs on

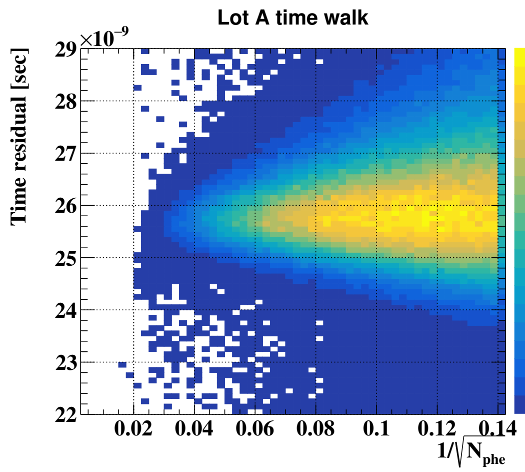

Figure 6.19: Distribution of $t_i - t_{\mathrm{ref}} - t_{\mathrm{prop},i}$ vs $1/\sqrt{N_{\mathrm{phe},i}}$ for the MPPCs from the production lot A [46].

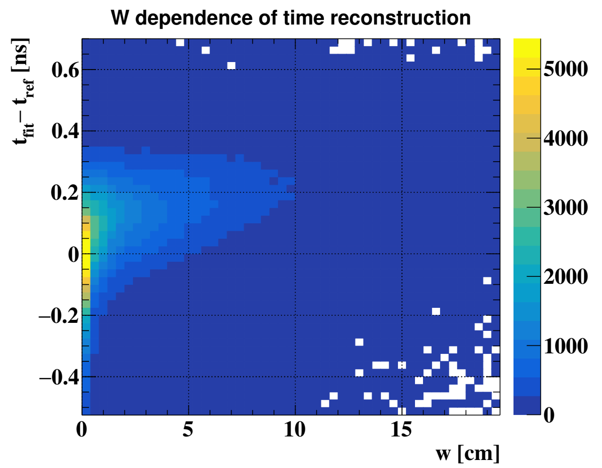

Figure 6.20: w_γ dependence of $t_{\mathrm{fit}} - t_{\mathrm{ref}}$ [46].

the lateral faces, and the MPPCs for different production lots, given the difference in the waveform shape. Figure 6.19 shows the $t_i - t_{\mathrm{ref}} - t_{\mathrm{prop},i}$ distribution as a function of $N_{\mathrm{phe},i}$ for the MPPCs from the production lot A. The time offset $t_{\mathrm{offset},i}$ is, then, obtained for each channel as a constant offset remaining after the $t_{\mathrm{walk},i}$ correction.

Position dependence of the time offset The fitted time in Eq. (4.6) has a position-dependent bias. Figure 6.20 shows the w_γ dependence of the fitted time $t^{\mathrm{LXe}}_{\gamma,\mathrm{fit}} - t_{\mathrm{ref}}$, which is especially strong. This was corrected by introducing the correction term $F_t(u_\gamma, v_\gamma, w_\gamma)$ in Eq. (4.7), which consisted of three one-dimensional functions of u_γ, v_γ, and w_γ:

$$F_t(u_\gamma, v_\gamma, w_\gamma) = F_{tu}(u_\gamma) + F_{tv}(v_\gamma) + F_{tw}(w_\gamma). \tag{6.14}$$

Long-term stability of time offset The time offset was monitored by the LED illumination signal and found to be drifted by 200 ps on average during the run 2022 (Fig. 6.21 for a PMT). This effect, observed only with PMTs, resulted in the time drifting of both $t_{\mathrm{PMT}} - t_{\mathrm{MPPC}}$ and $t_{\mathrm{e}\gamma}$, causing 40 ps difference of $t_{\mathrm{e}\gamma}$ offset between the beginning and the end. Though it is concluded that this effect did not deteriorate the $t_{\mathrm{e}\gamma}$ resolution $\sigma_{t_{\mathrm{e}\gamma}}$ substantially, it is still harmful in the likelihood analysis in the use of a period-dependent PDF set. Therefore, the period of the run 2022 was divided into seven periods in total (each with roughly ten days of "livetime") when calibrating $t_{\mathrm{e}\gamma}$ offset, which is discussed in Sect. 6.8.1.

6.2.7 Face factor to correct position dependence of light collection efficiency

The face factors give a uniform N_{sum} distribution by mitigating the position dependence of light collection efficiency as introduced in Sect. 4.1.5. The factors $F_{\mathrm{face},f=0\text{–}5}$ are expressed by a product of independent functions of each of u_γ, v_γ, or w_γ, that is,

$$F_{\mathrm{face},f}(u_\gamma, v_\gamma, w_\gamma) = F_{\mathrm{face},f}(u_\gamma) \times F_{\mathrm{face},f}(v_\gamma) \times F_{\mathrm{face},f}(w_\gamma). \tag{6.15}$$

The idea of the optimisation is to search for the best combination of $F_{\mathrm{face},0\text{–}5}$ so that the N_{sum} peak for monochromatic photons becomes narrowest for each position. It has the following steps:

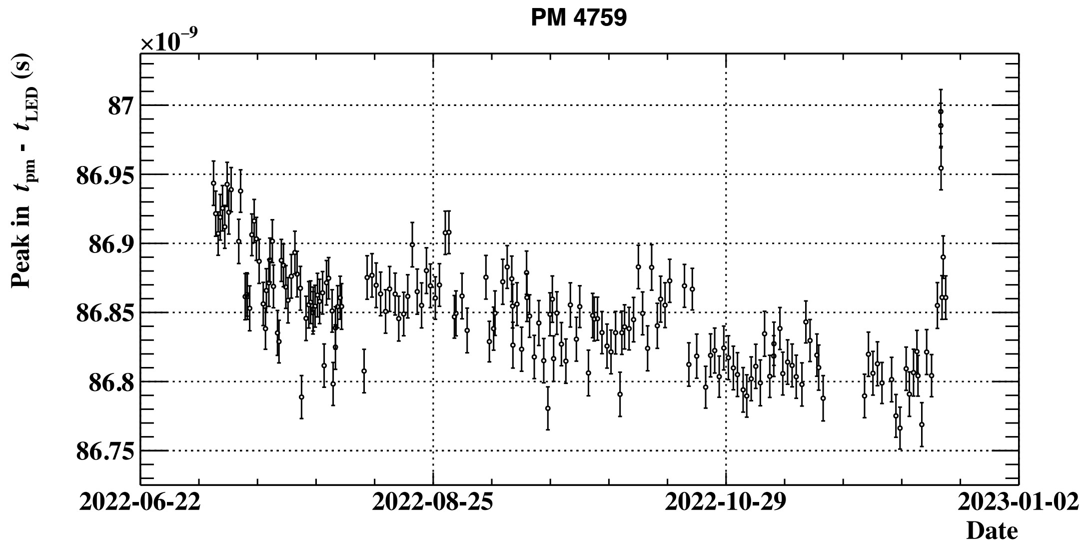

Figure 6.21: Temporal variation of the pulse time from the LED illumination signal during the run 2022.

(1) Calculate the combination in each segmented uv region,

(2) Model the best factors as a function of u or v with appropriate functions, $F_{\text{face},f}(u_\gamma)$ or $F_{\text{face},f}(v_\gamma)$, and

(3) Do the above procedures for w axis only for the inner face $F_{\text{face},0}(w_\gamma)$ with $F_{\text{face},f}(u_\gamma) \times F_{\text{face},f}(v_\gamma)$ fixed.

The face factors were optimised using 17.6 MeV photons for the run 2021 [59] and 54.9 MeV photons for the run 2022. The 54.9 MeV photons are optimal to calibrate the face factors because our interest is signal photons with 52.83 MeV. Reference [59], however, had to utilise the 17.6 MeV photons for the run 2021 since the full scan of the whole detector was not completed as discussed in Sect. 3.3.

The calculation in the first step requires a segmentation of the uv plane. The uv plane was segmented into 6×16. In each segment, I minimised a variance $\sigma^2_{N_\text{sum}}$ defined as

$$\sigma^2_{N_\text{sum}} = \left(N_\text{target} - \sum_{f=0}^{5} f_{\text{face},f} \times N_f \right)^2 , \tag{6.16}$$

where N_target is a peak N_sum value without the face factor; N_f is the summed number of photons detected in a face f; and $f_{\text{face},f}$ is "local" face factors (i.e. weights on the face in a segment), which are floating parameters. Note that the local face factors $f_{\text{face},f}$ are not required to be described as a functional form. Figure 6.22 shows local face factors calculated with the 54.9 MeV photons in a uv plane. The factors on lateral faces tend to be greater when the photon position is close to the face; for instance, a greater factor on the top face is required when a photon comes near the top face.

I then modelled and parametrised the local face factors in Fig. 6.22. The purposes are not only for the response to be smooth over the acceptance and to avoid the unstable factors, but also to avoid overfitting by training on a specific sample. The fit functions are defined as in Table 6.2 for each year. Figure 6.23 shows the face factors $F_{\text{face},f}$ in a uv plane. They reasonably represent the trends in Fig. 6.22.

Finally, the inner face factor as a function of w, $F_{\text{face},0}(w)$, is introduced only for the run 2022. The w axis in the range between 0.1 cm and 20 cm was logarithmically segmented into 12. The

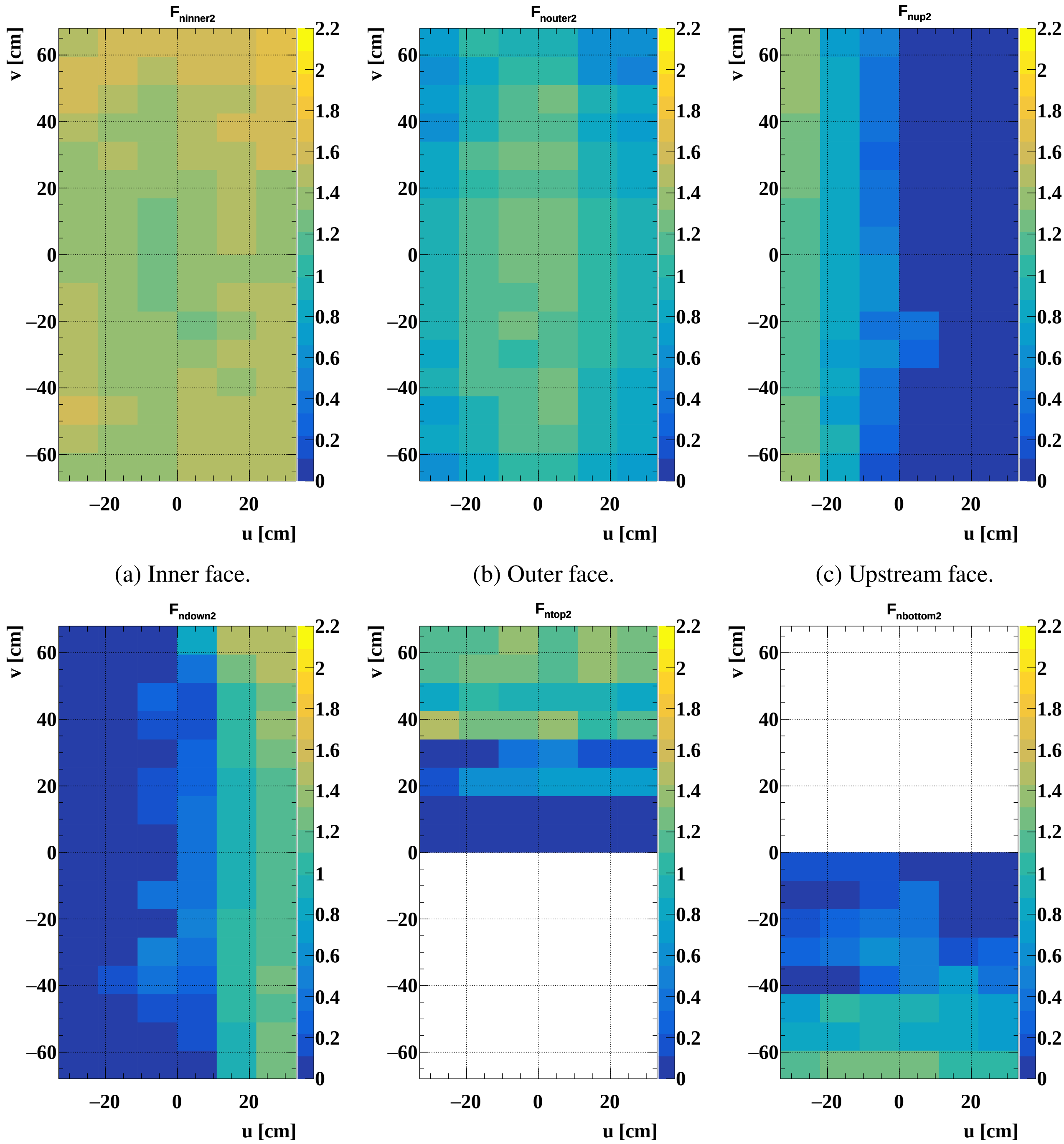

(a) Inner face. (b) Outer face. (c) Upstream face.

(d) Downstream face. (e) Top face. (f) Bottom face.

Figure 6.22: Local face factors in a uv plane calculated with the 54.9 MeV photons taken in 2022. The factors on the top and bottom faces are set to zero where the photon position is far from the faces ($v < 0$ cm for the top face and $v > 0$ cm for the bottom face). The factors for the run 2021 are available in Fig. 7.3 of Ref. [59].

Table 6.2: Fit functions of face factors. $c_{f,i}$ is coefficients for a face f.

Face factor	2021	2022
$F_{\text{face},0}(u) \cdot F_{\text{face},0}(v)$	$(c_{0,0} + c_{0,1}u^2) \cdot (c_{0,2} + c_{0,3}v^2)$	$c_{0,0} + c_{0,1} \cos(c_{0,2}v)$
$F_{\text{face},1}(u) \cdot F_{\text{face},1}(v)$	$(c_{1,0} + c_{1,1}u^2) \cdot (c_{1,2} + c_{1,3}v^2)$	$(c_{1,0} + c_{1,1}u^2) \cdot (c_{1,2} + c_{1,3}v^2)$
$F_{\text{face},2}(u) = -F_{\text{face},3}(u)$	$c_{2,0} + c_{2,1}u$	$c_{2,0} + c_{2,1}u$
$F_{\text{face},4}(v) = -F_{\text{face},5}(v)$	$c_{4,0} + c_{4,1}v$	$c_{4,0} + c_{4,1}v$

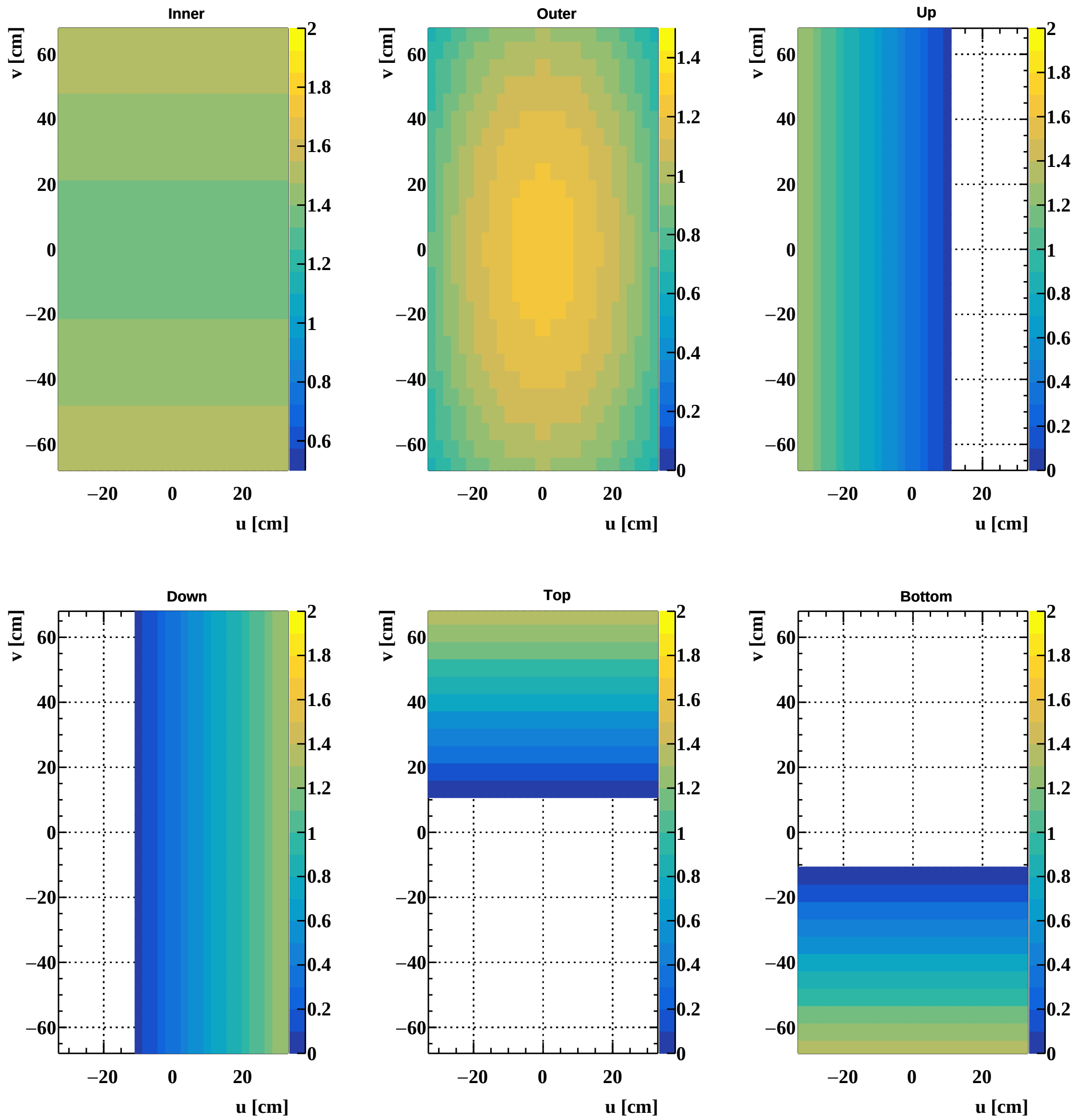

Figure 6.23: Face factors used for Eq. (4.10) for the run 2022. The factors on the top and bottom faces are set to zero where the photon position is far from the faces ($v \lesssim 10$ cm for the top face and $v \gtrsim -10$ cm for the bottom face). The factors for the run 2021 are available in Fig. 7.4 of Ref. [59].

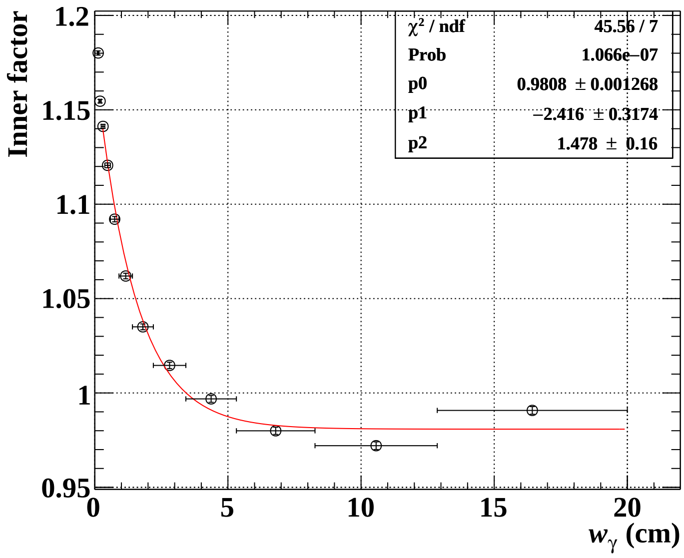

Figure 6.24: Inner face factor as a function of w. A red function is an exponential fitting function with parametrisation defined as Eq. (6.17).

minimisation in Eq. (6.16) was performed with the face factors in a uv plane, $F_{\text{face},f}(u, v)$, fixed. Figure 6.24 shows the best inner face factor as a function of w. The best factors are parametrised with the fit function defined as

$$F_{\text{face},0}(w) = c_{0,4} + \exp\left(-\frac{w - c_{0,5}}{c_{0,6}}\right). \tag{6.17}$$

6.2.8 Inner excess factor to correct temporal dependence of MPPC and PMT response difference

As discussed in Sect. 4.1.5, the temporal evolution of the MPPC and PMT response difference is corrected by the IEF $F_{\text{IE}}(t)$. Overall MPPC (PMT) response was monitored by the weighted summed number of scintillation photons $N_{\text{MPPC(PMT)}}$. Peaks in the $N_{\text{MPPC(PMT)}}$ distribution for monochromatic photons with energies of 17.6 MeV and 54.9 MeV and cosmic-ray muons give the response difference by taking the ratio of N_{MPPC} to N_{PMT}.

Peak extraction

The peak extraction requires the correction of a conversion depth dependence for photon events since $N_{\text{MPPC(PMT)}}$ is larger (smaller) as the depth is closer to the inner face. Figure 6.25 shows the depth dependence of $N_{\text{MPPC(PMT)}}$ for 17.6 MeV photons and the correction function. The position dependence not only in depth but also in u was observed during the run 2022. This was also corrected for the run 2022.

17.6 MeV **photons** Figure 6.26 shows $N_{\text{MPPC(PMT)}}$ distribution for 17.6 MeV photons, described in Sect. 2.4.4, after applying the position dependence correction. The distribution around the peak was fitted with a Gaussian function. The best-fit mean of the Gaussian function represents the $N_{\text{MPPC(PMT)}}$ peak value at a set of daily calibration runs. Figure 6.28 shows the temporal evolutions during the run 2022 of the N_{MPPC}, N_{PMT}, and $N_{\text{MPPC}}/N_{\text{PMT}}$ for 17.6 MeV photons, moving-averaged by three dots to

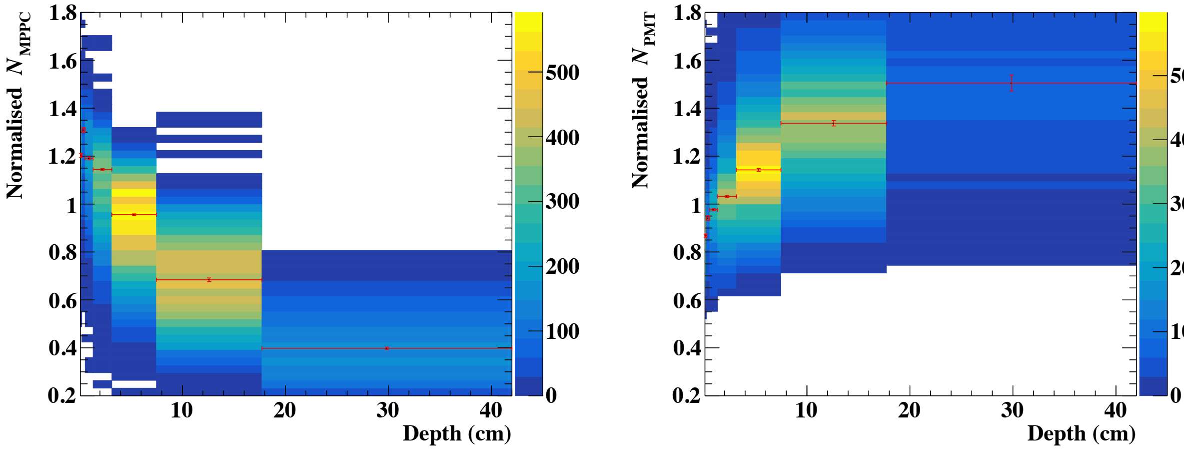

(a) MPPC.

(b) PMT.

Figure 6.25: Depth dependence of (a) N_{MPPC} and (b) N_{PMT} for 17.6 MeV photons.

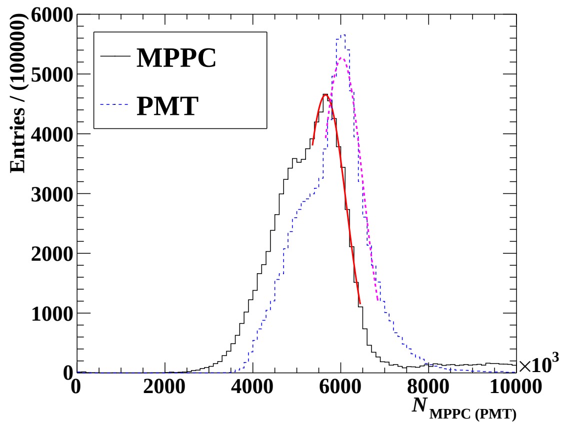

Figure 6.26: N_{MPPC} and N_{PMT} distributions for 17.6 MeV photons. Position dependence in the u and depth directions is corrected. The peak is fitted with a Gaussian function drawn in red and magenta.

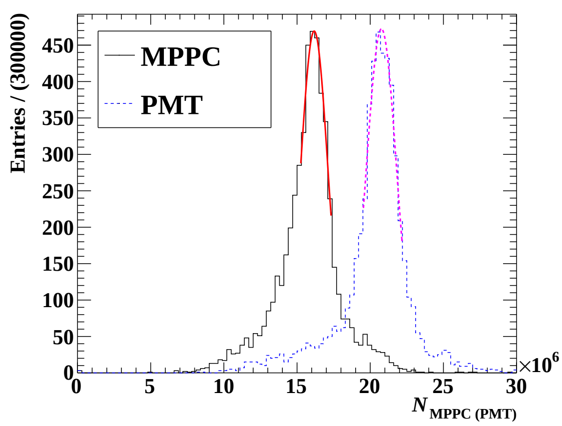

Figure 6.27: N_{MPPC} and N_{PMT} distributions for 54.9 MeV photons. Position dependence in the u and depth directions is corrected. The peak is fitted with a Gaussian function drawn in red and magenta.

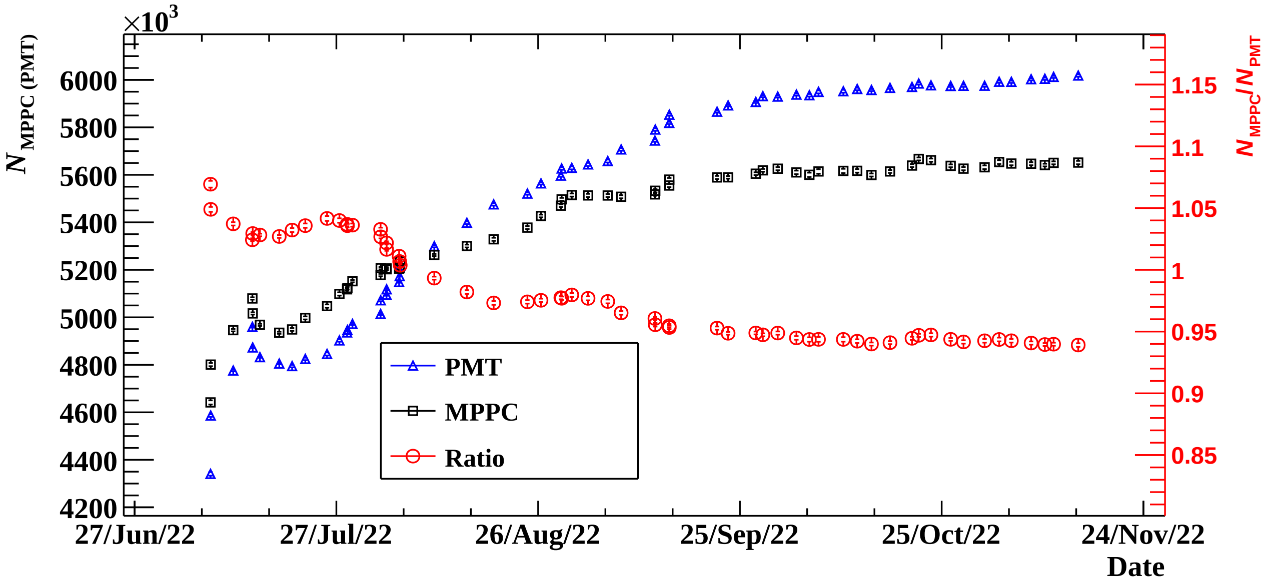

Figure 6.28: The temporal evolution of N_{MPPC} (black), N_{PMT} (blue), and $N_{\mathrm{MPPC}}/N_{\mathrm{PMT}}$ (red) for 17.6 MeV photons during the run 2022. Both N_{MPPC} and N_{PMT} increased over time, thanks to gaseous purification in parallel with the run.

suppress a statistical uncertainty on the peak extraction. Both N_{MPPC} and N_{PMT} increased over time due to the xenon purity recovery, discussed in Sect. 3.1. The different increase speeds of N_{MPPC} and N_{PMT} are discussed later.

54.9 MeV **photons** The N_{MPPC} and N_{PMT} peaks were also monitored by 54.9 MeV photons from $\pi^0 \rightarrow \gamma\gamma$, decribed in Sect. 2.4.4, taken in π^0 calibration runs. One can select events where approximately 54.9 MeV photons impinge on the LXe detector by imposing the following cuts:

- The number of detected pulses is one in the BGO crystals in order to avoid pileup events,
- Central four BGO crystals have the maximum energy deposit in all the crystals in order to minimise the energy loss in the BGO crystals due to a shower leakage,
- Energy measured by the BGO crystals is [65 MeV, 90 MeV],
- Time coincidence of 10 ns,
- The opening angle of two photons $\Theta_{\gamma\gamma}$ is wider than 170°, and
- Pileup event category is *NoPileup* or *Unfolded*.

The N_{MPPC} and N_{PMT} peak extraction requires the conversion depth correction as done for 17.6 MeV photons. Figure 6.27 shows the $N_{\mathrm{MPPC(PMT)}}$ distribution for 54.9 MeV after applying the position dependence correction.

Cosmic-ray muons Those peaks were also monitored by cosmic rays passing through the detector. The energy deposit is distributed in a Landau distribution by selecting a particular path length as shown in Fig. 6.29 because most cosmic rays pass through the detector. I selected cosmic-ray events in which it goes into the outer (inner) face and out from the inner (outer) face, with the criteria of

- $N_{\mathrm{inner}}/N_{\mathrm{outer}} < 1.6(1.0)$ for the run 2021 (2022), where $N_{\mathrm{inner(outer)}}$ is the weighted sum of scintillation photons detected on the inner (outer) face, and

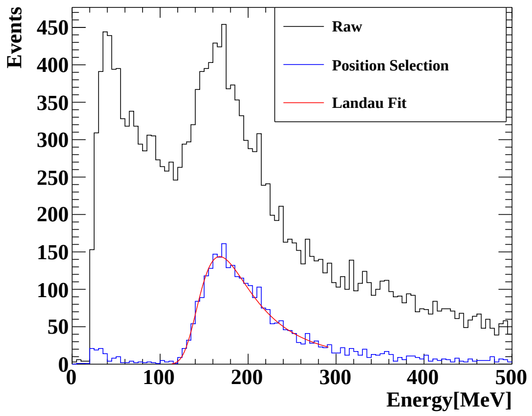

Figure 6.29: Energy spectra for the cosmic-ray muons with (blue) and without (black) event selection [59]. A red line is a Landau function fitted to the spectrum.

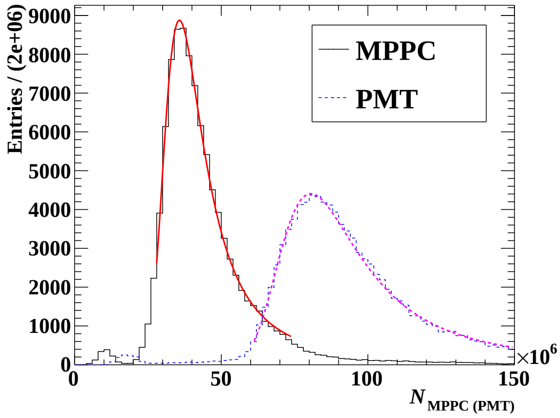

Figure 6.30: N_{MPPC} and N_{PMT} distributions for cosmic-ray muons. The peak is fitted with a Landau function convoluted with a Gaussian function drawn in red and magenta.

- Volume cut ($|u| < 20\,\mathrm{cm}$ and $|v| < 60\,\mathrm{cm}$ and $w < 10\,\mathrm{cm}$).

By imposing these selections, the typical path length of the cosmic rays would be the detector's depth. The $N_{\mathrm{MPPC(PMT)}}$ distributions of the selected events are fitted with a Landau function convoluted with a Gaussian function to take the detector response into account, as shown in Fig. 6.30. The most probable value (MPV) of the Landau function represents the peak value of the $N_{\mathrm{MPPC(PMT)}}$ distribution.

Building correction function $F_{\mathrm{IE}}(t)$

Figure 6.31 shows the temporal evolutions of $N_{\mathrm{MPPC}}/N_{\mathrm{PMT}}$ for 17.6 MeV and 54.9 MeV photons, and cosmic-ray muons during the runs 2021 and 2022. In 2021, the increasing trend can be interpreted to be due to effects on visible light that were not absorbed in the gain calibration, for instance, a difference in PDE and QE for visible light and VUV light. It is, however, not fully understood.

On the other hand, in the run 2022, I observed a descending trend for 17.6 MeV photons, despite a constant one within 5 % for cosmic-ray muons. This descending trend for 17.6 MeV photons came from a larger increase in N_{PMT} than N_{MPPC} (Fig. 6.28). Let me discuss a difference in the scintillation light distribution between the EM shower from photons and cosmic-ray muons, illustrated in Fig. 6.32. Since the scintillation light originating from photons is distributed near the inner face, the light propagates to the PMTs with a longer distance than that to the MPPCs. At the beginning of the run 2022, when the LXe purity was low, the scintillation light was absorbed and less detected by PMTs. On the other hand, the scintillation light from cosmic-ray muons is emitted along their path, and the absorption has a smaller effect on N_{PMT}. Since the scintillation light distribution from signal photons is similar to that from 17.6 MeV photons, constructing correction function $F_{\mathrm{IE}}(t)$ relied on the response to the 17.6 MeV photons.

6.2.9 Light yield and energy scale

The last calibration for the photon energy reconstruction with the LXe detector is the energy scale: a correction function of the temporal variation $T(t)$, a correction function of the position dependence $U(u_\gamma, v_\gamma, w_\gamma; t)$, and a conversion factor S_{E_γ}, in Eq. (4.8). This subsection introduces energy scale

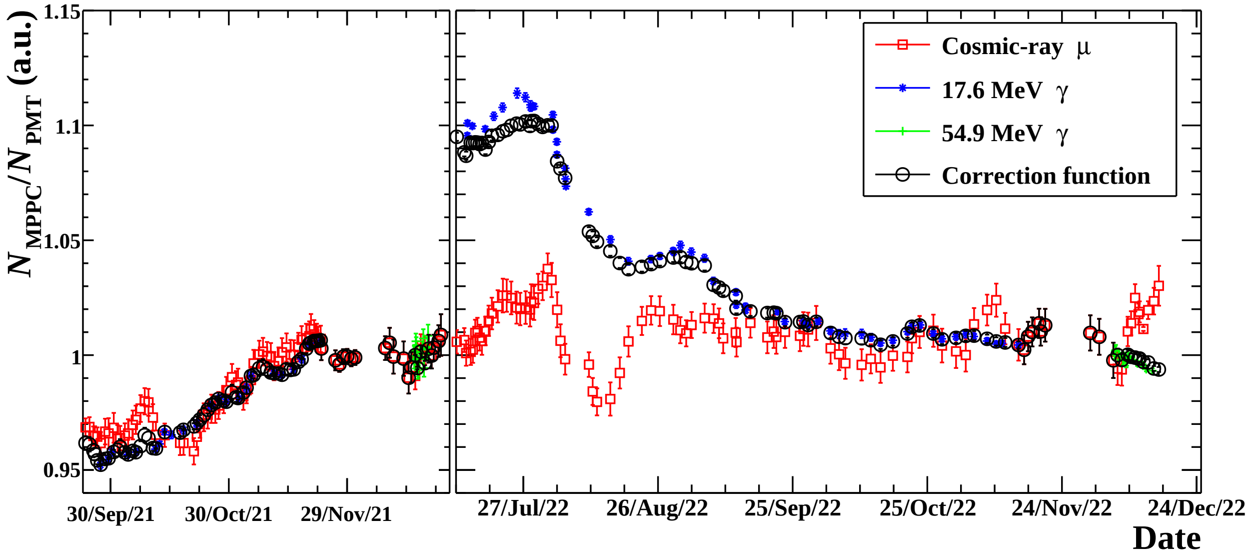

Figure 6.31: The temporal evolution of a ratio $N_{\mathrm{MPPC}}/N_{\mathrm{PMT}}$ for 17.6 MeV and 54.9 MeV photons, and cosmic-ray muons. Black dots and lines show a combination of three histories and are utilised as the correction function for Eq. (4.9).

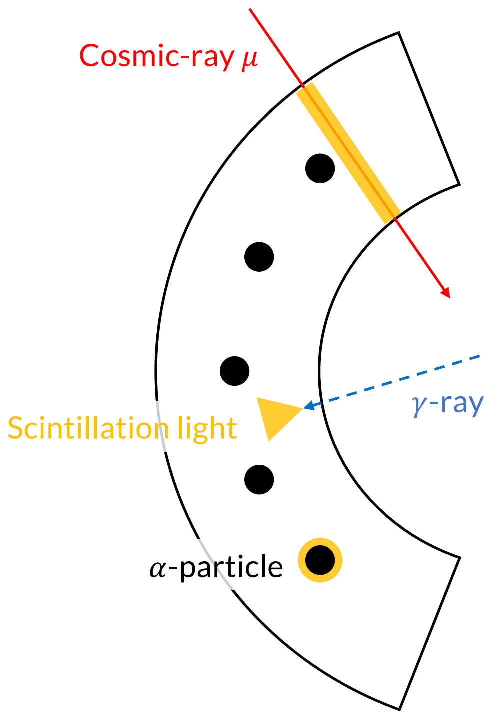

Figure 6.32: Scheme of scintillation light emission from α particles, photons, and cosmic-ray muons. Scintillation light from γ rays is emitted around EM showers, while that from cosmic rays is emitted along their path. The difference results in a different ratio of N_{MPPC} to N_{PMT} between photons and cosmic rays.

Table 6.3: Fitting functions for peak extraction.

Dataset	Fitting function
9 MeV photons	A single Gaussian
17.6 MeV photons	Double Gaussian cooresponding to 14.6 MeV and 17.6 MeV peaks
54.9 MeV photons	A Gaussian-exponential (*ExpGaus*) function defined as Eq. (6.19)
Cosmic-ray muons	A Landau function convoluted with a Gaussian

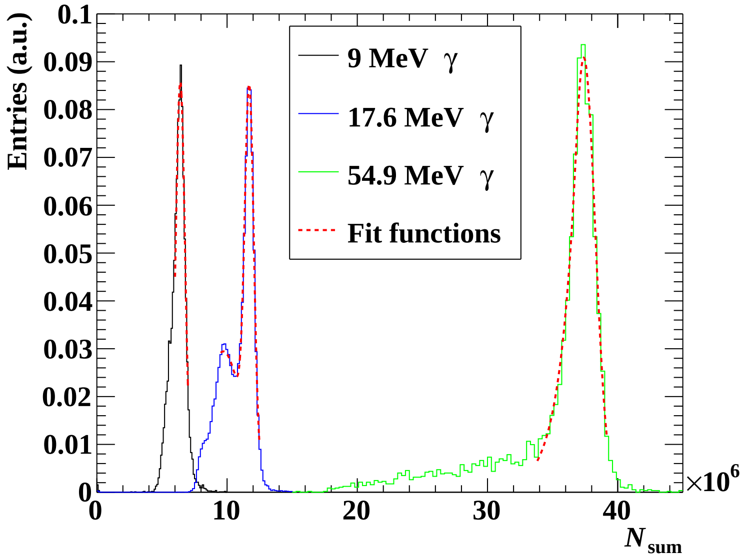

Figure 6.33: N_{sum} distributions for monochromatic photons. Red dotted lines show the fitting function.

estimation methods at first, and then describes the construction of the correction functions T and U and the conversion factor S_{E_γ}.

The correction function of the non-uniformity of the energy scale U is composed of one-dimensional corrections G, a two-dimensional correction M standing for finer correction than one-dimensional ones, a depth dependence correction depending on uv position D, and an additional two-dimensional correction A:

$$U(u_\gamma, v_\gamma, w_\gamma; t) = G(u_\gamma; t) \cdot G(v_\gamma; t) \cdot G(w_\gamma; t) \cdot M(u_\gamma, v_\gamma) \cdot D(w_\gamma | u_\gamma, v_\gamma) \cdot A(u_\gamma, v_\gamma). \quad (6.18)$$

Here, one-dimensional corrections G depend on time to take the temporal evolution of the absorption length into account. The additional two-dimensional correction A has rougher detector volume segmentation but finer temporal segmentation than M, additionally using a background photon sample.

Energy scale estimation methods

Let me introduce methods to estimate the energy scale from each dataset before discussing the correction function construction. Monochromatic photons and cosmic-ray muons give the energy scale by extracting peak values of the N_{sum} distribution. The functions tabulated in Table 6.3 are fitted to the distributions. Figure 6.33 shows the N_{sum} distributions and the best-fit functions for monochromatic photons. In addition to the monochromatic photons, the background photon spectrum can be used to estimate the energy scale.

9 MeV **photons** Photons emitted from a thermal neutron reaction (Sect. 2.4.4) have an energy of 9 MeV. This peak is fitted with a single Gaussian function. The best-fit mean gives the energy peak.

17.6 MeV **photons** The energy peaks at 14.6 MeV and 17.6 MeV are fitted with a double Gaussian function. The best-fit mean for the 17.6 MeV peak gives the energy peak.

54.9 MeV **photons** The quasi-monochromatic photons at 54.9 MeV are selected by imposing the criteria described in Sect. 6.2.8. The observed energy spectrum is fitted by a so-called *ExpGaus* function [106], a Gaussian function connected with an exponential low-energy tail, defined as

$$f(x) = \begin{cases} A \exp\left[-\dfrac{\left(x - \mu_{E_\gamma}\right)^2}{2\sigma_{E_\gamma}^2}\right] & \text{if } x > \mu_{E_\gamma} + \tau, \\ A \exp\left[\dfrac{\tau\left(\tau/2 - x + \mu_{E_\gamma}\right)}{\sigma_{E_\gamma}^2}\right] & \text{if } x \leq \mu_{E_\gamma} + \tau, \end{cases} \tag{6.19}$$

where A, μ_{E_γ}, and σ_{E_γ} are amplitude, mean, and sigma parameters in a Gaussian function, respectively; and τ is a transition parameter characterising energy leaks from a calorimeter. The best-fit mean μ_{E_γ} gives the energy peak.

Cosmic-ray muons As discussed in Sect. 6.2.8, I selected cosmic-ray muons passing through the inner and outer faces. The deposited energy is fitted by a Landau function convoluted with a Gaussian function. The MPV of the function gives the energy peak.

Background photon spectrum fit One can estimate the energy scale with background photons by comparing the observed energy spectrum with the simulated one. The background spectrum is modelled as

$$[(\mathcal{F}_{\mathrm{sim}} \otimes \mathcal{G}_{\mathrm{additional}}) + r_{\mathrm{CR}} \cdot \mathcal{F}_{\mathrm{CR}}] \times \mathcal{A}_{\mathrm{TRG}}, \tag{6.20}$$

where $\mathcal{F}_{\mathrm{sim}}$ is the spectrum of reconstructed energy in background simulations; $\mathcal{G}_{\mathrm{additional}}$ is a Gaussian term to additionally smear it; $\mathcal{F}_{\mathrm{CR}}$ is a cosmic-ray spectrum measured without a beam renormalised by the r_{CR} factor; and $\mathcal{A}_{\mathrm{TRG}}$ is an acceptance function to represent the E_γ trigger threshold window. As the reconstructed spectrum on the simulation samples is used for the $\mathcal{F}_{\mathrm{sim}}$ term in Eq. (6.20), the effect of shower leakage and so on is already included. The additional Gaussian smearing is, thus, intended to account for the resolution difference between the data and the simulation.

The background spectrum introduces the cosmic-ray component to describe the non-negligible contribution in the high E_γ region, where the photon contribution is vanishing. Figure 6.34 shows the observed spectrum and the best-fit polynomial function. Here, it has a sharp event loss in 50–55 MeV, which makes the polynomial ill-representing in $E_\gamma \lesssim 55$ MeV region. This is understood to be due to electrons into which cosmic-ray muons decay in or near the detector.

The trigger acceptance function is represented as a product of two error functions, one for a low energy threshold around 44 MeV and the other for a high energy threshold around 90 MeV. The shape of the trigger window is based on an evaluation with E_γ trigger data. This is then further corrected for the low E_γ side, which gets impact from the data pre-selection, which dropped $E_\gamma < 44$ MeV reconstructed events before the final calibration became ready.

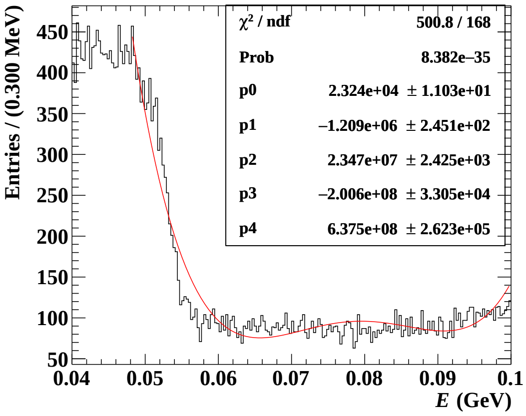

Figure 6.34: Cosmic-ray spectrum in the range from 40 MeV to 100 MeV.

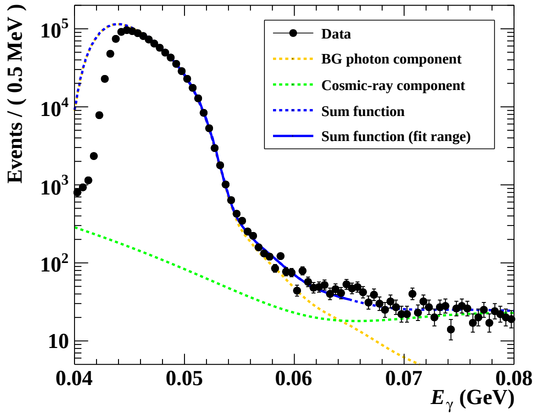

Figure 6.35: Fit of background spectrum in time sideband. Black points show the data; orange, green, and blue curves show the simulated spectrum with a Gaussian smearing, measured cosmic-ray spectrum, and the best-fit summed spectrum of orange and blue spectra.

The background spectrum in the physics data in the wide time side-bands, defined as $1\,\mathrm{ns} < |t_{e\gamma}| < 10\,\mathrm{ns}$[2], is finally fitted to estimate the energy scale parameter and the other parameters. A cosmic-ray spectrum renormalisation factor r_{CR} is estimated by counting events in the range of 70 MeV to 90 MeV, where the cosmic-ray events dominate. The estimated factor and uncertainty are given to the spectrum fitting with a Gaussian constraint. The low trigger threshold parameters are also constrained with a Gaussian distribution based on the dedicated fitting described above. Figure 6.35 shows the background spectrum and the best-fit model spectrum, in which the fit range is 48 MeV to 65 MeV.

This method requires a certain calibration level to reliably estimate the energy scale and the additional smearing parameter. Thus, the energy scale estimated from the background spectrum is used to refine the correction functions.

Temporal evolution correction T

There are the following two steps to build the correction function T:

(1) Trace light yield emitted from α particles, monochromatic photons with energies of 9 MeV, 17.6 MeV and 54.9 MeV, and cosmic-ray muons.

(2) Finely calibrate the temporal evolution using the energy scale estimated by fitting the photon background spectrum.

In both steps, I applied one-dimensional non-uniformity correction G, which is discussed later, in order to better extract a peak for the monochromatic energies and estimate the energy scale.

Light yield calibration Figure 6.36 shows the temporal evolution of the peak position in the N_{sum} distribution and of the $\langle N^{\mathrm{data}}_{\mathrm{phe},i}\rangle / \langle N^{\mathrm{MC}}_{\mathrm{pho},i}\rangle$ in Eq. (6.12) averaged for PMTs for α particles. At the

[2] Time side-bands for the analysis to search for $\mu \to e\gamma$ is again defined in Sect. 8.1.

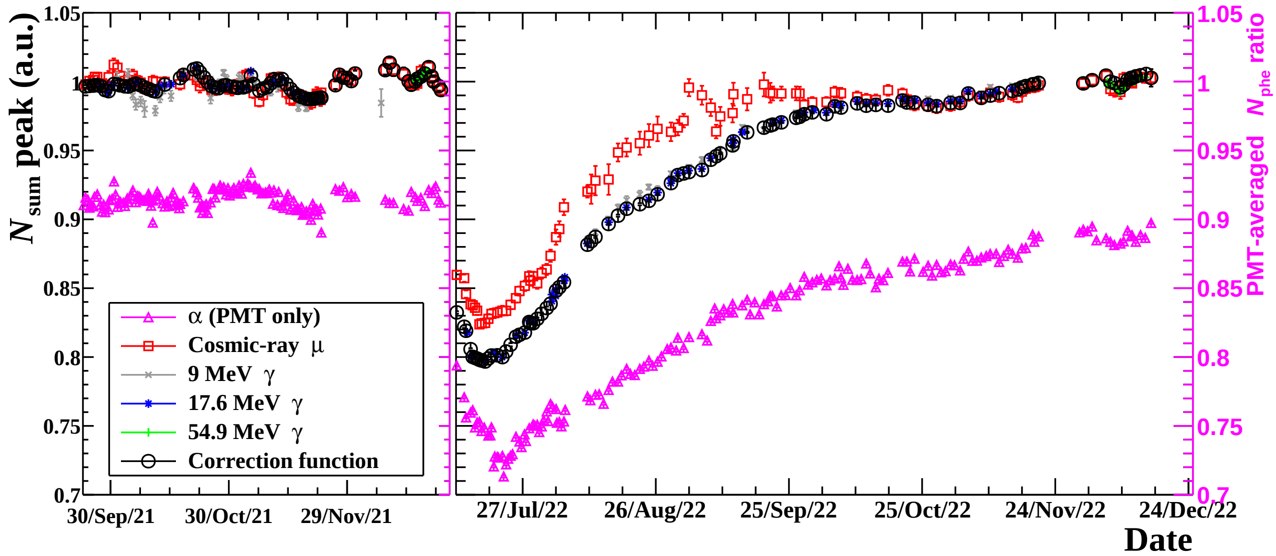

Figure 6.36: Temporal evolution of light yield traced by N_{sum} peaks. Black dots and lines show a combination of four histories and are utilised as the correction function for Eq. (4.8).

beginning of the run 2022, the light yield was about 20 % lower than that at the end of the run 2021 and increased over time thanks to the Xe purification discussed in Sect. 3.1. The first-step correction function T was built using the light yield monitored by photons and cosmic-ray muons. Here, the light yield history monitored by α particles is not utilised because the scintillation light emission process differs from that of photons. In addition to the α particles, the history monitored by cosmic-ray muons is not utilised for the first three months of the run 2022 because the light yield recovery speed looked faster than that of photons. This speed difference came from the difference in the scintillation light distribution, as illustrated in Fig. 6.32. The black dots in Fig. 6.36 are utilised as the correction function $T(t)$.

Fine calibration with background spectra To trace the temporal variation, the physics data in the wide time side-bands were grouped every 10^5 event. The E_γ-trigger data were divided into several periods because the threshold changed over time, and it would affect the fitting. Given the statistics, the E_γ-trigger data taken in 2021 (2022) were divided into five (twelve) samples. The cosmic-ray spectra were obtained yearly from the daily calibration without a beam. The spectrum fit provided the best-fit energy scale parameter, and its temporal variation was utilised to finely build the correction function T.

Figure 6.37 shows the temporal variation of the energy scale and the resolution after calibration with the non-uniformity correction U discussed below. The standard deviation of the energy scale distribution projected onto the y axis of the top plots in Fig. 6.37 provides the variation, which becomes a source of the uncertainty on the energy scale. The standard deviation for the 17.6 MeV (background) photons was calculated as 0.16 % (0.32 %) in 2021 and 0.13 % (0.25 %) in 2022. The other systematic of the energy scale comes from the statistical uncertainty on the Landau peak extraction for cosmic-ray muons, which plays an essential role in connecting the energy scale between the physics and π^0 calibration runs. It was assessed to be 0.11 % in 2021 and 0.14 % in 2022. The resolution stability is thanks to the non-uniformity correction described below.

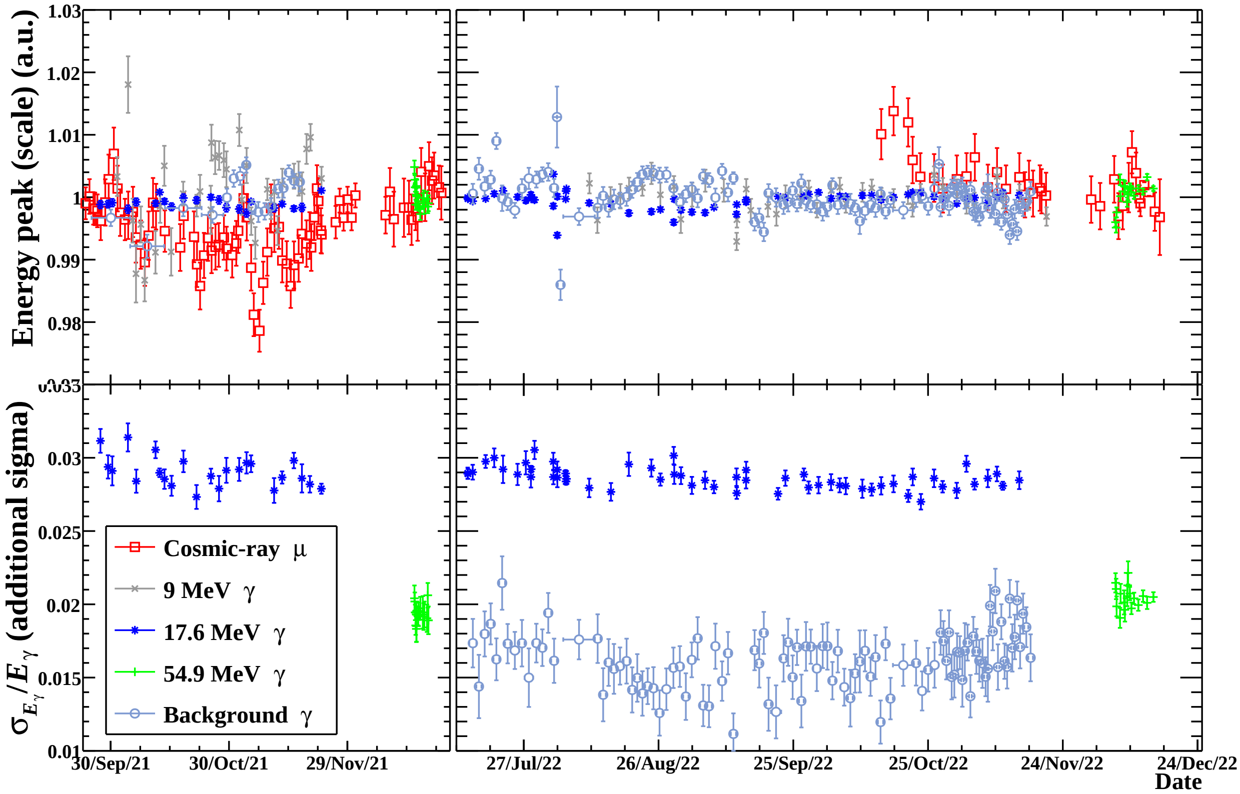

Figure 6.37: Temporal variation of the energy scale (top) and the resolution (bottom) during the runs 2021 and 2022 after calibration. The non-uniformity correction U, which is discussed later, is also applied. The y axis of the top plots is the peak position in the energy distribution for monochromatic photons and cosmic-ray muons or the best-fit energy scale parameter in the spectrum fit for background photons. The y axis of the bottom ones is the resolution or the additional sigma parameter in Eq. (6.20).

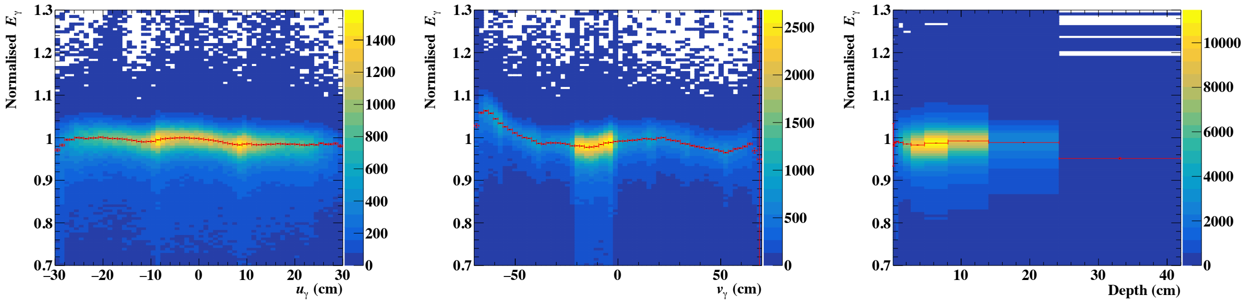

(a) u. (b) v. (c) Depth.

Figure 6.38: E_γ dependence on photon conversion position for 54.9 MeV photons in 2022. Red histograms stand for the global corrections G.

Non-uniformity correction U

The non-uniformity correction $U(u_\gamma, v_\gamma, w_\gamma; t)$ in Eq. (6.18) is built in the following steps:

(1) One-dimensional corrections G using 54.9 MeV photons,
(2) The temporal variation of the one-dimensional corrections $G(t)$ using 17.6 MeV photons,
(3) A two-dimensional correction $M(u_\gamma, v_\gamma)$ using 17.6 MeV and 54.9 MeV photons,
(4) An uv-position-dependent depth correction $D(w_\gamma|u_\gamma, v_\gamma)$ using 54.9 MeV photons, and
(5) An additional two-dimensional correction $A(u_\gamma, v_\gamma)$ using the background photon spectrum.

The calibration of the temporal evolution of the light yield and the energy scale $T(t)$ is applied to build the non-uniformity correction[3].

One-dimensional corrections G The first step of the non-uniformity correction construction is to build the one-dimensional corrections G using 54.9 MeV photons. Although the face factors F_{face} are introduced, the non-uniformity remains in the energy scale. Figure 6.38 show the position dependence of E_γ for 54.9 MeV photons measured during the π^0 calibration run 2022. To correct the non-uniformity, the peak energy is extracted for each sliced sub-position, illustrated as red dots in Fig. 6.38.

Temporal-dependent one-dimensional corrections G The temporal variation of the position dependence was observed during the run 2022, in which higher energy was reconstructed near the edges of the LXe detector than in the central region at the beginning of the run. This was mainly because the lower IEF F_{IE} at the beginning of the run 2022 (a reciprocal of the black function in Fig. 6.31), meaning smaller N_{MPPC}, resulted in a more significant contribution to summing $N_{\mathrm{pho},i}$ up from lateral faces. The temporal variation was calibrated for each axis (u, v, depth) independently, using the 17.6 MeV photons.

The peak energy for the 17.6 MeV photons was estimated by the position sub-ranges, as done for the 54.9 MeV photons (Fig. 6.38). It is known that the response to the 52.8 MeV signal photons is more similar to that to the 54.9 MeV ones than the 17.6 MeV ones because the EM shower development depends on the photon energy. In order to avoid miscalibrating the non-uniformity by using the

[3] A technical comment is left: the first and second steps to build G and the construction of T are iterated in a few times.

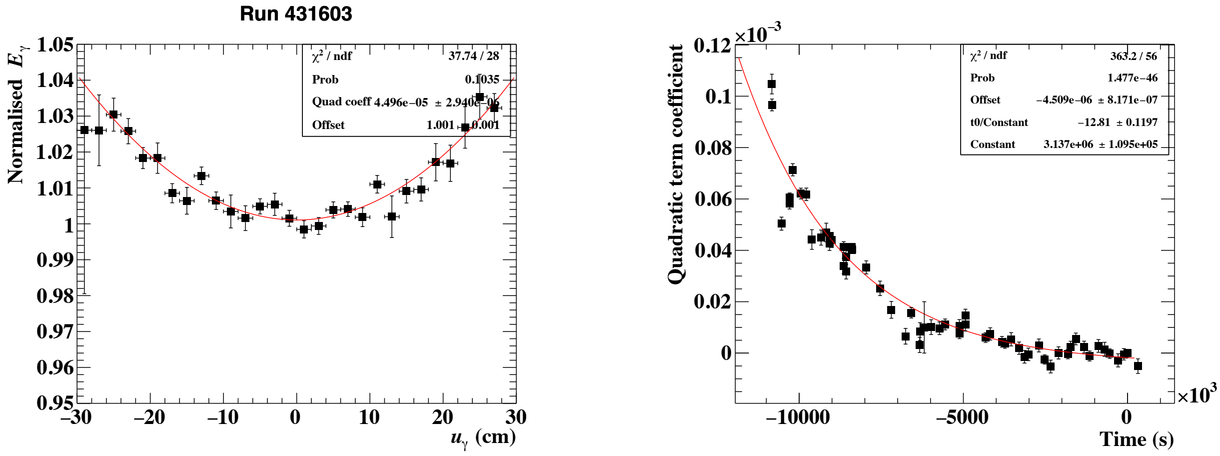

(a) E_γ at a set of calibration runs with respect to that at the reference set as a function of u.

(b) History of a coefficient of the quadratic term.

Figure 6.39: Temporal evolution of the energy scale dependence on the u axis.

17.6 MeV photons, the observed position dependence was normalised by the reference one, i.e. the position dependence measured with the reference set of 17.6 MeV photons. Here, let me clarify that the "normalisation" was applied position dependently: The position-dependent energy scale of the calibration set of interest was estimated after slicing the calibration data into different position sub-ranges, which was then divided by the energy scale of the reference set in the same position sub-range. Figure 6.39a shows the u_γ dependence of the E_γ ratio.

The dependence on u_γ was parametrised by a quadratic function expressed by

$$p_0 u^2 + p_1 \tag{6.21}$$

where parameters $p_{0,1}$ are the coefficients of the quadratic term and the offset, respectively. The coefficient of the quadratic term p_0 represents the position dependence, which contains the temporal evolution, as shown in Fig. 6.39b. The temporal evolution is parametrised as an exponential function,

$$p_0(t) = \exp\left(-\frac{t - t_0}{\tau}\right) + p_{0,0}, \tag{6.22}$$

where t_0, τ, and $p_{0,0}$ are a time offset, a time constant, and the coefficient at the infinite time, respectively. Finally, the temporal-dependent position dependence modified the one-dimensional corrections G; that is,

$$G(u_\gamma; t) = (p_0(t)u^2 + p_1) \cdot G(u_\gamma). \tag{6.23}$$

The above procedure was also applied to the v and depth axes. The only difference for the depth dependence was the functional model representing the position dependence on the E_γ ratio, which was a logarithmic function instead of a quadratic function of Eq. (6.21):

$$p_0(t) \log_{10}(w_\gamma) + p_1. \tag{6.24}$$

Two-dimensional correction M One-dimensional corrections G were not enough to correct the observed non-uniformity. To correct the remaining non-uniformity, a two-dimensional correction $M(u_\gamma, v_\gamma)$ was built based on a combination of the 17.6 MeV and 54.9 MeV photons. I segmented the uv plane of the detector into 12×32 and calculated the E_γ peak in each segment. Figure 6.40 shows the uv position dependence of the energy scale during the run 2022 by applying the temporal

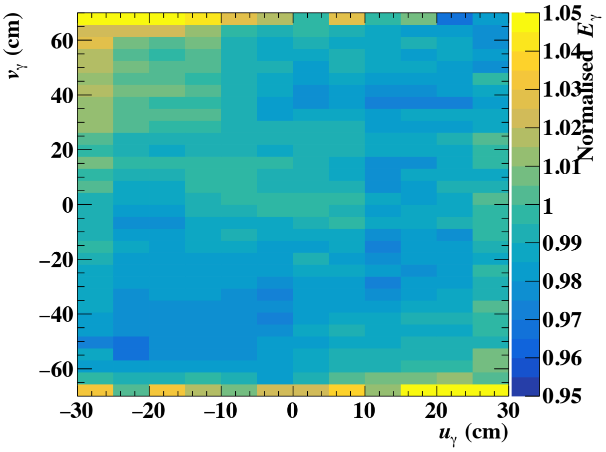

(a) 17.6 MeV photons.

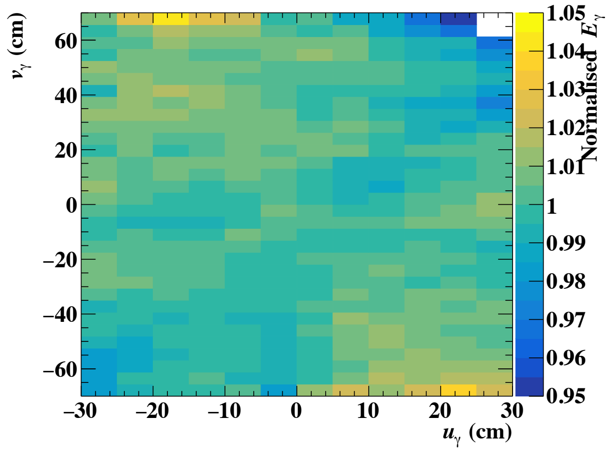

(b) 55 MeV photons.

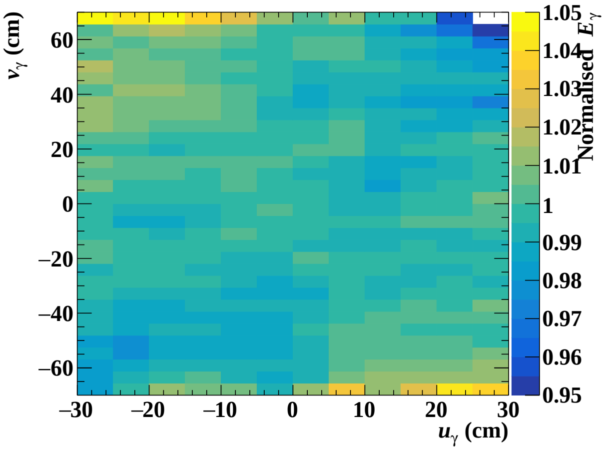

(c) Combined.

Figure 6.40: uv position dependence of the energy scale during the last physics run period of the run 2022.

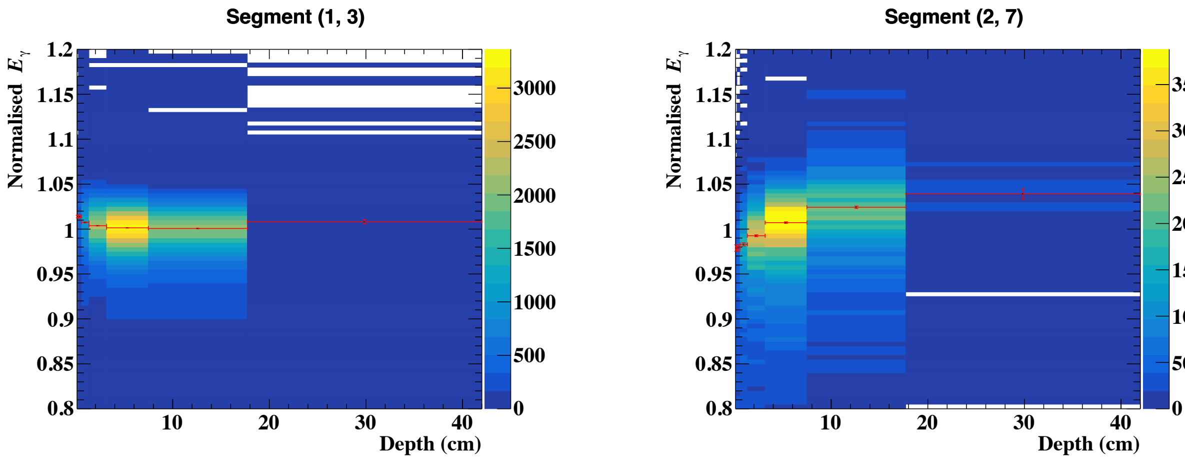

(a) A central segment.

(b) A segment at the edge.

Figure 6.41: Depth dependences of E_γ in (a) a central region ($-10\,\mathrm{cm} < u_\gamma < 10\,\mathrm{cm}$ and $-17.5\,\mathrm{cm} < v_\gamma < 0\,\mathrm{cm}$) and (b) an edge region ($10\,\mathrm{cm} < u_\gamma < 30\,\mathrm{cm}$ and $52.5\,\mathrm{cm} < v_\gamma < 70\,\mathrm{cm}$). The red histograms show the depth correction D.

variation correction T and the one-dimensional non-uniformity correction G. The different trends in the non-uniformity between the 17.6 MeV and 54.9 MeV photons are interpreted as the temporal variation of the position dependence and as the energy dependence on an EM shower development. In order to cope with the temporal variation of the non-uniformity, four different corrections were built for the run 2022, depending on periods, while only one correction was for the run 2021 (Fig. 6.43). Those which were made from 17.6 MeV and 54.9 MeV photons were combined by taking a weighted average, being used as the correction M, as shown in Fig. 6.40c. As discussed in Sect. 3.3, the scanning of the LXe detector volume was not completed in the π^0 calibration run 2021. Only the 17.6 MeV photons were, thus, used to build the correction M in the segments where there were insufficient statistics of 54.9 MeV photons.

uv-dependent depth dependence correction D It was observed that the depth dependences of the energy scale differed in the uv position. Since the one-dimensional depth dependence correction $G(w_\gamma)$ was made by averaging the measured dependence in a whole region and applied for the entire region, the non-uniformity remains after applying $G(w_\gamma)$. Therefore, uv-position-dependent correction of the depth dependence D was built with 54.9 MeV photons and applied. Because the conversion depth distribution and the energy scale dependence on depth depend on photon energy E_γ, 54.9 MeV photons were chosen to build the correction D. The uv plane was segmented into 3×8, and the depth dependence of reconstructed energy was computed in each segment. Figure 6.41 shows the depth dependence of E_γ in the central and edge segments after applying the temporal variation correction T and the non-uniformity correction introduced above $G \times M$. The extracted correction function $D(w_\gamma | u_\gamma, v_\gamma)$ is also drawn in Fig. 6.41, which was computed by the peak energy in each position sub-range.

Additional two-dimensional correction A The two-dimensional correction M was constructed based on 17.6 MeV and 54.9 MeV photons. Although it is expected to well calibrate the energy scale with those photons, both have their own possibilities of causing miscalibration: the 17.6 MeV photons would have a different shower development from the signal ones at 52.83 MeV; and the 54.9 MeV photons were collected at a different time from the physics run. Therefore, the energy scale estimated

Table 6.4: Systematic uncertainties on the position-dependent energy scale estimation for a period in the run 2022.

Dataset	Value	Systematics
Background photons	0.5 % at the v edge	Cosmic-ray events disturb estimating energy scale with high precision.
17.6 MeV and 54.9 MeV photons	0.13 %	Statistical uncertainty on extracting 54.9 MeV peak.

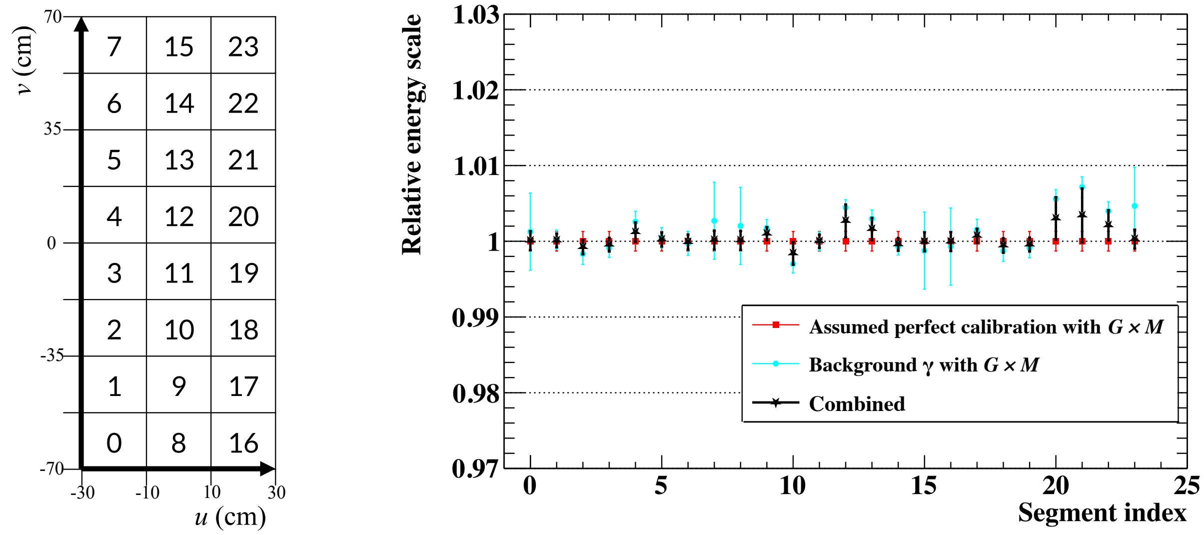

(a) Segment index definition.

(b) Energy scale as a function of segment index.

Figure 6.42: uv position dependence observed with the background spectrum and correction function A for a period in the run 2022.

by the background photon spectrum was also used to correct the non-uniformity in the uv plane. The depth dependence correction must fully rely on the response to the 54.9 MeV photons because the simulated spectrum $\mathcal{F}_{\text{sim}}$ is averaged over the whole fiducial volume although the spectrum shape differs in the conversion depth, which is not fully represented by the Gaussian smearing $\mathcal{G}_{\text{additional}}$. Here, I focused on the temporal variation rather than the fine structure of the non-uniformity to build the additional correction A: the period of the run 2022 was separated into eight instead of four for M as illustrated in Fig. 6.43, and the uv plane of the LXe detector was segmented into 3×8 instead of 12×32 for M.

Figure 6.42 shows the uv position dependence observed with the background spectrum for a period in the run 2022. At the edge of the v axis, more cosmic-ray events were contaminated in the background spectrum, resulting in an uncert energy scale estimation with the background spectrum fit. Therefore, a systematic uncertainty of 0.5 % was added to the statistic uncertainty on the estimated energy scale. On the other hand, it was expected that the previous corrections with G, M, and D would estimate the energy scale for the signal photons well within a statistical uncertainty in extracting the 54.9 MeV peak. They were combined by taking a weighted average, which was used as the correction function A.

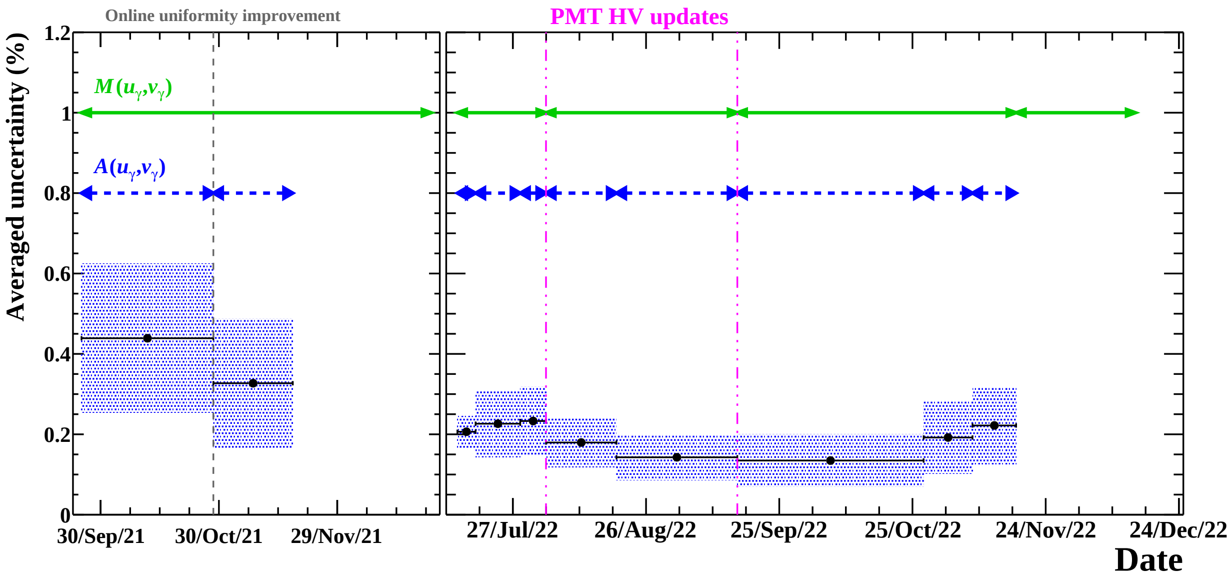

Figure 6.43: Energy scale uncertainty averaged over segments as a function of time. Blue rectangles represent the standard deviation of the energy scale in the segments. Two-dimensional non-uniformity corrections M and A are built depending on the periods shown by arrows.

The consistency of the estimated energy scales S_j in the j-th segment was assessed by

$$\chi^2/(n-1) = \sum_i^n \frac{1}{\delta S_{j,i}^2} \left(S_{j,i} - \langle S_j \rangle\right)^2 / (n-1), \tag{6.25}$$

where $\delta S_{j,i}$ is the uncertainty on the energy scale estimated by the i-th dataset, $\langle S_j \rangle$ is the weighted average of the energy scales, and $n = 2$ is the number of datasets. If the reduced χ^2 is less than one, the estimated energy scales are regarded as consistent. On the other hand, if not, the energy scales are regarded as inconsistent, and there could be unknown systematics. The error on the weighted averaged energy scale was scaled by $\sqrt{\chi^2/(n-1)}$ to take into account the unknown systematics [7]. Thus, the error bars at the segments 20, 21 and 22 in Fig. 6.42b were larger than the others.

Figure 6.43 shows the energy scale uncertainty averaged over segments as a function of time. In general, the uncertainty was smaller in the run 2022 than in the run 2021, thanks to the higher statistics of background photons. The blue rectangles represent the standard deviation of the energy scale in the segments; i.e., a longer rectangle means a larger position dependence on the uncertainty. The large position dependence was derived from that of the unsolved discrepancy between the estimated energy scales by the background spectrum and monochromatic 17.6 MeV and 54.9 MeV photons.

Conversion factor

The best-fit peak of the N_{sum} distribution for the 54.9 MeV (Fig. 6.33) with all corrections T and U applied gives the conversion factor S_{E_γ}, by being divided by 54.9 MeV. Since the energy of 54.9 MeV is very close to the signal photon energy of 52.83 MeV, the non-linearity of the energy scale is negligible (0.01 %). The uncertainty on the conversion factor comes from the statistical uncertainty on the peak extraction, which is evaluated as 0.03 %.

Table 6.5: Systematic uncertainty on the energy scale.

Source	Uncertainty (%)	
	2021	2022
Temporal variation during the physics run	0.14	0.11
Connection between physics and π^0 calibration runs	0.11	0.14
Statistical uncertainty on S calculation	0.03	0.03
Linearity	0.01	0.01
Total	0.18	0.18

Uncertainty on the energy scale

The systematic uncertainty on the energy scale is estimated as 0.18 % in total and its breakdown is tabulated in Table 6.5. In the last analysis, it was assessed to be 0.3 % [45]. The use of 17.6 MeV photons contributed to the suppression of the uncertainty from the temporal variation during the physics run. In addition, the energy scale estimation with the background spectrum was improved by constraining fit parameters based on other samples, resulting in a smaller uncertainty. The uncertainty coming from the uniformity is not considered here because the likelihood analysis to search for $\mu \to e\gamma$ adopts position-dependent photon energy PDFs, as discussed in Sect. 8.4. This means the non-uniformity can be mitigated by segmenting the detector volume, and the uncertainty on the energy scale must be assessed per segment based on Fig. 6.42.

6.3 pTC calibrations

The measured signal time for a given channel, denoted as t_i, includes its own time offsets $t_{\mathrm{offset,Ch1(2)}}$, which, if uncorrected, lead to misalignment in the reconstructed hit times and positions. From Eqs. (4.17), (4.18), it is more effective to calibrate the linear combinations of these offsets rather than treating them separately.

6.3.1 Intra-counter time offset

The reconstruction of the hit position w_{hit} in Eq. (4.18) requires calibration of both v_{eff} and the intra-counter time offset, defined as:

$$t_{\mathrm{offset,intra}} = \frac{t_{\mathrm{offset,Ch1}} - t_{\mathrm{offset,Ch2}}}{2}. \tag{6.26}$$

This calibration utilises the w_{hit} distribution obtained from the Michel positron events. The physical length of the scintillator tile, L_{counter}, is precisely controlled within ($O(10\,\mu\mathrm{m})$) and serves as a boundary condition. The centre of the w_{hit} distribution reflects $t_{\mathrm{offset,intra}}$, while its width is sensitive to v_{eff}. The precision of this method was evaluated to be 1.1 mm [45], which is significantly better than the typical w_{hit} resolution of 10 mm.

6.3.2 Inter-counter time offset

The hit time t_{hit} reconstruction requires calibration of the inter-counter time offset for each scintillator tile:

$$t_{\mathrm{offset,inter}} = \frac{t_{\mathrm{offset,Ch1}} + t_{\mathrm{offset,Ch2}}}{2} + \frac{L_{\mathrm{counter}}}{2v_{\mathrm{eff}}}. \tag{6.27}$$

Two complementary methods have been developed for this calibration: a track-based method using Michel positrons and a laser-based one employing a dedicated laser system. A detailed description of the laser-based method is available in Ref. [56].

In the track-based method, a set of inter-counter time offsets $t_{\text{offset,inter},k}$ for each counter $k = 1, \cdots, 512$ is determined by minimising the following χ^2 over a dataset of Michel positron clusters,

$$\chi^2 = \sum_{j \in \text{clusters}} \sum_{i \in \{1,\cdots,n_{\text{pTC}}\}} \left[\frac{t^j_{\text{hit},i} - \left(t^j_{\text{e}} + t^{\text{TOF},j}_{\text{e},i} + t_{\text{offset,inter},k_i} \right)}{\sigma^j_i} \right]^2 , \tag{6.28}$$

where $t^j_{\text{hit},i}$ is the measured time at the i-th counter in the j-th cluster, $t^j_{\text{e}} + t^{\text{TOF},j}_{\text{e},i}$ gives the i-th hit time of the j-th cluster, and σ^j_i is the uncertainty of each measurement represented by the mean counter time resolution. The minimisation is solved with a linear least squares fit using Millepede II [107].

The track-based method is inherently insensitive to the global time offset between the upstream and downstream sectors, as well as to temporal variations of $t_{\text{offset,inter},k}$. To address these limitations, a complementary laser-based calibration technique is employed. This method utilises a precisely timed laser pulse as a reference and determines the time offset by measuring the difference between the hit time and the laser reference time. The uncertainty associated with the laser-based calibration was evaluated as 27 ps [56]. Only in the run 2021, the residual offset of (32 ± 3) ps between the upstream and downstream sectors remained even after the laser-based calibration, which was not fully understood. This residual was finally corrected.

The time offsets obtained by these two methods exhibit good agreement, with a standard deviation of 31 ps [45], primarily attributed to the intrinsic uncertainty in the laser method. The overall accuracy of the time offset calibration was estimated to be approximately 15 ps [45], which is negligible in comparison to the single-counter time resolution of $\sigma_{\text{single}} \sim 110$ ps, as discussed in Sect. 7.2.3.

6.4 CDCH calibrations

6.4.1 Wire alignment

Although the wire positions were measured during the chamber's construction, systematic deviations were observed between these measurements and the positions calculated from physics data using the tracking algorithm and measured DOCA. These discrepancies degrade the tracking resolutions and necessitate wire-by-wire alignment based on the positron tracking.

The alignment procedure involves iteratively adjusting the wire coordinates to minimise the mean residuals. For each wire, the residual r is modelled as a parabolic function of the longitudinal coordinate z:

$$r(z) = p_0 + p_1 z + p_2 \left[\left(\frac{2z}{L_{\text{wire}}} \right)^2 - 1 \right] , \tag{6.29}$$

where the parameter p_0 represents a global wire displacement, the linear term p_1 accounts for wire inclination relative to the chamber axis, and the quadratic term p_2 takes into account the wire sagitta due to the electrostatic and gravitational forces acting on the wire. The sagitta term p_2 can reach magnitudes of approximately 100 µm. Figure 6.44 shows the hit residual distributions for a layer along the x and y axes before and after the alignment iterations. Initially, residuals were on the order of 100 µm (top plots of Fig. 6.44), but after iterative alignment, the spread was reduced to approximately 5 mm [45].

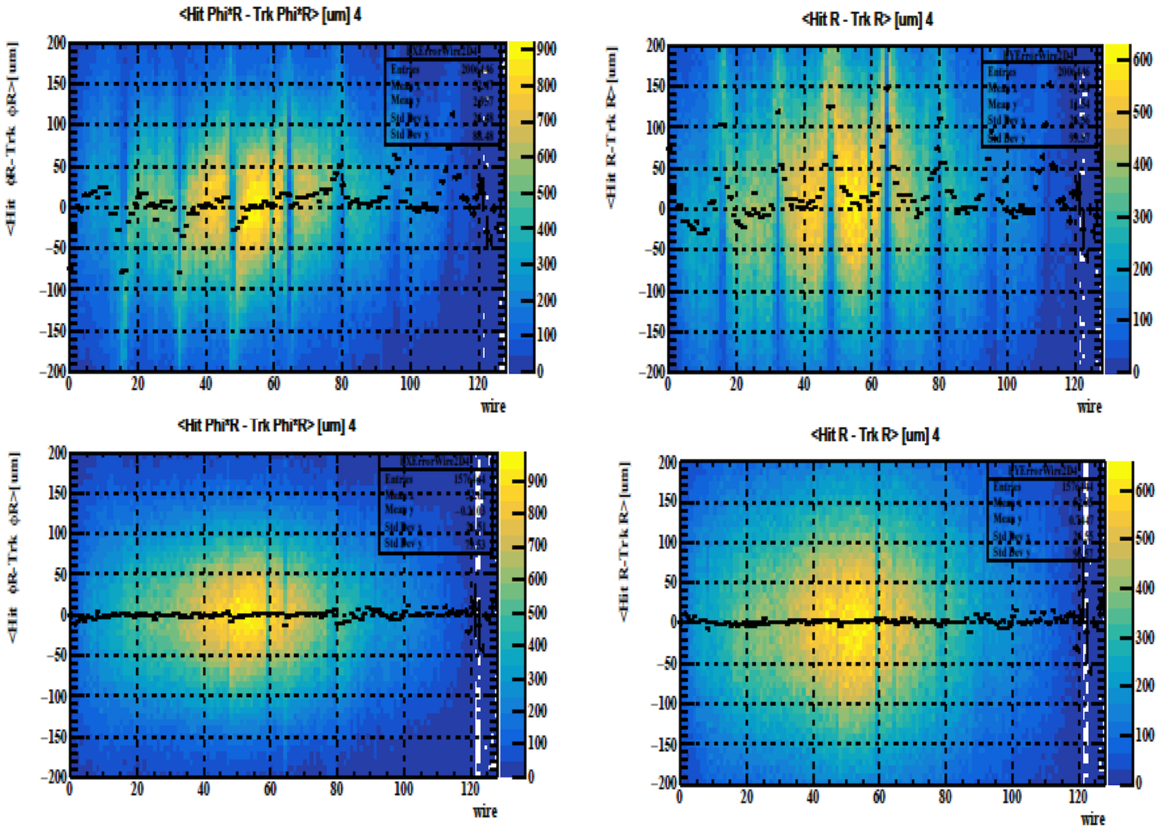

Figure 6.44: Examples of hit residuals before (top) and after (bottom) wire alignment iterations in the x (left) and y (right) axes.

6.4.2 Strength and alignment of magnetic field

The magnetic field strength determines the energy scale of the spectrometer, and the gradient magnetic field misalignment with respect to the CDCH causes a non-uniformity of the energy scale. To calibrate the energy scale, the energy spectrum of Michel positrons is fitted with the following model:

$$(\mathcal{F}_{\text{Michel}} \times \mathcal{A}_{\text{e}}) \otimes \mathcal{G}_{E_{\text{e}}}, \tag{6.30}$$

where $\mathcal{F}_{\text{Michel}}$ is the theoretical Michel positron spectrum including radiative corrections [37] (Fig. 1.5); $\mathcal{A}_{\text{e}}$ is the acceptance function, describing the E_{e}-dependent detection efficiency, modelled by error functions; and $\mathcal{G}_{E_{\text{e}}}$ is the resolution function modelled by a sum of three Gaussian functions. Figure 6.45 shows the fit result for the reconstructed energy spectrum. The energy scale was calibrated with a 0.01 % precision by correcting the offset of the response function [97].

The magnetic field is aligned to minimise the observed energy scale dependence on the positron emission angle shown in Fig. 6.46. The optimal configuration was achieved by shifting the magnetic field by $(x, y, z) = (100\,\mu\text{m}, 700\,\mu\text{m}, 300\,\mu\text{m})$ relative to the nominal position, resulting in the minimum non-uniformity, with an estimated alignment accuracy of 100–200 μm, for both runs 2021 and 2022. After the shift, there is no more bias as shown in Fig. 6.46. The scatter, on the order of about 10 keV, is negligible when compared to the energy resolution of 90 keV, which is discussed in Sect. 7.2.2.

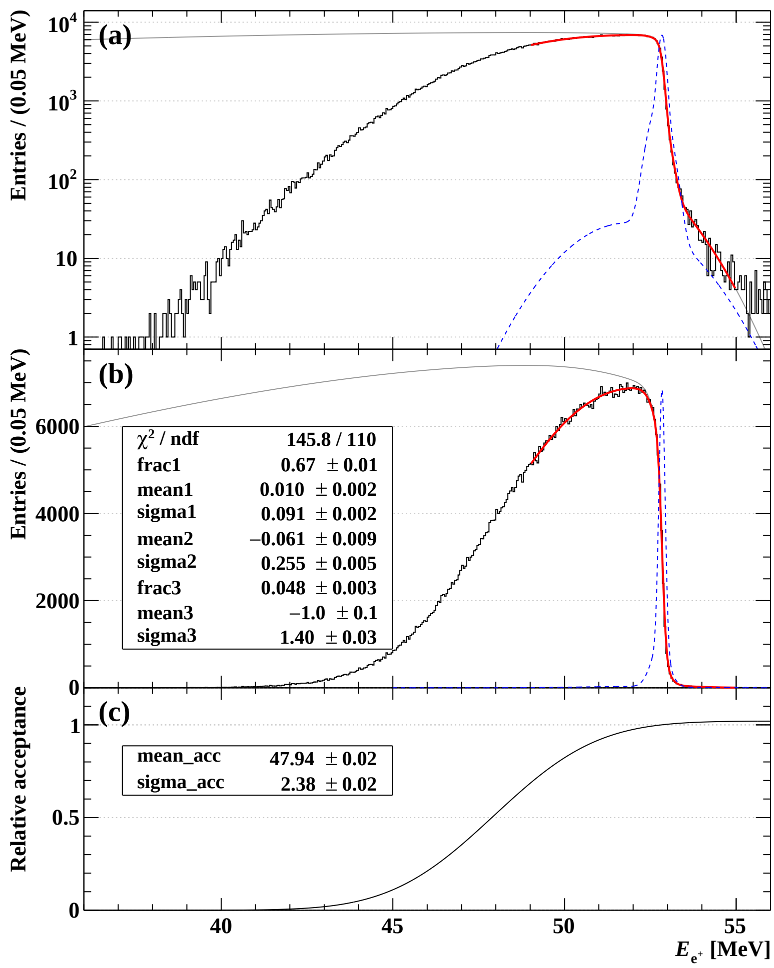

Figure 6.45: Fit of the Michel positron spectrum in logarithmic (a) and linear (b) scales [45]. The black histogram is the measured distribution, the blue curve is the sum of three Gaussian functions describing the resolution around the signal region, and the red curve is the fitted function of Eq. (6.30). (c) The acceptance curve of the spectrometer modelled with an error function.

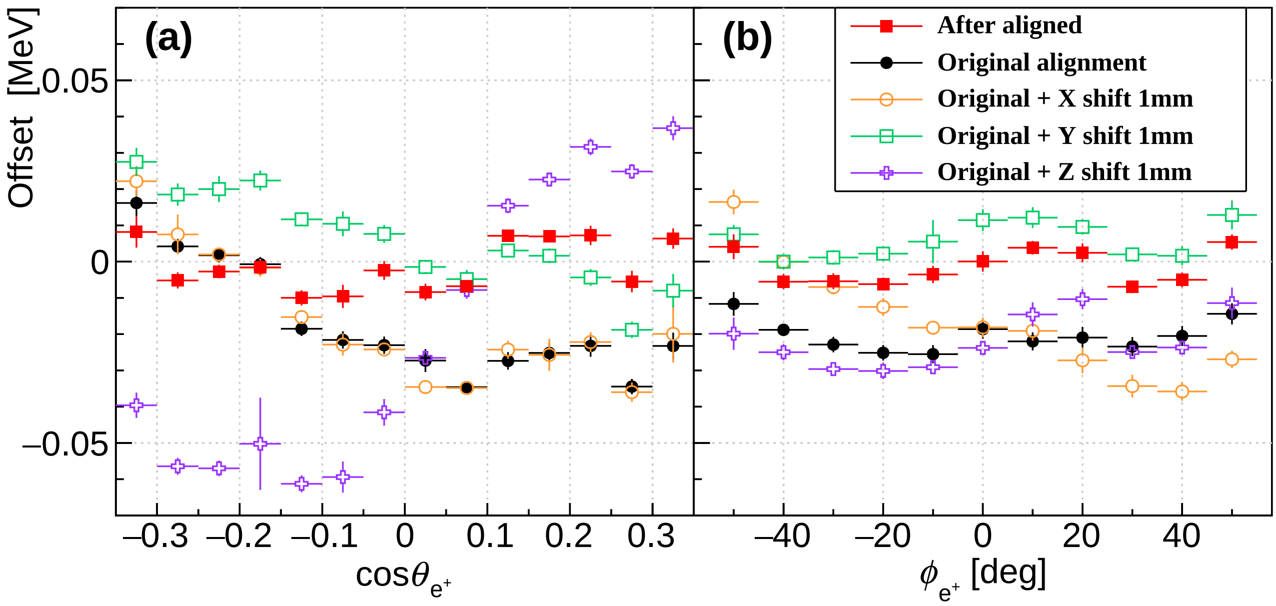

Figure 6.46: Angular dependence of the positron energy scale versus the angular kinematic variables before and after alignment [45]. The offset on the y-axis is the difference between the measured value and the expected value of the Michel edge. The three superimposed plots show the effects of shifting the magnetic field by 1 mm in x, y, and z.

6.5 RDC calibrations

6.5.1 Energy scale

Crystal energy scale The energy scale S_i for the i-th crystal in Eq. (5.11) is calibrated with the intrinsic radioactivity of LYSO crystals, temperature and bias corrections:

$$S_i = \left(S_{\text{calib},i} + f_{\text{temp}} \times \Delta T\right) / f_{\text{bias}}, \tag{6.31}$$

where $S_{\text{calib},i}$ is calculated with the energy peak of 597 keV, f_{temp} is 0.114 MeV $\cdot\,(10^9\text{e})^{-1}\cdot\text{K}^{-1}$ for temperature correction, ΔT is a difference between temperatures at a run and the calibration run, and f_{bias} is 1.122 to correct a bias in the energy scale calibration [39].

The highest energy peak of 597 keV (88 + 202 + 307 keV) in a charge distribution is fitted with a function of the theoretical energy spectrum including γ rays and β decays convoluted with a Gaussian function [45]. Figure 6.47 shows the charge spectrum of the self-luminescence of an LYSO crystal and the fitted function.

As mentioned in Sect. 3.1, the thermometers did not work stably during the run 2022, which turned off the temperature correction. This means $f_{\text{temp}} = 0$ for the run 2022. The effect on the energy scales is estimated to be 5 %.

Plate energy scale The energy scale S_i for the i-th plate in Eq. (5.6) is calibrated by comparing the MPV of the Landau distribution in a charge spectrum with that of a true energy spectrum (Fig. 6.48). If the Landau peak cannot be observed as shown in Fig. 5.19, the mean of the charge spectrum is used as MPV to avoid overestimating the deposited energy.

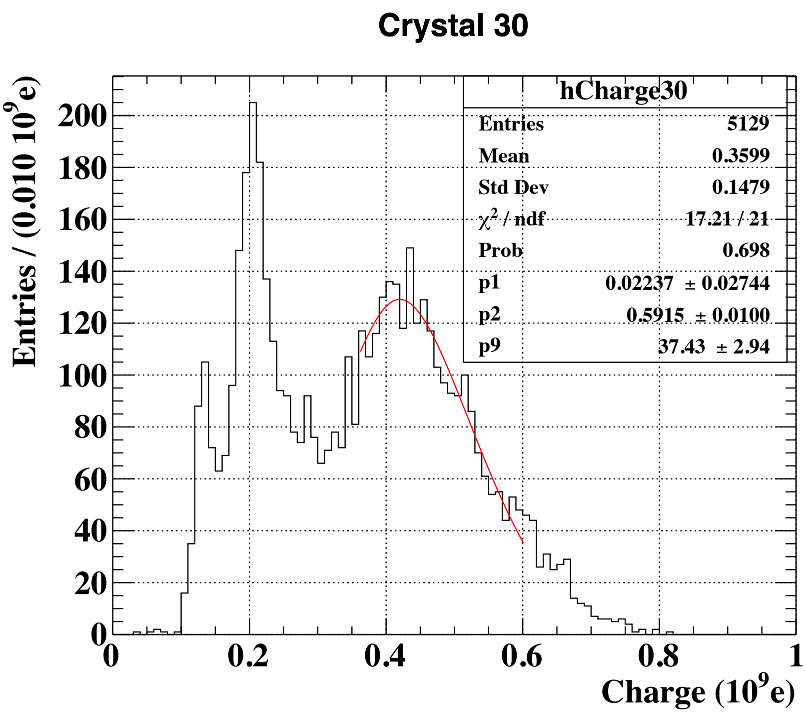

Figure 6.47: Charge spectrum of self-luminescence. A red function is the fitting function.

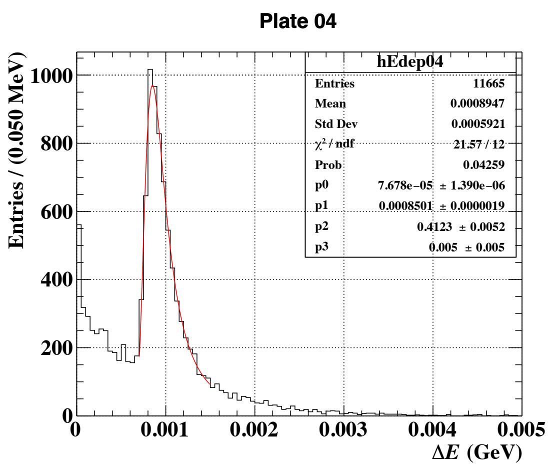

(a) True deposit energy spectrum.

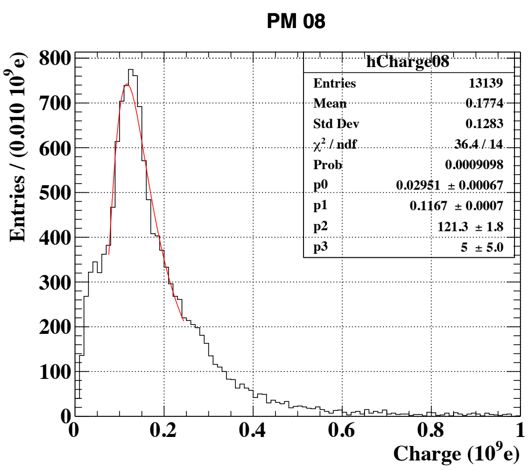

(b) Charge spectrum.

Figure 6.48: Plate energy calibration.

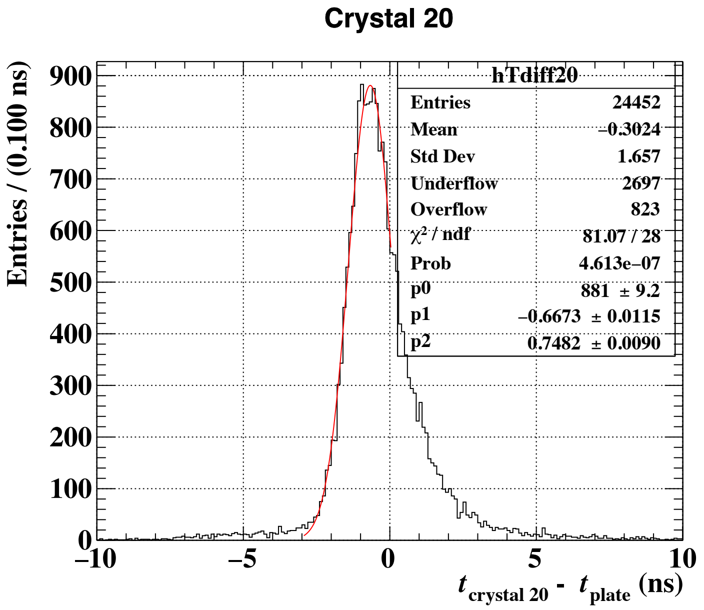

Figure 6.49: Time difference between a crystal and plate hits. A red function is a Gaussian function for the fitting.

6.5.2 Time offset

Intra- and inter-plate time offset The length of the cables connecting MPPCs in the plates to the readout electronics differed among the plate channels, causing intra-plate and inter-plate detection time differences. It is corrected by the nominal cable length divided by the signal propagation speed in the cable.

Plate-Crystal time offset Hit clustering in crystals requires the inter-crystal time offset calibration between plates and each crystal. Moreover, hit matching between plates and crystals requires time offset calibration between them. The time offset is computed by extracting the peak in the distribution of the time difference between a crystal and a plate hit, $t_{\mathrm{crystal},i} - t_{\mathrm{plate}}$ (Fig. 6.49).

6.6 Target alignment

Since the muon decay vertex is reconstructed as the crossing point between the positron's fitted track and the target foil (Sect. 4.2.4), the misalignment of the target foil causes the angle misreconstruction. The target shape was measured by a CT scan before the installation, and the position and orientation were measured by an optical survey after the installation. Tracing the temporal variation of the target transformation and deformation during the run utilises the printed dot markers reconstructed in the photograph data. References [50, 51] give the details of the marker reconstruction method.

A lot of target movements due to the Li target installation for the LXe detector calibration using 17.6 MeV photons caused the temporal variation of the target translation and rotation. Figure 6.50 shows the temporal variation of the x position of the target centre. To correct it, 68 (33) geometry configurations representing the transformation are prepared for the run 2022 (2021).

While the target shape did not significantly change during the run 2021, it changed at a level of 100 µm over time during the run 2022. Therefore, the physics run period was separated into four, and the deformation parameters were extracted for each sub-period.

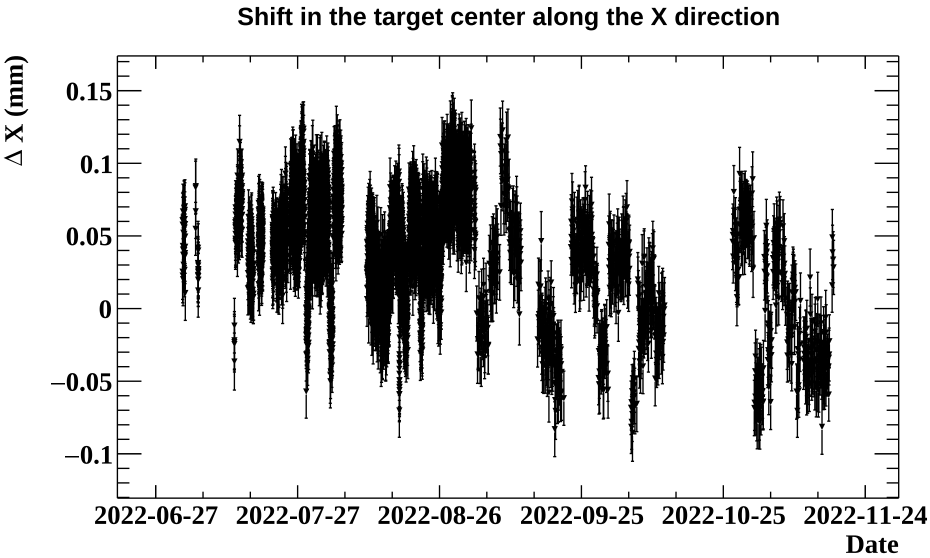

Figure 6.50: Target position shift in the x axis over time during the run 2022. The y axis shows the difference between the target centre traced by the camera and the optical survey result at the beginning of the run 2022.

6.7 Global detector alignment

Precise angle measurements require the alignment among the muon stopping target, the CDCH and the LXe detector. Table 6.6 summarises the global alignment results with respect to the CDCH. Most alignment results are consistent except for the δy of the target in the run 2022, as discussed in Sect. 6.7.1.

6.7.1 Alignment between target and CDCH

The alignment between the muon stopping target and the CDCH utilises six holes on the target, which are seen in the reconstructed positron emission position distribution in Fig. 6.51 after applying the temporal variation correction on the target transformation and deformation (Sect. 6.6). While the y- and z-coordinates of the holes can be easily estimated from the distribution, the x-coordinate alignment exploits the dependence of the estimated y position of each hole on ϕ_e. The precision of the hole-by-hole position estimation consisted of 20–80 µm (100–200 µm) statistical uncertainty for the 2022 (2021) data and the systematic uncertainty of $(x, y, z) = (50\,\mu\text{m}, 100\,\mu\text{m}, 200\,\mu\text{m})$.

From the combination of the results on different holes, the global translation was estimated as summarised in Table 6.6. The discrepancy from the magnetic field alignment result in 2022 can be understood as the uncertainty of the optical survey on the target. The global rotation was not significant within an uncertainty of 6 mrad (1.4 mrad) around the target long (short) axis.

6.7.2 Alignment between LXe detector and CDCH

The alignment between the LXe detector and the CDCH utilises the cosmic-ray straight tracks crossing both sub-detectors without the magnetic field. Since the position reconstruction in the LXe detector is optimised for the photon measurement, as discussed in Sect. 4.1.3, the cosmic-ray crossing point to the inner face of the LXe detector is reconstructed with a different method: Using the position of the MPPC having the maximum $N_{\text{pho},i}$. This method can be used because the scintillation light

Table 6.6: Global detector alignment with respect to the CDCH.

(a) 2021.

Sub-detector		δx	δy	δz
Magnetic field	Sect. 6.4.2	(100 ± 100) µm	(700 ± 200) µm	(300 ± 100) µm
Muon stopping target	Sect. 6.7.1	(80 ± 100) µm	(860 ± 100) µm	(500 ± 100) µm
LXe detector	Sect. 6.7.2	No evaluation	No evaluation	(540 ± 410) µm

(b) 2022.

Sub-detector		δx	δy	δz
Magnetic field	Sect. 6.4.2	(100 ± 100) µm	(700 ± 200) µm	(300 ± 100) µm
Muon stopping target	Sect. 6.7.1	(80 ± 35) µm	(240 ± 35) µm	(570 ± 100) µm
LXe detector	Sect. 6.7.2	No evaluation	No evaluation	(560 ± 290) µm

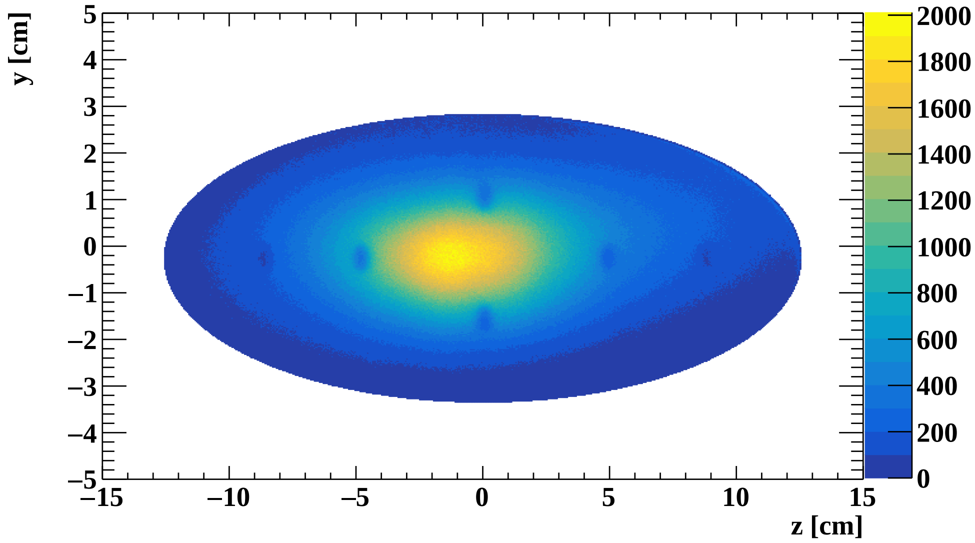

Figure 6.51: Reconstructed positron emission position distribution projected on the yz plane. Six holes are visible as the dips of the distribution.

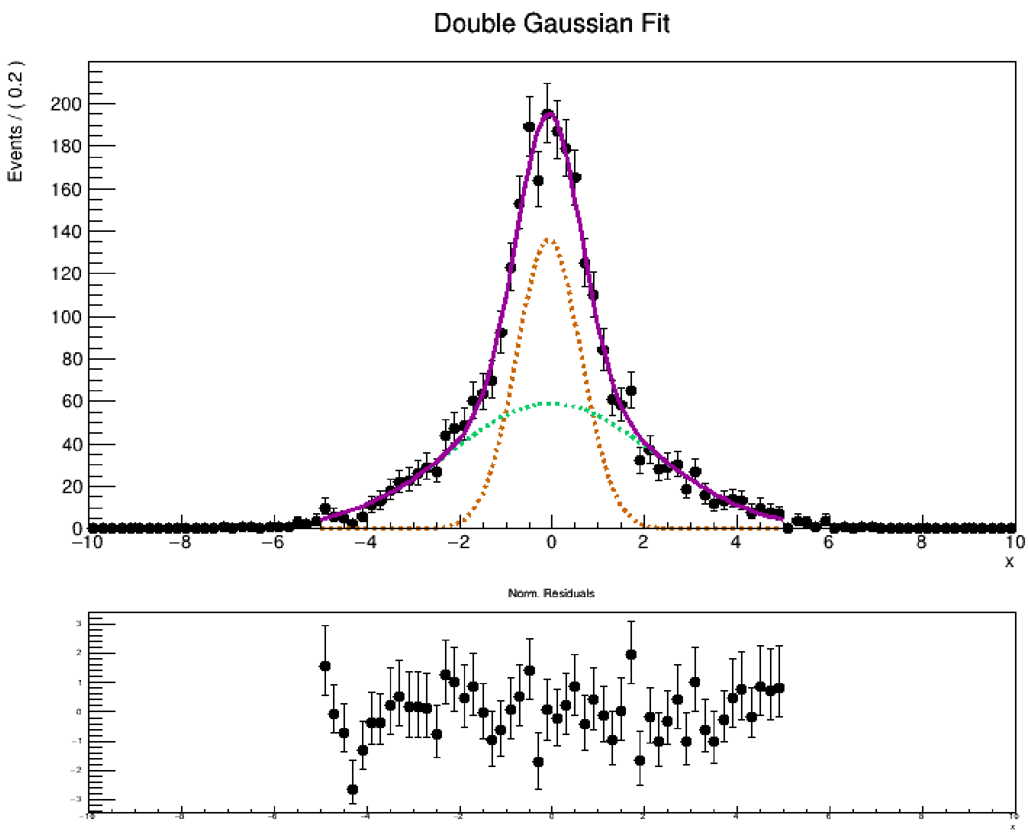

Figure 6.52: Distribution of the reconstructed z position residual between the LXe detector and the CDCH. The magenta function is a double Gaussian function fitted to the distribution. The orange (blue) one is the core (tail) component of the best-fit double Gaussian function.

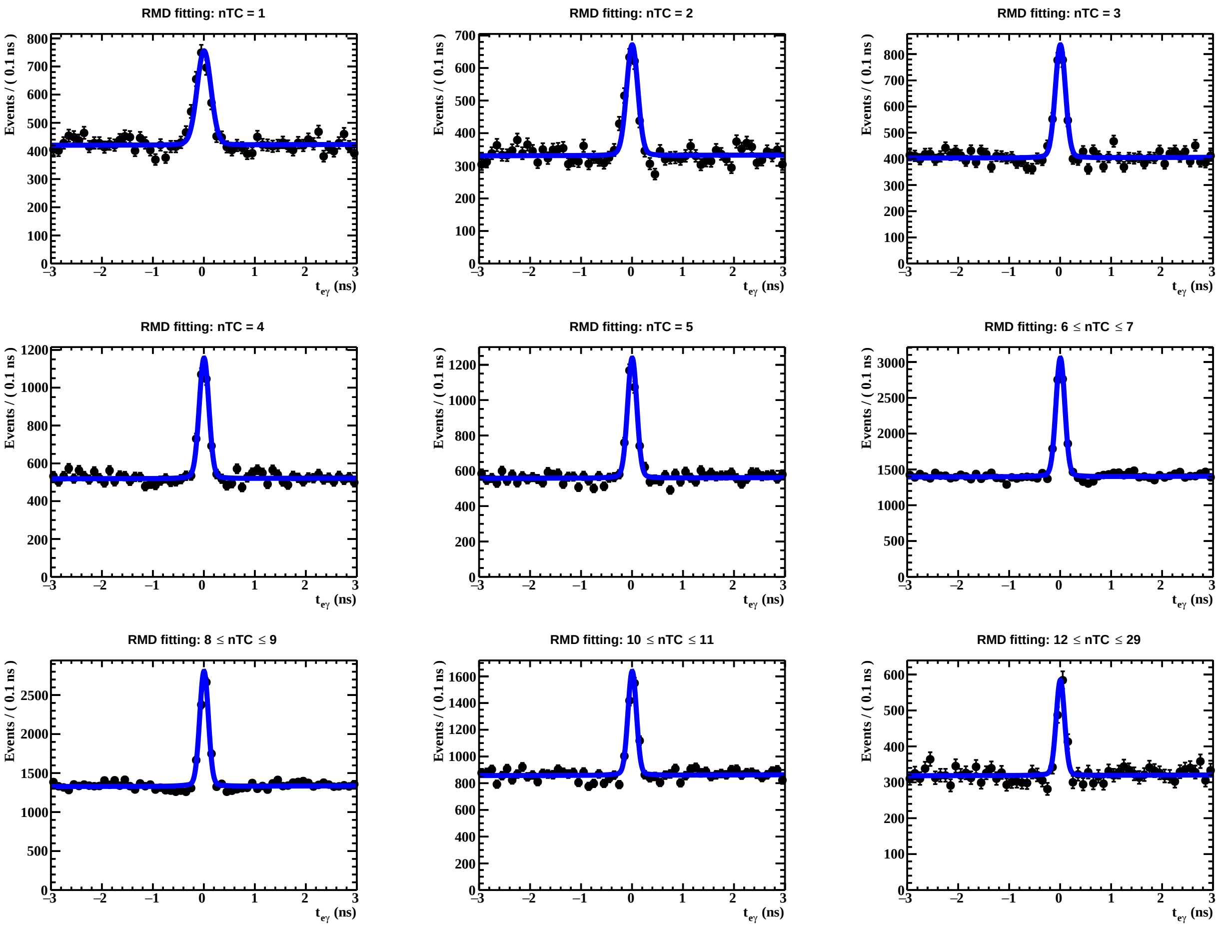

Figure 6.53: $t_{\mathrm{e}\gamma}$ distribution for n_{pTC}-divided subsets after the offset calibration and its dependence correction.

is emitted along the cosmic-ray path and is expected to concentrate on the photosensors in the path. Figure 6.52 shows the distribution of the reconstructed z position residual between the LXe detector and the CDCH and the fitted function composed of a sum of two Gaussian functions. The mean value of the core component represents the misalignment between these sub-detectors, which was (650 ± 370) µm ((850 ± 730) µm) in 2022 (2021). The uncertainty is dominated by the statistical one.

The cosmic-ray-based results are finally combined with the yearly optical survey results that have an uncertainty of 500 µm [104]. Here, the results on the alignment of the magnetic field and the target imply that the CDCH is displaced by 400 µm in the z-coordinate from the fiducial optical marker. Therefore, the optical survey on the LXe detector, discussed in Sect. 6.2.4, provides the (400 ± 500) µm misalignment with respect to the CDCH. By taking weighted averages, the LXe detector is aligned with the shifts and uncertainties summarised in Table 6.6.

6.8 Relative time calibrations

6.8.1 $t_{\mathrm{e}\gamma}$ offset

The $t_{\mathrm{e}\gamma}$ offset is calibrated with the energy side-band sample ($45\,\mathrm{MeV} < E_\gamma < 48\,\mathrm{MeV}$) defined in Sect. 8.1. Concerning t_γ, since the time offset in the PMTs varied by 200 ps over time (Sect. 6.2.6), the $t_{\mathrm{e}\gamma}$ offset calibration separates the run 2022 into seven to correct the temporal variation in $t_{\mathrm{e}\gamma}$.

The $t_{e\gamma}$ offset has dependences on the n_{pTC} at a level of 100 ps and ϕ_e at 50 ps level, independently, in which the latter is suspected to have some systematic biases in the inter-counter time offset calibration in the pTC. The above dependences affecting $t_{e\gamma}$ are corrected, and the $t_{e\gamma}$ offset is calibrated with a precision of 4 ps, as shown in Fig. 6.53.

6.8.2 $t_{RDC-\gamma}$ offset

A time difference between RDC hits and a photon $t_{RDC-\gamma}$ is distributed asymmetricaly and much more widely than $\sigma_{t_\gamma} \sim 70$ ps and $\sigma_{t_{plate}} \sim 90$ ps due to the variation of the positron TOF, as shown in Fig. 5.24. The $t_{RDC-\gamma}$ offset is defined to maximise the number of RDC hits in events with $E_\gamma \in [48\,\mathrm{MeV}, 58\,\mathrm{MeV}]$. Even though the time offset was dependent at $O(0.1\,\mathrm{ns})$ on the period mainly due to t_γ drifting, which was discussed in Sect. 6.2.6, the dependence is ignorable since it is small enough compared with the $t_{RDC-\gamma}$ deviation.

Chapter 7

Performance

This chapter describes the detector performance. The performance of the RDC is discussed in Sect. 5.3.3.

7.1 Performance of LXe detector

This section describes the resolutions of photon position, time, and energy measured by the LXe detector, and the detection efficiency. A more detailed description of the position resolution measurement and the detection efficiency evaluation is given by Ref. [59], and on the time resolution measurement by Ref. [46]. Performance of multiple photons elimination is described in Sect. 5.2.2.

7.1.1 Position resolutions

The position resolutions are evaluated by imaging a lead collimator with 17.6 MeV photons. The collimator, measuring 240×240×25 mm^3, featured eight slits, each 5 mm wide and 80 mm long, spaced 50 mm apart. It was installed between the LXe detector and the COBRA magnet in a dedicated run. Figure 7.1 shows the two-dimensional distribution of reconstructed photon positions corresponding to the collimated photons. The sharpness of the imaged slits serves the v resolution. The u-resolution is assessed by rotating the collimator by 90°. The position resolutions in the u and v directions were quantified by fitting a MC simulation model with a resolution function composed of two Gaussian components, to the measured data. The resulting resolutions were found to be $\sigma_{u_\gamma,v_\gamma} = 2.5$ mm (4.0 mm) for $w < 2$ cm (> 2 cm) in u and v. The position resolution in w was estimated from the MC simulation to be $\sigma_{w_\gamma} = 5.0$ mm. Figure 7.2 illustrates the estimated core resolutions as a function of w for signal photons.

7.1.2 Time resolution

The time resolution evaluation utilises the $\pi^0 \to \gamma\gamma$ events, in which one of the two photons is detected by the pre-shower counter, as done in Sect. 6.2.6. The peak width of the time difference between the two photons detected by the LXe detector and the pre-shower counter, $\sigma_{\mathrm{LXe-PS}}$, gives the time resolution. Here, since the unknown π^0 decay vertex has a non-negligible contribution to the time resolution evaluation, it must be subtracted from the evaluation, that is,

$$\sigma_{\mathrm{LXe-PS}} = \sigma_{t_\gamma} \oplus \sigma_{t_{\mathrm{PS}}} \oplus \sigma_{\mathrm{vertex}}. \tag{7.1}$$

where σ_{vertex} is the time dispersion due to the π^0 decay vertex spread.

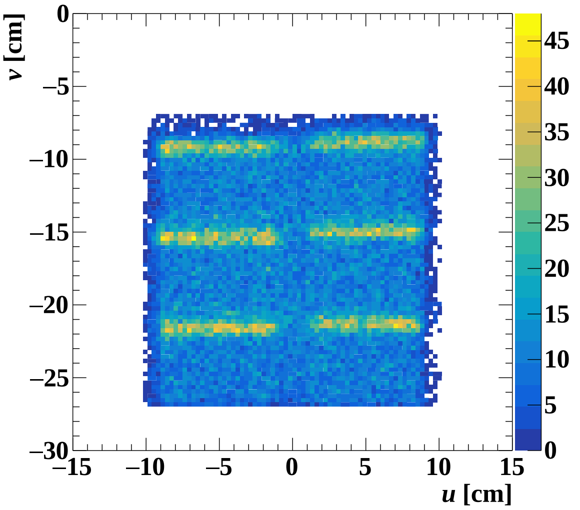

Figure 7.1: The position distribution of the 17.6 MeV photons with the collimator for the v-resolution measurement [45]. The readout region covers six out of eight slits, which are imaged as horizontal lines.

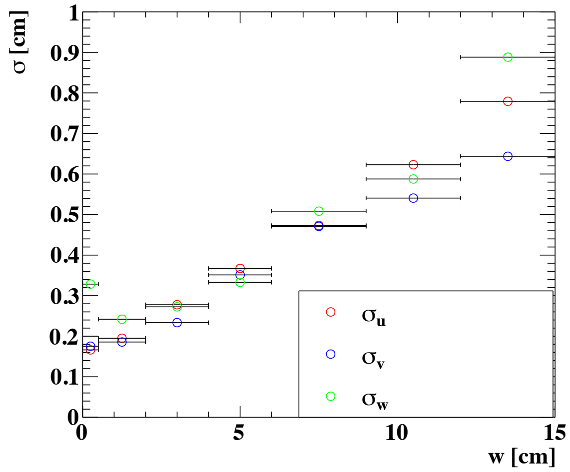

Figure 7.2: Estimated core resolutions as a function of w for signal photons [59].

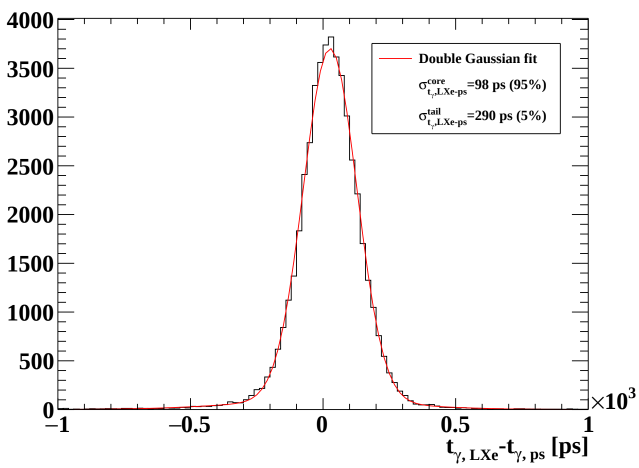

Figure 7.3: Distribution of the difference between the photon time measured by the LXe detector and that by the pre-shower counter [45]. The red line is the fitted function consisting of two Gaussian functions.

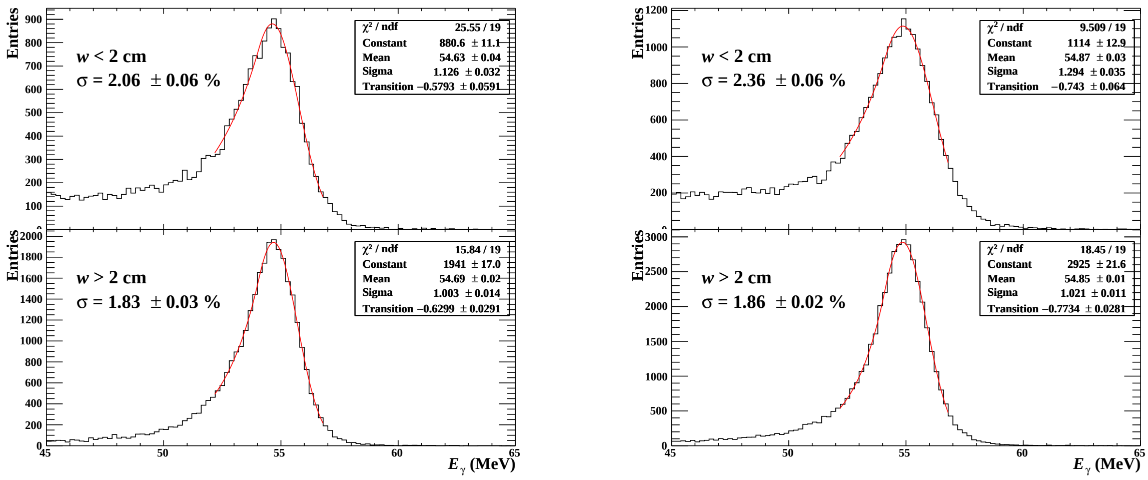

(a) 2021.　　(b) 2022.

Figure 7.4: Response to 54.9 MeV photons in the central region of $-10\,\text{cm} < u_\gamma < 10\,\text{cm}$ and $-30\,\text{cm} < v_\gamma < -10\,\text{cm}$. The top distribution uses events at $w_\gamma < 2\,\text{cm}$ and the bottom does at $w_\gamma > 2\,\text{cm}$. Red curves are the fit function, *ExpGaus* function defined as Eq. (6.19).

Figure 7.3 shows the distribution of the time difference between the LXe detector and the pre-shower counter in the π^0 calibration run 2021. A double Gaussian function was fitted to the distribution, resulting in $\sigma_{\text{LXe}-\text{PS}} = 98\,\text{ps}$ in the core part (102 ps for 2022). The contribution from the pre-shower counter resolution was estimated to be $(28.2 \pm 0.2)\,\text{ps}$ from the intrinsic time difference between the two plates. The contribution from the vertex spread was measured to be $\sigma_{\text{vertex}} = (68 \pm 6)\,\text{ps}$ ($(72 \pm 2)\,\text{ps}$) with a dedicated measurement in 2021 (2022). Finally, the time resolution of the LXe detector is evaluated to be $\sigma_{t_\gamma} = (65 \pm 6)\,\text{ps}$ ($(63 \pm 4)\,\text{ps}$) in 2021 (2022).

7.1.3 Energy resolution and linearity

The energy resolution of the LXe detector is evaluated by 54.9 MeV photons. Figure 7.4 shows the response to the 54.9 MeV photons in the central region of $-10\,\text{cm} < u_\gamma < 10\,\text{cm}$ and $-30\,\text{cm} < v_\gamma < -10\,\text{cm}$ depending on the conversion depth and the fit function defined as Eq. (6.19). Here, I imposed the event selection discussed in Sects. 4.1.6 and 6.2.8. The sigma parameter in the *ExpGaus* function represents the resolution. While the resolutions for deep events are consistent between two years, the ones for shallow events have a discrepancy between $(2.06 \pm 0.06)\,\%$ in 2021 and $(2.36 \pm 0.06)\,\%$ in 2022, whose quadratic difference is 1.2 %. I conducted numerous studies to understand the resolution degradation in shallow regions, including the MPPC non-linearity, MPPC gain variation, and further face factor optimisation. Moreover, I evaluated the energy resolution using 17.6 MeV photons, obtaining comparable or even better resolutions in the run 2022. Despite such studies, it remains unclear. This resolution worsening degrades the sensitivity to $\mu \to e\gamma$ by 3 %, which is an acceptable level given the current understanding.

Energy dependence on the resolution for a realistic calorimeter can be given [108] by

$$\frac{\sigma_E}{E} = \sqrt{\left(\frac{a}{\sqrt{E}}\right)^2 + \left(\frac{b}{E}\right)^2 + (c)^2}, \tag{7.2}$$

where the first term on the right-hand side is called the "Stochastic term", the second is the "noise term", and the third is the "constant term". Each term expresses the following effects:

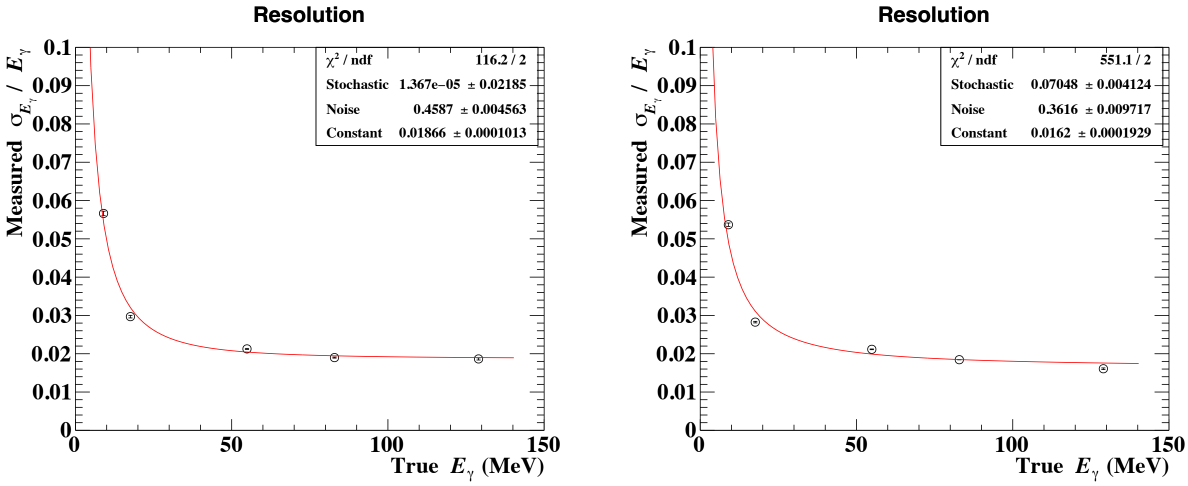

(a) 2021. (b) 2022.

Figure 7.5: Energy resolution as a function of true energy. The fit function is given by Eq. (7.2).

(1) Stochastic term: Shower intrinsic fluctuations,

(2) Noise term: Electric noise of the readout chain, and

(3) Constant term: Variations of the calorimeter response, e.g. non-uniformity.

Figure 7.5 shows the energy resolution as a function of true energy for monochromatic photons. Here, the 82.9 MeV and 129 MeV photons, introduced in Sect. 2.4.4, were used as well as the 9, 17.6 and 54.9 MeV photons, that were already discussed in Sects. 6.2.8 and 6.2.9. The 82.9 MeV photon selection requires energy of 40–65 MeV measured by the BGO crystals. Here, all events in the fiducial volume are used for the evaluation. Let me discuss the coefficients for each term. Concerning the Stochastic term, I evaluated a coefficient of $(0.00 \pm 0.03)\,\mathrm{MeV}^{1/2}$ for 2021 and $(0.072 \pm 0.004)\,\mathrm{MeV}^{1/2}$ for 2022. The larger coefficient in 2022 than in 2021 seems consistent with the fact that I observed unknown resolution degradation in shallow regions in 2022. The noise term coefficient of approximately 0.4 MeV is one order larger than $\sigma_{E_{\mathrm{ped}}}$ shown in Fig. 6.3. Although the discrepancy is not understood, this noise term is not a dominant factor in the energy resolution. The constant term coefficient of $(1.89 \pm 0.04)\,\%$ in 2021 and $(1.65 \pm 0.02)\,\%$ in 2022 seems to have the remaining non-uniformity as well as something unknown contributing to the difference from the resolution in a simulation (0.8 %).

The linearity of the energy scale is evaluated with the reconstructed peak energies for the 9, 17.6, 54.9, 82.9 and 129 MeV photons. It is within 1.5 % in the range of 17.6 MeV to 129 MeV, although the 9 MeV photons were reconstructed to be 4 % higher than the true energy. As discussed in Sect. 6.2.9, however, because the energy scale was calibrated with the 54.9 MeV photons, the effect of the non-linearity on the signal photon measurement is negligible.

7.1.4 Detection efficiency

The detection efficiency for signal photons is initially estimated using the MC simulation, yielding a value of 69 % [44]. To validate and refine this estimate, a cross-check was performed using data from the $\pi^0 \to \gamma\gamma$ calibration run. In this calibration setup, the detection of an 82.9 MeV photon by the BGO calorimeter implies the simultaneous emission of a 54.9 MeV photon in the opposite direction, directed towards the LXe detector. By counting the number of events in which the LXe detector detects photons in the BGO-triggered events, the detection efficiency of the LXe detector

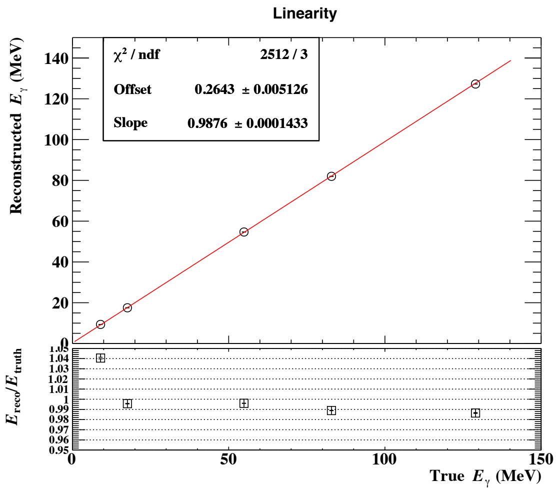

(a) 2021.

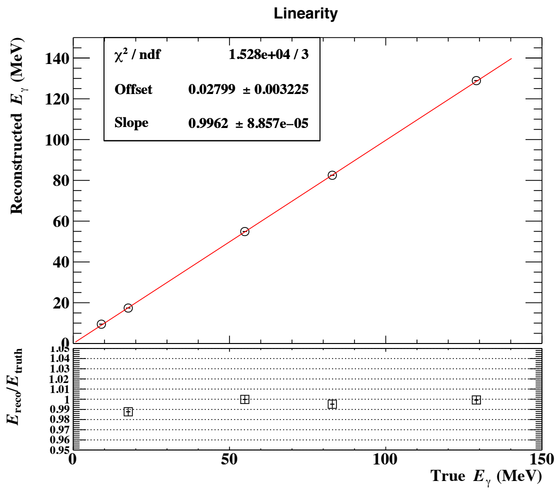

(b) 2022.

Figure 7.6: Linearity of the reconstructed energy.

can be evaluated. To account for differences in measurement conditions between the calibration and physics runs, such as the presence of additional material for the LH_2 target system, a dedicated MC simulation was performed for this measurement. This simulation yields a detection efficiency of 64 %, while the efficiency from the data was (61 ± 1) %. If this discrepancy comes from the misunderstanding of the LH_2 target material, it is irrelevant to the signal photon detection efficiency. On the other hand, if it comes from the material budget in the inner face of the real LXe detector, it affects the detection efficiency. This discrepancy has not yet been resolved and is accounted for in the systematic uncertainty. Therefore, the best estimate of the detection efficiency for the signal photons is the mean of the two cases (69 % and 65 %), which is (67 ± 2) %. Combining the analysis efficiency of (93.4 ± 0.6) %, the overall photon efficiency is $\varepsilon_\gamma = (63 \pm 3)$ %.

7.2 Performance of positron spectrometer

This section summarises the performance of the positron spectrometer, including the CDCH and pTC. A more detailed description of the CDCH performance is given by Ref. [97], and of the pTC performance by Ref. [45].

7.2.1 Vertexing and angular resolutions

The vertexing and angular resolutions are evaluated using a dedicated double-turn analysis. Approximately 15 % of positron tracks traverse the chamber volume five times, passing through 9×5 sense wire layers. These tracks segment into two independent track portions ("turns") with the first comprising two chamber crossings and the second comprising three, as illustrated in Fig. 7.7. Each track segment is reconstructed independently and extrapolated to a common reference plane situated between the two turns, parallel to the target. By comparing the kinematic variables derived from each segment, the resolution of vertex and angular measurements can be estimated from the distribution of their differences. The resulting vertexing and angular resolutions at $R_\mu = 3 \times 10^7\ \mathrm{s}^{-1}$ are described in Table 7.1.

Figure 7.7: An example double-turn track [46]. The first turn track (the dashed part) and the second turn track (the solid part) are fitted independently and compared at the border point. The green markers are hits used in the track fitting.

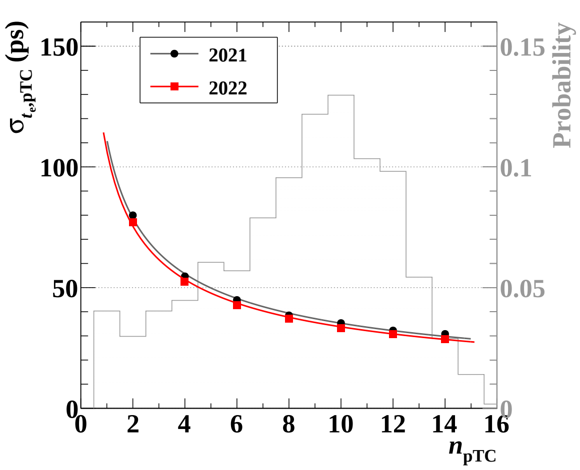

Figure 7.8: Time resolution of pTC as a function of the number of hits evaluated by the even-odd analysis on the 2021 and 2022 data.

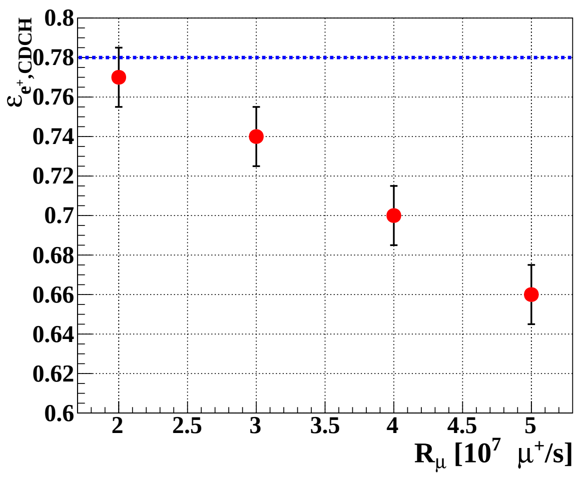

Figure 7.9: CDCH tracking efficiency as a function of R_μ for signal positrons [45]. The blue dotted line is the design value [44].

7.2.2 Momentum resolution

The momentum resolution is estimated from the response function in the fitting function of Eq. (6.30) in the Michel positron spectrum. The result with the 2021 dataset is shown in Fig. 6.45 in both logarithmic (a) and linear (b) scales. The σ of the core Gaussian function is $\sigma_{E_e} = 89\,\mathrm{keV}$.

7.2.3 Time resolution

The pTC time resolution is assessed using the "even-odd" analysis method, which reconstructs the positron emission time t_e, as defined in Eq. (4.20), independently from two subsets of hits within a cluster. These subsets correspond to hits indexed by $i \in \{2k\}$ and $i \in \{2k+1\}$, where k is an integer. The difference between the two results provides a measure of the time precision. Figure 7.8 shows the time resolution as a function of n_{pTC}. By weighting the multi-hit resolution values according to the n_{pTC} distribution obtained by the MC simulation, an average time resolution of $\sigma_{t_e} \sim 40\,\mathrm{ps}$ is achieved.

7.2.4 Detection efficiency

The CDCH tracking efficiency is defined as the ratio of the number of reconstructed positrons within the signal energy region to the number of positrons emitted towards the direction opposite to the LXe fiducial region (Eq. (4.15)) and detected by the pTC. Figure 7.9 shows the CDCH tracking efficiency for signal positrons $\varepsilon_{\mathrm{e,CDCH}}$ as a function of the muon stopping rate R_μ. As R_μ increases, the probability of pileup also rises, which degrades the performance of the track-finding algorithm by complicating the association of hits to individual tracks. The blue dotted line in this figure represents the design specification, which is nearly achieved at the lowest value of R_μ. Given a pTC detection efficiency of (91 ± 2) % [45], the overall positron efficiency was evaluated as approximately 67 % at $R_\mu = 3 \times 10^7\,\mathrm{s}^{-1}$.

7.3 Combined performance

7.3.1 Combined $t_{\mathrm{e}\gamma}$ resolution

The combined $t_{\mathrm{e}\gamma}$ resolution is evaluated as a function of n_{pTC} because the pTC time resolution depends on it. I decomposed the resolution into the contributions from the pTC time resolution and the others, where the pTC one is different event-by-event and the other is constant, that is,

$$\sigma_{t_{\mathrm{e}\gamma}} = \sigma_{\mathrm{const}} \oplus \frac{\sigma_{\mathrm{single}}}{\sqrt{n_{\mathrm{pTC}}}}, \tag{7.3}$$

where σ_{const} is the contribution independent from n_{pTC}, and $\sigma_{\mathrm{single}} = 106\,\mathrm{ps}$ (112 ps) is the single-counter time resolution estimated from the even-odd analysis with the 2022 (2021) dataset, described in Sect. 7.2.3.

The constant term represented by σ_{const} is estimated by simultaneously fitting Eq. (7.3) to n_{pTC}-divided subsets of the RMD samples (Fig. 6.53). The σ_{const} is estimated to be (80 ± 2) ps ((82 ± 5) ps) for the 2022 (2021) dataset. There is a discrepancy from $\sigma_{t_\gamma} = (63 \pm 4)$ ps measured with 54.9 MeV photons in the π^0 calibration run 2022, described in Sect. 7.1.2. As being suspected to arise from systematics in the $\pi^0 \to \gamma\gamma$ measurement, this discrepancy is ignored in resolution evaluation. An average $t_{\mathrm{e}\gamma}$ resolution for signal events is 91 ps (94 ps) for the 2022 (2021) dataset, which is obtained by weighting the $\sigma_{t_{\mathrm{e}\gamma}}$ with the n_{pTC} distribution from the signal MC simulation.

7.4 Performance summary

The detector performance is summarised in Table 7.1, with comparisons to previous results. The positron spectrometer's performance is significantly improved compared to the MEG experiment, particularly in terms of momentum and time resolutions, as well as efficiency. The LXe detector position resolution is twice as good as that of the MEG experiment, thanks to a highly granular readout with MPPCs. These performance improvements contribute to the highest sensitivity to search for $\mu \to \mathrm{e}\gamma$ in the MEG II experiment.

When comparing the achieved detector performance in the first result and this work, the positron angular and vertexing resolutions are slightly improved, thanks to the improvement in the ghost track selection discussed in Sect. 4.2.5. The efficiencies are also improved: the photon efficiency is improved by 1 % due to the pileup unfolding improvement discussed in Sect. 5.2.2; and the trigger efficiency is improved by 14 % due to the trigger logic improvement and the trigger efficiency estimation update that are discussed in Sect. 8.6. However, the photon energy resolution is worsened to 2.4 % in events where photons convert at $w_\gamma < 2\,\mathrm{cm}$, as discussed in Sect. 7.1.3.

Table 7.1: Summary of the detector performance.

	MEG [44]	MEG II first result [1]	MEG II achieved in this work
Resolutions			
E_γ (%) $(w_\gamma < 2\,\mathrm{cm})/(w_\gamma > 2\,\mathrm{cm})$	2.4/1.7	2.0/1.8	2.4/1.9
u_γ, v_γ, w_γ (mm)	5, 5, 6	2.5, 2.5, 5	2.5, 2.5, 5
t_γ (ps)	67 [43]	65 [46]	63
E_e (keV)	380	90	89
θ_e, ϕ_e (mrad)	9.4, 8.7	7.2, 4.1	6.2, 5.2
z_e, y_e (mm)	2.4, 1.2	2.0, 0.7	1.76, 0.61
t_e (ps)	102 [43]	~40	~40
$t_{\mathrm{e}\gamma}$ (ps)	122	78	78
Efficiencies			
ε_γ (%)	63	62	63
ε_e (%)	30	67	67
ε_TRG (%)	≈99	80	91

Chapter 8

Analysis of $\mu^+ \to e^+\gamma$ search

The data-taking and event reconstruction have been described in previous chapters (Chaps. 2–7). This chapter describes the analysis of the $\mu \to e\gamma$ search.

8.1 Analysis overview

The analysis strategy is a combination of maximum likelihood and blind analyses to estimate the number of signal events N_{sig}, as done in the MEG experiment [42]. The maximum likelihood analysis is employed to mitigate boundary effects at the borders of the analysis region and to enhance sensitivity by accurately accounting for the probabilities of events arising from signal, accidental, or RMD background. The analysis region for the maximum likelihood fit is defined as

- $48\,\mathrm{MeV} < E_\gamma < 58\,\mathrm{MeV}$,
- $52.2\,\mathrm{MeV} < E_\mathrm{e} < 53.5\,\mathrm{MeV}$,
- $|t_{\mathrm{e}\gamma}| < 0.5\,\mathrm{ns}$,
- $|\theta_{\mathrm{e}\gamma}| < 40\,\mathrm{mrad}$, and
- $|\phi_{\mathrm{e}\gamma}| < 40\,\mathrm{mrad}$.

The blind analysis is chosen to prevent any biases in developing the event reconstruction algorithm and evaluating the PDFs used in the maximum likelihood analysis. The blind box is defined with two observables of E_γ and $t_{\mathrm{e}\gamma}$ as

- $48\,\mathrm{MeV} < E_\gamma < 58\,\mathrm{MeV}$ and
- $|t_{\mathrm{e}\gamma}| < 1\,\mathrm{ns}$,

which covers the analysis region, as seen in Fig. 8.1. Once the PDFs of observables used to discriminate signal from background are ready to build a likelihood function, the hidden data are released and used to extract a confidence interval for the expected number of signal events N_{sig}.

In addition, several side-bands are defined in order to examine background events: the "time side-bands" defined as $1\,\mathrm{ns} < |t_{\mathrm{e}\gamma}| < 3\,\mathrm{ns}$ and the "energy side-band" defined as $46.5\,\mathrm{MeV} < E_\gamma < 48\,\mathrm{MeV}$.

Conversion to the branching ratio The maximum likelihood fit estimates the number of signal N_{sig}. As formalised in Eq. (1.15), the branching ratio $\mathcal{B}$ is converted from N_{sig} with the normalisation factor k, $\mathcal{B} = N_{\mathrm{sig}}/k$. Section 8.6 discusses the estimation of the factor k.

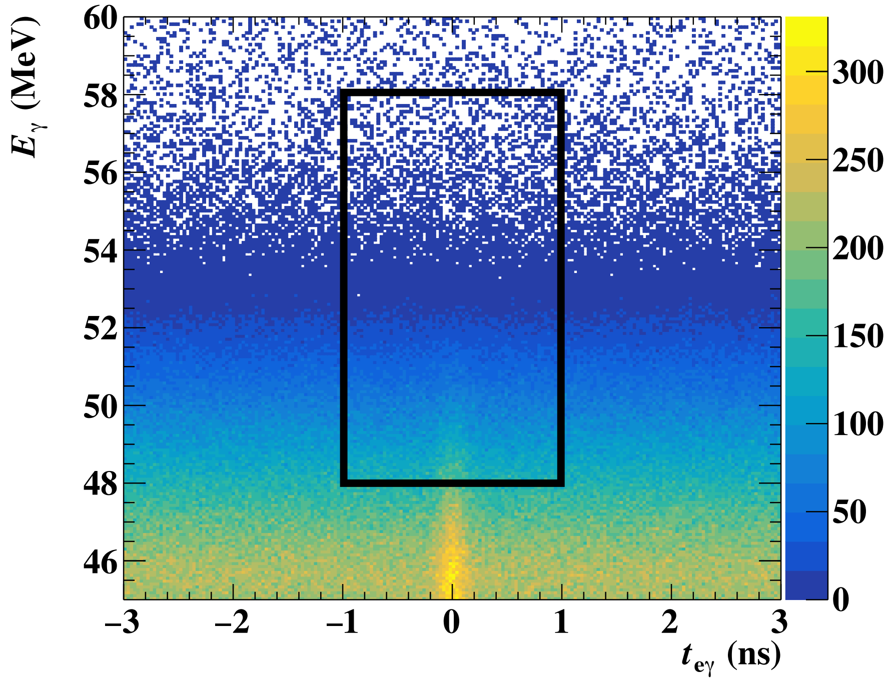

Figure 8.1: Event distribution on $(t_{e\gamma}, E_\gamma)$ plane. A black square shows the blind box defined as $48\,\text{MeV} < E_\gamma < 58\,\text{MeV}$ and $|t_{e\gamma}| < 1\,\text{ns}$. The time side-bands are defined as $1\,\text{ns} < |t_{e\gamma}| < 3\,\text{ns}$ and the energy side-band is defined as $45\,\text{MeV} < E_\gamma < 48\,\text{MeV}$.

8.2 Maximum likelihood fit

An extended unbinned maximum likelihood fit [109] is performed on the data samples to estimate the number of signal and background events in the dataset. As discussed in Sect. 1.2.2, two types of background are considered: the physics background derived from the RMD and the accidental one. The numbers of these background events, N_{RMD} and N_{ACC}, respectively, are treated as nuisance parameters in the fitting to incorporate part of the systematic uncertainties. In addition to the numbers, a parameter representing the misalignment of the muon stopping target (Sect. 6.7) is also introduced as a nuisance parameter, denoted as X_{T}. The extended likelihood function is thus described as

$$
\begin{aligned}
\mathcal{L}(N_{\mathrm{sig}}, N_{\mathrm{RMD}}, N_{\mathrm{ACC}}, X_{\mathrm{T}}) = \exp&\left[-\frac{X_{\mathrm{T}}^2}{2\sigma_{\mathrm{T}}^2}\right] \\
&\times \exp\left[-\frac{(N_{\mathrm{RMD}} - \langle N_{\mathrm{RMD}}\rangle)^2}{2\sigma_{\mathrm{RMD}}^2}\right] \times \exp\left[-\frac{(N_{\mathrm{ACC}} - \langle N_{\mathrm{ACC}}\rangle)^2}{2\sigma_{\mathrm{ACC}}^2}\right] \\
&\times \frac{e^{-N}}{N_{\mathrm{obs}}!}\prod_{i=1}^{N_{\mathrm{obs}}}\left[N_{\mathrm{sig}}S(\vec{x}_i) + N_{\mathrm{RMD}}R(\vec{x}_i) + N_{\mathrm{ACC}}A(\vec{x}_i)\right].
\end{aligned} \tag{8.1}
$$

The first and second lines in Eq. (8.1) stand for Gaussian constraint terms for the detector alignment uncertainty and the number of background events. These constraints are based on uncertainties from measurements. The last line in Eq. (8.1) is the extended likelihood term. Here, $N = N_{\mathrm{sig}} + N_{\mathrm{RMD}} + N_{\mathrm{ACC}}$ is the best estimate of the total number of events and N_{obs} is the total number of detected events in the analysis window. S, R and A are the PDFs for the signal, RMD background, and accidental background events, respectively. Section 8.4 describes the building of these PDFs. $\vec{x}_i$ is a set of observables for the i-th event.

Table 8.1: Handling of the RDC observables.

Condition	Used $t_{\mathrm{RDC}-\gamma}$	Used E_{RDC}
$\lvert t_{\mathrm{RDC}-\gamma}\rvert < 9.5\,\mathrm{ns} \wedge E_{\mathrm{RDC}} < 17\,\mathrm{MeV}$	Measured $t_{\mathrm{RDC}-\gamma}$	Measured E_{RDC}
$\lvert t_{\mathrm{RDC}-\gamma}\rvert < 9.5\,\mathrm{ns} \wedge E_{\mathrm{RDC}} > 17\,\mathrm{MeV}$	Measured $t_{\mathrm{RDC}-\gamma}$	17 MeV
$\lvert t_{\mathrm{RDC}-\gamma}\rvert < 9.5\,\mathrm{ns} \wedge$ No relavant hit on crystals	Measured $t_{\mathrm{RDC}-\gamma}$	−1 MeV
No RDC hit in $\lvert t_{\mathrm{RDC}-\gamma}\rvert < 9.5\,\mathrm{ns}$	10 ns	−1 MeV

Observables The set of observables $\vec{x}_i$ for the i-th event consists of the following parameters:

(1) E_γ; photon energy
(2) E_e; positron energy
(3) $t_{\mathrm{e}\gamma}$ (Eq. (4.23)); time difference between photon and positron
(4) n_{pTC}; the number of positron hits on the pTC
(5) $\theta_{\mathrm{e}\gamma}$ (Eq. (4.21)); relative polar angle between positron and photon
(6) $\phi_{\mathrm{e}\gamma}$ (Eq. (4.22)); relative azimuthal angle between positron and photon
(7) $t_{\mathrm{RDC}-\gamma}$ (Eq. (5.14)); time difference between positron hit on the RDC and photon
(8) E_{RDC}; positron energy measured by the RDC

As discussed in Sect. 7.2, the $t_{\mathrm{e}\gamma}$ resolution has a relevant dependence on the number of hits in the pTC, n_{pTC}. In order to take this into account, and considering that n_{pTC} has significantly different distributions in signal and background, this quantity is also included in the list of observables.

The RDC observables ($t_{\mathrm{RDC}-\gamma}$, E_{RDC}), newly introduced in the MEG II experiment, give additional information on the background likelihood. The RDC parameter ranges are defined as $\lvert t_{\mathrm{RDC}-\gamma}\rvert < 10\,\mathrm{ns}$ and $-1\,\mathrm{MeV} < E_{\mathrm{RDC}} < 17\,\mathrm{MeV}$. Since the RDC does not always detect a positron in an event, the events with no RDC hit have to be appropriately expressed to keep the integrated PDF at one with practical ease. Such events are treated to have $t_{\mathrm{RDC}-\gamma} = 10\,\mathrm{ns}$ and $E_{\mathrm{RDC}} = -1\,\mathrm{MeV}$. In addition, since the crystals do not always detect hits relevant to the hit on the plates, a dedicated category for such plate hits is prepared. When the RDC hit is detected only by plastic scintillators (i.e. no LYSO crystal hit matches the plastic scintillator hit), such events are classified into the special category, expressed as $E_{\mathrm{RDC}} = -1\,\mathrm{MeV}$. In addition, when measured E_{RDC} is higher than 17 MeV, such events are treated to have 17 MeV so as to suppress the statistical uncertainty for events with high E_{RDC}. Table 8.1 summarises the handling of the RDC observables.

8.3 Background estimation

The side-band samples estimate the Gaussian constraints for the number of background events in Eq. (8.1).

Number of accidental background The number of accidental background events was directly counted in the time side-bands ($1\,\mathrm{ns} < \lvert t_{\mathrm{e}\gamma}\rvert < 3\,\mathrm{ns}$). I counted 1456 events, which gives

$$\langle N_{\mathrm{ACC}}\rangle \pm \sigma_{\mathrm{ACC}} = 364.00 \pm 9.54. \tag{8.2}$$

Number of RMD background The number of the RMD background events is estimated by extrapolating that in the energy side-band ($46.5\,\mathrm{MeV} < E_\gamma < 48\,\mathrm{MeV}$) with wider $\Theta_{e\gamma}$ and E_e regions ($\Theta_{e\gamma} > 176°$ and $E_e > 49\,\mathrm{MeV}$) than the analysis window. When it is estimated with low E_e and non-collinear RMD samples, the number of the RMD background events in the analysis window deviates by 5 %. Considering the deviation and the statistical uncertainty of the RMD samples in the energy side-band, an uncertainty of 15 % is assigned.

$$\langle N_{\mathrm{RMD}} \rangle \pm \sigma_{\mathrm{RMD}} = 10.1 \pm 1.7 \tag{8.3}$$

8.4 Probability density function

This likelihood fit approach uses different PDFs for each event, called "event-by-event PDFs" because the detector resolutions depend on the detector conditions and the hit position in the detector. Incidentally, the physics model uncertainty on the signal polarisation appears in the θ_e distribution, as discussed in Sect. 1.1. This analysis does a model-independent search for $\mu \to e\gamma$, which means any θ_e dependencies are integrated out from all the PDFs. Therefore, θ_e and $\theta_\gamma \Leftrightarrow u_\gamma$ are not used as a conditional observable in the PDFs.

8.4.1 Signal PDF

The signal PDF is decomposed as

$$\begin{aligned} S(E_\gamma, E_e, t_{e\gamma}, \theta_{e\gamma}, \phi_{e\gamma}, t_{\mathrm{RDC}-\gamma}, E_{\mathrm{RDC}}, n_{\mathrm{pTC}}|\vec{q}) &= S_1(E_\gamma|v_\gamma, w_\gamma) \\ &\times S_2(E_e|\vec{\sigma}_e) \\ &\times S_3(t_{e\gamma}, n_{\mathrm{pTC}}|E_\gamma, E_e) \\ &\times S_4(\theta_{e\gamma}|E_e, w_\gamma, \vec{\sigma}_e, X_T) \\ &\times S_5(\phi_{e\gamma}|E_e, \theta_{e\gamma}, w_\gamma, \vec{\sigma}_e, \phi_e, X_T) \\ &\times S_6(t_{\mathrm{RDC}-\gamma}, E_{\mathrm{RDC}}), \end{aligned} \tag{8.4}$$

where $\vec{q}$ is a set of conditional observables consisting of v_γ, w_γ, $\vec{\sigma}_e$, ϕ_e, and X_T.

Signal E_γ PDF

The signal response is modelled as the sum of two *ExpGaus* functions defined in Eq. (6.19), which is used for the PDF $S_1(E_\gamma|v_\gamma, w_\gamma)$. The position dependence was included by segmenting the vw plane of the LXe detector into 10 (22) for the 2021 (2022) data, as illustrated in Fig. 8.2. Miscorrecting u position dependence of the energy scale could worsen the resolution when the u_γ dependence is integrated out. Such an effect was incorporated by making ensembles of u-integrated PDFs, in which each sampled PDF models different u-dependent energy scale miscalibration.

The whole procedure to make the signal PDF in an ensemble is

(1) Extract the spectra in different u regions measured with 54.9 MeV photons,
(2) Randomise the energy scale according to the uncertainty of the energy scale in each u region per vw-based segment,
(3) Simulate the u_γ distribution of signal events including efficiencies,
(4) Integrate u_γ-segmented spectra with a weight according to the simulated u_γ distribution.

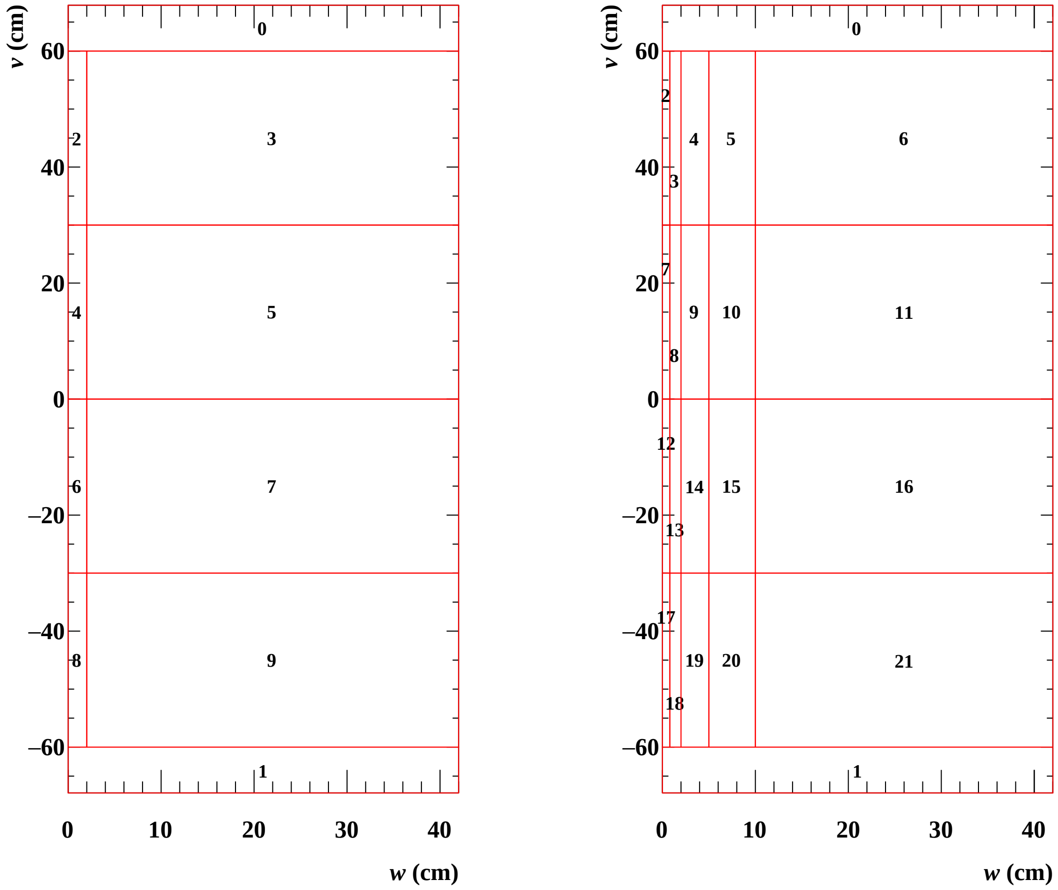

(a) 2021. (b) 2022.

Figure 8.2: Segmentation for E_γ PDFs.

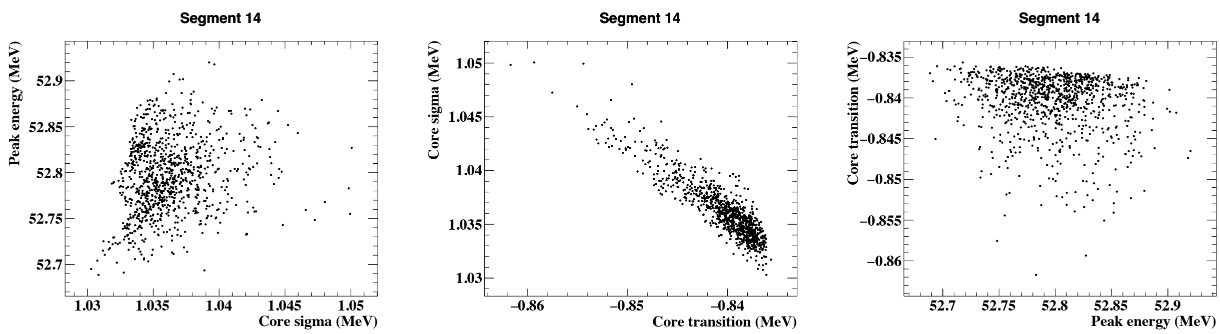

(a) Peak vs sigma. (b) Sigma vs transition. (c) Transition vs peak.

Figure 8.3: Distribution of signal E_γ PDF parameters in a segment, estimated with an ensemble of 1000 PDFs.

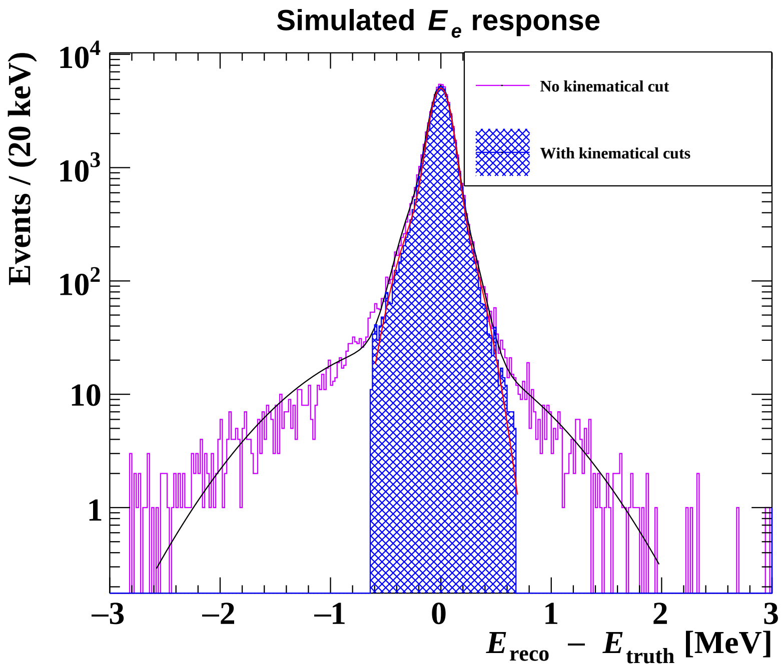

Figure 8.4: Positron response function in detector simulation [46]. The violet histogram is a distribution without any kinematical cuts and is fitted with a triple Gaussian function (black line). The hatched blue histogram is a distribution after applying angle and momentum cuts and is fitted with a double Gaussian function (red line). The long tail component reduction originates from the angle cut.

In an iteration of the above procedure, an ensemble of 1000 PDFs was generated in each of the segments divided by v and w. Figure 8.3 shows the core component distribution of PDF parameters in this ensemble. Here, the mean of each distribution corresponds to the best estimate of the PDF parameters, including the effects of the energy scale calibration uncertainty in u integration. On the other hand, the covariance of each distribution and the variance of each parameter give them uncertainty.

Uncertainty of signal E_γ PDF The uncertainty of the energy scale has two contributions: a global uncertainty that is common among all the segments and a segment-by-segment uncertainty. The global one comes from the temporal variation of the energy scale and the statistical uncertainty of the conversion factor calculation, which is 0.18 %, as summarised in Table 6.5. It was suppressed down to 60 % compared to the previous analysis [1] thanks to better use of the 17.6 MeV photons' data. The segment-by-segment uncertainty comes from different trends of the energy scale uniformity among different calibration sources, which is summarised in Fig. 6.43. Further details of estimating the above uncertainties were discussed in Sect. 6.2.9. In addition to the energy scale uncertainty, the uncertainties of the PDF shapes are also included based on the parameters' distribution in an ensemble, discussed above.

Signal E_e PDF

The signal E_e PDF $S_2(E_e|\vec{\sigma}_e)$ is parametrised as a double Gaussian function. It has a conditional observable: the covariance $\vec{\sigma}_e$ of the fit uncertainty estimated by the Kalman filter, which has a strong correlation with the sigma parameter in Gaussian functions. The Michel fit technique, described in Sect. 7.2, calculated the PDF parameters.

An error of E_e is equivalent to an error in the estimated track radius, which changes the back-propagated trajectory between the CDCH and the target. It then geometrically results in an error of ϕ_e.

The angle cut of $|\phi_{e\gamma}| < 40\,\mathrm{mrad}$ defining the analysis window diminishes the long tail component due to this correlation. This cannot be incorporated when the parameters are estimated from the background spectrum. Therefore, the detector simulation evaluated the effect of the angle cut on the signal PDF. The angle cut increased the fraction of two Gaussian components by 5–10 %, and that did not change the resolution, as shown in Fig. 8.4. The core-to-tail fraction parameter estimated by the Michel fit technique is corrected to finalise the signal E_e PDF.

Uncertainty of signal E_e PDF The uncertainty is based on the fit uncertainty of the response function in the Michel fitting and additional uncertainties from the corrections based on the detector simulation. The simulation-based corrections were adopted to the core-to-tail fraction of the double Gaussian function, which yields a 3 % additional uncertainty to the parameter.

Signal $t_{e\gamma}$ PDF

The signal $t_{e\gamma}$ PDF $S_3(t_{e\gamma}, n_{pTC}|E_\gamma, E_e)$ is decomposed into two PDFs:

$$S_3(t_{e\gamma}, n_{pTC}|E_\gamma, E_e) = S_{3a}(n_{pTC}) \times S_{3b}(t_{e\gamma}|n_{pTC}, E_\gamma, E_e). \tag{8.5}$$

The n_{pTC} PDF $S_{3a}(n_{pTC})$ is obtained from an MC simulation, shown in Fig. 7.8. When the reconstructed n_{pTC} is larger than 16, $n_{pTC} = 16$ is used instead, and the overall time resolution of the pTC measurement is also calculated accordingly. This is because the t_e resolution improvement as $\sigma_{single}/\sqrt{n_{pTC}}$ saturates there.

The $t_{e\gamma}$ PDF $S_{3b}(t_{e\gamma}|n_{pTC}, E_\gamma, E_e)$ is parametrised as a double Gaussian function based on the RMD samples in the energy side-band. Section 7.3.1 discussed the core parameters of the resolution function, giving an averaged core time resolution for signal events of 91 ps (94 ps) for the 2022 (2021) data.

There is a correlation between $t_{e\gamma}$ and E_e because E_e reconstruction error results in TOF measurement error. This small effect of $(18.9 \pm 0.5)\,\mathrm{ps/MeV}$ is included in the signal PDF. The correlation between $t_{e\gamma}$ and E_γ is also included as a resolution dependence on E_γ, which was evaluated with the π^0 calibration dataset.

Uncertainty of signal $t_{e\gamma}$ PDF The n_{pTC} uncertainty comes from the Poissonian statistical uncertainty of the simulation sample. The σ_{single} uncertainty is dominated by the systematic uncertainty of the even-odd analysis, which gives 5 % uncertainty. As the σ_{const} evaluation uses σ_{single} as an input, their uncertainties are correlated, which was evaluated by profiling σ_{single} parameter in the RMD peak fitting. This correlation changes σ_{const} by -1 ps when σ_{single} is overestimated by 5 %. The uncertainties in the global time offset and the PDF shape come from the fit uncertainty in the RMD peak fitting.

Signal angle PDFs

The signal angle PDFs $S_4(\theta_{e\gamma}|E_e, w_\gamma, \vec{\sigma}_e, X_T)$ and $S_5(\phi_{e\gamma}|E_e, \theta_{e\gamma}, w_\gamma, \vec{\sigma}_e, \phi_e, X_T)$ are modelled by a double Gaussian function representing the detector resolutions. The first contribution to the angular resolution comes from photon position resolution discussed in Sect. 7.1.1. Since it is dependent on w_γ, an event-by-event resolution of u_γ and v_γ is included in the signal PDFs. The other contribution is the positron vertexing and angular resolutions discussed in Sect. 7.2.1. They are parametrised by multiplying the pull resolution[1] with the event-by-event tracking uncertainty $\vec{\sigma}_e$.

[1]The pull resolution is defined as a true resolution divided by a nominal reconstruction uncertainty.

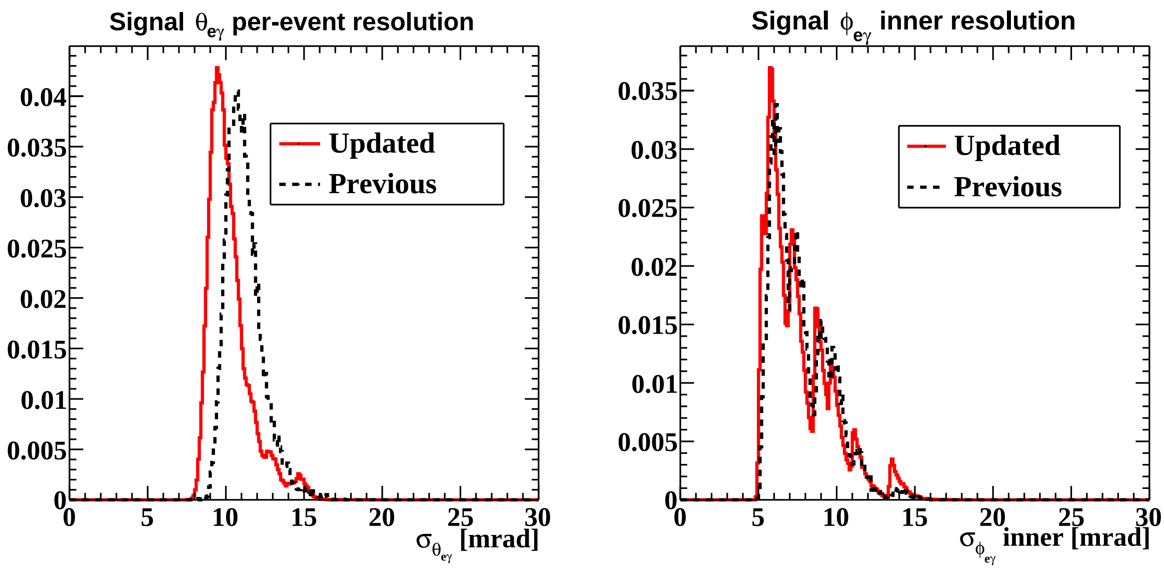

Figure 8.5: Distribution of event-by-event angular resolution in this analysis (red solid) and the previous one [1] (black dashed). The resolution is 10 % (5 %) better in $\theta_{e\gamma}$ ($\phi_{e\gamma}$) thanks to the positron selection update.

Figure 8.5 shows the event-by-event angular resolution distribution. Thanks to the positron selection update, discussed in Sect. 4.2, the resolution was improved by 10 % (5 %) in $\theta_{e\gamma}$ and $\phi_{e\gamma}$.

Correlations Complicated correlations among observables due to a geometrical mechanism must be considered to appropriately model the signal response, whose full description is given by Ref. [46]. Some correlation corrections were obtained from the data-driven double-turn analysis, and the others were from the signal MC simulation. The $\phi_{e\gamma}$ centre depends on the $\theta_{e\gamma}$, as shown in Fig. 8.6. The $\phi_{e\gamma}$ distribution is narrower after correlation correction, as shown in Fig. 8.7.

Uncertainty of signal angle PDFs The PDF uncertainty comes from both the detector alignment and the correlation and pull parameters. A wrong choice of the correlation and pull parameters changes only the PDF shape. On the other hand, the alignment causes a shift of the peak positions of the PDFs.

The correlation and pull parameters' uncertainties differ depending on their estimation methods. The data-driven double-turn analysis estimated some of the correlation parameters and all the pull parameters, which gives 5 % uncertainties to their parameters. The other correlation parameters estimated only from a simulation have 10 % uncertainties according to the agreement between the double-turn analysis on data and the simulation.

The misalignment between the CDCH and the target (LXe detector) changes the θ_e and ϕ_e (θ_γ and ϕ_γ) reconstructions. Since the target misalignment affects the angle PDFs by changing the track propagation, the misalignment in the direction perpendicular to the target plane is important. The alignment uncertainty between the CDCH and the target is estimated as 50 µm, as discussed in Sect. 6.7.1. The uncertainty on the alignment between the CDCH and the LXe detector is estimated to be 400 µm, as discussed in Sect. 6.7.2.

Signal RDC PDF

The signal RDC PDF $S_6(t_{\mathrm{RDC}-\gamma}, E_{\mathrm{RDC}})$ is built in a histogram-based format, which means the use of a step function in the unbinned likelihood fitting. The parameter width in the step function, i.e. the bin

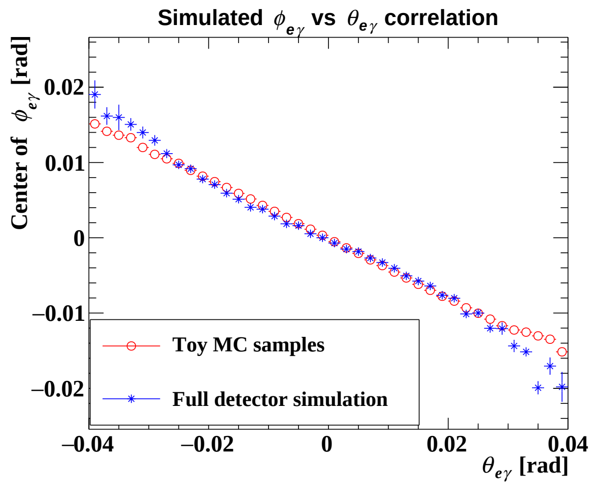

Figure 8.6: Simulated correlation between $\phi_{e\gamma}$ centre vs $\theta_{e\gamma}$ [46].

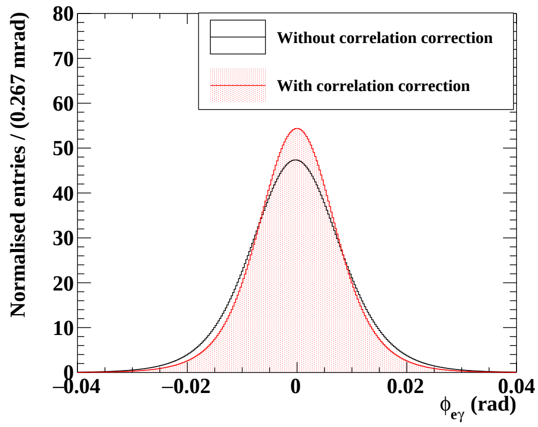

Figure 8.7: Signal $\phi_{e\gamma}$ distribution with (red hatched) and without (black) the correction. The distributions are normalised to one after integration.

width of the histogram, varies flexibly according to the tradeoff between the available statistics and the importance of information within each bin.

The PDF was estimated using the MEG-triggered samples in the off-peak region in Fig. 5.24, as shown in Fig. 8.11(f) and (g). It strongly depends on run periods for two reasons. The first one is the hit rate of accidental positrons, which is mainly determined by the muon stopping rate on the target. This makes a difference in the probability of having events in the off-peak region of the timing distribution. The other reason is the fact that the RDC was not installed for several periods for safety reasons (Chap. 3), in particular, at the beginning of the run 2021.

Uncertainty of signal RDC PDF The uncertainty of the PDF comes from the statistics used in the PDF evaluation. The bin-by-bin uncertainties are assigned according to the Poisson fluctuation.

8.4.2 Accidental background PDF

The accidental background PDF is decomposed as

$$\begin{aligned} A(E_\gamma, E_e, t_{e\gamma}, \theta_{e\gamma}, \phi_{e\gamma}, t_{\mathrm{RDC}-\gamma}, E_{\mathrm{RDC}}, n_{\mathrm{pTC}}|\vec{q}) = {} & A_1(E_\gamma|v_\gamma, w_\gamma) \\ & \times A_2(E_e|\vec{\sigma}_e) \\ & \times A_3(t_{e\gamma}, n_{\mathrm{pTC}}|E_e, w_\gamma) \\ & \times A_4(\theta_{e\gamma}) \\ & \times A_5(\phi_{e\gamma}|v_\gamma) \\ & \times A_6(t_{\mathrm{RDC}-\gamma}, E_{\mathrm{RDC}}|E_\gamma). \end{aligned} \tag{8.6}$$

Accidental E_γ PDF

The accidental E_γ PDF $A_1(E_\gamma|v_\gamma, w_\gamma)$ is modelled as Eq. (6.20), using events in time side-bands. Since background spectra differ in photon positions, for instance, larger cosmic-ray contribution at the v edges, the PDF is built separately by segments (Fig. 8.2). The spectra also depend on the beam intensity, resulting from imperfect pileup elimination. Thus, the PDF is period-dependently built.

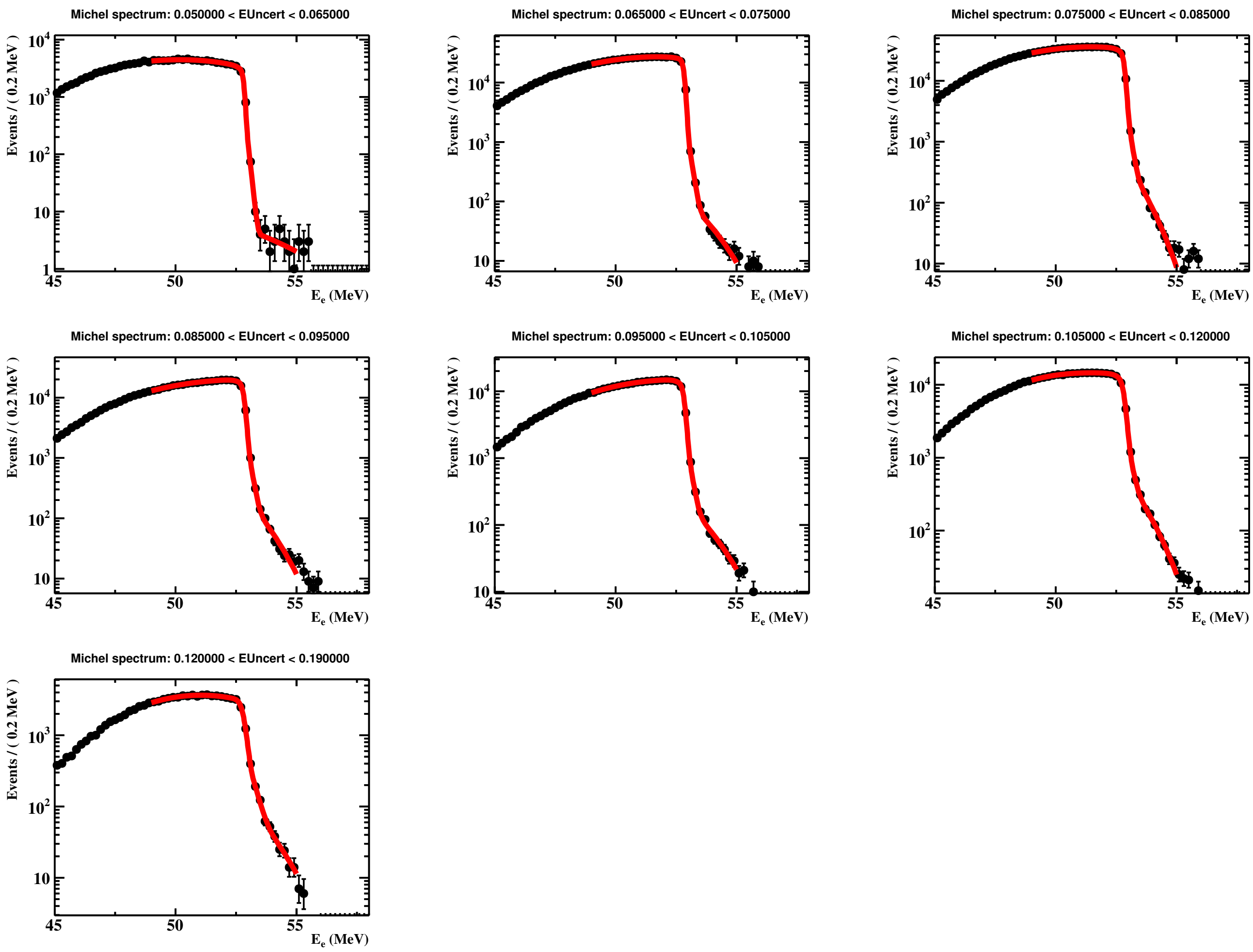

Figure 8.8: Evaluation of accidental E_e PDF, with σ_{E_e}-based categorisation [46].

Accidental E_e PDF

The accidental E_e PDF $A_2(E_\mathrm{e}|\vec{\sigma}_\mathrm{e})$ is extracted from time side-bands with the parametrisation of Eq. (6.30). The PDF is conditioned by $\vec{\sigma}_\mathrm{e}$ as well as the signal PDF. Contrary to Eq. (6.30), the acceptance function additionally introduces inefficiency in the high-momentum side as well as the low-momentum side to account for the detector material distribution, which affects the tracking uncertainty via scattering.

Figure 8.8 shows distributions of background data samples and their fit in each Kalman-covariance-based category. The increased trend in the fraction of the long-tail resolution component can be seen with a larger σ_{E_e} value.

Accidental $t_{\mathrm{e}\gamma}$ PDF

With the similar idea to the signal PDF, the accidental $t_{\mathrm{e}\gamma}$ PDF $A_3(t_{\mathrm{e}\gamma}, n_\mathrm{pTC}|E_\mathrm{e}, w_\gamma)$ is also decomposed into two:

$$A_3(t_{\mathrm{e}\gamma}, n_\mathrm{pTC}|E_\mathrm{e}, w_\gamma) = A_{3\mathrm{a}}(n_\mathrm{pTC}|E_\mathrm{e}) \times A_{3\mathrm{b}}(t_{\mathrm{e}\gamma}|w_\gamma). \tag{8.7}$$

The n_pTC PDF $A_{3\mathrm{a}}(n_\mathrm{pTC}|E_\mathrm{e})$ was evaluated from the time side-band samples. With the observed correlation shown in Fig. 8.9, the n_pTC parameter is conditioned by E_e.

The $t_{\mathrm{e}\gamma}$ PDF $A_{3\mathrm{b}}(t_{\mathrm{e}\gamma}|w_\gamma)$ is expected to be flat. However, the time-walk effect in the trigger, discussed in Sect. 3.2, caused the non-flat $t_{\mathrm{e}\gamma}$ distribution only during run 2021, which was parametrised

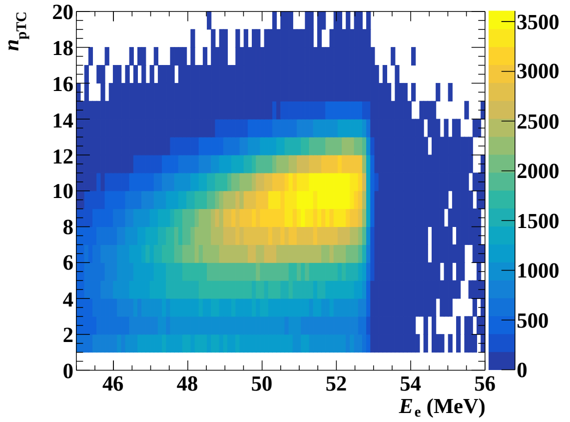

Figure 8.9: n_{pTC} dependence on E_{e}, observed in time side-bands.

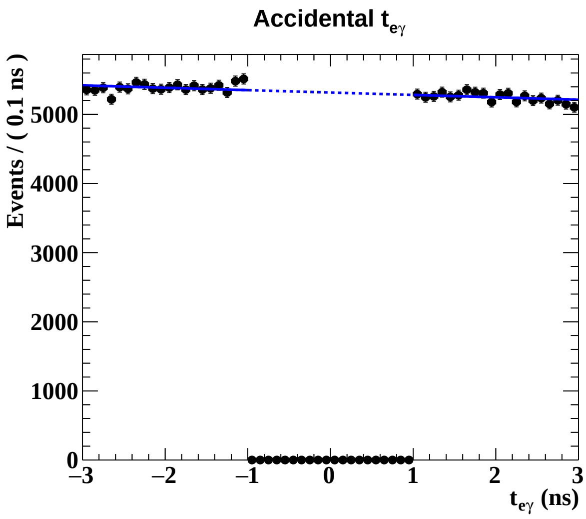

Figure 8.10: $t_{e\gamma}$ distribution for the accidental background events in 2021 and its fit with a linear function (blue line) [46]. No events are found in $|t_{e\gamma}| < 1$ ns due to the blinding.

by a linear function. The slope parameter was correlated only with w_γ.

Accidental angle PDFs

The accidental angle PDFs $A_4(\theta_{e\gamma})$ and $A_5(\phi_{e\gamma}|v_\gamma)$ are investigated with the time side-band data and parametrised with polynomial functions up to the fourth order. Since the $\phi_{e\gamma}$ distribution has a strong dependence on v_γ due to the edge effect of the fiducial cut of Eq. (4.15), the $\phi_{e\gamma}$ PDF was evaluated after slicing the full acceptance range into five v_γ ranges.

Accidental RDC PDF

The accidental RDC PDF $A_6(t_{\mathrm{RDC}-\gamma}, E_{\mathrm{RDC}}|E_\gamma)$ is built in a histogram-based format and depending on the run period, as done for the signal RDC PDF. The PDF is conditioned by E_γ because the difference in the E_γ spectra originating from RMD and AIF induces E_γ dependence on the $t_{\mathrm{RDC}-\gamma}$ and E_{RDC} distributions, as discussed in Chap. 5. The binning was finer for the 2022 data than the 2021 data since there were approximately seven times higher statistics. The extraction used the MEG-triggered samples around the peak in Fig. 5.24.

8.4.3 RMD background PDF

The RMD background PDF is decomposed as

$$\begin{aligned} R(E_\gamma, E_{\mathrm{e}}, t_{e\gamma}, \theta_{e\gamma}, \phi_{e\gamma}, t_{\mathrm{RDC}}, E_{\mathrm{RDC}}, n_{\mathrm{pTC}}|\vec{q}) = {} & R_1(E_\gamma, E_{\mathrm{e}}, \theta_{e\gamma}, \phi_{e\gamma}|v_\gamma, w_\gamma) \\ & \times R_2(t_{e\gamma}, n_{\mathrm{pTC}}|E_{\mathrm{e}}, E_\gamma) \\ & \times S_6(t_{\mathrm{RDC}-\gamma}, E_{\mathrm{RDC}}). \end{aligned} \tag{8.8}$$

Here, the RDC PDF is shared with the signal because they are identical; the detected RDC hit is accidental and not associated with the detected photon in both signal and RMD events.

RMD kinematics PDF

The RMD kinematical PDF $R_1(E_\gamma, E_e, \theta_{e\gamma}, \phi_{e\gamma}|v_\gamma, w_\gamma)$ building begins with the theoretical differential branching ratio given in Ref. [26]. The opening angle parameter is transformed into the $(\theta_{e\gamma}, \phi_{e\gamma})$ parameter space. The theoretical spectrum is modified to incorporate the detector responses, i.e. efficiency and resolution.

RMD $t_{e\gamma}$ PDF

The RMD $t_{e\gamma}$ PDF $R_2(t_{e\gamma}, n_{\mathrm{pTC}}|E_e, E_\gamma)$ can be decomposed into

$$R_2(t_{e\gamma}, n_{\mathrm{pTC}}|E_e, E_\gamma) = A_{3b}(n_{\mathrm{pTC}}|E_e) \times R_{2b}(t_{e\gamma}|n_{\mathrm{pTC}}, E_\gamma), \tag{8.9}$$

where the same n_{pTC} PDF is used as that for the accidental backgrounds. $R_{2b}(t_{e\gamma}|n_{\mathrm{pTC}}, E_\gamma)$ is similar to the signal PDF, with the resolution parametrised as Eq. (8.5). The only difference is that the E_e dependence is removed because the RMD positron has a continuous spectrum, and the correlation between the TOF error and E_e is negligible.

8.4.4 Period-dependent event weight

As the accidental background rate increases with a more intense beam, the signal-to-background ratio depends on the period. The dataset is divided into different years and periods according to the beam intensity, and period-dependent weights are included as PDFs. The period indices are defined as follows:

- Run 2021: 0, 1, 2 and 3 stand for 3, 2, 4 and $5 \times 10^7\ \mathrm{s}^{-1}$, and
- Run 2022: 4, 5 and 6 stand for 3, 4 and $5 \times 10^7\ \mathrm{s}^{-1}$,

respectively.

The weight of the accidental background events is evaluated by counting the number of events in time side-bands for each period. Similarly, the weight of the signal events is obtained from the Michel positron counting result in each period. Since the RMD rate is expected to be proportional to the normalisation factor k, the weight assigned to the RMD background events is identical to that for the signal.

8.4.5 Summary of PDFs

The projected PDFs of the observables are shown in Fig. 8.11 to see the response difference between signal and background events. Here, I generated a pseudo experiment with $(N_{\mathrm{sig}}, N_{\mathrm{ACC}}, N_{\mathrm{RMD}}) = (2500, 2500, 2500)$ to take the event-by-event PDFs approch into account. The best-fit values are consistent within the uncertainties.

Relative signal likelihood The relative signal likelihood R_{sig} is defined as

$$R_{\mathrm{sig}} = \log_{10}\left(\frac{S(\vec{x})}{(1-r)\cdot A(\vec{x}) + r\cdot R(\vec{x})}\right) \tag{8.10}$$

where r is the expected fraction of the RMD background events to the total background ones, which is 2.7 ‰ according to Sect. 8.3. Figure 8.12 shows the R_{sig} distributions in massive pseudo experiments with 1×10^8 events for each event type (signal, accidental background, and RMD background). The R_{sig} for the signal events is concentrated around the high-R_{sig} edge of the background R_{sig} distribution.

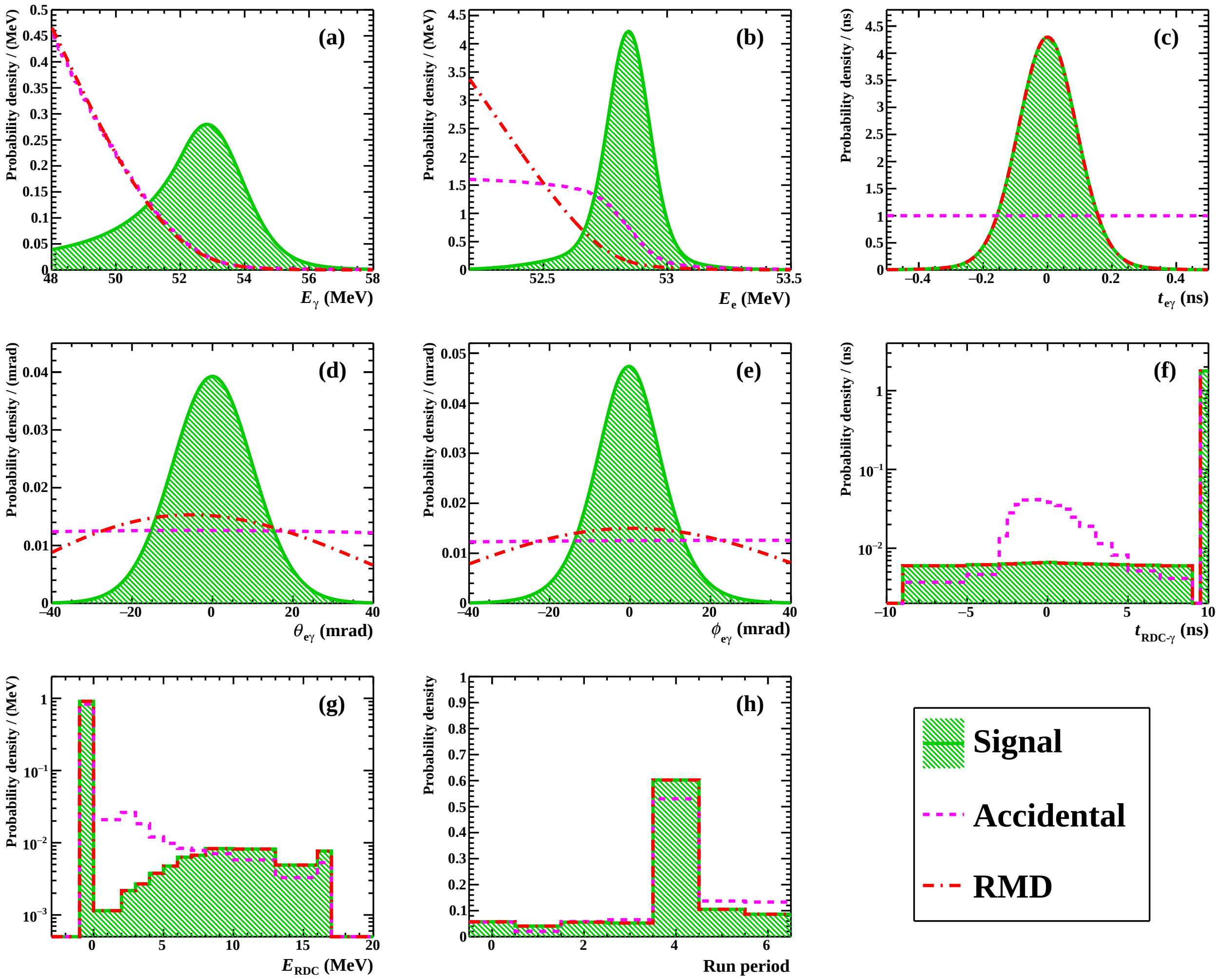

Figure 8.11: Projected one-dimensional PDFs for the signal (green solid), accidental (magenta dashed), and RMD background (red dashed-dotted).

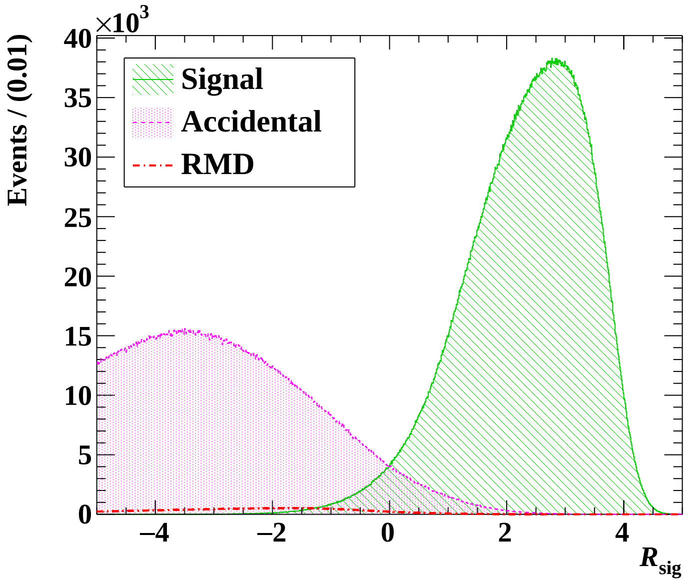

Figure 8.12: R_{sig} distributions for the signal (green), accidental (magenta), and RMD background events (red). The distribution for the RMD background is scaled based on $r = 2.7\,\%$.

8.5 Confidence interval

The confidence interval of N_{sig} is calculated based on the Feldman-Cousins approach [110] with the profile-likelihood ratio ordering [7]. To be used as a test statistic, the profile-likelihood ratio λ_p is defined as

$$\lambda_p(N_{\mathrm{sig}}) = \begin{cases} \dfrac{\mathcal{L}\left(N_{\mathrm{sig}}, \hat{\hat{N}}_{\mathrm{ACC}}(N_{\mathrm{sig}}), \hat{\hat{N}}_{\mathrm{RMD}}(N_{\mathrm{sig}}), \hat{\hat{X}}_{\mathrm{T}}(N_{\mathrm{sig}})\right)}{\mathcal{L}\left(\hat{N}_{\mathrm{sig}}, \hat{N}_{\mathrm{ACC}}, \hat{N}_{\mathrm{RMD}}, \hat{X}_{\mathrm{T}}\right)} & \text{if } \hat{N}_{\mathrm{sig}} \geq 0, \\[2ex] \dfrac{\mathcal{L}\left(N_{\mathrm{sig}}, \hat{\hat{N}}_{\mathrm{ACC}}(N_{\mathrm{sig}}), \hat{\hat{N}}_{\mathrm{RMD}}(N_{\mathrm{sig}}), \hat{\hat{X}}_{\mathrm{T}}(N_{\mathrm{sig}})\right)}{\mathcal{L}\left(0, \hat{\hat{N}}_{\mathrm{ACC}}(0), \hat{\hat{N}}_{\mathrm{RMD}}(0), \hat{\hat{X}}_{\mathrm{T}}(0)\right)} & \text{if } \hat{N}_{\mathrm{sig}} < 0, \end{cases} \tag{8.11}$$

where the single-hat variables ($\hat{N}_{\mathrm{sig}}, \hat{N}_{\mathrm{ACC}}, \hat{N}_{\mathrm{RMD}}, \hat{X}_{\mathrm{T}}$) are the values that maximise the likelihood; the double-hat variables ($\hat{\hat{N}}_{\mathrm{ACC}}(N_{\mathrm{sig}}), \hat{\hat{N}}_{\mathrm{RMD}}(N_{\mathrm{sig}}), \hat{\hat{X}}_{\mathrm{T}}(N_{\mathrm{sig}})$) are the values that maximise the likelihood for the specified N_{sig}. Equation (8.11) has two cases because the best-fit $\hat{N}_{\mathrm{sig}}$ is required to be within the physical region, namely $N_{\mathrm{sig}} \geq 0$. This test statistic gives a suitable property for a statistical test; a larger $-\log \lambda_p(N_{\mathrm{sig}})$ suggests that the tested value of N_{sig} is less likely the case.

Pseudo experiment

Pseudo experiments are massively generated based on the PDFs to evaluate the distribution of the profile-likelihood ratio $\lambda_p(N_{\mathrm{sig}})$. N_{sig} is scanned from 0 to 30 with appropriate steps of 0.3 to 5, with finer steps in regions of interest. The number of pseudo experiments with a specified N_{sig} is an order of 10^5 to suppress the statistical uncertainty of a confidence level determination.

Confidence interval calculation

A confidence level is defined as the probability of a negative log-profile-likelihood ratio, $-\log \lambda_p(N_{\mathrm{sig}})$, being less than the observed $-\log \lambda_p(N_{\mathrm{sig}})$ when testing a specified N_{sig} value, which is notated as

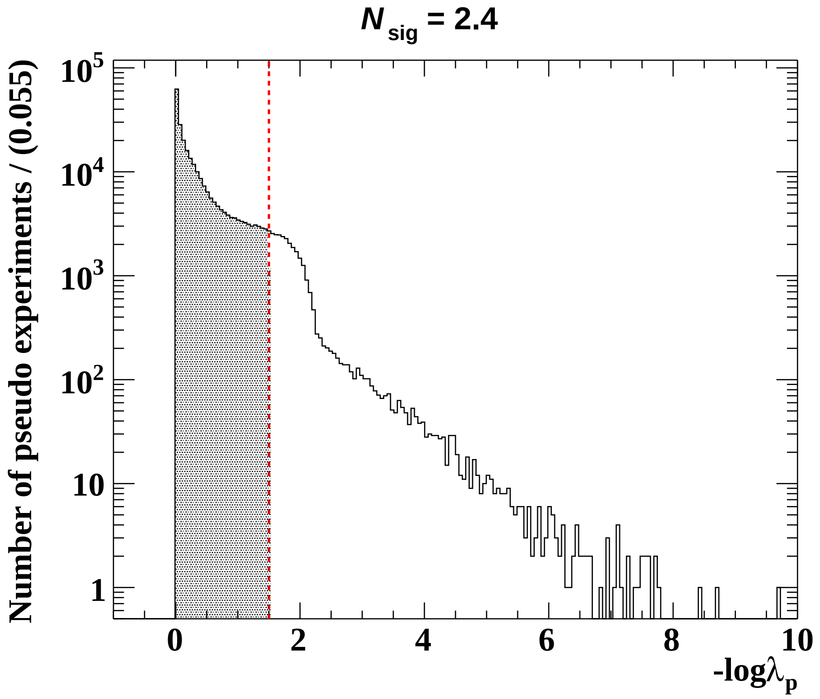

Figure 8.13: Profile likelihood ratio distribution at N_{sig} of 2.4 and an example of confidence level calculation. If the observed $-\log\lambda_p(N_{\text{sig}} = 2.4)$ is 1.5 shown by the red dashed line, the confidence level at a given N_{sig} of 2.4 is calculated as 89.8 % by counting the number of pseudo experiments having $-\log\lambda_p < 1.5$.

$CL(N_{\text{sig}})$. This probability is directly calculated from an ensemble of pseudo experiments with the given N_{sig}, as illustrated in Fig. 8.13. The confidence level at $N_{\text{sig}} = 0$ gives p-value for a test on the null-signal hypothesis, by $1 - CL(0)$.

The confidence interval for N_{sig} is then calculated by requiring CL to exceed the defined threshold: 90 % in this analysis. The 90 % confidence interval of N_{sig} is finally translated to that of the branching ratio $\mathcal{B}$ by the normalisation factor k.

8.5.1 Incorporation of systematic uncertainties

Systematic uncertainties associated with the PDFs and the normalisation factor k are incorporated into the analysis using two complementary approaches. The first involves profiling these uncertainties as nuisance parameters within the likelihood function, while the second applies stochastic variations to the PDFs based on their estimated uncertainties. Although the profiling method is generally regarded as more robust, it is computationally intensive. Consequently, this approach is reserved for the largest source of systematic uncertainty, which is the detector misalignment parameter X_{T}. All other sources of systematic uncertainty are treated using the random fluctuation method to balance computational efficiency with analytical precision.

8.6 Normalisation

The normalisation factor k, defined in Eq. (1.15), is evaluated by counting Michel positrons and correcting the number with effects of the trigger and detector responses. An independent estimation method based on counting RMD photon-positron pairs gives a cross-check.

Table 8.2: Parameters for the normalisation factor estimation based on the Michel positron counting method.

	2021 previous (partially modified from [46])	2021	2022
$N^{e\nu\bar{\nu}}$	114 739	115 587	474 612
$P^{e\nu\bar{\nu}}$	2×10^6–7×10^6 [a]	2×10^6–7×10^6 [a]	3×10^6–1.6×10^7 [a]
$P^{e\gamma}$	1–20 [a]	1–20 [a]	1
$\varepsilon_{\mathrm{TRG}}^{e\gamma}$	0.80 ± 0.01 [45]	0.88 ± 0.02	0.91 ± 0.02
$\varepsilon_{\mathrm{TRG}}^{e\nu\bar{\nu}}$	0.91 ± 0.01 [b]	0.91 ± 0.01 [b]	0.98 ± 0.01 [b]
$\varepsilon_{e}^{e\gamma}/\varepsilon_{e}^{e\nu\bar{\nu}}$	1.09	1.07	1.04
ε_γ	$0.67 \pm 0.02 \times 0.92 \pm 0.02$	$0.67 \pm 0.02 \times 0.93 \pm 0.01$	$0.67 \pm 0.02 \times 0.93 \pm 0.01$
$A_\gamma^{e\gamma}$	0.97 ± 0.01	0.97 ± 0.01	0.97 ± 0.01
$\varepsilon_{\mathrm{sel}}^{e\gamma}$	0.93 ± 0.03	0.93 ± 0.03	0.93 ± 0.03
k_{Michel}	$(2.6 \pm 0.1) \times 10^{12}$	$(2.8 \pm 0.1) \times 10^{12}$	$(1.05 \pm 0.05) \times 10^{13}$

[a] Depending on periods.
[b] Depending on beam intensities R_μ.

8.6.1 Michel positron counting method

Counting Michel positrons above 50 MeV in the pre-scaled pTC-triggered data gives the calculation of the normalisation factor k_{Michel} with several corrections considering response differences between Michel and signal positron-photon pairs:

$$\begin{aligned} k_{\mathrm{Michel}} &= \frac{N^{e\nu\bar{\nu}}}{\mathcal{B}^{e\nu\bar{\nu}}} \cdot \frac{P^{e\nu\bar{\nu}}}{P^{e\gamma}} \cdot \frac{\varepsilon_{\mathrm{TRG}}^{e\gamma}}{\varepsilon_{\mathrm{TRG}}^{e\nu\bar{\nu}}} \cdot \frac{\varepsilon_{e}^{e\gamma}}{\varepsilon_{e}^{e\nu\bar{\nu}}} \cdot \varepsilon_\gamma \cdot A_\gamma^{e\gamma} \cdot \varepsilon_{\mathrm{sel}}^{e\gamma} \\ &= (1.34 \pm 0.07) \times 10^{13}, \end{aligned} \tag{8.12}$$

where $N^{e\nu\bar{\nu}}$ is the number of Michel positrons at $E_e > 50$ MeV; $\mathcal{B}^{e\nu\bar{\nu}} = 0.101$ is the branching ratio of the decay with $E_e > 50$ MeV; P is pre-scaling factors for triggering; ε is efficiencies; and A is an acceptance correction. The following paragraphs explain each parameter tabulated in Table 8.2.

Pre-scaling factors Pre-scaling factors $P^{e\gamma}$ and $P^{e\nu\bar{\nu}}$ are the ones of the MEG trigger and the pTC trigger, respectively. $P^{e\gamma}$ was not 1 at the beginning of run 2021, whose period dependence was shown in Fig. 3.5, in order to keep the data rate below the capacity. In the other periods, including run 2022, $P^{e\gamma}$ was 1. $P^{e\nu\bar{\nu}}$ ranged between 3×10^6–1.6×10^7 (2×10^6–7×10^6) during run 2022 (2021), depending on the period.

Trigger efficiency correction The efficiency for the MEG trigger $\varepsilon_{\mathrm{TRG}}^{e\gamma}$ was evaluated by a product of efficiencies for three trigger logics: E_γ, time coincidence, and direction match (DM), which was described in Sect. 2.6.2. The E_γ and time coincidence trigger efficiencies were evaluated based on the E_γ and $t_{e\gamma}$ distributions with different thresholds [45]. These efficiencies were improved by 3 % (4 %) for the E_γ (time coincidence) trigger from run 2021 to 2022. The improvement of the E_γ trigger efficiency was thanks to a lower threshold and its better uniformity, as shown in Fig. 3.6; and that of the time coincidence trigger efficiency was thanks to time-walk effect mitigation due to the use of PMTs for online t_γ computation, as discussed in Sect. 3.2.

The DM trigger efficiency was evaluated by measuring the matching efficiency of the DM look-up table for pairs of the positron and photon positions at the trigger level in artificial back-to-back events. Since there is no physical source of back-to-back positron-photon pairs, a set of artificial events is produced by setting the point on the inner face of the LXe detector to which the positron track is back-propagated from the target as the reconstructed photon hit position, based on the pTC-triggered events taken during the physics runs. The positron and photon hit positions at the trigger level are calculated as follows:

- *Position hit position at the trigger level*: The positron hit position at the trigger level is calculated by the positron first impact counter in the pTC. The positron track was reconstructed based on the offline reconstruction in the previous analysis, whereas it is based on the results calculated in the FPGA in this analysis. The FPGA calculation sometimes fires multiple counters for a single positron track, resulting in more trigger candidates.
- *Photon hit position at the trigger level*: The photon hit position at the trigger level is calculated based on the size of the signal measured with a unit of WaveDREAM boards corresponding to 16 MPPCs. The offline- and online-reconstructed photon positions were compared using E_γ-triggered events taken with the muon beam in the previous analysis, but are compared using 17.6 MeV photons to suppress a statistical uncertainty on the E_γ-triggered sample in this analysis.

As a result of these estimation updates, it was found that the previous analysis underestimated the DM trigger efficiency by 8 % and its uncertainty: this evaluation gives (95.3 ± 1.4) % while the previous one did (88.5 ± 0.5) % for the 2021 dataset. The additional systematic uncertainty is considered, based on the fact that the DM trigger efficiency depends on the positron energy (1.4 % difference at (52.8 ± 0.5) MeV). The efficiency was assessed to be (92.1 ± 1.8) % for the 2022 dataset, which decreased due to the reduction of fake positron candidates aimed at achieving a higher overall trigger efficiency. In summary, the MEG trigger efficiency $\varepsilon_{\mathrm{TRG}}^{\mathrm{e}\gamma}$ was (88 ± 2) % for 2021 and (91 ± 2) % for 2022.

The deadtime of the trigger logic (50 ns in run 2021 and 12.5 ns in run 2022) caused the pTC trigger inefficiency. The $\varepsilon_{\mathrm{TRG}}^{\mathrm{e}\nu\bar{\nu}}$ was assessed to be approximately 98 % (91 %) with an uncertainty of 1 %, depending on the muon beam rate.

Positron efficiency correction In the Michel positron counting method, the pTC-triggered sample was fitted with Eq. (6.30). Since the DM logic in the MEG trigger causes the positron efficiency dependent on E_e, the efficiency difference must be corrected. The correction factor $\varepsilon_\mathrm{e}^{\mathrm{e}\gamma}/\varepsilon_\mathrm{e}^{\mathrm{e}\nu\bar{\nu}}$ was estimated as 1.04 (1.07) for the 2022 (2021) dataset. The yearly difference comes from the efficiency difference in the low-momentum region, which arises from the difference in the beam profile on the target. The previous factor for the 2021 dataset (1.09) was overestimated because it used a non-final reconstructed sample.

Photon efficiency correction Since the Michel positron counting method is independent of photon measurement, the photon efficiency must be taken into account. The photon efficiency ε_γ is given by a product of a detection efficiency of (67 ± 2) % (Sect. 7.1.4) and an analysis efficiency of (93.4 ± 0.6) % (Sect. 4.1.6).

Acceptance correction The positron acceptance is defined by the uv fiducial region at $w = 0$ cm of the LXe detector. When a photon paired with a positron track is converted in a deep region, such a photon can be reconstructed outside the fiducial volume of the LXe detector in the large $|\theta_\gamma|$ region, which is the inefficiency to be corrected here. The correction factor for the geometrical acceptance $A_{\gamma}^{e\gamma}$ was evaluated as (97 ± 1) %.

Selection efficiency correction The selection efficiency correction $\varepsilon_{\mathrm{sel}}^{e\gamma}$ is introduced to correct two major inefficiencies that are relevant to the likelihood analysis. The first inefficiency is positron missing-turn tracks dropped in the pair timing selection, which is 4 %. The other is tails in angular and momentum measurements outside the analysis window, which gives 3 %. In total, the correction factor $\varepsilon_{\mathrm{sel}}^{e\gamma}$ is 93 % with an uncertainty of 3 %.

8.6.2 Cross-check by RMD-based method

The other method for the normalisation factor estimation uses RMD events distributed in the energy side-band in the MEG-triggered data. As in the Michel positron counting method, k_{RMD} is expressed as

$$k_{\mathrm{RMD}} = \frac{N^{e\nu\bar{\nu}\gamma}}{\mathcal{B}^{e\nu\bar{\nu}\gamma}} \cdot \frac{\varepsilon_{\mathrm{TRG}}^{e\gamma}}{\varepsilon_{\mathrm{TRG}}^{e\nu\bar{\nu}\gamma}} \cdot \frac{\varepsilon_{\mathrm{e}}^{e\gamma}}{\varepsilon_{\mathrm{e}}^{e\nu\bar{\nu}\gamma}} \cdot \frac{\varepsilon_{\gamma}^{e\gamma}}{\varepsilon_{\gamma}^{e\nu\bar{\nu}\gamma}} \cdot \frac{\varepsilon_{\mathrm{sel}}^{e\gamma}}{\varepsilon_{\mathrm{sel}}^{e\nu\bar{\nu}\gamma}}, \tag{8.13}$$

where $N^{e\nu\bar{\nu}\gamma}$ is the number of RMD events in the energy side-band with wider E_{e} and opening angle $\Theta_{e\gamma}$ ranges than the signal region ($E_{\mathrm{e}} > 49\,\mathrm{MeV}$ and $\Theta_{e\gamma} > 176°$, respectively); $\mathcal{B}^{e\nu\bar{\nu}\gamma} \sim 8.2 \times 10^{-11}$ is the partial branching ratio of RMD in the relevant kinematic range; and ε is efficiencies on the anology of Eq. (8.12), discussed later.

The normalisation factor was calculated yearly as

$$\begin{aligned} k_{\mathrm{RMD}}^{2021} &= (2.4 \pm 0.4) \times 10^{12}, \\ k_{\mathrm{RMD}}^{2022} &= (0.94 \pm 0.07) \times 10^{13}, \end{aligned} \tag{8.14}$$

where only the statistical uncertainty is written. The systematic uncertainty is estimated as 10 % based on the self-consistency with different kinematical sub-ranges. Equation (8.14) is consistent with the Michel positron counting method k_{Michel}, tabulated in Table 8.2, within the uncertainties.

Trigger efficiency correction The kinematical difference between the signal and RMD events causes the difference in the trigger efficiency between the two channels. It consists of two inefficiencies from DM and E_{γ} threshold logics, which make RMD event collection less efficient. The DM effect is evaluated by analysing $\Theta_{e\gamma}$-dependent efficiency with accidental events. The E_{γ} threshold effect is evaluated in the background spectrum fitting, explained in Sect. 6.2.9.

Positron efficiency correction E_{e}-dependent detection efficiency, i.e. acceptance, is extracted from the Michel fitting.

Photon efficiency correction The counting of events with the limited photon energy range has both inefficiencies (the true photon energy inside the range but the reconstructed one outside the range) and overestimations (vice versa) due to the finite resolution. The correction factor for these effects is evaluated by convoluting the RMD theoretical spectrum with the signal E_{γ} PDF.

Selection efficiency correction The inefficiencies due to the kinematical tails are smaller in the $N^{e\nu\bar{\nu}\gamma}$ estimation because of the wider cut ranges and the continuous spectrum.

Chapter 9

Results and discussion

9.1 Sensitivity

The sensitivity is defined as the median of 90 % upper limit on the branching ratio in pseudo experiments with a null-signal hypothesis, i.e. $N_{\mathrm{sig}} = 0$. Figure 9.1 shows the simulated 90 % upper limit distribution. The median value of the limit is 2.2×10^{-13} (2.1×10^{-13}) with (without) systematics, which is illustrated as a dashed line in Fig. 9.1. The contribution to the sensitivity due to the systematic uncertainties is 3 %, whose breakdown is tabulated in Table 9.1.

9.1.1 Sensitivity cross-check in time side-bands

A likelihood analysis of the time side-bands is performed for the sanity check of the analysis. The data in the time side-bands can essentially be regarded as pure accidental background. The likelihood function is modified for the time side-bands in two ways: the constraint term for the N_{RMD} in Eq. (8.1) is removed, and the $t_{\mathrm{e}\gamma}$ centre is shifted. The time side-band regions were divided into four sub-ranges; $[-3\,\mathrm{ns}, -2\,\mathrm{ns}]$, $[-2\,\mathrm{ns}, -1\,\mathrm{ns}]$, $[1\,\mathrm{ns}, 2\,\mathrm{ns}]$, and $[2\,\mathrm{ns}, 3\,\mathrm{ns}]$. The fit results on these four side-bands are overlaid in Fig. 9.1. The third time side-band ($1\,\mathrm{ns} < t_{\mathrm{e}\gamma} < 2\,\mathrm{ns}$) obtained the best-fit value of $N_{\mathrm{sig}} = 1.92$ and the 8 % p-value for the background-only hypothesis, which set an interval of $0.02 < N_{\mathrm{sig}} < 6.98$. It is interpreted as the upward fluctuation of accidental background events. In general, they are statistically consistent with null-signal pseudo experiments.

Table 9.1: Breakdown of the impact of systematic uncertainties on sensitivity. The largest uncertainty is due to detector alignment, and the second largest is due to the photon energy scale.

Source	Impact on sensitivity
Angle (including both $\theta_{\mathrm{e}\gamma}$ and $\phi_{\mathrm{e}\gamma}$) uncertainty	1.4 %
E_γ uncertainty	1.0 %
Normalisation uncertainty	0.4 %
E_{e} uncertainty	0.1 %
$t_{\mathrm{e}\gamma}$ uncertainty	< 0.1 %
RDC uncertainty	< 0.1 %
Total	3 %

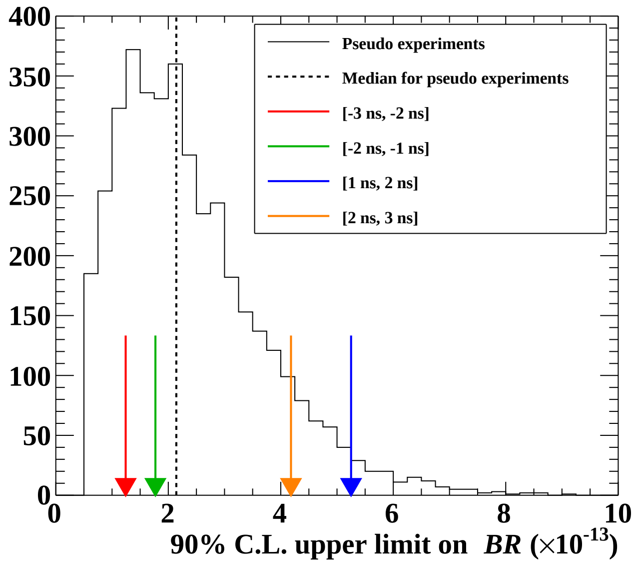

Figure 9.1: Distribution of a 90 % upper limit on the branching ratio in pseudo experiments and time side-bands. A dashed line indicates the median of the distribution, corresponding to a sensitivity of 2.2×10^{-13}. Arrows show the branching ratio estimated in time side-bands.

Table 9.2: Comparison in analysis with the 2021 dataset.

	k_{2021}	Sensitivity without systematic uncertainty
Last analysis [1]	$(2.64 \pm 0.12) \times 10^{12}$	8.4×10^{-13}
This analysis	$(2.76 \pm 0.14) \times 10^{12}$	8.0×10^{-13}

9.1.2 Sensitivity only with the 2021 dataset

This work reanalysed the 2021 dataset to apply several analysis improvements as follows:

- Photon reconstruction mainly for multi-photon events (Sects. 4.1 and 5.2),
- LXe detector calibration (Sect. 6.2),
- Positron ghost selection (Sect. 4.2),
- RDC reconstruction (Sect. 5.3), and
- Trigger efficiency re-evaluation (Sect. 8.6).

The sensitivity for the 2021 dataset was improved by 5 % compared to the last analysis [1], mainly thanks to an increase in the normalisation factor k_{2021}, which was discussed in Sect. 8.6.

9.2 Result

Event distribution There were 357 events in the analysis window, and no excess of events was observed in the signal region. Figure 9.2 shows the event distributions in the $(E_{\mathrm{e}}, E_{\gamma})$ and $(\cos\Theta_{\mathrm{e}\gamma}, t_{\mathrm{e}\gamma})$ planes. The contours of the averaged signal PDFs are also shown by green curves in Fig. 9.2. The marker colour and size are changed according to the R_{sig} defined in Eq. (8.10). Table 9.3 lists the top 10 events with the highest R_{sig} value.

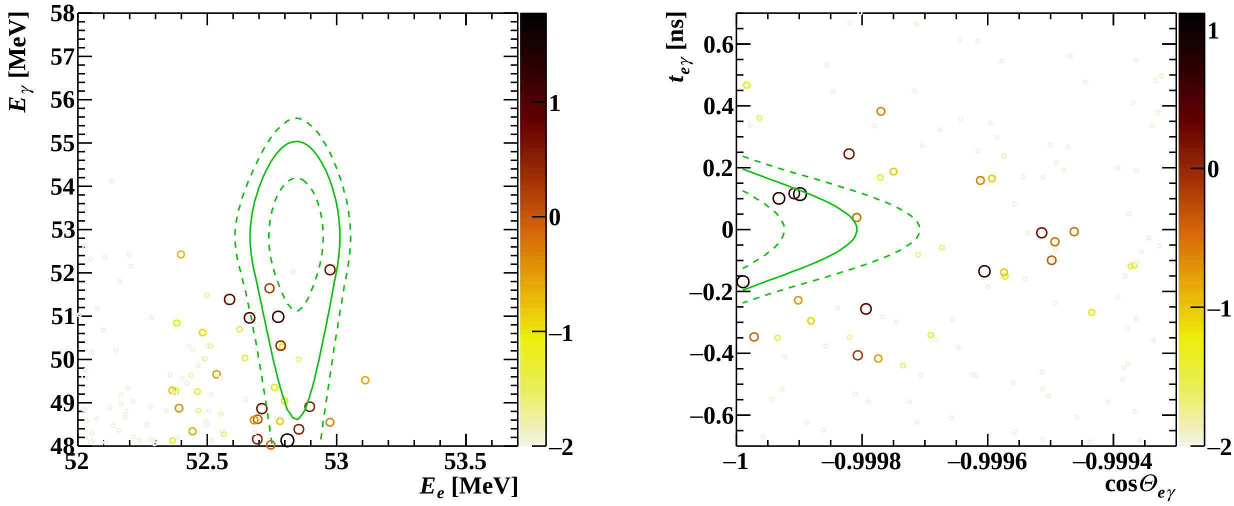

(a) (E_e, E_γ) plane with selections of $\cos\Theta_{\mathrm{e}\gamma} < -0.9995$ and $|t_{\mathrm{e}\gamma}| < 0.2$ ns.

(b) $(\cos\Theta_{\mathrm{e}\gamma}, t_{\mathrm{e}\gamma})$ plane with selections of $49.0\,\mathrm{MeV} < E_\gamma < 55.0\,\mathrm{MeV}$ and $52.5\,\mathrm{MeV} < E_\mathrm{e} < 53.2\,\mathrm{MeV}$.

Figure 9.2: Event distributions on the (a) (E_e, E_γ)- and (b) $(\cos\Theta_{\mathrm{e}\gamma}, t_{\mathrm{e}\gamma})$-planes with marker size and colour based on R_sig. Events with $R_\mathrm{sig} < -2$ are clipped to be displayed as $R_\mathrm{sig} = -2$. Selection criteria are set to have 93 % signal efficiency for E_γ and 97 % signal efficiency for the other observables. The signal PDF contours (1σ, 1.64σ, and 2σ) are shown.

Table 9.3: List of highly ranked events.

Rank	Year	Run	Event	R_sig	E_e (MeV)	E_γ (MeV)	t_γ (ns)	$\theta_{\mathrm{e}\gamma}$ (mrad)	$\phi_{\mathrm{e}\gamma}$ (mrad)	t_RDC (ns)	E_RDC (MeV)
1	2022	448 495	2312	1.776	52.810	48.132	0.077	4.811	−7.606	10	−1
2	2021	405 459	510	1.119	52.774	50.985	0.115	11.241	8.911	10	−1
3	2022	458 058	2495	0.806	52.663	50.961	−0.168	3.715	−2.720	10	−1
4	2022	436 135	4	0.693	52.586	51.386	0.101	−5.912	10.288	10	−1
5	2022	464 868	3839	0.653	52.711	48.865	−0.037	−4.972	6.956	10	−1
6	2021	401 563	1286	0.587	52.974	52.071	−0.135	−28.042	−1.903	10	−1
7	2022	443 464	2931	0.425	52.693	48.160	0.118	11.718	2.131	10	−1
8	2022	450 480	2903	0.420	52.854	48.388	−0.101	−19.289	6.884	10	−1
9	2022	470 525	2524	0.409	52.896	48.909	−0.074	20.958	−1.586	2.873	11.839
10	2022	448 461	2470	0.335	52.784	50.320	0.117	−3.649	−13.123	10	−1

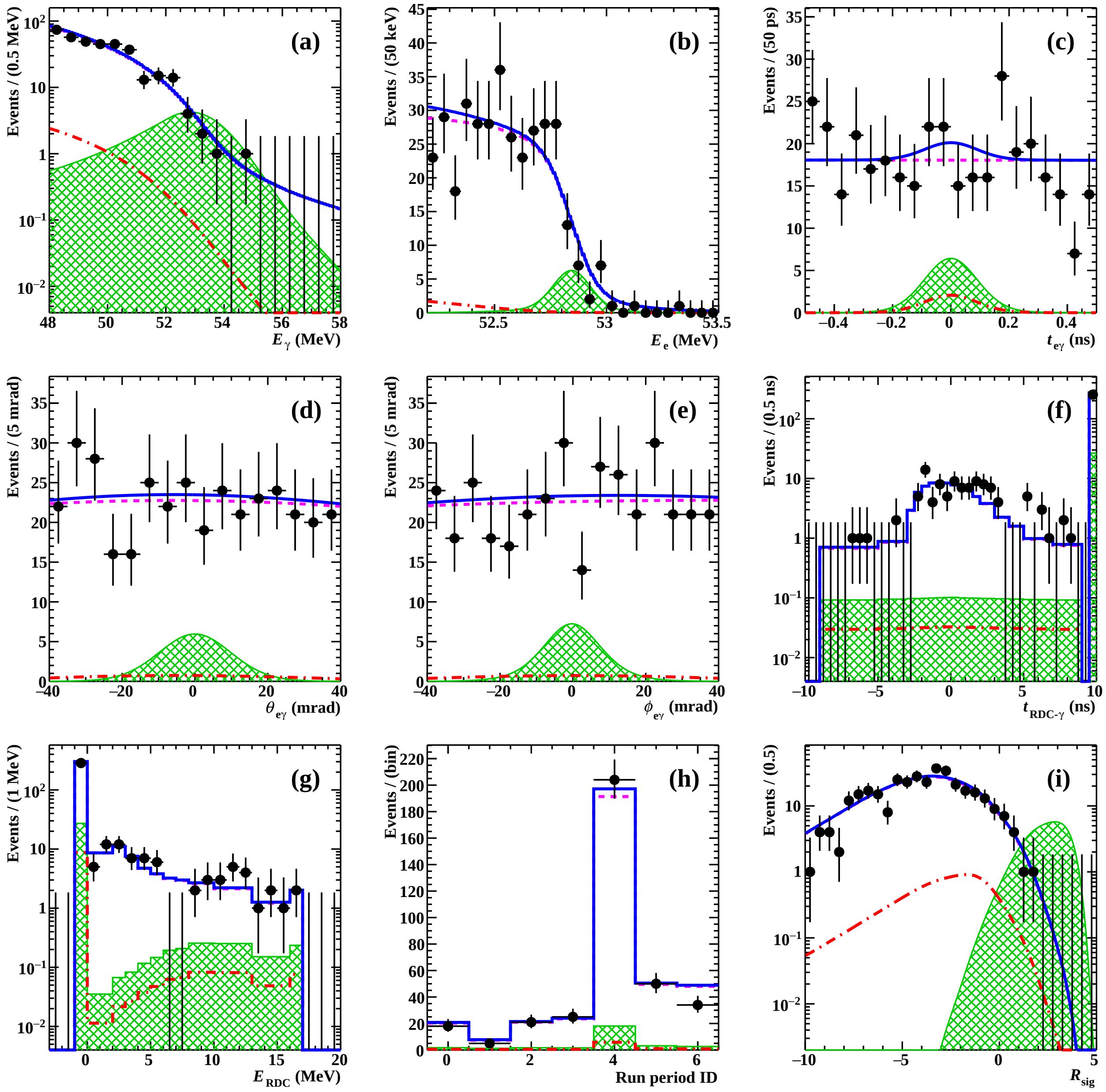

Figure 9.3: Projected distribution of observed events on the parameter space of eight fit observables and R_{sig} parameter (black marker), and the expected shape of the distribution according to the best-fit number of events (blue solid line). The magenta dashed (red dash-dotted) line represents the component of the accidental background (RMD background) in the fitted PDF. The green hatched region shows the signal PDF with $N_{\text{sig}} = 30$, which is ten times larger than the upper limit on N_{sig}.

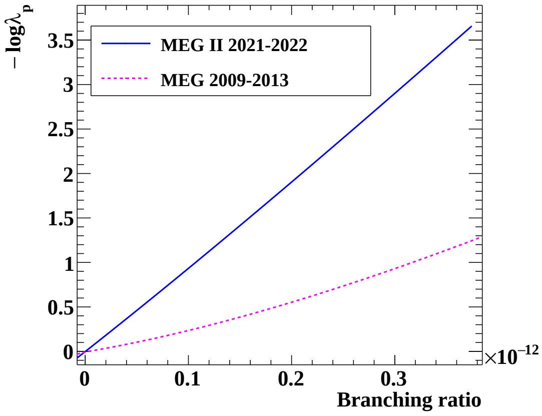

Figure 9.4: The negative log profile-likelihood-ratio (λ_p) as a function of the branching ratio. The blue solid (magenta dashed) curve corresponds to the MEG II 2021–2022 dataset (the MEG full dataset [42]).

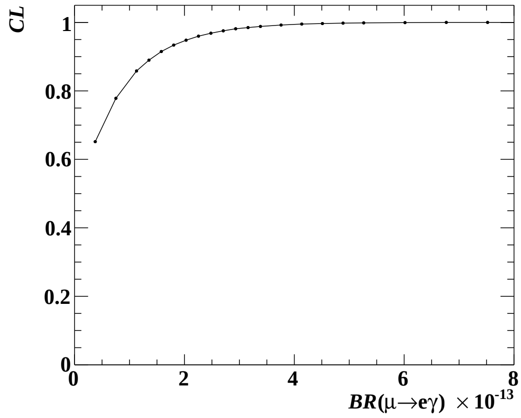

Figure 9.5: CL curve. The curve crosses $CL = 0.9$ at $\mathcal{B}(\mu \to e\gamma) = 1.5\times10^{-13}$, giving a 90 % C.L. upper limit accordingly.

Fit results The maximum likelihood fit estimated the number of signal and background events to be $(\hat{N}_{\mathrm{sig}}, \hat{N}_{\mathrm{RMD}}, \hat{N}_{\mathrm{ACC}}) = (-5.01 \pm 1.21, 9.71 \pm 1.68, 361.91 \pm 8.58)$ without the physical constraint that requires the positive number of events. In case that the physical constraint is imposed, the best fits were $(\hat{N}_{\mathrm{sig}}, \hat{N}_{\mathrm{RMD}}, \hat{N}_{\mathrm{ACC}}) = (0.00 \pm 0.73, 9.67 \pm 1.68, 360.94 \pm 8.58)$. The projections onto the eight observables are shown in (a)–(h) of Fig. 9.3. All data distributions are well-fitted by their background PDFs. The data distribution for R_{sig} also shows a good agreement with the distribution expected from the likelihood fit result, as shown in Fig. 9.3(i).

The likelihood fit in the analysis window was also performed without the constraints on N_{RMD} and N_{ACC} described in the second line of Eq. (8.1). The best estimates of $N_{\mathrm{RMD}} = 0 \pm 8$ and $N_{\mathrm{ACC}} = 357 \pm 19$ are consistent with the side-band estimates described in Sect. 8.3.

Upper limit on branching ratio Figure 9.4 shows the observed profile-likelihood-ratio λ_p, defined as Eq. (8.11), as a function of the branching ratio. Figure 9.5 shows the CL curve, introduced in Sect. 8.5. The results are consistent with the sensitivity calculated from the pseudo-experiment with a null-signal hypothesis, yielding an upper limit on the branching ratio of

$$\mathcal{B}(\mu \to e\gamma) < 1.5 \times 10^{-13} \tag{9.1}$$

at 90 % C.L.

9.2.1 Comparison with previous analysis

Since several event reconstruction updates are also applied to the 2021 dataset, the reconstructed observables and the fit results changed from those in the previous analysis. Figure 9.6 shows the event-by-event comparison in the observables for the top five highly ranked events in either or both the current or previous analysis of the 2021 dataset. The five most highly ranked events from the previous analysis remain the most highly ranked ones in this analysis, with slight changes in the reconstructed observables. The positron observables were changed only when a different positron ghost track from the previous analysis was selected. The third-highest-ranked event in this analysis has a different ghost

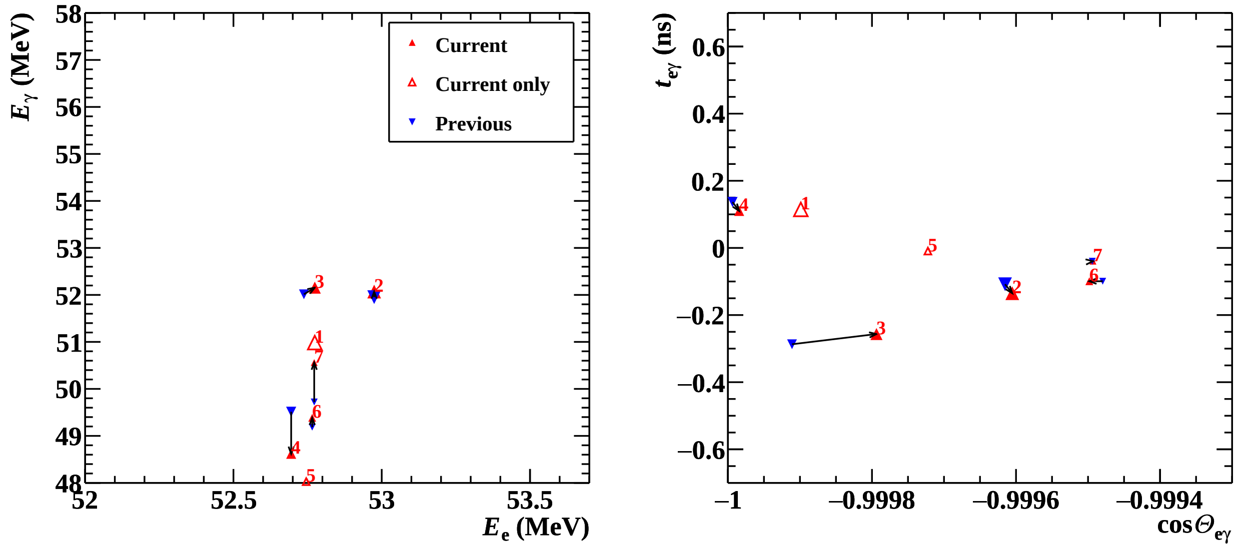

Figure 9.6: Event-by-event comparison for the top five highly ranked events in the current (red) and previous (blue) analyses. The number represents the rank. The marker size represents R_{sig} value. In the previous analysis, two open triangle markers were outside the blind box.

track from the previous analysis, having a different E_{e}, whereas E_{e} remains unchanged in the other highly ranked events, as shown in Fig. 9.6. On the other hand, the photon observables were changed in all the events due to updates in the photon reconstruction algorithm and the LXe detector calibration. These photon observable changes were sometimes observed across the blind box boundary, which is the case for the first and fifth highest-ranked events in this analysis of the 2021 dataset, as shown by the red open triangles in Fig. 9.6. These two events were outside the blind box in the previous analysis. The highest-rank event, which is ranked as top 2 in the analysis of the 2021–2022 dataset, had an update in t_γ by 1.8 ns thanks to the t_γ reconstruction improvement in pileup events discussed in Sect. 4.1.4. The fifth-highest-rank event had a change in E_γ of 34 keV near the boundary of the analysis window.

The maximum likelihood fit was performed only on the 2021 dataset, setting an upper limit of $\mathcal{B}(\mu \to e\gamma) < 8.4 \times 10^{-13}$ at the 90 % C.L. The upper limit was 12 % higher than that in the previous analysis, which was understood due to the most highly ranked event being missed in the previous one.

9.3 Discussion

This work set the most stringent upper limit on the $\mu \to e\gamma$ branching ratio to date, as shown in Fig. 9.7. The sensitivity of this analysis on the 2021–2022 dataset is a factor of 2.4 better than that with the MEG full dataset [42]. While the statistics of the MEG full dataset collected in 2009–2013 was $k = (1.71 \pm 0.06) \times 10^{13}$ [82], that of this dataset collected only for two years is $k = (1.34 \pm 0.07) \times 10^{13}$ thanks to the stable data-taking and the positron efficiency improvement with respect to the MEG experiment. The sensitivity improvement even with 22 % lower statistics was achieved by the resolution improvements described in Sect. 7.4.

The most stringent upper limit of $\mathcal{B}(\mu \to e\gamma) < 2.2 \times 10^{-13}$ excludes the parameter space of new physics models. As an example of the parameter space exclusion, Fig. 9.8 shows the (κ, Λ) space, defined by Eqs. (1.8) and (1.9) respectively, excluded by this work, with the same concept as Fig. 1.2. In the region of $\kappa \ll 1$, this work excluded the new physics scale Λ of 2000 TeV.

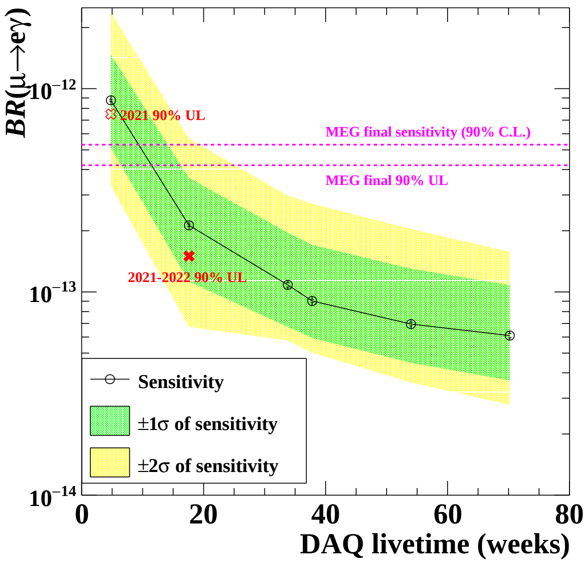

Figure 9.7: Upper limit on the branching ratio so far and expected sensitivity in the future MEG II data taking over time.

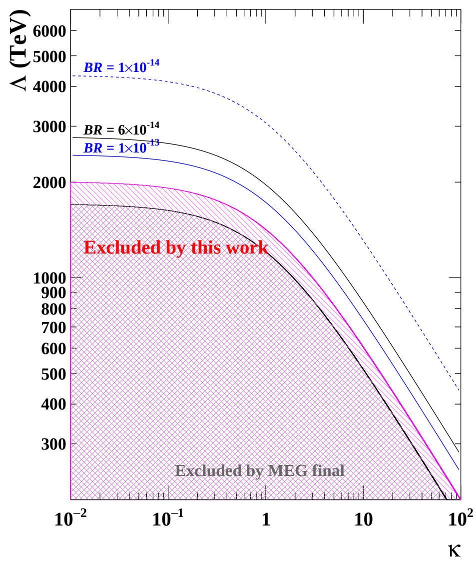

Figure 9.8: (κ, Λ) parameter space excluded by this work (magenta hatched region). The grey depicted region is the parameter space excluded by the MEG result ($\mathcal{B} < 4.2 \times 10^{-13}$ at 90 % C.L.). The black function represents the space to be searched with the MEG II target sensitivity of 6×10^{-14}.

The significant improvement in sensitivity from the analysis of the 2021 dataset is attributed to the five-fold increase in statistics and the maintenance of excellent detector performance during the 18-week data-taking period in the run 2022. Especially, the energy scale and energy resolution of the LXe detector were uniform over time, thanks to careful calibration, although there was a 20 % change in the xenon purity during the run. I argue that this result demonstrates further sensitivity improvement with increased statistics collected by long-term data-taking and encourages long-term data-taking until 2026, when the MEG II data-taking is planned to end.

A comparison in the analysis of the 2021 dataset validated that reconstruction and calibration updates improved reconstruction quality, especially for events with photon pileup. Since the number of events affected by the updates was very limited, the sensitivity improvement was not significant, while a better understanding of the trigger resulted in a 5 % higher normalisation factor k_{2021} and sensitivity. However, it is possible that the signal event is reconstructed with low quality and finally missed, as in the case of two highly ranked events found in this analysis. This work also highlighted the importance of developing reconstruction algorithms and calibrating detectors to prevent missing rare signal events.

9.4 Prospects

The continuous data-taking and further detector performance improvements lead to a more sensitive search for $\mu \to e\gamma$ in the MEG II experiment. This section discusses them in detail.

Increase in statistics The MEG II collaboration has taken data for 22 weeks in the run 2023 and for 4 weeks in the run 2024 at $R_\mu = 4 \times 10^7\ \mathrm{s}^{-1}$, which projects a 2.5 times higher statistics in the analysis on the 2021–2024 dataset than this analysis. Hence, the sensitivity of the analysis on the 2021–2024 dataset is expected to reach down to 10^{-14}, as shown in Fig. 9.7. The collaboration also plans to continue taking data in the coming years. The data-taking, however, will be stopped due to the proton accelerator shutdown in 2027 for the IMPACT project [111]. This suggests that the collaboration must maximise the amount of data to be taken in 2025 and 2026. Based on the experimental conditions so far, there will be an additional expected 2.6-fold increase in statistics, leading to a target sensitivity of 6×10^{-14} at the end of run 2026. An increase in the muon beam rate up to $R_\mu = 5 \times 10^7\ \mathrm{s}^{-1}$ is considered to further enhance statistics within a limited time, which requires the analysis improvement discussed later.

Understanding of detector performance The LXe detector performance is not yet fully understood, especially in terms of energy resolution. The photon energy resolution for 54.9 MeV photons in the π^0 calibration run 2022 was worse than run 2021, especially for events with a very shallow conversion point, as discussed in Sect. 7.1.3. Although the cause is not fully understood, a suspicious candidate is of lower calibration quality primarily due to the non-linear MPPC response with a higher PDE. The calibration of the non-linear response is under study. In addition to the non-linearity, the angular dependence of the MPPC PDE will be studied. The dependence was reported in Ref. [112] but has not been taken into account in the $N_{\mathrm{pho},i}$ reconstruction so far due to a lack of understanding. I plan to study the dependence for more precise reconstruction of $N_{\mathrm{pho},i}$, expecting improvement in position and energy resolution.

Another item that should be understood is a dicrepancy in the energy resolution of the LXe detector between the simulation (1.0 %) and data (1.9 % in 2022), which was observed also in the MEG experiment. Although many efforts have been made to understand the discrepancy, it remains largely unexplained. I doubt that the scintillation light emission process in LXe is reproduced well. A possible study is to simulate the scintillation light emission process using NEST models [113], which are commonly used in dark matter search experiments using noble gases.

Not only the photon energy resolution but also the tagged-RMD fraction show a disagreement between the MC simulation and the data, as discussed in Sect. 5.3.3. The analysis improvement to better identify the two-photon events originating from AIF is essential, as discussed later. Another approach is to study photon emission at the muon stopping target and through positron trajectories and their consistency between the MC simulation and data, considering more photon background incident on the LXe detector. It should not be easy to obtain information on photon emission in data, but it is worthwhile to study MC configurations to better understand the detector performance.

Possible improvements Positron tracking reconstruction efficiency degrades as the muon beam rate is higher, as discussed in Sect. 7.2.4. The track-finding algorithm, a local-forwarding pattern recognition, limits it. Two candidate algorithms based on machine learning are under study: One is based on the Transformer [114, 115], and the other is based on the graph neural network (GNN) [116, 117]. Both techniques have been studied in other experiments and have shown promising results. Suppose those algorithms also fit the MEG II case and show promising results. In that case, the muon beam rate can be increased up to $5\times10^{7}\ \mathrm{s}^{-1}$ without a significant loss of the positron tracking efficiency, gaining much higher statistics than the current expectation.

Further optimisation of photon background reduction and signal efficiency maximisation requires additional studies on multi-photon event analysis. Chapter 5 discussed the miscategorisation of a fraction of RMD-originating photons as *Coincidence* event. One of the possible improvements is the multi-photon event identification algorithm based on the DL technique, developed by Ref. [39]. Since it was trained on a simulation and applied to a simulation, it was difficult to use it on data without retraining. By obtaining a good training sample and precisely reconstructing $N_{\mathrm{pho},i}$ per photosensor, as discussed above, the DL-based algorithm will help the optimisation.

Installing the upstream RDC is a possible hardware improvement. As discussed in Sect. 2.5, although two RDCs was initially planned to be installed, the upstream one is still under development due to technical difficulties in satisfying a low-mass design, a high-rate capability, and a high efficiency for a few MeV positrons. The best candidate for the upstream RDC is an resistive plate chamber (RPC) based on diamond-like carbon (DLC). The small-size prototype detector with a low-mass design demonstrated high-rate capability with sufficient efficiency [118, 119, 120]. Ageing studies were also conducted with the prototype detector, showing no apparent performance degradation at half of the expected dose during the MEG II one-year run [121]. The detector design for a larger detector size is being investigated. The full-scale detector will be installed in 2026, if everything goes smoothly, and is expected to contribute to the further background event discrimination by tagging the 90 % of RMD-originating photons with the downstream one.

If all these improvements work effectively in addition to the increased statistics, the final sensitivity shown in Fig. 9.7 can be improved by 10–20 %. The sensitivity of the MEG II experiment will finally reach the target sensitivity of 6×10^{-14}.

Chapter 10
Conclusion

The MEG II experiment has been searching for the charged-lepton-flavour-violating muon decay $\mu^+ \to e^+\gamma$ as a probe to search for new physics beyond the Standard Model. This work analysed the data collected during runs 2021 and 2022 with several improvements as follows:

- Statistics are five times higher in comparison with the previous result, only with the 2021 data, by adding the 2022 data with careful detector calibrations,
- New photon pileup unfolding algorithm increases the efficiency by 2 % and improves reliability to analyse multi-photon events, and
- RDC analysis updates give 17 % efficiency improvement.

As a result, the sensitivity was 2.2×10^{-13}, whose improvement compared to Ref. [42] amounted to a factor 2.4. No signal excess was found, and the most stringent upper limit to date was set as

$$\mathcal{B}(\mu^+ \to e^+\gamma) < 1.5 \times 10^{-13}$$

at 90 % C.L.

In the MEG II experiment, the data have been taken during runs 2023 and 2024, with a projected statistic 1.5-fold higher than in runs 2021 and 2022. In addition, it is planned to take data until 2026 with an additional expected 2.6-fold increase in statistics and to study analysis and hardware improvements in order to reach a sensitivity to $\mu^+ \to e^+\gamma$ of 6×10^{-14}.

Appendix A

Implementation of LXe detector yearly alignment

The concept of a virtual ideal (VI) detector, assumed to be perfectly aligned, was born to simplify the definition of the local coordinate system (Sect. 2.4) and the implementation of the yearly survey results (Sect. 6.2.4). This appendix describes the construction of the VI detector and implementation of the yearly survey results.

Construction of the virtual ideal detector

The MPPCs supports in the real detector are segmented along ϕ and consist of four pieces of CFRP support structure, as shown in Fig. A.1. Those CFRP structures are not perfectly aligned since installation, resulting in a four-cylindrical structure in the MPPC w position on the inner face (Fig. A.2). The VI detector is idealised as being as perfectly cylindrical as possible and being aligned with the z axis. I call it *virtual*, since the LXe detector was never in this exact position.

I use a set of six parameters $(\Delta x, \Delta y, \Delta z, \phi, \theta, \psi)$ to represent transformations. The first three denote shifts in the global coordinate system, and the last three are the three Euler angles in the intrinsic zxz convention: First, rotate the detector by ϕ around z, then by θ around the *new* x axis, and ultimately by ψ around the *new* z axis.

These transformations can also be expressed using a 4×4 matrix such that $(x, y, z, 1)_{\text{year}} = T \cdot (x, y, z, 1)_{\text{VI}}$:

$$T = \begin{pmatrix} & & & \Delta x \\ & \text{rotation} & & \Delta y \\ & & & \Delta z \\ 0 & 0 & 0 & 1 \end{pmatrix}. \tag{A.1}$$

That way, subsequent transformations can be combined by multiplication. Fitting a cylinder to the MPPC positions leaves two degrees of freedom:

(1) Translation along the x axis
(2) Rotation around the z axis

Therefore, additional steps are necessary to determine ψ and Δz. The last rotation ψ is chosen such that the detector is symmetrical with respect to the xz plane (i.e. $\langle y \rangle = 0$) and Δz is chosen such that the detector is symmetrical with respect to the xy plane (i.e. $\langle z \rangle = 0$).

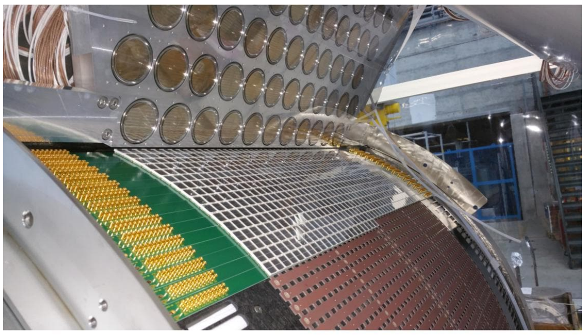

Figure A.1: Installing MPPC-mounted PCB strips onto the inner face [44].

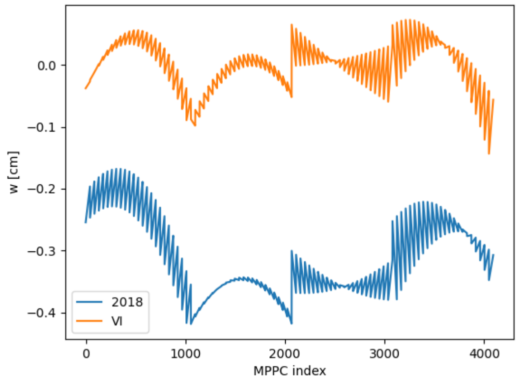

Figure A.2: w position of MPPCs. An orange line shows the VI w positions. A blue line shows the w positions based on the 2018 measurement with the designed R_{in} value and without considering the detector transformation.

Defining the local coordinates of Eq. (2.3) requires the radius R_{in} on which the MPPCs lie. It is defined by minimising the following squared residual of

$$\sum_{i}^{\text{MPPCs}} \left(x_i^2 + y_i^2 - R_{\text{in}}^2\right), \tag{A.2}$$

where (x_i, y_i) is the i-th MPPC position.

The above calculation with the MPPC positions measured in 2018 results in the following transformation parameters.

$$\begin{aligned} \Delta x &= -0.289\,\text{cm} \\ \Delta y &= -0.0197\,\text{cm} \\ \Delta z &= 0.273\,\text{cm} \\ \phi &= -3.33\,\text{mrad} \\ \theta &= 0.83\,\text{mrad} \\ \psi &= 0.00\,\text{mrad} \end{aligned} \tag{A.3}$$

Here, I notate the transformation matrix corresponding to the above parameters as T_{2018}^{-1}. Note that T_{year} is defined as the transformation from the VI to each year. The best fit of the inner radius is also obtained:

$$R_{\text{in}} = 64.76\,\text{cm}. \tag{A.4}$$

This R_{in} gives a better interpretation of the w axis as the conversion depth compared with the design R_{in} value and no consideration of the transformation as of the measurement in 2018 (Fig. A.2).

Yearly alignment

The yearly alignment requires finding a transformation matrix T_{year} that transforms the MPPC positions in the VI to the positions in each year based on the survey results. However, it is not straightforward:

Table A.1: Transformation parameters from the VI to 2021 and 2022. See the text for the parameter definition.

	2021	2022
Δx	0.0993 cm	0.302 cm
Δy	−0.105 cm	−0.0620 cm
Δz	−0.267 cm	−0.258 cm
ϕ	179.07°	173.02°
θ	0.0556°	0.0466°
ψ	−178.92°	−172.87°

the transformation matrix must be calculated on the basis of the survey results from 2018 because there were no survey results from the VI.

Let me take the year 2021 as an example. The survey results from 2021 are compared to the ones in 2018, providing a transformation 2018 → 2021 $T_{2018\to 2021}$. The desired VI → 2021 matrix T_{2021} can be calculated using the VI → 2018 transformation matrix T_{2018}, that is

$$T_{2021} = T_{2018\to 2021} \cdot T_{2018}. \tag{A.5}$$

Table A.1 summarises the calculated transformation parameters. The transformation for 2022 is calculated analogously to the above.

An advantage of the method with Eq. (A.5) is that no cumulative uncertainty increases throughout the years since the results only depend on measurements in 2018 and each year. Therefore, the MPPC position uncertainty is expected to be equal for all years.

Appendix B

Finding correct assignment of PMT channels in LXe detector

This appendix describes the full details of methods to find a correct assignment of the PMT channels in the LXe detector. A brief description is in Sect. 6.2.5.

LED-based method The LED data taken during LXe filling into the detector uncovered the channel misassignment of PMTs on the top face. Figure B.1 shows the channel map of PMTs on the top face. PMTs located in the lower w position, named the first, second, ... row, were covered as more LXe was transferred to the detector. PMTs above the liquid level detect less light because most of the light from LEDs in LXe reflects at the surface of LXe. I traced integrated charge Q_i normalised by the charge at a reference time $Q_i(t_0)$ in LED data during filling LXe to measure a temporal evolution of the liquid level. Figure B.2 shows the integrated charge ratio as a function of the channel index. A PMT with index 4628 was expected to measure a small charge as the surrounding PMTs did when LXe was filled up to the second row. It, however, measured a larger charge than expected, which suggested that the PMT is located in the above rows rather than the second row. Unexpected charges were also measured when LXe was filled up to the third row: three PMTs with indices 4625, 4626 and 4628 detected smaller charges than the surrounding ones; and three PMTs with indices 4636, 4637 and 4639 detected larger charges than the surrounding ones. A doubt about different locations suggests channel misassignment. This analysis is, however, sensitive to channel misassignment only in the vertical direction. Thus, a method to identify the correct assignment is required, which will be discussed later.

α-particle-based method Another analysis using scintillation light from α particles detected channel misassignment on the outer face. This analysis compares $N_{\mathrm{phe},i}$ between data and a simulation from 25 α-particle sources and expects a linear correction between them as discussed in Sect. 6.2.3. When PMT channels are misassigned, a linear fit to the correction gives extremely large χ^2 value as shown in Fig. B.3 because $N_{\mathrm{phe},i}$ for several α particles in data differs from that in simulation due to different distances between a photosensor and α-particle sources. This analysis requires a long enough distance difference to detect misassignment and will not be sensitive if PMTs are next to each other.

Time-based method The consistency of channel assignment was quantified by comparing the timing of different PMTs to each other. With the notation used in Sect. 4.1.4, the j-th PMT and k-th PMT are compared in a correlation plot of $t_{\mathrm{pm},j} - t_{\mathrm{pm},k}$ vs $t_{\mathrm{prop},j} - t_{\mathrm{prop},k}$, which are from γ-ray events. If the channel assignment for j, k is both correct, this correlation plot is expected to have a slope of one in a linear fitting (Fig. B.4a). Otherwise, in case the channel assignment is swapped or in the opposite

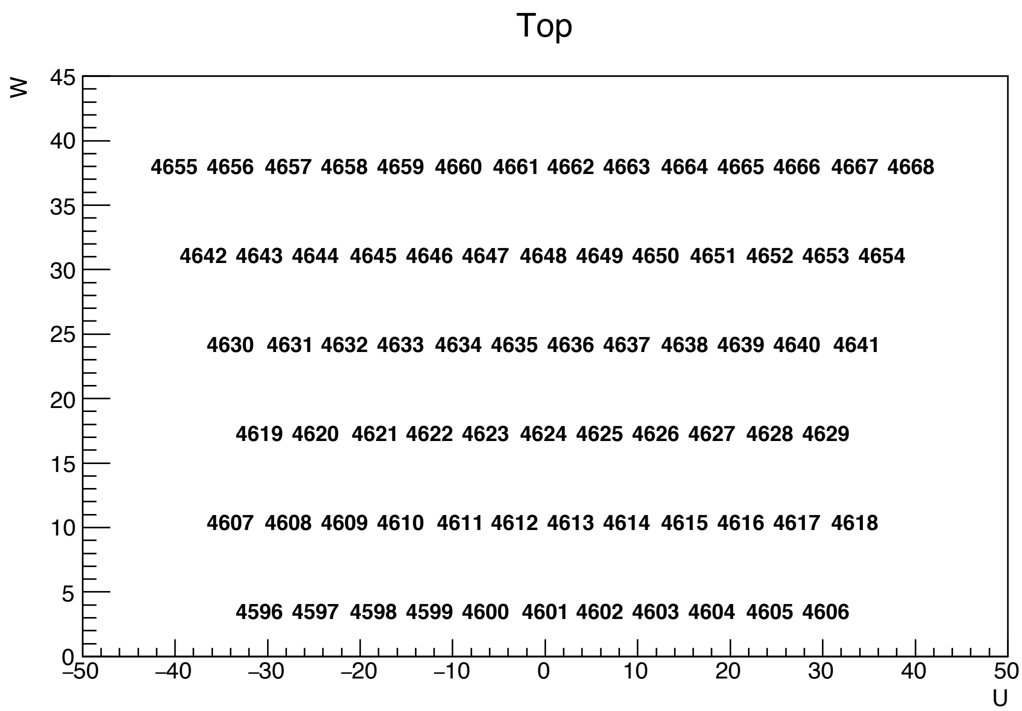

Figure B.1: Channel map for PMTs on the top face. Smaller w means a lower position in the vertical direction. Also, I assign row indices from the smallest w row.

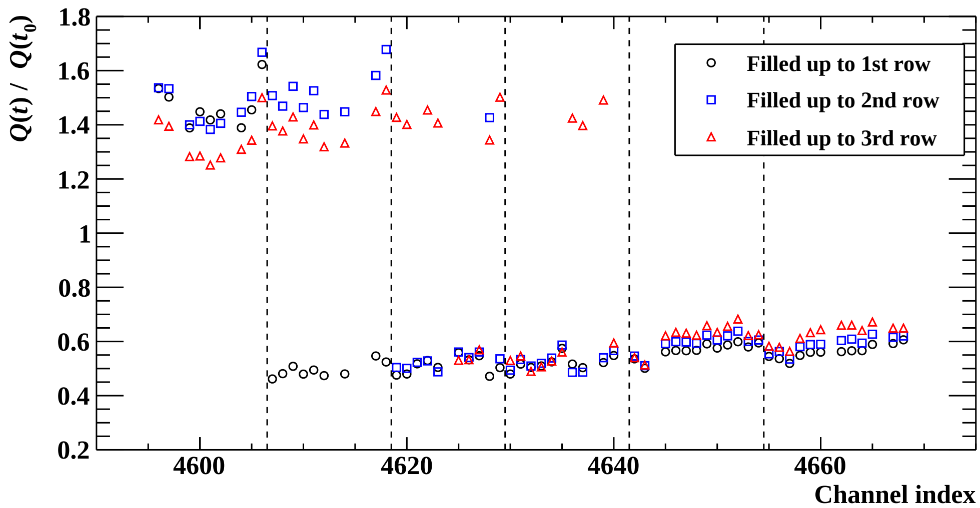

Figure B.2: Integrated charge ratio as a function of PMT channel indices. Black, blue, and red markers represent the ratio when LXe was filled up to the first, second, and third rows, respectively.

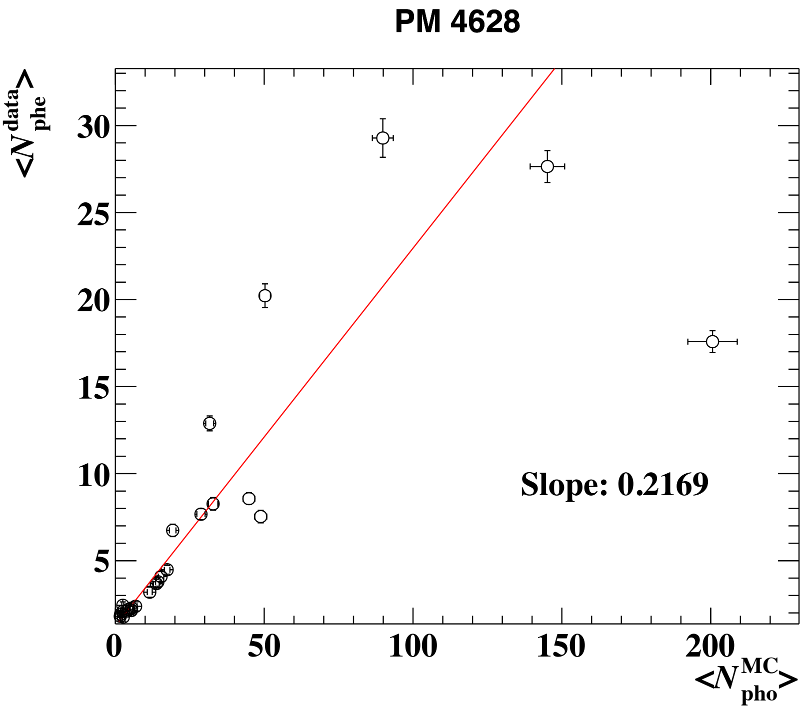

Figure B.3: A correlation in $N_{\text{phe},i}$ between data and a simulation. It is less linear with respect to Fig. 6.14.

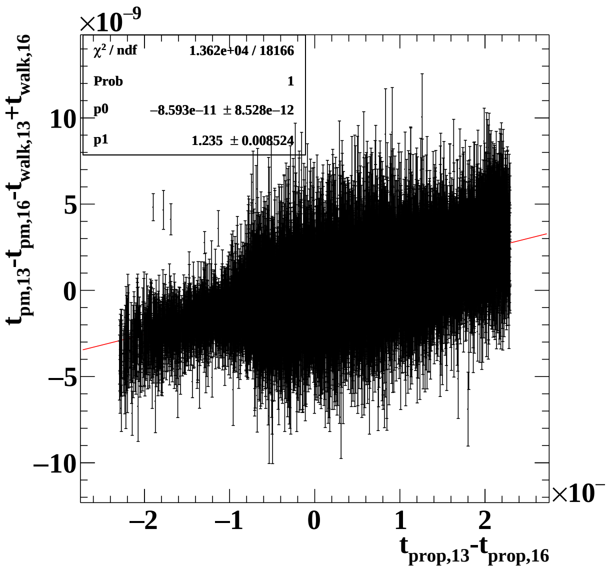

(a) Channals 13 vs 16.

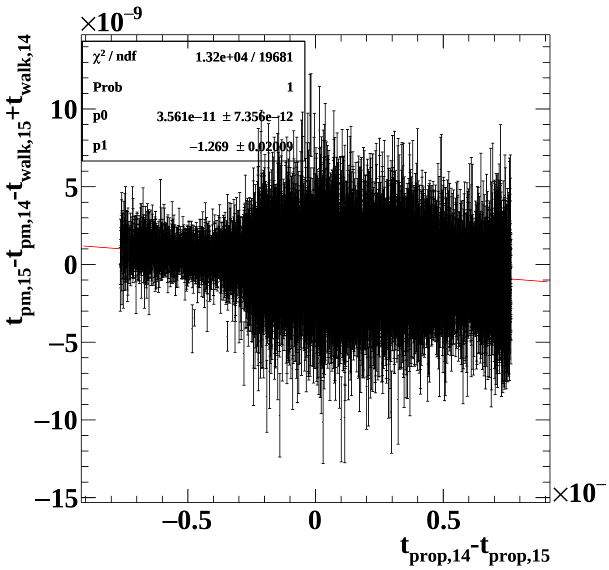

(b) Channals 14 vs 15.

Figure B.4: Pattern of $t_{\text{pm},j} - t_{\text{pm},k} - t_{\text{walk},j} + t_{\text{walk},k}$ vs $t_{\text{prop},j} - t_{\text{prop},k}$ plots compared for different channel sets. Indices shown in the plot are arranged correctly on a row of PMTs on the top face; however, the observed scatter plots emulate the situation where 14 $\leftrightarrow$ 15 swapping happens. (a): Channels 13 and 16 are correctly assigned, so the slope of the linear fit to the scatter plot is consistent with 1. (b): Behaviour of scatter plots when these two channels swap with each other. Due to the inconsistency in the real location and assumed location of the channels, the linear coefficients in the fit deviate from 1.

direction to the nominal one, the slope is fitted to be negative (Fig. B.4b). Even when the direction of the relative channel position is correct, a wrong assumption of the distance in between results in a positive but not a linear coefficient in the fitting. By making many sets of (j, k) pairs, usually making all possible pairs of PMTs arranged in the u direction on the same row, the PMT position can be identified. The difficulty of this method is the amount of $O(n^2)$ pairs when n PMTs are tested. In addition, when more than two channels are involved in a set of permuted channels, i.e. not just a swapping, some trial and error are usually necessary to fully identify the correct assignment.

Acknowledgements

During my postgraduate life, I have received much support from many people. I would like to express my gratitude to all the people involved with me.

First and foremost, I would like to express my deepest gratitude to my (officially former) supervisor, Dr. Toshinori Mori, for his great insight and solid advice. His deep understanding and enthusiasm for physics have inspired me throughout my research. I would like to express my sincere gratitude to Prof. Wataru Ootani for his guidance and constant support. He always encouraged me and gave advice on my study and presentation skills. Especially in these months, he has been a great help in preparing this thesis as my supervisor.

I would like to express my gratitude to the MEG II collaboration. Dr. Mori and Dr. Alessandro M. Baldini have been leading the MEG II collaboration as spokespersons of the MEG II experiment. I am grateful to them for their leadership in making progress on the experiment and for providing me with the opportunity to work on this exciting project. I would also like to thank the run coordinators, Dr. Toshiyuki Iwamoto, Dr. Malte Hildebrandt, and Prof. Angela Papa, for their great organisation. Dr. Iwamoto has been an enormous help not only in the experiment, but also in life in Switzerland. Dr. Hildebrandt supported me in my research at PSI, especially when I worked on the upstream RDC studies. Prof. Papa always motivated me when we saw each other.

My analysis work was also supported by many collaborators. Dr. Atsushi Oya has been a great mentor for me, and I cannot complete this thesis without his mentoring. Prof. Ootani and Dr. Francesco Renga have had a lot of discussions to complete this analysis as the analysis coordinators. Dr. Yusuke Uchiyama gave me advice and shared his experience in the MEG experiment. Dr. Satoru Kobayashi, Dr. Sei Ban, Dr. Lukas G. Gerrizen, and Ms. Ayaka Matsushita discussed the photon analysis with the LXe detector. Mr. Antoine Venturini contributed to the positron analysis. Dr. Luca Galli and Dr. Marco Francesconi made a significant contribution to the trigger. I would like to express my gratitude to them for their huge cooperation.

My Swiss life has been enriched by people around PSI. Mr. Taku Yonemoto, who started postgraduate life at the same time, spent a lot of time. Many funny conversations with him made me happy at the office at PSI. Dr. Gerrizten took me to many places in Switzerland, and I had a lot of fun with him. He also gave me a chance to join the music club in a village around PSI, and I really enjoyed the music with the band. Mr. Masato Takahashi, Mr. Weiyuan Li and I performed happy RPC R&D work together. Dr. Giovanni Dal Maso, Dr. Hicham Benmansour, and Dr. Bastiano Vitali had a lot of conversations with me at any time, including in the experimental hall at midnight. Ms. Matsushita and I enjoyed drinking, drinking and drinking. Mr. Ryusei Umakoshi always made me smile, and now we have a good "tunnel" between our hearts.

The former and current group members have also spent a great time in Tokyo. I would also like to express my gratitude to the secretary of the ICEPP. Their support helped me immensely in my research life in Japan and Switzerland.

I received financial support from the World-leading Innovative Graduate Study Program for Quantum Science and Technology (WINGS-QSTEP) at the University of Tokyo and the Japan Society for the Promotion of Science (JSPS).

There are many people whom I cannot mention here, but I would like to thank all the people who have been involved with me. At last, I am deeply grateful to my family for their constant support.

Acronyms

ADC	analog-to-digital converter	33
AIF	annihilation in flight	10
BGO	bismuth germanium oxide	28
BTS	beam transport solenoid	15
CDCH	cylindrical drift chamber	16
CE	collection efficiency	83
CEX	charge exchange	26
CFRP	carbon fibre reinforced plastics	91
C.L.	confidence level	3
CLFV	charged lepton flavour violation	2
COBRA	constant bending radius	13
C-W	Cockcroft-Walton	25
DAQ	data acquisition	24
DCB	data concentrator board	31
DL	deep learning	56
DM	direction match	35
DOCA	distance of closest approach	56
DRS	domino ring sampler	31
ECF	excess charge factor	23
EM	electromagnetic	21
FPGA	field programmable gate array	33
GUT	grand unified theory	6
HV	high voltage	33
IEF	inner excess factor	52
LED	light emitting diode	24
LFV	lepton flavour violation	2
LH_2	liquid hydrogen	27
LXe	liquid xenon	13
LYSO	lutetium-yttrium oxyorthosilicate	31

MC	Monte Carlo	17
MPPC	multi-pixel photon counter	22
MPV	most probable value	101
PCB	printed circuit board	23
PDE	photon detection efficiency	23
PDF	probability density function	36
PMT	photomultiplier tube	16
PSI	Paul Scherrer Institut	13
pTC	pixelated timing counter	16
QE	quantum efficiency	23
RDC	radiative decay counter	13
RMD	radiative muon decay	8
ROI	region of interest	33
RPC	resistive plate chamber	160
SiPM	silicon photomultiplier	19
SM	Standard Model	2
SUSY	Supersymmetry	2
TCB	trigger concentrator boards	31
TOF	time of flight	57
VI	virtual ideal	162
VUV	vacuum ultraviolet	20
WaveDREAM	waveform DRS4 readout module	31

List of Figures

List of Tables

References

[1] K. Afanaciev *et al.*, A search for $\mu^+ \to e^+\gamma$ with the first dataset of the MEG II experiment, The European Physical Journal C 84 (2024) 216. doi:10.1140/epjc/s10052-024-12416-2.

[2] K. Afanaciev *et al.*, Erratum to: A search for $\mu^+ \to e^+\gamma$ with the first dataset of the MEG II experiment, The European Physical Journal C 84 (2024) 1042. doi:10.1140/epjc/s10052-024-13352-x.

[3] S. Weinberg, Implications of dynamical symmetry breaking, Physical Review D 13 (1976) 974–996. doi:10.1103/PhysRevD.13.974.

[4] S. Weinberg, Implications of dynamical symmetry breaking: An addendum, Physical Review D 19 (1979) 1277–1280. doi:10.1103/PhysRevD.19.1277.

[5] E. Gildener, Gauge-symmetry hierarchies, Physical Review D 14 (1976) 1667–1672. doi:10.1103/PhysRevD.14.1667.

[6] L. Susskind, Dynamics of spontaneous symmetry breaking in the weinberg-salam theory, Physical Review D 20 (1979) 2619–2625. doi:10.1103/PhysRevD.20.2619.

[7] S. Navas *et al.*, Review of Particle Physics, Physical Review D 110 (2024) 030001. doi:10.1103/PhysRevD.110.030001.

[8] S. P. Martin, A supersymmetry primer (1997). doi:10.1142/9789812839657_0001.

[9] H. Georgi, S. L. Glashow, Unity of All Elementary-Particle Forces, Physical Review Letters 32 (1974) 438–441. doi:10.1103/PhysRevLett.32.438.

[10] N. Aghanim *et al.*, *Planck* 2018 results, Astronomy & Astrophysics 641 (2020) A6. doi:10.1051/0004-6361/201833910.

[11] Y. Fukuda *et al.*, Evidence for Oscillation of Atmospheric Neutrinos, Physical Review Letters 81 (1998) 1562–1567. doi:10.1103/PhysRevLett.81.1562.

[12] S. Mihara *et al.*, Charged Lepton Flavor–Violation Experiments, Annual Review of Nuclear and Particle Science 63 (2013) 531–552. doi:10.1146/annurev-nucl-102912-144530.

[13] R. Bernstein, P. S. Cooper, Charged lepton flavor violation: An experimenter's guide, Physics Reports 532 (2013) 27–64. doi:10.1016/j.physrep.2013.07.002.

[14] Y. Kuno, Rare lepton decays, Progress in Particle and Nuclear Physics 82 (2015) 1–20. doi:10.1016/j.ppnp.2015.01.003.

[15] L. Calibbi, G. Signorelli, Charged Lepton Flavour Violation: An Experimental and Theoretical Introduction, La Rivista del Nuovo Cimento 41 (2018) 71–174. doi:10.1393/ncr/i2018-10144-0.

[16] M. Ardu, G. Pezzullo, Introduction to Charged Lepton Flavor Violation, Universe 8 (2022) 299. doi:10.3390/universe8060299.

[17] A. M. Baldini *et al.*, Measurement of the radiative decay of polarized muons in the MEG experiment, The European Physical Journal C 76 (2016) 108. doi:10.1140/epjc/s10052-016-3947-6.

[18] R. R. Crittenden, W. D. Walker, J. Ballam, Radiative Decay Modes of the Muon, Physical Review 121 (1961) 1823–1832. doi:10.1103/PhysRev.121.1823.

[19] W. Bertl *et al.*, Search for the decay $\mu^+ \to e^+e^+e^-$, Nuclear Physics B 260 (1985) 1–31. doi:10.1016/0550-3213(85)90308-6.

[20] S. Bilenky, S. Petcov, B. Pontecorvo, Lepton mixing, $\mu \to e+\gamma$ decay and neutrino oscillations, Physics Letters B 67 (1977) 309–312. doi:10.1016/0370-2693(77)90379-3.

[21] S. T. Petcov, The Processes $\mu \to e + \gamma, \mu \to e + \bar{e}, \nu' \to \nu + \gamma$ in the Weinberg-Salam Model with Neutrino Mixing, Sov. J. Nucl. Phys. 25 (1977) 340, [Erratum: Sov.J.Nucl.Phys. 25, 698 (1977), Erratum: Yad.Fiz. 25, 1336 (1977)].

[22] M. Aker *et al.*, Direct neutrino-mass measurement based on 259 days of KATRIN data, Science 388 (2025) 180–185. doi:10.1126/science.adq9592.

[23] Z. Maki, M. Nakagawa, S. Sakata, Remarks on the Unified Model of Elementary Particles, Progress of Theoretical Physics 28 (1962) 870–880. doi:10.1143/PTP.28.870.

[24] B. Pontecorvo, Neutrino Experiments and the Problem of Conservation of Leptonic Charge, Soviet Journal of Experimental and Theoretical Physics 26 (1968) 984.

[25] A. de Gouvêa, P. Vogel, Lepton flavor and number conservation, and physics beyond the standard model, Progress in Particle and Nuclear Physics 71 (2013) 75–92. doi:10.1016/j.ppnp.2013.03.006.

[26] Y. Kuno, Y. Okada, Muon decay and physics beyond the standard model, Reviews of Modern Physics 73 (2001) 151–202. doi:10.1103/RevModPhys.73.151.

[27] A. de Gouvêa, N. Saoulidou, Fermilab's Intensity Frontier, Annual Review of Nuclear and Particle Science 60 (2010) 513–538. doi:10.1146/annurev-nucl-100809-131949.

[28] Y. Kuno, Y. Okada, Proposed $\mu \to e\gamma$ Search with Polarized Muons, Physical Review Letters 77 (1996) 434–437. doi:10.1103/PhysRevLett.77.434.

[29] R. Barbieri, L. Hall, A. Strumia, Violations of lepton flavour and CP in supersymmetric unified theories, Nuclear Physics B 445 (1995) 219–251. doi:10.1016/0550-3213(95)00208-A.

[30] J. Hisano *et al.*, Exact event rates of lepton flavor violating processes in supersymmetric SU(5) model, Physics Letters B 391 (1997) 341–350. doi:10.1016/S0370-2693(96)01473-6.

[31] L. Calibbi *et al.*, Lepton flavor violation from supersymmetric grand unified theories: Where do we stand for MEG, PRISM/PRIME, and a super flavor factory, Physical Review D 74 (2006) 116002. doi:10.1103/PhysRevD.74.116002.

[32] L. Calibbi *et al.*, Status of supersymmetric type-I seesaw in SO(10) inspired models, Journal of High Energy Physics 2012 (2012) 40. doi:10.1007/JHEP11(2012)040.

[33] J. Hisano *et al.*, Lepton-flavor violation via right-handed neutrino Yukawa couplings in the supersymmetric standard model, Physical Review D 53 (1996) 2442–2459. doi:10.1103/PhysRevD.53.2442.

[34] T. Goto *et al.*, Lepton flavor violation in the supersymmetric seesaw model after the LHC 8 TeV run, Physical Review D 91 (2015) 033007. doi:10.1103/PhysRevD.91.033007.

[35] S. Eckstein, R. Pratt, Radiative muon decay, Annals of Physics 8 (1959) 297–309. doi:10.1016/0003-4916(59)90024-7.

[36] C. Fronsdal, H. Überall, μ-Meson Decay with Inner Bremsstrahlung, Physical Review 113 (1959) 654–657. doi:10.1103/PhysRev.113.654.

[37] T. Kinoshita, A. Sirlin, Radiative Corrections to Fermi Interactions, Physical Review 113 (1959) 1652–1660. doi:10.1103/PhysRev.113.1652.

[38] Y. Kuno, A. Maki, Y. Okada, Background suppression for $\mu \rightarrow e\gamma$ with polarized muons, Physical Review D 55 (1997) R2517–R2520. doi:10.1103/PhysRevD.55.R2517.

[39] R. Onda, Suppression of γ-ray backgrounds for highest sensitivity of $\mu^+ \rightarrow e^+\gamma$ search in MEG II experiment, Ph.D. thesis, The University of Tokyo (2021).
URL https://meg.web.psi.ch/docs/theses/onda_phd.pdf

[40] A. M. Baldini *et al.*, Muon polarization in the MEG experiment: predictions and measurements, The European Physical Journal C 76 (2016) 223. doi:10.1140/epjc/s10052-016-4047-3.

[41] J. Adam *et al.*, New Constraint on the Existence of the $\mu^+ \rightarrow e^+\gamma$ Decay, Physical Review Letters 110 (2013) 201801. doi:10.1103/PhysRevLett.110.201801.

[42] A. M. Baldini *et al.*, Search for the lepton flavour violating decay $\mu^+ \rightarrow e^+\gamma$ with the full dataset of the MEG experiment, The European Physical Journal C 76 (2016) 434. doi:10.1140/epjc/s10052-016-4271-x.

[43] J. Adam *et al.*, The MEG detector for $\mu^+ \rightarrow e^+\gamma$ decay search, The European Physical Journal C 73 (2013) 2365. doi:10.1140/epjc/s10052-013-2365-2.

[44] A. M. Baldini *et al.*, The design of the MEG II experiment, The European Physical Journal C 78 (2018) 380. doi:10.1140/epjc/s10052-018-5845-6.

[45] K. Afanaciev *et al.*, Operation and performance of the MEG II detector, The European Physical Journal C 84 (2024) 190. doi:10.1140/epjc/s10052-024-12415-3.

[46] A. Oya, Search for $\mu \rightarrow e\gamma$ with the first year data of the MEG II experiment, Ph.D. thesis, The University of Tokyo (2023).
URL https://meg.web.psi.ch/docs/theses/oya_phd.pdf

[47] K. Afanaciev *et al.*, New limit on the $\mu^+ \to e^+\gamma$ decay with the MEG II experiment, Physics Review Letters (Submitted) (2025).
URL http://arxiv.org/abs/2504.15711

[48] J. Grillenberger, C. Baumgarten, M. Seidel, The High Intensity Proton Accelerator Facility, SciPost Physics Proceedings (2021) 002doi:10.21468/SciPostPhysProc.5.002.

[49] D. Kiselev *et al.*, The Meson Production Targets in the high energy beamline of HIPA at PSI, SciPost Physics Proceedings (2021) 003doi:10.21468/SciPostPhysProc.5.003.

[50] G. Cavoto *et al.*, A photogrammetric method for target monitoring inside the MEG II detector, Review of Scientific Instruments 92 (2021). doi:10.1063/5.0034842.

[51] D. Palo *et al.*, Precise photographic monitoring of MEG II thin-film muon stopping target position and shape, Nucl. Instrum. Meth. A 944 (2019) 162511. doi:10.1016/j.nima.2019.162511.

[52] H. Nishiguchi, An Innovative Positron Spectrometer to Search for the Lepton Flavour Violating Muon Decay with a Sensitivity of 10^{-13}, Ph.D. thesis, The University of Tokyo (2008).
URL https://meg.web.psi.ch/docs/theses/nishiguchi_phd.pdf

[53] A. Baldini *et al.*, Gas distribution and monitoring for the drift chamber of the MEG II experiment, Journal of Instrumentation 13 (2018) P06018–P06018. doi:10.1088/1748-0221/13/06/P06018.

[54] A. Baldini *et al.*, Detailed analysis of chemical corrosion of ultra-thin wires used in drift chamber detectors, Journal of Instrumentation 16 (2021) T12003. doi:10.1088/1748-0221/16/12/T12003.

[55] M. Nishimura *et al.*, Full system of positron timing counter in MEG II having time resolution below 40 ps with fast plastic scintillator readout by SiPMs, Nucl. Instrum. Meth. A 958 (2020) 162785. doi:10.1016/j.nima.2019.162785.

[56] G. Boca *et al.*, The laser-based time calibration system for the MEG II pixelated Timing Counter, Nucl. Instrum. Meth. A 947 (2019) 162672. doi:10.1016/j.nima.2019.162672.

[57] G. Boca *et al.*, Timing resolution of a plastic scintillator counter read out by radiation damaged SiPMs connected in series, Nucl. Instrum. Meth. A 999 (2021) 165173. doi:10.1016/j.nima.2021.165173.

[58] S. Ogawa, Liquid xenon detector with highly granular scintillation readout to search for $\mu^+ \to e^+\gamma$ with sensitivity of 5×10^{-14} in MEG II experiment, Ph.D. thesis, The University of Tokyo (2020).
URL https://meg.web.psi.ch/docs/theses/ogawa_phd.pdf

[59] S. Kobayashi, Full Commissioning of Liquid Xenon Scintillation Detector to Search for $\mu^+ \to e^+\gamma$ with the Highest Sensitivity in MEG II Experiment, Ph.D. thesis, The University of Tokyo (2022).
URL https://meg.web.psi.ch/docs/theses/kobayashi_phd.pdf

[60] E. Aprile, T. Doke, Liquid xenon detectors for particle physics and astrophysics, Reviews of Modern Physics 82 (2010) 2053–2097. doi:10.1103/RevModPhys.82.2053.

[61] K. Fujii *et al.*, High-accuracy measurement of the emission spectrum of liquid xenon in the vacuum ultraviolet region, Nucl. Instrum. Meth. A 795 (2015) 293–297. doi:10.1016/j.nima.2015.05.065.

[62] S. Kubota, M. Hishida, J. Raun, Evidence for a triplet state of the self-trapped exciton states in liquid argon, krypton and xenon, Journal of Physics C: Solid State Physics 11 (1978) 2645–2651. doi:10.1088/0022-3719/11/12/024.

[63] S. Mihara, MEG liquid xenon detector, Journal of Physics: Conference Series 308 (2011) 012009. doi:10.1088/1742-6596/308/1/012009.

[64] A. Baldini *et al.*, Absorption of scintillation light in a 100 l liquid xenon γ-ray detector and expected detector performance, Nucl. Instrum. Meth. A 545 (2005) 753–764. doi:10.1016/j.nima.2005.02.029.

[65] M. Berger *et al.* Xcom: Photon cross sections database [online] (2010). doi:10.18434/T48G6X.
URL https://www.nist.gov/pml/xcom-photon-cross-sections-database

[66] S. Mihara *et al.*, Development of a method for liquid xenon purification using a cryogenic centrifugal pump, Cryogenics 46 (2006) 688–693. doi:10.1016/j.cryogenics.2006.04.003.

[67] T. Haruyama, Development of a High-Power Coaxial Pulse Tube Refrigerator for a Liquid Xenon Calorimeter, in: AIP Conference Proceedings, Vol. 710, AIP, 2004, pp. 1459–1466. doi:10.1063/1.1774839.

[68] Y. Nishimura, A Search for the Decay $\mu^+ \to e^+\gamma$ Using a High-Resolution Liquid Xenon Gamma-Ray Detector, Ph.D. thesis, The University of Tokyo (2010).
URL https://meg.web.psi.ch/docs/theses/nishimura_phd.pdf

[69] H. Jin *et al.*, It's a trap! On the nature of localised states and charge trapping in lead halide perovskites, Materials Horizons 7 (2020) 397–410. doi:10.1039/C9MH00500E.

[70] Hamamatsu photonics [online, cited 29th April 2025].
URL https://www.hamamatsu.com

[71] K. Ieki *et al.*, Large-area MPPC with enhanced VUV sensitivity for liquid xenon scintillation detector, Nucl. Instrum. Meth. A 925 (2019) 148–155. doi:10.1016/j.nima.2019.02.010.

[72] K. Ieki *et al.*, Study on degradation of VUV-sensitivity of MPPC for liquid xenon scintillation detector by radiation damage in MEG II experiment, Nucl. Instrum. Meth. A 1053 (2023) 168365. doi:10.1016/j.nima.2023.168365.

[73] Toyoda gosei co., ltd. [online].
URL https://www-jlc.kek.jp/~tauchi/index/LXeTPC/meetings/d070524-components/LED/E1L49_xxxxx_JEA.pdf

[74] Kingbright electronic co, ltd [online, cited 29th April 2025].
URL https://www.kingbright.com/attachments/file/psearch/000/00/20160808bak/KA-3021QBS-D(Ver.7B).pdf

[75] K. Technologies. 81150A Pulse Function Arbitrary Noise Generator [online].
URL https://www.keysight.com/product/81150A/81150a-pulse-function-arbitrary-noise html

[76] A. Baldini *et al.*, A radioactive point-source lattice for calibrating and monitoring the liquid xenon calorimeter of the MEG experiment, Nucl. Instrum. Meth. A 565 (2006) 589–598. doi:10.1016/j.nima.2006.06.055.

[77] J. Adam *et al.*, Calibration and monitoring of the MEG experiment by a proton beam from a Cockcroft–Walton accelerator, Nucl. Instrum. Meth. A 641 (2011) 19–32. doi:10.1016/j.nima.2011.03.048.

[78] A. Papa, Search for the Lepton Flavour Violation in $\mu \rightarrow e\gamma$. The calibration methods for the MEG experiment., Ph.D. thesis, University of Pisa (2009).
URL https://meg.web.psi.ch/docs/theses/Angela.pdf

[79] J. Spuller *et al.*, A remeasurement of the Panofsky ratio, Physics Letters B 67 (1977) 479–482. doi:10.1016/0370-2693(77)90449-X.

[80] A. Papa *et al.*, A liquid hydrogen target for the calibration of the MEG-II LXe calorimeter, Nucl. Instrum. Meth. A 1069 (2024) 169836. doi:10.1016/j.nima.2024.169836.

[81] B. Vitali *et al.*, A liquid hydrogen target to fully characterize the new MEG II liquid xenon calorimeter, Nucl. Instrum. Meth. A 1049 (2023) 168020. doi:10.1016/j.nima.2023.168020.

[82] D. Kaneko, The final result of $\mu^+ \rightarrow e^+\gamma$ search with the MEG experiment, Ph.D. thesis, The University of Tokyo (2016).
URL https://meg.web.psi.ch/docs/theses/kaneko_phd_2ed.pdf

[83] A. Matsushita, Calibration and Timing Resolution Evaluation of Liquid Xenon Gamma Ray Detector in MEG II experiment, Master's thesis, The University of Tokyo (2023).
URL https://meg.web.psi.ch/docs/theses/matsushita_master.pdf

[84] R. Iwai, Background identification system in MEG II experiment based on high-rate scintillation detector with SiPM readout, Journal of Instrumentation 12 (2017) C02023–C02023. doi:10.1088/1748-0221/12/02/C02023.

[85] M. Francesconi *et al.*, The WaveDAQ integrated Trigger and Data Acquisition System for the MEG II experiment, Nucl. Instrum. Meth. A 1045 (2023) 167542. doi:10.1016/j.nima.2022.167542.

[86] L. Galli *et al.*, WaveDAQ: An highly integrated trigger and data acquisition system, Nucl. Instrum. Meth. A 936 (2019) 399–400. doi:10.1016/j.nima.2018.07.067.

[87] Midas [online, cited 28th April 2025].
URL https://daq00.triumf.ca/MidasWiki/

[88] S. Ritt, The DRS chip: cheap waveform digitizing in the GHz range, Nucl. Instrum. Meth. A 518 (2004) 470–471. doi:10.1016/j.nima.2003.11.059.

[89] S. Ritt, Design and performance of the 6 GHz waveform digitizing chip DRS4, in: 2008 IEEE Nuclear Science Symposium Conference Record, IEEE, 2008, pp. 1512–1515. doi:10.1109/NSSMIC.2008.4774700.

[90] D. Nicolo *et al.*, Real-Time Particle Identification in Liquid Xenon, IEEE Transactions on Nuclear Science 68 (2021) 2630–2636. `doi:10.1109/TNS.2021.3099296`.

[91] S. Agostinelli *et al.*, Geant4–a simulation toolkit, Nucl. Instrum. Meth. A 506 (2003) 250–303, see also `https://geant4.web.cern.ch`. `doi:10.1016/S0168-9002(03)01368-8`.

[92] H. Schindler, R. Veenhof, Garfield++ user guide (version 2025.1) (2025).
URL `https://garfieldpp.web.cern.ch/documentation/`

[93] The spice home page [online, cited 25th April 2025].
URL `https://bwrcs.eecs.berkeley.edu/Classes/IcBook/SPICE/`

[94] T. Iwamoto *et al.*, The liquid xenon detector for the MEG II experiment to detect 52.8 MeV *upgamma* with large area VUV-sensitive MPPCs, Nucl. Instrum. Meth. A 1046 (2023) 167720. `doi:10.1016/j.nima.2022.167720`.

[95] M. Nishimura, Positron Timing Mesurement to Search for Lepton Flavor Violating Decay in MEG II, Ph.D. thesis, The University of Tokyo (2018).
URL `https://meg.web.psi.ch/docs/theses/miki_phd.pdf`

[96] M. Usami, Innovative positron spectrometer for $\mu^+ \to e^+\gamma$ search beyond 10^{-13} sensitivity with most intense μ^+ beam, Ph.D. thesis, The University of Tokyo (2021).
URL `https://meg.web.psi.ch/docs/theses/usami_doctor.pdf`

[97] A. M. Baldini *et al.*, Performances of a new generation tracking detector: the MEG II cylindrical drift chamber, The European Physical Journal C 84 (2024) 473. `doi:10.1140/epjc/s10052-024-12711-y`.

[98] R. Frühwirth, Application of Kalman filtering to track and vertex fitting, Nucl. Instrum. Meth. A 262 (1987) 444–450. `doi:10.1016/0168-9002(87)90887-4`.

[99] R. Frühwirth, A. Strandlie, Track fitting with ambiguities and noise: A study of elastic tracking and nonlinear filters, Computer Physics Communications 120 (1999) 197–214. `doi:10.1016/S0010-4655(99)00231-3`.

[100] J. Rauch, T. Schlüter, Genfit — a generic track-fitting toolkit, Journal of Physics: Conference Series 608 (2015) 012042. `doi:10.1088/1742-6596/608/1/012042`.

[101] K. Yamamoto *et al.*, Photon energy reconstruction with the MEG II liquid xenon calorimeter, EPJ Web of Conferences 320 (2025) 00030. `doi:10.1051/epjconf/202532000030`.

[102] S. Nakaura, Development of Radiative Decay Counter for ultimate sensitivity of MEG II experiment, Master's thesis, The University of Tokyo (2015).
URL `https://meg.web.psi.ch/docs/theses/nakaura_master.pdf`

[103] S. Kobayashi *et al.*, Precise measurement of 3D-position of SiPMs in the liquid xenon gamma-ray detector for the MEGII experiment, Nucl. Instrum. Meth. A 936 (2019) 189–191. `doi:10.1016/j.nima.2018.10.170`.

[104] T. Libeiro *et al.*, Novel X-ray scanning technique for in-situ alignment of photo-detectors in the MEGII calorimeter, Nucl. Instrum. Meth. A 1048 (2023) 167901. `doi:10.1016/j.nima.2022.167901`.

[105] R. Umakoshi, Study on the Radiation Damage of the VUV-MPPC in the MEG II Liquid Xenon Detector, Master's thesis, The University of Tokyo (2025).
URL https://meg.web.psi.ch/docs/theses/umakoshi_master.pdf

[106] P. L. Slocum, The Panofsky Ratio, and the Response of the PIBETA Calorimeter to Photons and Positrons, Ph.D. thesis, University of Virginia (1999).
URL http://pibeta.phys.virginia.edu/docs/publications/penny_diss/slocum_diss.pdf

[107] V. Blobel, Software alignment for tracking detectors, Nucl. Instrum. Meth. A 566 (2006) 5–13. doi:10.1016/j.nima.2006.05.157.

[108] C. W. Fabjan, F. Gianotti, Calorimetry for particle physics, Reviews of Modern Physics 75 (2003) 1243–1286. doi:10.1103/RevModPhys.75.1243.

[109] R. Barlow, Extended maximum likelihood, Nucl. Instrum. Meth. A 297 (1990) 496–506. doi:10.1016/0168-9002(90)91334-8.

[110] G. J. Feldman, R. D. Cousins, Unified approach to the classical statistical analysis of small signals, Physical Review D 57 (1998) 3873–3889. doi:10.1103/PhysRevD.57.3873.

[111] R. Eichler et al., IMPACT conceptual design report, PSI Bericht (22-01) (2022).
URL https://www.dora.lib4ri.ch/psi/islandora/object/psi%3A41209

[112] S. Kobayashi, Research on precise gamma-ray position measurement with MEG II liquid xenon detector, Master's thesis, The University of Tokyo (2019).
URL https://meg.web.psi.ch/docs/theses/kobayashi_master.pdf

[113] M. Szydagis *et al.*, A review of NEST models for liquid xenon and an exhaustive comparison with other approaches, Frontiers in Detector Science and Technology 2 (2025). doi:10.3389/fdest.2024.1480975.

[114] A. Vaswani *et al.*, Attention is all you need (2017).
URL http://arxiv.org/abs/1706.03762

[115] S. V. Stroud *et al.*, Transformers for charged particle track reconstruction in high energy physics (2024).
URL http://arxiv.org/abs/2411.07149

[116] F. Scarselli *et al.*, The graph neural network model, IEEE Transactions on Neural Networks 20 (2009) 61–80. doi:10.1109/TNN.2008.2005605.

[117] J. Duarte, J.-R. Vlimant, Graph Neural Networks for Particle Tracking and Reconstruction, WORLD SCIENTIFIC, 2022, pp. 387–436. doi:10.1142/9789811234033_0012.

[118] K. Yamamoto *et al.*, Development of ultra-low mass and high-rate capable RPC based on Diamond-Like Carbon electrodes for MEG II experiment, Nucl. Instrum. Meth. A 1054 (2023) 168450. doi:10.1016/j.nima.2023.168450.

[119] K. Ieki *et al.*, Prototype study of 0.1 % X_0 and MHz/cm^2 tolerant Resistive Plate Chamber with Diamond-Like Carbon electrodes, Nucl. Instrum. Meth. A 1064 (2024) 169375. doi:10.1016/j.nima.2024.169375.

[120] M. Takahashi *et al.*, Development of the high-rate capable DLC-RPC based on the current evacuation pattern, Journal of Instrumentation (Submitted) (2025).
URL http://arxiv.org/abs/2501.05128

[121] M. Takahashi *et al.*, Radiation hardness studies of RPC based on diamond-like carbon electrodes for MEG II experiment, Nucl. Instrum. Meth. A 1066 (2024) 169509. doi:10.1016/j.nima.2024.169509.